THE NIELS BOHR INSTITUTE

FACULTY OF SCIENCE
UNIVERSITY OF COPENHAGEN
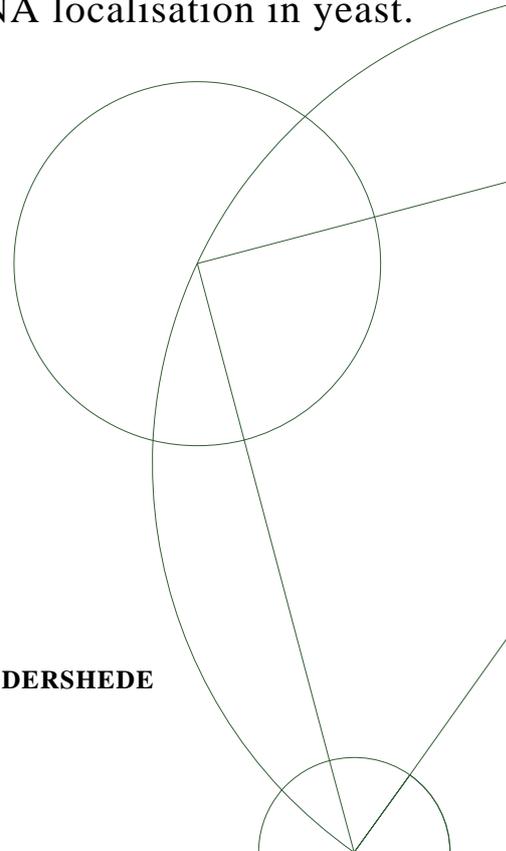
PhD thesis

MARIE DOMANGE JORDÖ

OPTICAL STUDIES OF TWO BIOPHYSICAL MODEL SYSTEMS:

Vesicle deformation and DNA localisation in yeast.

ACADEMIC SUPERVISOR : LENE ODDERSHEDE

Submitted: 13th of October 2010

Abstract

We have looked at two model systems commonly used in biophysics and biology; giant unilamellar vesicles (GUVs) and the fission yeast *Schizosaccharomyces pombe* (*S. pombe*). GUVs can be deformed by short electric pulses in the presence of 80 nm gold particles. This gives rise to cylindrical deformations, either tube-like or disc-like, depending on the conductivity ratio between the inner and outer vesicle solutions. Although the participation of the gold particles in the directionality of the deformation is unclear, we have shown that they are likely to contribute to the flattening of the deformed vesicles. We also studied the deformation of GUVs by means of optical tweezers. Repeated exposure to the focused laser light led to a decrease in vesicle size followed by the formation of vesicle aggregates. Vesicle size and the phase of its bilayer largely influences the degree of deformation at a given laser power. We believe that the observed deformations are due to the scattering force pushing the membrane in the direction of propagation of the light. The last chapter looks at silencing in *S. pombe*. The heterochromatic part of the mating-type region in fission yeast is delimited by two so-called boundary elements, *IR-L* and *IR-R*. By replacing *IR-R* with a piece of rDNA a strong silencing of the mating-type region as well as its relocalisation closer to the nucleolus was observed. The distance in 3D between the mating-type region and the nucleolus was measured using a custom made Matlab program. We are currently investigating possible silencing mechanisms.

Preface

This thesis summaries three years of PhD in biophysics in the broad sense of the term. It took me from the field of membrane physics, I had started to explore during my master thesis, into the world of molecular biology and genetics. To me biophysics is an exciting field since it is by definition multidisciplinary. It removes walls between sister-branches of science that during the past centuries got more and more separated. This poses the great challenge of taking advantage of each others knowledge and techniques. Looking at a problem from different view points can only lead to a better understanding of the studied system. We have come to speak different dialects of science, but the language barrier can be overcome. I truly believe the Niels Bohr Institute and the Biology Institute at the University of Copenhagen are such places were scientists take pleasure in collaborating not only across the park, but also across the boarder between physics and biology. Let us hope that this will be allowed to develop and flourish.

We will present two experimental model systems, each representing one type of approach; giant unilamellar vesicles (GUVs) and the unicellular eukaryote *Schizosaccharomyces Pombe*. The first approach, illustrated here by the GUVs, is the following. By getting a deeper physical understanding for each constituent of a system one can better understand the whole. As a model system, GUVs are becoming increasingly flexible in their degree of complexity. The properties of pure lipid membranes as well as biological membranes, such as lung surfactant, can be studied in a cell sized system. Additional lipid components or proteins can easily be added.

This model based approach is much more difficult when it comes to gene regulation and expression. Of course single pathways can be studied, but experimentally they can not be taken out of context, in this case the cell. Everything is to some degree connected. To learn something about the role of one component you need the rest of the system to function normally. *S. Pombe* presents the advantage of being well characterised and relatively easy to modify. Together with the budding yeast *Saccharomyces cerevisiae*, *S. pombe* is the most common model system for unicellular eukaryotes. Since they parted evolutionarily several hundred million years ago, comparing the two make it possible to identify conserved features in higher eukaryotes.[46]

The first part of the thesis is called **Optical and electrodeformation of lipid vesicles**. After a short introduction to lipid membranes and GUVs more specifically, we will present results on the deformation of vesicles by short electric pulses in the presence of gold nanoparticles. The last chapter of Part I deals with the deformation of vesicles by means of optical tweezers. For both studies, the results will be outlined followed by a discussion of possible deformation mechanisms. The second part of the thesis, **Nuclear organisation and silencing** touches the subject of gene silencing in heterochromatic regions. The mating-type region, one of the few heterochromatic regions of *S. Pombe*, was modified by the insertion of a piece of rDNA replacing one of its boundary elements. Silencing and localisation of the region was then characterised. Current efforts are now put into identifying the underlying mechanisms.

Acknowledgments

Contents

Part I

Optical and electrodeformation of lipid vesicles

CHAPTER 1

Introduction

Part I is concerned with the deformation of lipid membranes by electric fields. In this introduction we will present the basic properties of lipid membranes, electroformation as a method to form giant unilamellar vesicles (GUVs) and discuss their use as a model system. Chapter 2 discusses the influence of gold nanoparticles on the shape adopted by giant unilamellar vesicles exposed to short electric pulses, whereas Chapter 3 looks at the effect of tightly focused laser light on GUVs.

Electrodeformation and optical trapping are only two out of many techniques that can be used to study the physical properties of lipid membranes deformations. Other commonly used methods include analysis of the thermal fluctuations in shape, using micropipette aspiration where a single GUV is held and stretched, and studying the deformations of GUVs in a shear flow.[35]

By studying the deformations induced by thermal or external forces, it is possible to gain information about the elastic moduli of the lipid membrane, and how this depends on membrane composition and phase state.

1.1 Lipid membranes

Lipids can have various structures, head group sizes, chain lengths and charges. They are a chemically diverse group of molecules which includes fats, sterols, mono- and diglycerides, phospholipids, and others. Since we are interested in lipid bilayers this introduction will focus on the polar lipids. These have a hydrophilic head group and a hydrophobic tail. The tail is composed of two hydrocarbon chains (fatty acid chains), which are not necessarily

identical in length or saturation. The three types of lipids used in the two next chapters are all phospholipids. This means their head group and fatty acid chain are connected not only by a glycerol, but also by a phosphate group PO_4, see figure 1.1. L-α-phosphatidylcholine (EggPC) was used in the study of electrodeformation of vesicles in the presence of gold nanoparticles presented in Chapter 2. Instead a 50:50 mixture of 1,2-dimyristoyl-sn-glycero-3-phosphocholine (DMPC) and 1,2-dipalmitoyl-sn-glycero-3-phosphocholine (DPPC) was used in Chapter 3 on optically induced deformations of lipid membranes.
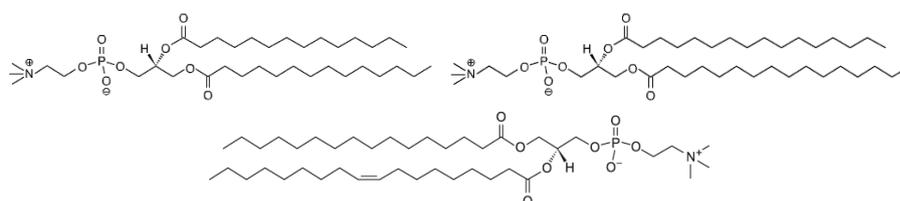
Figure 1.1: Molecular structure of the lipids used in this thesis: DMPC (top left), DPPC (top right) and EggPC (bottom). All three phospholipids have identical head groups. DMPC and DPPC differ in length by only two carbon atoms. They have fourteen respectively sixteen carbons in each fatty acid chain. EggPC has one 16:0 and one 18:1 chain, meaning that the chain that is eighteen carbons long carries a double bond. The structures were found on Avanti's homepage.

The amphiphilic nature of polar lipids gives them the property of self-assembling and forming 2D and 3D structures in the presence of water. Usually the lipids spontaneously form bilayers as the system tries to shield the hydrophobic tails from contact with the water phase, and finally forms uni- or multilamellar vesicles. Depending on the lipid to water ratio there are several other structures that are possible, such as micelles and inverse micelles, but also more uncommon structures have been found, such as cubic and inverse hexagonal phases. Lastly, if there are surfaces nearby, lipids will also migrate there and lower the surface tension, which is the reason for their use as soaps.

The phase of a material reflects its degree of order. Lipids have two sets of degrees of freedom, positional (translational) and orientational (configurational). The number and type of phases vary depending on the type of lipids present in the membrane. In the case of phospholipids, like the phosphocholines DMPC and DPPC that we are studying, we have a main phase transition between a solid-ordered and a liquid-disordered phase also called gel and fluid phases. Solid and liquid refer to the positional degree of free-

dom, i.e. the order in the head groups. Ordered and disordered refer to the orientational degree of freedom, i.e if the fatty acid chains are all oriented in the same direction or if they are bent [85]. Phosphocholines also have a pre-transition that precedes a ripple phase, where ripples form on the membrane surface, showing a periodicity of a few tens of nanometers. The conformation of the lipids in this phase is still unclear, but it has been suggested that the appearance of ripples is due to the melting of a small fraction of lipids at the pre-transition temperature, which then arrange to form linear arrays [56]. The amplitude of the ripple phases increase with chain length [103].

Also lipid mixtures show a phase transition. In the main transition phase coexistence of fluid and gel state lipids occurs, giving rise to domain formation. For instance in a DMPC/DPPC mixture, the DMPC having a lower melting temperature will in the transition mainly be in the liquid-disordered phase and the DPPC will mostly be in the solid-ordered phase. The existence of domains or so-called rafts in biological membranes is still debated. The phase transition is in theory a first order transition for the one component systems, but is in practice a much more continuous process with quite strong fluctuations [85]. By integrating heat capacity profiles like the ones shown in Figure 3.10 it is possible to measure the enthalpy that needs to be added in order for the phase transition to take place.

An important and interesting aspect of the phase transition is that not only do the microscopic configuration of the lipids change, but also the macroscopic properties of the membrane as a whole change. As the membrane undergoes the transition (melts), thickness decreases and the area increases, but more interestingly both the elastic moduli, fluctuation timescales, and membrane permeability have all been shown to change dramatically within the phase transition [56].

1.2 Vesicle formation

In this section we will discuss the subject of vesicle formation and more specifically electroformation. The protocols will be presented in the Material and Methods sections of the two following chapters. For a good review of current electroformation methods see reference [83]. This will rather be an overview of what is known about the phenomenon itself. Although a lot of expertise has been gained in the art of producing vesicles of various sizes and compositions, little is known about the actual mechanisms by which the vesicles are formed. In the case of electroformation, indium tin oxide coated coverslips (ITOs) [6] or platinum wires (Pt-wires) [8] are covered by a thin

lipid film and an electric field is applied across the two electrodes.

Experiments have been made were the sample was observed during vesicle formation [6][77]. The strength of the electric field and the thickness of the dried lipid film are two of the critical parameters for vesicle electroformation. The thinner the lipid film is, the higher the yield of unilamellar vesicles. 6μl of a 1 mg/ml lipid solution, spread over 1cm^2, would correspond to approximately twelve bilayers stacked on each other. Swelling occurs almost immediately after applying an electric field over the sample. According to Angelova et al. [6] structures with a circular contour grow to a size of approximately 10μm after what a fusion process starts. Vesicles fuse together and grow to be tens of μm in diameter and finally detach, letting new vesicles grow out of the lipid film. This was also observed by Mathivet et al. [77]. After approximately one hour the sample stays more or less unchanged. For successful electroformation one more condition has to be fulfilled. The temperature during vesicle formation should be well above the melting temperature [9]. One could imagine that this process would be favoured in the phase transition, where the membrane has a lower bending modulus and where it has been shown to be more permeable [16], but experience has shown that the lipid membrane has to be in the fluid phase in order for large vesicles to form.

So what drives the vesicles to form? Observations were made of a oscillating motion of all the vesicles in a sample matching the frequency of the applied electric field. It could be controlled by varying the intensity and the frequency of the field. This mechanical agitation must at least be one of the mechanisms of vesicle electroformation [6]. Also, lowering the frequency and increasing the amplitude facilitates the detachment of vesicles after formation. The formation of GUVs requires lipid layer separation and bending. It has been shown that AC fields have a strong effect on the normal forces that cause repulsion between the lipid layers. They can potential influence the bilayer topology as well. Pore formation can occur, favouring the hydration of the lipid film, thus facilitating vesicle formation [9][37]. We will describe in more detail the interaction between lipid bilayers and AC fields in section 2.2.1 of Chapter 2.

Other methods can be used to form GUVs, such as the gentle hydration and the solvent evaporation methods. The pros and cons of these different methods have been investigated in [115] and [9]. Electroformation seems to give rise to a higher yield of non-defect unilamellar vesicles with a more homogeneous size distribution (mostly between 10 and 30μm in diameter), compared to the gentle hydration method. In return, the latter can be used for making GUVs containing a quite high percentage of charged lipids, which is difficult to obtain using electroformation [115].

1.3 The giant unilamellar vesicle as a model system

Biological membranes are composed of hundreds of different lipids, as well as many proteins and protein complexes [56, p. 29]Their lipid composition varies a lot with the type of tissue they are part of, some being particularly rich in e.g. sterols, unsaturated, or charged lipids. These systems are highly complex, but the basic physics governing lipid membrane behaviour stays the same. In order to systematically investigate properties such as elasticity, permeability or conductance, simplifying the system is necessary. Many groups work with two or three component systems, investigating for example the role of cholesterol or unsaturated lipids [47].

Without entering the discussion of the existence or non-existence of domains or so-called rafts in biological membranes, it is interesting to note that growth or body temperature of organisms have been shown to lie just above the melting transition of their lipid membranes. As example we can take E. coli. which is known to adapt its lipid composition to a new growth temperature [57]. Factors such as pH, salinity, lateral pressure, molecules (anesthetics), binding of proteins can shift the phase transition either to higher or lower temperatures [56]. This is in itself an indication of the importance of carefully regulating the phase state (and therefore physical properties) of the membranes.

Attempts to make giant unilamellar vesicles out of native membranes have been successfully conducted [84]. Vesicles were grown starting with intact red blood cells, hence containing not only lipids, but also proteins. Vesicle electroformation has also been shown possible under physiological conditions, i.e. high salinity [110][84]. It is now possible to tune the lipid composition and growth conditions of GUVs in order to focus on more general or more cell type specific properties of lipid membranes.

CHAPTER 2

Electrodeformation of lipid membranes

2.1 Introduction

This study was carried out during a visit to the Biophysics group of Dr. Rumiana Dimova at the Max Planck Institute for Colloids and Interfaces, Golm, Germany. My stay there was part of the EU Marie Curie Early Stage Training program on biomimetics in which I participated during the first half of my PhD. The focus of Dimova's groups lies in understanding the interaction between lipid membranes and electric fields, both AC (alternating current) fields and short DC (direct current) pulses. More specifically, the aim of this project was to characterise the effect of colloidal gold particles on the shape adopted by vesicles during a strong DC pulse. This work was inspired by prior results showing cylindrical deformation of vesicles exposed to the same type of pulses in the presence of salt [114].

The behaviour of GUVs in electric fields is of general interest since both AC fields and DC pulses are widely used in medicine. Poration especially is a popular method for transfection of DNA into cells [89][107], drug delivery to cancer cells [45] or even cell fusion [91]. To induce fusion an AC field is first applied in order to align the cells, followed by a short pulse to porate and induce fusion. In order to better understand the underlying mechanisms of electrodeformation and poration, GUVs can serve as model system for cells.

Gold nanoparticles are also increasingly popular in research concerning new drug delivery systems. They can be functionalised to target cancer cells specifically [62]. They can also be used for photothermal therapy [108] or even for imaging [65]. In addition to biocompatibility, they also stand out as being very stable [32]. Particles potentially used for medical purposes are smaller than the ones we used in this study. Typically they would have a

radius of about 10 nm, whereas ours were 80 nm in diameter. The reason for this was that we thought of a different application for these particles. They are easily trapped by optical tweezers [54] and could therefore be used as handles inside cells for accurate force measurements.

On a more physical note, a lot can be learned about the physical properties of lipid membranes by analysing their response to deformations, for example the effect of cholesterol on the bending rigidity [47]. In short a lot can be gained from understanding the interaction between electric fields, lipids and gold nanoparticles, not least the pleasure in observing these remarkable shape changes.

2.2 Background

In order to put the present work into context, we will make an overview of previous findings in Dimova's group, as well as mention the work of other groups. We will describe the behaviour of GUVs exposed to AC fields and DC pulses, putting emphasis on the shape transitions that can occur as a response to changes in field frequency and conductivity conditions. What is presented in this introduction only concerns electrodeformation in the presence of salt.

2.2.1 Vesicle response to alternating electric fields

Vesicles exposed to an AC field adopt ellipsoidal shapes [35]. In the simplest case, in the absence of added ions and particles and at low frequencies, vesicles deform as prolates parallel to the electric field []. In general, the type of shape and the degree of deformation depends on factors such as the field strength E, the field frequency ω and the conductivities of the inner, λ_{in}, and outer, λ_{out}, vesicle solutions. Prolate and oblate (perpendicular to the field) deformations have been reported by several groups [][][], but they only partially explored the range of conductivity ratios and field frequencies available. Dimova's group constructed a morphological diagram showing the shapes of vesicles subjected to varying conductivity conditions and AC fields, see Figure 2.1 [7]. They reported three types of shape transitions. Two of them are related to the frequency of the field (Transitions 1 and 3). At high frequencies (several MHz) and independently of the previous deformation (prolate or oblate), the vesicles adopt a spherical shape. This corresponds to transition 1 in Figure 2.1. It could be explained by the fact that ions no longer follow the oscillations of the electric field. In the MHz regime, the

travel distance of an ion is of the order of nanometers. Transition 3 takes place in the kHz regime. Prolate vesicles become oblate with increasing frequency. The second type of shape transition is transition 2. It depends solely on the conductivity ratio $x = \lambda_{in}/\lambda_{out}$, where λ_{in} is the conductivity inside the vesicle and λ_{out} the conductivity of the exterior solution. At intermediate field frequencies (kHz to MHz regime), the vesicles deform into prolates if $x > 1$ and oblates if $x < 1$.[7]
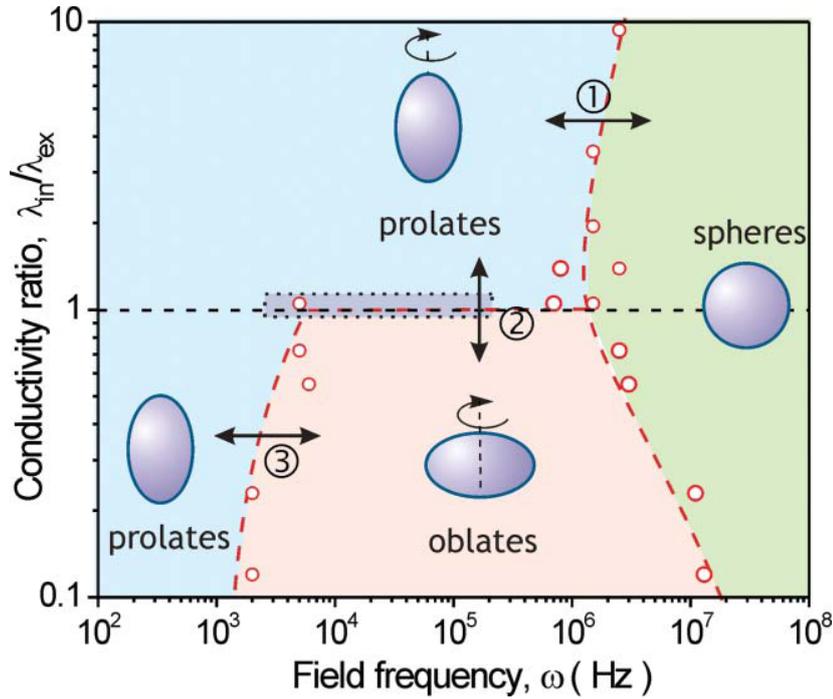
Figure 2.1: Morphological diagram of the shape adopted by vesicles subjected to AC fields at different conductivity conditions and for various field frequencies. The open circles correspond to experimental data, and the dashed lines are a guide to the eye for the boundaries between different shape regions. The electric field is pointing upwards. This figure was published by Dimova's group in reference [37].

These AC field dependent shape transitions have been studied and to some extent predicted theoretically. The first theoretical calculations for GUVs in water were presented by Winterhalter and Helfrich [134]. There are also more recent studies, such as the one from Peterlin et al. [105] or Vlahovska et al. [133] propose a model where electrohydrodynamic (EHD) flows are responsible for the oblate deformations. This theory is based on a force balance rather than an energy approach.

2.2.2 Vesicle response to DC-pulses

In the absence of salt, a vesicle will adopt a prolate shape when exposed to a DC pulse (see Figure 2.2B) [114][36]. In the presence of salt, a flattening of the vesicle can be observed leading to a cylindrical deformation, either tube-like (parallel to the electric field) or disc-like (perpendicular to the electric field). See Figure 2.2C and E. This flattening only lasts for up to a millisecond. These transient deformations could be observed by the group of Dimova due to the high temporal resolution of their experimental setup (20 000 and 30 000 fps).[114] In Figure 2.2F the aspect ratio, a/b, of the vesicles is plotted as a function of the conductivity ratio $x = \lambda_{in}/\lambda_{out}$, defined in the previous section. For $x < 1$, $\lambda_{in} < \lambda_{out}$, the observed deformations were disc-like. For $x > 1$, $\lambda_{in} > \lambda_{out}$, the observed deformations were tube-like. For $x \sim 1$ the cross-section of the deformed vesicles appeared squared.[114] This is very similar to transition 2 depicted in Figure 2.1 for vesicles exposed to AC fields. The mechanism of the conductivity-dependent shape transition from prolate (tube-like) to oblate (disc-like) described for AC fields is also valid in the case of DC pulses [133]. It should be noted that it only accounts for the directionality of the deformation, and not for the vesicle flattening observed during the first few hundred microseconds after the beginning of the pulse. We will present a model for this in the Discussion based on what Riske and Dimova have proposed [114].

There have been some experimental studies conducted by other groups on small vesicles [] and GUVs [], even cells [], exposed to DC pulses, but none worked at temporal resolutions high enough to capture the cylindrical deformations observed by the group of Dimova. This is the starting point of this project conducted in their laboratory. We will now discuss the effect of gold nanoparticles on the shape adopted by vesicles exposed to strong DC pulses.
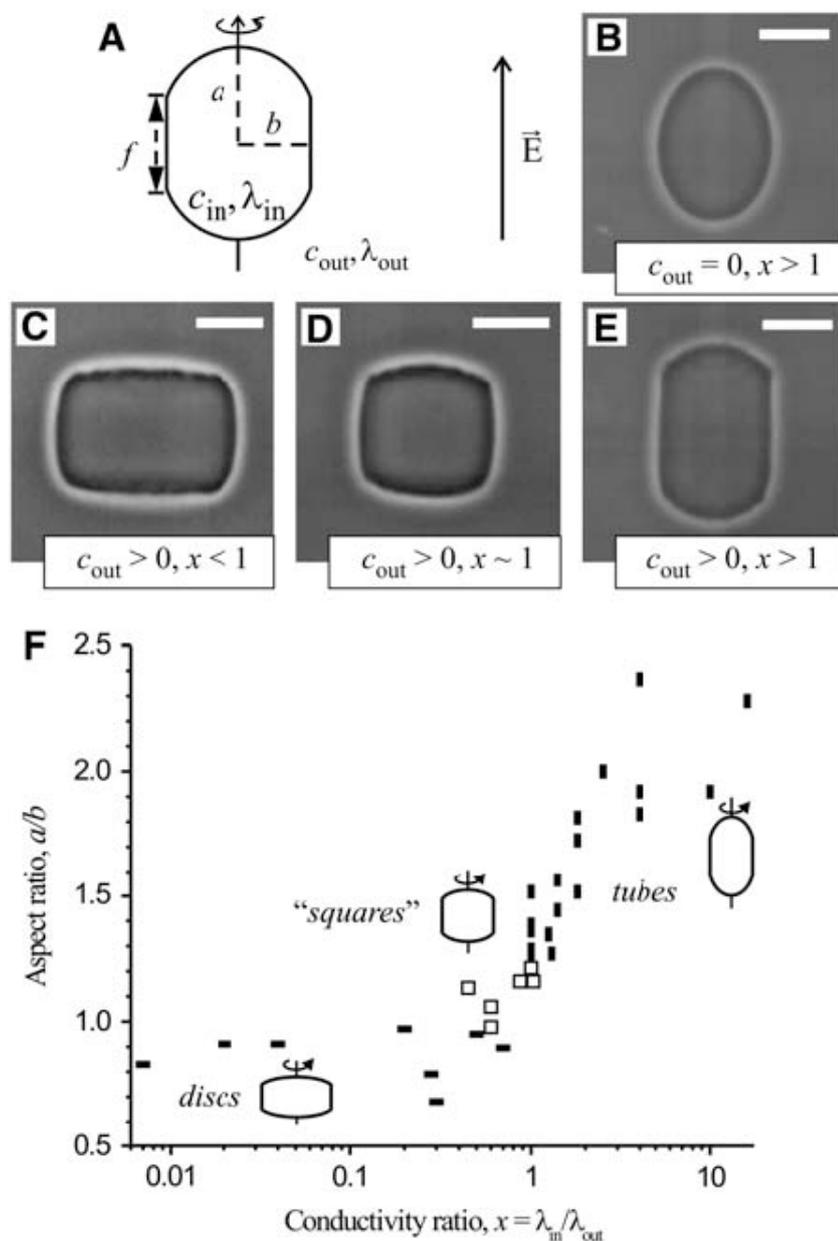
Figure 2.2: Vesicles deformed by a DC pulse under different conductivity conditions; **B)** In the absence of salt in the vesicle exterior, **C)** In the presence of salt and $x < 1$, **D)** In the presence of salt and $x \sim 1$, **E)** In the presence of salt and $x > 1$. The direction of the electric field is indicated by an arrow. The scale bars correspond to 17μm. **F)** shows vesicles maximum aspect ratio a/b as a function of conductivity ratio $x = \lambda_{in}/\lambda_{out}$. The duration of the pulses was 200μs and $E = 2kV/cm$.[114]

2.3 Materials and Methods

2.3.1 Sample preparation

Lipid solution

1 mg/ml samples of L-α-phosphatidylcholine (EggPC) were prepared by diluting a 100 mg/ml chloroform stock solution from Sigma-Aldrich. To allow for visualisation with confocal microscopy we added a fluorescent lipid-like dye, 1,1'-dioctadecyl-3,3,3',3'-tetramethylindocarbocyanine perchlorate (DiI), in the molar ratio DiI:lipids 1:500.

Gold solutions

The 80 nm gold nanoparticles (British Biocell International) we used were formed by the citrate reduction of a gold chloride solution [109]. The particles have a net negative charge and a citrate shell that keeps them in suspension. They will be characterised more in detail in section 2.4. 2 ml of the gold colloid solution, corresponding to a little more than the volume of the electroformation chamber, was spun down at 6000 rpm (rounds per minute) for 5 min. The supernatant was removed and a 100 mM sucrose solution was added to adjust the concentration. The eppendorf tube was then placed in a sonicator for 15 min . The gold solution was finally pushed through a filter with a pore size of 200 nm (Eppendorf) in order to remove large particle aggregates.

The preparation of the external solution, used during electrodeformation experiments, was identical except that a 107 mM glucose solution was added instead of the sucrose.

Some of the DC pulse experiments were conducted with the supernatant as interior or exterior solution. Between 50 and 200 μl of the aqueous solution in which the gold particles were suspended, were diluted in 2 ml 100 mM sucrose or 107 mM glucose solutions. We will refer to these solutions as 2.5 % to 10 % aqueous solutions. No or very few gold particles were then present.

2.3.2 Electroformation of giant unilamellar vesicles

Vesicles grown in the absence of gold

The vesicle electroformation procedure was the following. The electroformation chamber was made from two thick indium tin oxide coated coverslips (ITO) separated by a 2 mm thick teflon spacer. 12 μl of the 1 mg/ml EggPC solution was spread on each ITO and put into a vacuum incubator or a desiccator overnight. The chamber was assembled using silicon vacuum grease and paper clips. A syringe was then used to fill the chamber with 1.5 ml of a 100 mM sucrose solution. The electric connection between the ITOs and the wires was made using copper tape. The electroformation was carried out at 60 °C, well above the melting temperature of EggPC. The frequency of the electric field was set to 10 Hz and the voltage to 1.1 V. After one hour, it was changed to 5 Hz and 1.6 V and left for two hours in order to detach the vesicles from the ITO surface. The chamber was then gently opened with a scalpel and the vesicle solution was transferred into a little flask using a large pipette tip. The vesicle solution could be kept for a week at room temperature, if well protected from direct light. Vesicles were typically between 20 and 40 μm in diameter.

Vesicles grown in the presence of gold

Other vesicles were grown in the presence of 80 nm gold particles. The electroformation procedure was the same. What differed was the solution injected into the chamber. In this case, it was the gold/sucrose solution described in section 2.3.1 in the paragraph about gold solutions. The standard particle concentration was $2.2 \cdot 10^{10}$ particles/ml, but was varied for concentration dependence experiments.

2.3.3 Measurement of the gold colloids zeta potential

The zeta potential is the potential difference between the dispersion medium and the stationary layer of fluid around the dispersed particles [29]. It should not be confused with the surface potential of the particles. Colloids with a zeta potential between ± 40 and ± 60 mV are considered to have a good stability. This has to do with repulsion between the particles. The zeta potential of a dispersion is measured by applying an electric field across the sample. Particles in the dispersion will migrate toward the electrode of opposite charge with a velocity proportional to the magnitude of their zeta potential. This was measured using a zetasizer (Malvern).

2.3.4 The setup

The setup was identical to the one used in the previous studies reported in section 2.2. It consisted of a fast digital camera (HG-100K, Redlake) and a mercury lamp (HBO W/2) mounted on an inverted microscope (Axiovert 135, Zeiss). The mercury lamp was only used up to $10\,$s at the time during data recording to reduce sample heating. Riske et al. reported an increase in temperature of less than $2\,°$C after ten minutes of illumination of the sample [114]. A halogen lamp was used to select vesicles. We used a micro fusion chamber (see Figure 2.3) and the Multiporator from Eppendorf, commercialised for poration and fusion of cells. A pair of wire electrodes separated by $500\,\mu$m ensured a homogeneous field in the space between them.

Figure 2.3: Left: Micro fusion chamber from Eppendorf showing the electric connector and the sample hole with the two electrode wires. **Right:** Sketch of the gape between the two electrodes. The vesicles are shown as blue circles. The anode was on the side of the electric connector of the chamber.

2.3.5 The electrodeformation experiment

$40\,\mu$L of the sucrose vesicle solution, either with or without gold, was diluted in $850\,\mu$L of glucose with varying gold concentration. Because of the density difference between sucrose and glucose, the GUVs settled at the bottom of the electroporation chamber. The refractive index mismatch produced good optical contrast using a 20X Ph2 objective from Zeiss. A vesicle positioned between the two electrodes would be chosen. The multiporator was set to deliver a DC pulse of $200\,\mu$s and 170V ($E= 3.4\,$kV/cm). The mercury lamp was needed due to the short exposure time. It was turned on just prior to image acquisition and turned off immediately after. The acquisition rate was $20\,000$ frames per second, which corresponds to one image every $50\,\mu$s.

The same sample was used for three to five pulses. The chamber was then rinsed with millipore water and ethanol and dried under a stream of nitrogen, before filling it again with the wanted sample. Only vesicles with good contrast between interior and exterior solution were selected, indicating that they had not been subject to poration. Also the effect of multiple exposure would be interesting to study in itself. The experiment was carried out at room-temperature, well above the melting temperature $T_m = -10\,°\text{C}$ of EggPC [100], ensuring that the membrane was in the fluid phase.

2.4 Two types of cylindrical deformation

As mentioned earlier, DC pulses can induce vesicle poration and deformation. In the presence of ions an overall elongation as well as a flattening of the equatorial region can be observed. This gives rise to cylindrical shapes in the first phase of the deformation. We will focus this chapter on cylindrical deformations in the presence of 80 nm gold particles.

2.4.1 Characterisation of the pulse-induced deformations

The experiment was conducted both on vesicles grown in the absence and in the presence of gold particles. Although the electrodeformation conditions were identical, the vesicles deformed either perpendicular or parallel to the electric field, see Figure 2.4. Hence, the growth conditions influence the directionality of the deformation. We would expect the inner solutions of the two types of vesicle to be different.
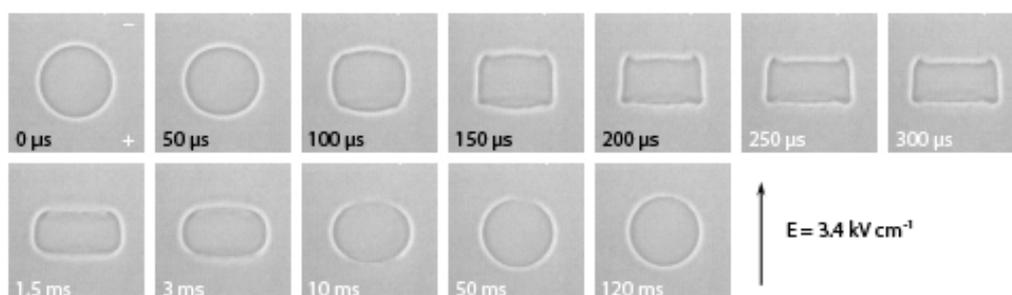
(a) **Vesicle grown in only sucrose** and exposed to a 200μs pulse with a field strength of 3.4 kV/cm. The field is on when the time is written in black. The exterior glucose solution had a gold nanoparticle concentration of $2.2 \cdot 10^{10}$particles/ml. This gave rise to a disc-like deformation.
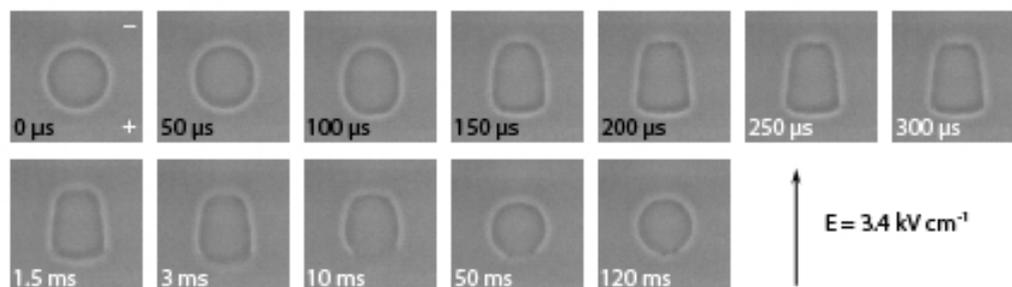
(b) **Vesicle grown in sucrose with a gold nanoparticle concentration of $2.2 \cdot 10^{10}$particles/ml** and exposed to a 200μs pulse (time in black) with a field strength of 3.4 kV/cm. The exterior glucose solution had a gold nanoparticle concentration of $2.2 \cdot 10^{10}$particles/ml, the same as in (a). This gave rise to a tube-like deformation.

Figure 2.4: Electrodeformation of vesicles grown either in the absence or the presence of gold nanoparticles.

We will use flattening and squaring as synonyms for cylindrical deformations. Disc-like and tube-like designates the orientation of the deformation, respectively perpendicular and parallel to the applied electric field.

Both in Figure 2.4a and 2.4b the squaring is first visible after 100μs. The cylindrical deformations last longer than the DC pulse itself. They subsist for up to a few milliseconds. In both cases, poration events are visible. They are characterised by a blurring of the vesicle contour or by dark eruptions of sucrose solution into the surrounding media. This is especially clear in Figure 2.4b, between 10 ms and 120 ms after the beginning of the pulse.

For both types of vesicles the electrodeformation conditions were the same. The DC pulse was $200 \mu s$ long and the field strength $E=$ 3.4 kVcm^{-1}. The only difference lied in the vesicle preparation. Vesicles formed in the absence of gold particles showed disc-like deformations, whereas vesicles formed in the presence of gold showed tube-like deformations. In earlier experiments on GUVs deformed by DC pulses in the presence of salt, it was the ratio between the inside and outside conductivities that was decisive for the resulting shape. If $\lambda_{in} > \lambda_{out}$ the vesicles would adopt a tube-like shape. Correspondingly, they would become disc-like if $\lambda_{in} < \lambda_{out}$.[114] We do not know if this is the case for vesicles deformed in the presence of gold nanoparticles. In order to investigate this, we will start by characterising the gold particles and discuss the potential presence of ions in the gold solution.

2.4.2 Characterisation of the gold colloids

Let us start by characterising the gold colloids used in the experiments. The zetasizer described in the material and methods section 2.3.3 was used both to verify the average size and measure the zeta potential of the gold particles, as well as to measure the conductivity at different gold concentrations. The mean size of a gold particle was measured to be 81.3 ± 3.9 nm in diameter.

For a sucrose solution with a gold concentration of $2.2 \cdot 10^{10}$ particles/ml, the zeta potential had a mean value of -55.9 ± 1.7 mV. It was measured to be a bit less at lower gold concentrations, for example -47.3 ± 4.8 mV at $2.2 \cdot 10^9$ particles/ml. This would indicate that the colloidal solution had a good stability [135]. Having a negative zeta potential, the particles migrate towards the anode during the pulse, but do they contribute to the conductivity?

The conductivity of the gold solution taken directly from the bottle, with a gold concentration of $2.2 \cdot 10^{10}$ particles/ml, was measured to be $240 \pm 2 \mu$S/cm. We spun it down and measured the conductivity of only the aqueous solution in which the colloids were suspended. We will refer to

Solution	Conductivity (μS/cm)
Gold solution directly from the bottle $2.2 \cdot 10^{10}$ part./ml	240$\pm$2
100% aqueous solution No particles	241$\pm$2.3
100mM sucrose solution with gold particles $2.2 \cdot 10^{10}$ part./ml	Between 17.6$\pm$1.5 and 33.8$\pm$4
100mM sucrose with 10% aqueous solution No particles	28.6$\pm$4.7
100mM sucrose	4
107mM glucose	2.5

Table 2.1: Table over conductivities measured for solutions containing 80 nm gold particles or only the aqueous solution in which they are normally suspended.

the particle-free aqueous solution as the aqueous solution. Without the gold particles the conductivity was $241 \pm 2.3 \, \mu$S/cm. Hence, the gold particles do not seem to contribute to the total conductivity of the solution. It has been shown that colloidal gold particles have a large molar conductivity, but due to their relatively low concentrations it is nearly impossible to detect with traditional methods, especially in the presence of salt [22].

We also looked at the conductivity of a 100 mM sucrose solution with a gold concentration of $2.2 \cdot 10^{10}$ particles/ml. Since we did not fully control how much of the aqueous solution was left, this measure was prone to quite large fluctuations from one sample to another. We measured it to be between 17.6$\pm$1.5 μS/cm and 33.8$\pm$4μS/cm. This is comparable to what we measured for a 100 mM sucrose with 10% aqueous solution, which has a conductivity of $28.6 \pm 4.7 \, \mu$S/cm. 100 μl is a reasonable upper estimate of the volume of aqueous solution left above the spun down gold after pipetting away the supernatant. It should be noted that the 100 mM sucrose and 107 mM glucose solutions have a low, but finite, conductivity of about 4 μS/cm and 2.5 μS/cm respectively. All conductivities reported above are shown in table 2.1.

We took confocal image of vesicles grown both in the absence and in the

presence of gold particles, see Figure 2.5. The lipid bilayer, marked with the lipid-like dye DiI, can be seen in green and the gold particles (in red) were visualised in reflection mode. Lipid molecules seemed to some extent to associate with gold particles in suspension, but we could not see any clear evidence of particles interacting with the lipid membrane of either type of vesicles. Rarely could we see particles present in the vesicle interior, even in the case of vesicles grown in a gold/sucrose solution. It is possible that particles could be out of focus, but still inside the observed vesicle, hence avoiding detection. We therefore scanned through the whole vesicle volume repeatedly. In about one out of twenty vesicles, we found gold particles. This could not account for the systematic tube-like deformation seen for vesicles grown in the presence of gold.
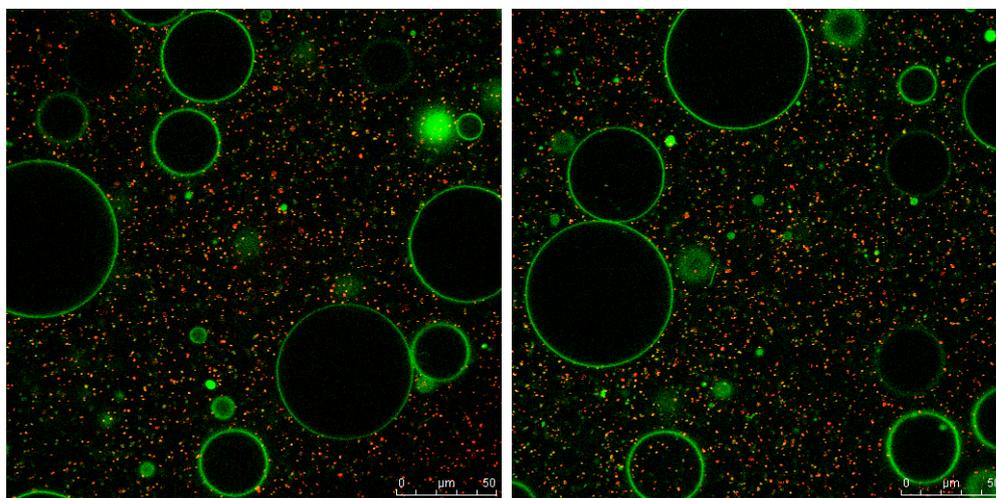
Figure 2.5: Confocal images of the equatorial cross-section of vesicles grown in a 100mM sucrose solution with 80 nm gold particles at a concentration of $4.4 \cdot 10^{10}$ particles/ml. The exterior solution was a 107mM glucose solution with 80 nm gold particles at a concentration of $4.4 \cdot 10^{10}$ particles/ml. The lipid membrane was marked with the fluorescent dye DiI and can be seen in green. The gold particles (in red) were visualised in reflection mode using the 514 nm band of the Argon laser. Only one vesicle shows gold particles in the vesicle interior. It can be found in the bottom left corner of the right-hand image.

In conclusion, even if the gold particles had contributed to the conductivity, it would not have explained the tube-like deformations observed for vesicles grown in the presence of gold. The particles did not seem imbedded in the lipid bilayer either, which could have contributed to a change in membrane elasticity. The only plausible explanation left is that ions are present

in the gold solutions, causing a difference between the conductivity inside and outside of the vesicle.

2.4.3 Counter ions

British Biocell International confirmed the presence of ions in the aqueous solution in which the gold colloids are suspended. They mentioned traces of tannic acid and potassium carbonate (K_2CO_3), but could not provide any accurate measurements of the actual ion concentrations. These ions were residues from the fabrication process. They also guaranteed that no surfactants were added to stabilise the colloids and keep them in suspension. In water potassium carbonate dissolves and forms potassium (K^+), bicarbonate ions (HCO_3^-) and hydroxide (OH^-) ions, contributing to the measured conductivity.

As mentioned in the previous section, the aqueous solution has a conductivity of $241 \pm 2.3\,\mu S/cm$. According to results kindly provided by Karmen Remde from Rumiana Dimova's group, this corresponds to a salt concentration of $2\,mM$ NaCl in $200\,mM$ glucose. At these relatively high conductivities, a difference of $100\,mM$ in the molarity of the glucose solution should not substantially affect the measured conductivity. In the previous study [114] inner and outer concentrations up to $3\,mM$ NaCl were explored. This would indicate that our experiment might in fact be a repetition of the previous work conducted with salt. We now want to address the role played by the gold particles themselves.

2.5 Do gold particles contribute to vesicle squaring?

From earlier studies we know that the ratio between the conductivity inside and outside of the vesicle governs the direction of the deformation. We now also know that only the ions present in the gold solution contribute to the conductivity. Although we cannot definitely exclude it, the gold particles are unlikely to influence the directionality of the deformations. This leads us to the question whether the gold particles participate in the squaring of vesicles or not. They have a negative zeta potential and would therefore be expected to migrate towards the anode during the pulse, potentially flattening the vesicles' equatorial region. We will in this section try to identify the role of both ions and particles in the squaring process.

2.5.1 Deformation without particles

First we wanted to test whether the aqueous solution in which the gold particles were suspended could, on its own, induce a squaring of vesicles exposed to a short electric pulse. As seen in the bottom row of the table in Figure 2.6, vesicles grown in sucrose with 10% aqueous solution show squaring. This leads to the conclusion that the ions present in the gold solution alone are enough to induce vesicle squaring in the first few hundred microseconds following a short DC pulse. Nevertheless, this does not exclude the possibility of a contribution from the gold particles themselves.

Vesicle Grown in \ External solution	Glucose and 2.2×10^{10} gold particles/ml	Glucose and 1mM NaCl	Glucose with 5% aqueous solution (no particles)
Sucrose			
Sucrose and 2.2×10^{10} gold particles/ml			
Sucrose and 0.2mM NaCl			
Sucrose with 10% aqueous solution (no particles)			
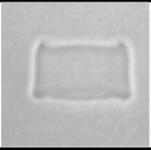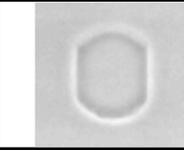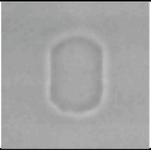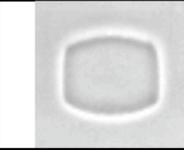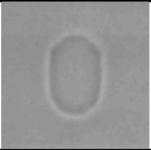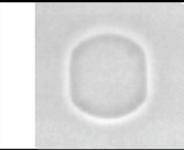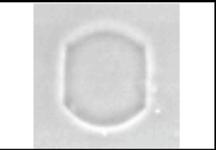
Figure 2.6: Table over deformation with varying internal and external solutions, thus conductivities. All vesicles were exposed to a $200\mu s$ DC pulse. $E = 2.6$ kV cm^{-1}. The internal vesicle solutions are all based on a 100mM sucrose solution, and the external solutions on a 107mM glucose solution.

Some of the inner and outer conditions we mentioned in section 2.4.2 are also summarised in this table. Looking at the second column, corresponding to a 1 mM NaCl external glucose solution, vesicles grown in a 100 mM sucrose solution with a gold concentration of $2.2 \cdot 10^{10}$ particles/ml (second row) show a similar behaviour to vesicles grown in a 100 mM sucrose solution with 10% aqueous solution (fourth row). The latter seems slightly more square than than the first, indicating a conductivity ratio closer to 1. We do not know the conductivity of the 1 mM NaCl and glucose solution, but we measured it to be $40.4 \pm 3.4\,\mu$S/cm for a 1mM NaCl and sucrose solution. Considering that glucose has a slightly lower conductivity than sucrose and that the conductivities of the two internal solutions was measured to be around $30\,\mu$S/cm (see section 2.4.2), this is consistent with the "square" vesicle cross-sections we observed.

2.5.2 Gold concentration dependence of the deformation

The following experiment was conducted on vesicles grown in sucrose without any gold particles or ions. A clear concentration dependent transition from a tube-like to a disc-like deformation could be observed with increasing gold concentration (see Figure 2.7). For the lowest explored concentration $c_{min} = 1.1 \cdot 10^8$ particles/ml, shown in Figure 2.7c, the vesicles exhibited a similar behaviour as in the absence of ions or particles, compare with the image in Figure 2.7a. The vesicles elongated in the direction of the field into a prolate shape. The particle concentration seems to influences the type of cylindrical deformation observed. At concentrations slightly above c_{min}, the vesicles adopted tube-like shapes parallel to the direction of the electric field. When the gold concentration was increased tenfold, 10 c_{min}, coexistence of "discs" and "tubes" occurred during the DC pulse, some of them almost looking "square" (2.7e and 2.7f). At even higher particle concentrations, the vesicles adopted only a disc-like shape (2.7g and 2.7h). This has been published in [36]. At that time we were not yet aware of the presence of ions in the gold solution. Of course, by varying the gold concentration we also varied the concentration of ions present in the exterior solution. No similar concentration dependent shape transition has been reported in the case of DC pulses in the presence of salt. We do not know if any systematic study has been conducted on sucrose filled vesicles (no salt in the vesicle interior) with increasing outer salt concentration.
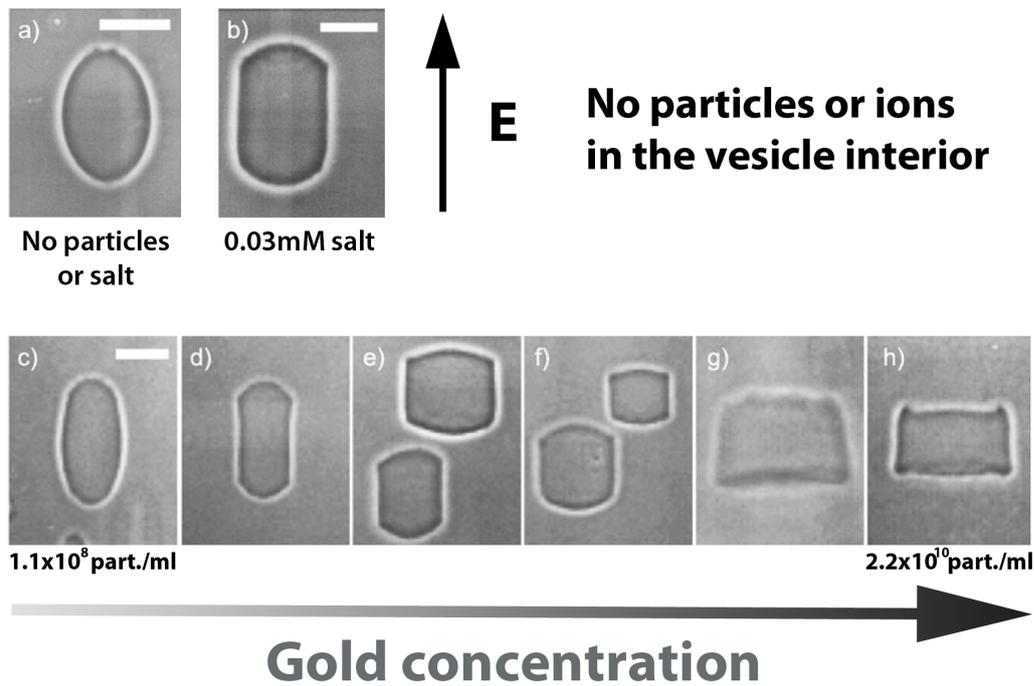
Figure 2.7: Vesicle response to 200μs DC pulses in the presence and absence of salt and gold particles in the vesicle exterior. The direction of the field is indicated by the vertical arrow. (a) shows a vesicle deformation in the absence of salt and particles. The field strength was 1.4 kV/cm. In the presence of 0.03mM salt in the vesicle exterior and no particles present, the vesicles adopted cylindrical shapes as shown in (b). In the latter, the field strength was 2 kV/cm. Snapshots (c) to (h) show vesicles deforming in the presence of 80 nm gold particles for a DC pulse with a field strength of 3.4 kV/cm. The gold concentration was successively increased from $1.1 \cdot 10^8$ particles/ml in (c), to $5.5 \cdot 10^8$ particles/ml in (d), $1.1 \cdot 10^9$ particles/ml in (e), $2.2 \cdot 10^9$ particles/ml in (f), $1.1 \cdot 10^{10}$ particles/ml in (g), and $2.2 \cdot 10^{10}$ particles/ml (h). There is a clear concentration dependence of the shape adopted by the deformed vesicles. Snapshots (a), (c), (e) and (f) were taken 150μs after the beginning of the pulse and (b), (d), (g) and (h) after 200μs. All scale bars correspond to 15μm.

At intermediate to high gold concentrations ($1.1 \cdot 10^9$ particles/ml to $2.2 \cdot 10^{10}$ particles/ml), it seems quite clear that the directionality of the deformation was dominated by the conductivity ratio. The conductivity outside was much higher than inside the vesicle. The ratio was estimated to be $x = 0.69$ for e), $x = 0.41$ for f), $x = 0.23$ for g) and $x = 0.16$ for h). The estimations for e) and f) are very crude. The conductivity measurements

conducted with the zetasizer at low gold particle concentrations tended to fluctuate between two values. Also, at low conductivities a small change in conductivity results in a large change in the ratio x. This should be kept in mind. Nevertheless, this is consistent with earlier results. If $x < 1$ vesicles adopt a disc-like shape, and if x approaches 1, coexistence can be observed.

What happens at a gold concentration of $5.5 \cdot 10^8$ particles/ml (see Figure 2.7d) is less clear. As we will show more in detail in the next section, we estimated $\lambda_{out} < 7 \mu$S/cm. The conductivity of the inner 100 mM sucrose solution is of the order of 4μS/cm. A glucose solution has lower conductivity than sucrose of the same molarity. We do not know the exact conductivity of the outer solution, but it is likely that λ_{in} in fact was larger than λ_{out}. In conclusion, the observed gold concentration dependence of the directionality of the deformations would again be a result of the conductivity ratio between inner and outer solutions.

2.5.3 Threshold conductivities for seeing cylindrical deformations

The lowest reported conductivity for which squaring was observed in the presence of salt was $\lambda_{out} = 12 \mu$S/cm. The outer and inner salt concentrations were $c_{out} = 0.05$ mM and $c_{in} = 0.1$ mM, respectively. $\lambda_{in} = 16.5 \mu$S/cm which gave a conductivity $x = 1.38$. The pulse duration was 200μs and the field strength $E = 2$ kV/cm. This gave rise to a tube-like deformation, although not very pronounced (see Figure 3 in [114]). The fact that the squaring was less pronounced could simply be due to the fact that the pulse was less strong than the one used in the experiments with gold particles. Unpublished data would suggest that $c_{out} = 0.03$ mM was the lowest salt concentration at which cylindrical deformations could be observed, see Figure 2.7b. That would correspond to a conductivity $\lambda_{out} = 6 \mu$S/cm.

The lowest gold concentration for which we saw squaring was $5.5 \cdot 10^8$ particles/ml, see Figure 2.7d. We do not know the conductivity for this concentration, but it was measured for $1.1 \cdot 10^9$ particles/ml in 107mM glucose. Out of six consecutive measurements of the same sample, five gave values quite close to each other, while one was a factor ten larger. At low concentration oscillations between two values were often the case. The mean of all six values is $7.2 \pm 7.4 \mu$S/cm. When removing the sixth data point the mean is $4.2 \pm 1.2 \mu$S/cm. Although these conductivity measurements can not be fully trusted, it should be safe to assume that the conductivity of a 107mM glucose solution with $5.5 \cdot 10^8$ particles/ml is lower than 7μS/cm.

Without making additional electrodeformation experiments with both salt and gold particles at lower concentrations, and remeasuring the relevant conductivities, we cannot draw any definite conclusions. Nevertheless, these results seem to indicate that squaring in the presence of gold particles might occur at outer conductivities lower than the outer conductivities necessary for seeing squaring in the presence of salt.

2.5.4 Two reasons for coexistence

As seen in Figure 2.7e) and f) there can be coexistence of tube-like and disc-like vesicles. This can have two reasons, or rather there can be two reasons for the conductivity ratio to be approximately 1.

A. $x \sim 1$: It is not the actual concentration, but the conductivity ratio between the inner and the outer solutions that dictates the shape adopted. Two vesicles with different inner and outer conductivities having the same conductivity ratio will show the same type of deformation. Any sample containing vesicles with $x \sim 1$ will show a coexistence between tube-like, disc-like and square deformations. See the left image in Figure 2.8. Vesicles deformed in solutions with similar inner and outer conductivities show coexistence already at the first or at the second pulse.

B. Repeated pulses : Repeated exposure to DC pulses increases the ratio of electroporated vesicles. Multiple poration leads to leakage and the homogenisation of the inner and outer solutions. This in turn results in a decrease in contrast. See the right image in Figure 2.8. Vesicles that had a conductivity ratio between 0.7 and 0.3 would often show coexistence or switching from disc-like to tube-like deformation after three or four pulses. The opposite transition, from a tube-like to a disc-like shape was only observed once. This can readily be explained. Ions leaking out from the vesicle would not lead to any big conductivity change of the exterior solution. On the other hand, ions leaking into the vesicle interior would lead to an increase of the inner conductivity due the small volume. As we mentioned earlier in section 2.4.2, the conductivity at one given gold particle concentration can vary a lot from one sample to another. Due to the small sample sizes the conductivity could not be measured prior to each experiment. The amount of ions left over in the gold solution could only be estimated based on previous conductivity measurements. Vesicles showing this type behaviour were more likely to have an actual conductivity ratio closer to 0.7 than 0.3.
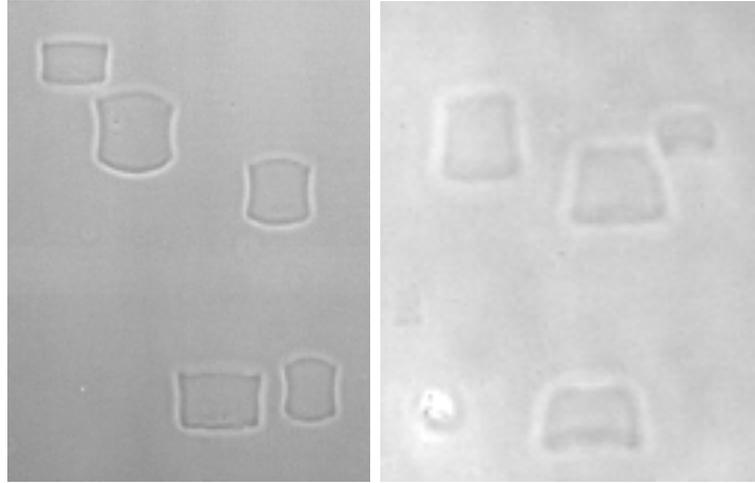
Figure 2.8: Left : Vesicles exposed to a second pulse, having an initial conductivity ratio $x \sim 1$. **Right :** Vesicles exposed to a fourth pulse, having an estimated initial conductivity ratio $x = 0.3$.

2.5.5 Asymmetry in the deformation

There is one peculiarity about vesicles deformed in the presence of gold that should be mentioned. They often deform asymmetrically. This can be seen in Figure 2.6, second row. Two vesicles grown in the same sucrose solution with a gold concentration of $2.2 \cdot 10^{10}$ particles/ml and exposed to the same DC pulse deform differently depending on their external solutions. The vesicle deformed in glucose with 1mM NaCl shows a typical tube-like deformation. The vesicle deformed in glucose with a gold concentration of $2.2 \cdot 10^{10}$ particles/ml also shows a tube-like deformation, but a trapezoidal rather than rectangular cross-section. The side of the vesicle facing the cathode is shorter than the side facing the anode. A similar asymmetry can be seen for vesicles grown in the absence of particles, but deformed in a gold solution, see Figure 2.6, first row. Also here the side facing the cathode is smaller. This asymmetry might be explained by the gold particles moving only in one direction, towards the anode.

A bending of the membrane could also be observed during the squaring phase of the deformation, often just at the end of the DC pulse (after 200 μs). This could be due to the presence of the gold particles in the vesicle exterior. Particle asymmetry across membrane interfaces has theoretically been shown to induce "spontaneous" curvature. In the case of non-adhesive particles, the membrane curves towards the larger particles.[72] After a few pulses it is more rare to see these induced curvatures and the asymmetric

deformations described above are more likely. There are exceptions, but we will advance the hypothesis that gold particles diffuse into the vesicles as a result of multiple poration, hence abolishing the particle asymmetry across the membrane. This would then result in the trapezoidal cross-sections observed. Our hypothesis as well as what we have presented on coexistence in section 2.5.4 is summarised in Figure 2.9.
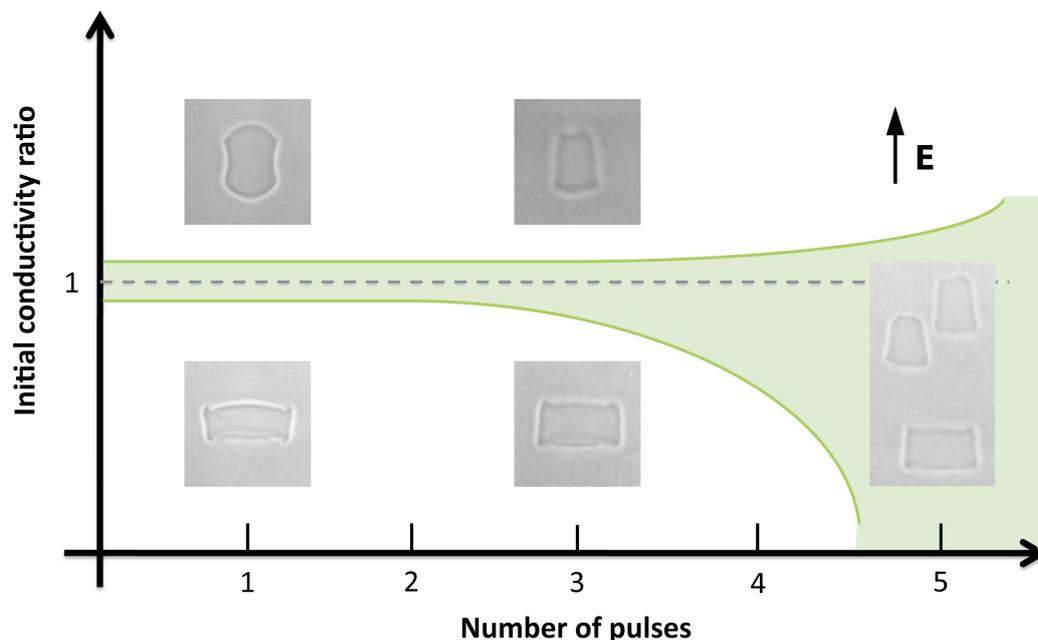
Figure 2.9: Schematic plot showing vesicles exposed to a 200μs DC pulse for the first, third and fifth time in the presence of $80\,$nm gold particles. For these vesicles the deformation was not only tube-like or disc-like. An induced curvature of the membrane was more common at the first or second exposure, whereas a trapezoidal cross-section was often seen for vesicles exposed for the third time or more. The coexistence domain is shown in green, including vesicles with a conductivity ratio $x \sim 1$ and those with $x < 1$, but exposed to repeated pulses. Above the dashed line $x > 1$ and below $x < 1$. The black arrow shows the direction of the electric field.

2.6 Discussion

2.6.1 Possible deformation mechanisms

As mentioned in the introduction, the directionality of the observed deformations has been well described theoretically. This is not the case for the cylindrical deformations observed for DC pulses, both in the presence of ions and gold particles. To our knowledge, only Dimova et al. have reported these deformations for vesicles. They also presented some possible mechanisms [114][68] we will discuss here. It should be noted that the cylindrical deformations are superimposed on the overall vesicle elongation or contraction.

In their study on the effect of salt on vesicles exposed to DC pulses [114], they made two experimental observations relevant to this discussion. Using divalent ions such Ca^{2+} or Mg^{2+} did not change the vesicle response to the electric pulses. They still showed the same conductivity ratio dependent deformation; tube-like when $\lambda_{in} > \lambda_{out}$ and disc-like when $\lambda_{in} < \lambda_{out}$. This would suggest that the flattening of the vesicle wall is independent of the type of ion or charged particle. It would be interesting to see if divalent positive ions induce an asymmetry in the observed deformation, as we saw with gold particles. Both would be expected to migrate only in one direction, the positive ions towards the cathode and the gold particles towards the anode. The second observation they made was the following. If the lipid vesicles were replaced by polymersomes composed of the block dipolymer polybutadiene-β-polyethyleneoxide (polymer made of two distinct blocks of one type of monomer each) [38], the same deformations could still be observed. This would suggest that the squaring of the vesicles is not directly related to lipid properties, but rather to the presence of salt or/and particles.

It has been shown that the kinetic energy of the sodium and chloride ions is sufficient to bend the membrane [114]. We will now estimate the kinetic energy of the gold particles during the pulse. Assuming that the applied field accelerates the particles quickly, they will reach a steady velocity v. The kinetic energy for one gold particle is

$$E_k = \frac{1}{2}mv^2. \tag{2.1}$$

The mass m of a $80\,\text{nm}$ gold particle is

$$m = \rho V = \frac{4}{3}\pi \rho R^3, \tag{2.2}$$

where ρ is the density of gold and V is the volume of the particle. The radius $R = 4 \cdot 10^{-8}\,\text{m}$ and $\rho = 19.3\,\text{g} \cdot \text{cm}^{-3} = 1.93 \cdot 10^7\,\text{g} \cdot \text{m}^{-3}$. This gives us a mass $m = 5.17 \cdot 10^{-17}\text{kg}$.

$$v = uE, \tag{2.3}$$

where u is the motility of the gold particles and E is the field strength. The zetasizer uses the motility of the particles to calculate the zeta potential. For 80 nm gold particles the motility was approximately $u = 4 \cdot 10^{-4} \text{cm}^2\text{s}^{-1}\text{V}^{-1}$. The field strength was E=3.4 kV/cm=3.4·10^3 V/cm. This gives us $v = 1.36$ cm/s. The total kinetic energy is simply

$$E_{kTot} = NE_k = \frac{N}{2}mv^2, \tag{2.4}$$

where N is the number of gold particles that could potentially flatten the vesicle. The distance travelled by a particle during the pulse is $d = t_p \cdot v = 2.72\mu m$, where $t_p = 200\mu s$ is the duration of the pulse. Let us consider a cylinder containing the vesicle (see Figure 2.10).
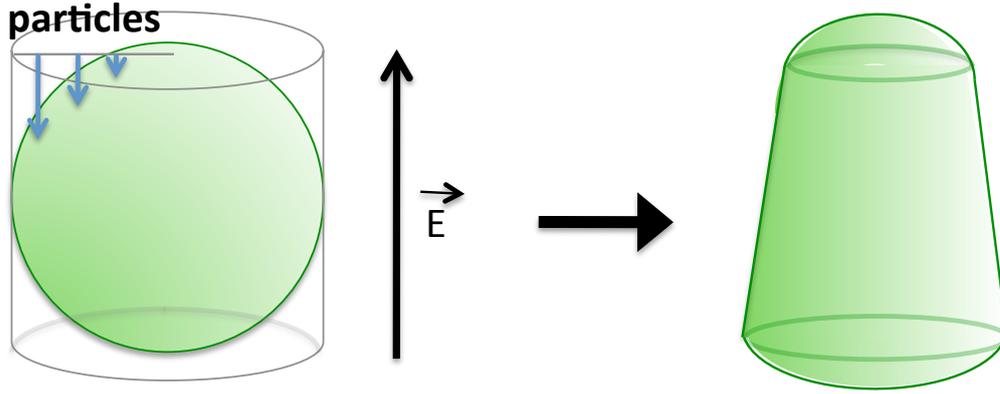
Figure 2.10: Sketch of a vesicle and the cylindrical volume in which we estimate particles to contribute to the deformation shown to the right. The blue arrows illustrate the movement of the gold particles in the electric field. Only particles on the cathode side of the vesicle will contribute.

The volume in which we estimate particles to contribute to the squaring is

$$V = V_{cylinder} - V_{vesicle} = 2\pi R^3 - \frac{4}{3}\pi R^3 = \frac{2}{3}\pi R^3. \tag{2.5}$$

Since the gold particles only move in one direction the final contributing volume is $V = \frac{1}{3}\pi R^3 = 1.05 \cdot 10^{-9}$ml. The particle concentration is $2.2 \cdot 10^{10}$ particles/ml. This gives us $N = 23$ particles. From 2.4 we get that $E_{kTot} = 8 \cdot 10^{-18}$J. The bending modulus K_b of a lipid membrane in the fluid phase is of the order of 10^{-19}J [76]. We can therefore conclude that it is theoretically

possible for the gold particles to alone deform the lipid bilayer. The minimum gold concentration needed for deforming the vesicles can be estimated to

$$c_{min} = \frac{N_{min}}{V} = \frac{K_b}{E_k \cdot V} = 2.7 \cdot 10^8 \text{particles/ml} \tag{2.6}$$

This is compatible with the experimental results presented in Figure 2.7. The lowest gold concentration for which we observed cylindrical deformations was $5.5 \cdot 10^8$particles/ml (see Figure 2.7d). At $1.1 \cdot 10^8$particles/ml only an elongation of the vesicle was visible (see Figure 2.7c).

Although the electrophoretic forces exerted by both ions and particles play a crucial role in the cylindrical deformations we have observed, this is not the only factor to take into consideration. If ions are present in the vesicle interior as well as exterior, there is an accumulation of charges on each side of the bilayer. The membrane can be seen as a charging capacitor. This induces a membrane potential V_m.

$$V_m = \frac{1}{2}R cos\theta E(1 - e^{-t/\tau}), \tag{2.7}$$

were θ is the angle between the electric field E and the membrane normal. t is time and τ is the membrane charging time.[24] The charging time depends on the interior and exterior conductivities. τ decreases with both increasing λ_{in} and λ_{out}. τ is on the order of a few hundred microseconds.[114] Because of its angle dependence, the membrane potential gives rise to a non-uniform electric tension $\sigma_{el} \propto V_m^2$ [87]. The induced electric tension is high at the poles and equal to zero in the equatorial region of the vesicle. This is of course only valid shortly after the beginning of the pulse, before the membrane tension equalises. In conclusion, one could imagine a deformation mechanism where a difference in membrane tension makes it easier for particles to deform the equatorial region than the poles of vesicles, leading to the cylindrical deformations observed.

2.6.2 Further experiments

The next natural step would be to try to wash the gold particles from most of the ions remaining from the fabrication process. One way would be to repeatedly spin them down and resuspend them in either water or sucrose. We started to explore this direction, but the particles tended to form aggregates. One additional wash might be enough to get the ion concentration below the squaring threshold. The conductivity of this new gold solution should be measured. If rinsing them twice is not sufficient, we could consider

coating the gold particles with polyethylene glycol (PEG), which would prevent them from sticking to each other. The washing procedure could then be repeated. Of course this might alter the interaction of the gold with the lipid membrane. Difference scanning calorimetry could help us investigating whether the gold particles, both PEG-coated and non-coated, interact or not with the bilayer. A shift in the heat capacity profile compared to a pure lipid system would indicate an interaction between particles and lipids.

Once we know the role played by the 80 nm particles, we could repeat the electrodeformation experiment with smaller particles that can be used in a medical context. It is very difficult to visualise them, so we would have to rely on the electrodeformation data.

It could also be interesting to conduct the DC pulse experiment on cells, both in the presence of salt and gold particles. The high temporal resolution would give use information on the first few hundred microseconds, which have not been reported earlier. It has been shown that non-spherical cells, such as fission yeast, orient parallel or perpendicular to an applied AC field. As for GUVs, this depends on the inner and outer conductivities as well as the field frequency.[138][60] It is unclear if cells would show cylindrical deformations or even adopt prolate or oblate shapes. This might vary with the stiffness of the cells studied. A red blood cell for instance is much easier to deform than a bacteria or yeast cell that has a very rigid cell wall. The cytoskeleton can also be more or less extensive. As we will mention in the next chapter about optical deformations, stretching of cells could potentially be used for diagnosing cancers or other diseases that induce changes in cellular rigidity. This could also be an application for electrodeformation, as indicated by a recent study in which different types of mammalian cells were successfully distinguished after being trapped and deformed in a non-uniform electric field [75].

2.7 conclusion

From experiments conducted earlier in Dimova's group, we knew that vesicles exposed to a DC pulse in the presence of salt showed cylindrical deformations. These deformations were very short-lived. The direction of deformation depended on the conductivity ratio between the inner and outer vesicle solutions. $x > 1$ gave rise to tube-like deformations, whereas $x < 1$ would lead to disc-like deformations. We observed the same deformations in the presence of 80 nm gold particles. As it turned out, the colloidal gold solution was not free from ions. Potassium carbonate left over from the fabrication process dissolved into K^+ and HCO_3^+, also leading to the enrichment of the

gold solution in OH$^-$. We tried to determine the respective roles of the ions and the gold particles in the cylindrical deformations observed. Although we cannot exclude that the gold particles contribute to the directionality of the deformation, it is more likely due to the presence of ions, which are sole contributors to the measured conductivities of the inner and outer vesicle solutions. What we have shown is that the gold particles could and most probably do participate in the flattening of vesicles equatorial region observed during strong DC pulses, acting alongside the ions. The gold particles also seem to affect membrane curvature as well as to induce asymmetry during the squaring of the vesicles. This could be due to particle asymmetry across the membrane and the fact that the gold particles only move in one direction in the electric field.

CHAPTER 3

Optically induced deformations of lipid membranes

3.1 Introduction

Optical tweezers were combined with fluorescence confocal microscopy to study the interaction between light and lipid membranes. The laser beam, tightly focused inside a giant unilamellar vesicle, gave rise to fluctuations and eventually the rupture or budding of the lipid bilayer. What motivated this study is the wide use of optical traps within the field of biophysics. Optical tweezers are well suited for working with biological samples, especially in the near infrared and infrared regions (750-1200 nm) where they show a minimum in light absorption. This window of near transparency is due to a decrease in absorption by biological chromophores, such as hemoglobin or proteins, and water absorption is still quite low at those wavelengths [88][126]. One common laser frequency to work with is 1064 nm, which we also used in our experiments.

With optical tweezers it is possible to measure forces in the picoNewton range. This makes them a perfect method for studying weak interactions such as the motion of single proteins in a plasma membrane [97][98] and the stretching of DNA [99]. In vitro studies are more common, but efforts are currently made to bring the accurate force measurements that optical tweezers present into the cell. This is what motivated this study. The laser light clearly has a direct effect on lipid membranes. This should be kept in mind when working with living cells. Deformations might not be observed due to the rigidity of the cytoskeleton or cell wall, but the membranes will experience forces that might influence their behaviour. We therefore wanted

to characterise the effect on a simpler system.

We will discuss the nature of the interaction between the focused laser light and the lipid bilayer. We will put forward the hypothesis that in our case the scattering force is the main contributor to the deformation of the giant unlamellar vesicles by the optical tweezers. We will discuss the validity of this hypothesis looking both at theoretical considerations and experimental data.

3.2 Experimental methods and their applications in biophysics

3.2.1 Optical trapping

Askin was the first to describe and implement optical trapping. The first laser traps consisted of two counter-propagating laser beams. Instead, optical tweezers have one single laser beam tightly focused by an objective with high numerical aperture. The principles of trapping with optical tweezers are the following.

A dielectric particle near the focus of a tightly focused laser beam will experience a force. This force has traditionally been divided into two components, a scattering force and a gradient force. Near the trap focus there is a net momentum transfer from the incident photons to the particle.[88] When light passes through a transparent object, fluctuating electric dipoles are induced [126]. The interaction of these dipoles with the inhomogeneous electric field at the focus gives rise to the gradient force [88]. This force is proportional to the spatial gradient in light intensity and acts in the direction of the gradient [126]. It is also proportional to the polarizability of the trapped dielectric. For stable trapping a very steep gradient is needed, hence the necessity to sharply focus the laser beam using an objective with high numerical aperture. With a steep gradient in light intensity the axial component of the gradient force overcomes the net scattering force pushing the particle away from the focus of the trap. This balance between the two forces results in an equilibrium position slightly beyond the focal point. The optical trap can be seen as a Hookean spring with a stiffness proportional to the light intensity.[88]

There are two limiting cases for which the forces on a sphere can be readily calculated. If the trapped particle is much larger than the wavelength of the trapping laser (the radius $a \gg \lambda$) the Mie regime is satisfied and simple
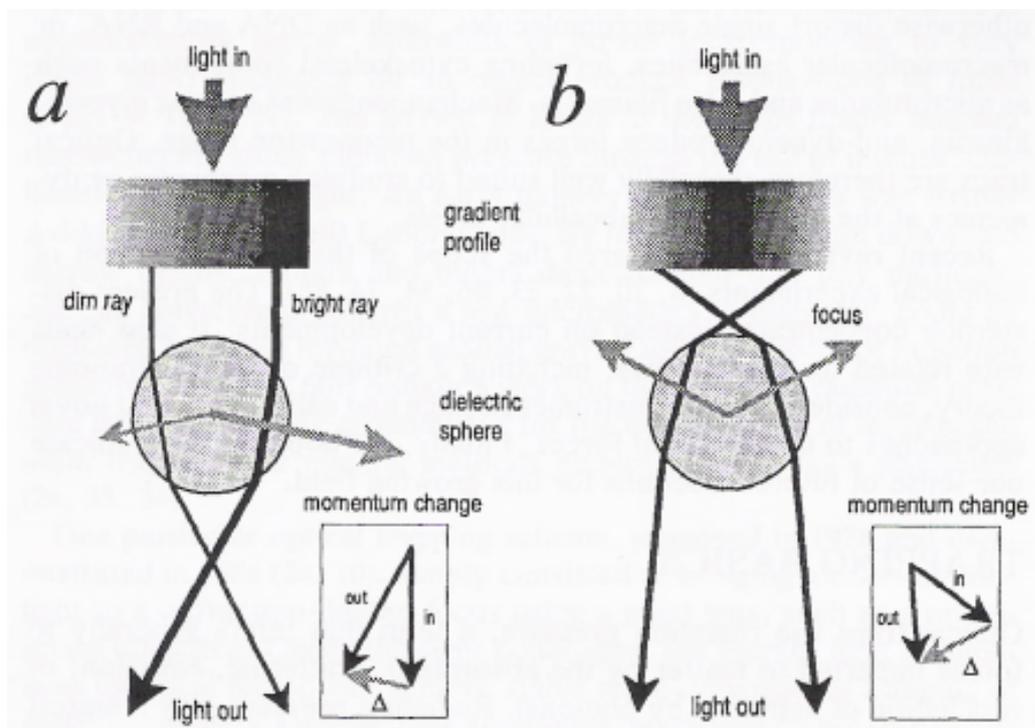
Figure 3.1: A ray-optic picture of the gradient force corresponding to the Mie regime. The dark gray arrows correspond the representative rays and the lighter rays correspond to the reaction forces. a) A parallel beam of light with a gradient in intensity shines through a transparent sphere with a higher refractive index than its background. The inset shows the change in momentum for the right ray. b) A single beam trap where the light is brought to a focus. This pulls the bead upwards. The inset shows the change in momentum for the left ray. [126]

ray optics apply, see Figure 3.1. In the Rayleigh regime the dimensions of the trapped particle are much smaller than the wavelength of the trapping laser (a $\ll \lambda$). The light can no longer be represented by rays. In this limit the electromagnetic field is uniform across the trapped dielectric particle, therefore it can be treated as a point dipole and the scattering and gradient components can be readily separated.[88][126] Most biological work falls into the intermediate regime when the size of the trapped object is comparable to λ. This has been treated theoretically by Rohrbach [116].

The simplest and most straight forward implementation of optical tweezers is the manipulation of dielectric objects. Particles with sizes varying from several nanometers up to tens of micrometers can be trapped [126]. Micrometer-sized polystyrene beads are good to work with since they are

symmetric and also easily coated with diverse molecules. This makes them useful as handles to manipulate objects that are either very small or are not easy to trap. The fact that they are spherical also makes it possible to do a precise position and force calibration [88].

3.2.2 Applications of optical tweezers in biophysics

More and more research within the field of biophysics makes its way into the cell, from *in vitro* studies to *in vivo* studies. Optical tweezers could potentially be a useful method especially for quantifying forces. Several major steps have been taken, but many challenges persist. To make accurate force measurements inside cell new calibration methods [43] are needed and a handle has to be used. As this is non trivial, several strategies could be considered. Either using something already on the right side of the plasma membrane such as lipid granules that can easily be trapped [122], or by inserting spherical particles such as gold nanoparticles or quantum dots. Depending on the cell type this can be more or less easily done. Also heating of the particles in the trap should be seriously considered [106][12].

There is not only the challenge of making accurate force measurements inside cells, but photodamage and phototixicity should be considered as well. Optical tweezers are often said to be harmless, but it is important to assess their effects on living organisms. It is not just the handle that is affected by the laser light, but also everything that is in its way. Absorption of light by proteins and other macromolecules can lead to damage. Certain wavelengths are more phototoxic than others. The wave being continuous is also important. A pulsed laser would do greater damage, e.g. facilitate DNA denaturation [73]. Regardless of the difficulties this is an exciting journey.

So what are our motivations for this study? When illuminating a cell the plasmamembrane also experiences forces. Deformation of red blood cells [33] and optical stretching of cells have been reported [52]. Even if the cytoskeleton preserves the shape of the cell, there are still forces acting on the membrane. These stresses can activate responses that potentially influence the outcome of an experiment.

3.2.3 Confocal imaging

Confocal microscopy combined with fluorescent labeling of the sample has become a powerful tool not only for 3D imaging of sample structure, but also for the imaging and understanding of cell function. In confocal microscopy almost all the out-of-focus light is eliminated. This allows sectioning of a sample without physically slicing it. The illumination of the sample is sequential. The light is focused onto a very small spot that scans the sample in a raster pattern. This already reduces the illumination of the areas out of focus and hence reduces the blur. But the major feature of the confocal microscope is a spatial filter, a pinhole, that only lets through the light coming from the focal plane (see figure 3.2).[78][5] The size of the focal spot and thus the resolution of confocal microscopy, as for any light microscopy, depends on the wavelength of the illuminating light and the numerical aperture (NA) of the objective [104]. We can distinguish between lateral (parallel to the focal plane) and axial (along the optical axis of the microscope) resolution. For confocal microscopy, lateral resolutions between 140 nm and 250 nm and axial resolutions between 500 nm and 1 μm have been reported [78][5][42].
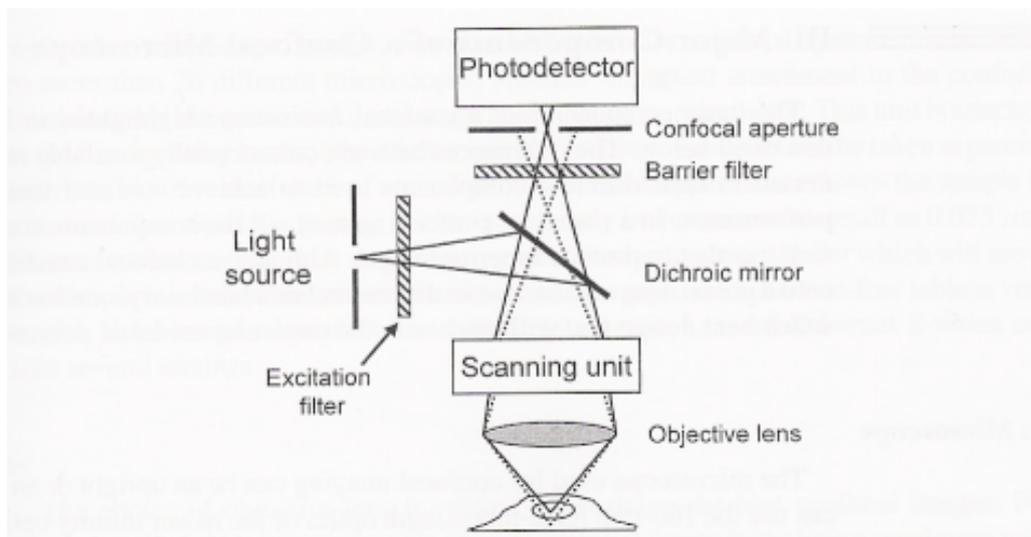
Figure 3.2: Basic design of a confocal microscope for use in fluorescence microscopy [78].

Beam scanning confocal microscopy, as we used, has a few limitations. First of all acquisition rates are slow, which makes the investigation of rapid process rather difficult. There is also a limited range of wavelengths available for fluorescent excitation [78]. When working with living cells one should be

careful not to overexpose the sample to the laser light since photodamage can be an issue [5].

We used a combination of optical tweezers and confocal microscopy. The specifications of the setup can be found in section 3.3.3.

3.3 Materials and Methods

3.3.1 Sample preparation

1mg/ml lipid stock solutions of DMPC and DPPC were prepared in dichloromethane/methanol in a volume ratio of 2:1. Also the lipid-like fluorescent marker DiI-C18 (1,1'-dioctadecyl-3,3,3',3'- tetramethylindocarbocyanine perchlorate)(DiI) from Invitrogen was used. The DMPC and DPPC stock solutions were mixed in a molar ratio of 50:50. DiI was added at a concentration of 0.125×10^3 mol/L in the molar ratio DiI:lipids 1:500. The solvent was then evaporated by heating under a gentle air stream. When dried, Trifluoroethanol (TFE) was added to the sample in the same amount as the dichloromethane/methanol present before evaporation ($200 \, \mu$l). The sample was stored in the freezer. When preparing for experiments, $6 \, \mu$l of the sample was put on an Indium Tin Oxide coated 0.17 mm thick Borosilicate Thin Glass coverslip (ITO). The prepared ITOs where put in a desiccator overnight to remove all solvent residues.

3.3.2 Electroformation of giant unilamellar vesicles

The electroformation was carried out in a custom made chamber used both for growing unilamellar vesicles and for microscopy. Two indium tin oxide coated coverslips (ITOs) were separated by a very thin (300-500μm) spacer made from peek (a very heat resistant plastic). The short spacing would allow for accurate force measurements. The spacer was mounted on a temperature controlled sample holder, through which water was circulated. See Figure 3.3. The sample could then be heated up to a temperature above the phase transition of the studied lipid mixture; condition necessary for vesicle formation. When growing DMPC:DPPC 50:50 vesicles the temperature of the heat bath thermostat was set to 50 °C. This corresponded to a temperature of about 43 °C inside the sample chamber. The electrical connection between the bottom ITO and its corresponding electrode was verified. The lipid film on the bottom ITO was rehydrated with preheated Millipore water with a minimum resistance of 18 MΩ. Vacuum grease was used to make the ITOs stick to the spacer. A small hole, sealed with vacuum grease was made in the top ITO (1 mm thick) in order to monitor the temperature with a thermocoupler during the experiments. The spacer was electrically connected to a function generator supplying 10 Hz sinusoidal alternative current. By monitoring the sample with a 20X air objective on a standard inverted fluorescence microscope, we could fine-tune the voltage at which the

electroformation was optimal. We let the vesicles grow for about one hour in the dark, to avoid photobleaching of the dye. This method yields mostly semi-spherical or truncated vesicles attached to the bottom ITO. Most GUVs formed were in the range of 10 to $40\,\mu$m in diameter. The sample was then cooled down gradually to the desired experimental temperature.
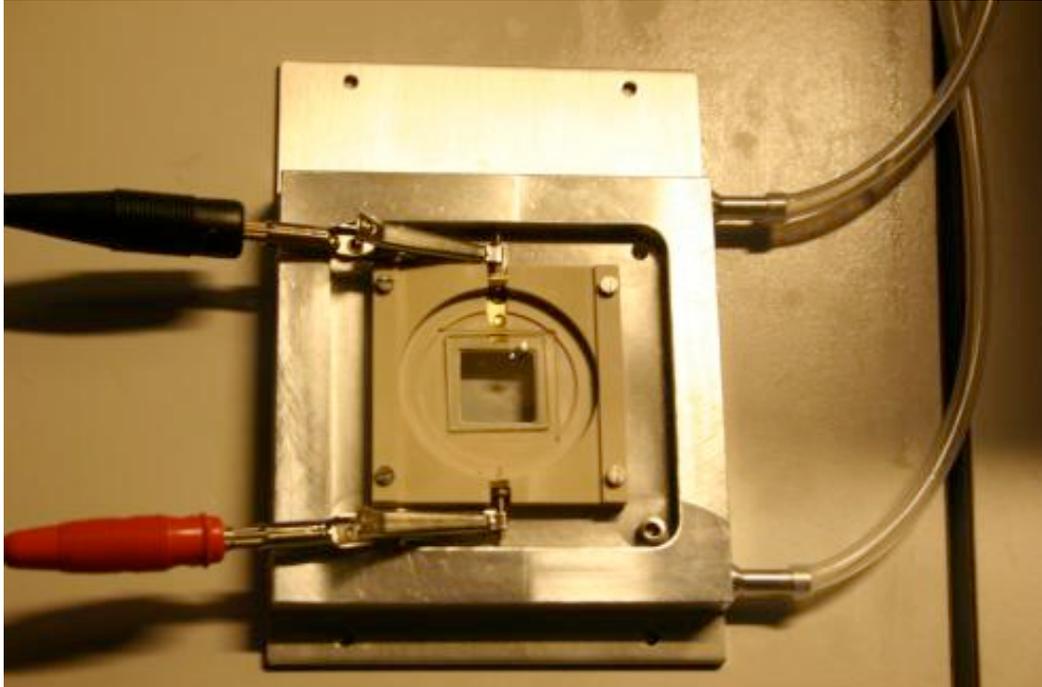
Figure 3.3: Sample holder for electroformation and confocal microscopy.

3.3.3 Setup

The optical tweezers setup was based on a Leica DMI6000 inverted microscope. The laser used was a continuous wave Nd:YVO$_4$ laser (Spectra-Physics J20-BL106Q) with a wavelength of 1064 nm. Before entering the microscope the laser beam was walked through a series of lenses and mirrors. The telescope at the end of the optical path used one of the lenses inside the microscope. The back aperture of the microscope objective ((HCX, PL, APO, 100x/1.4 NA, oil, Leica) was slightly overfilled with the laser beam to ensure that the light converged to a tight spot. The light from the sample was collected by a high numerical aperture condenser and projected on a quadrant photodiode (Hamamatsu S5981) for tracking of the trapped parti-
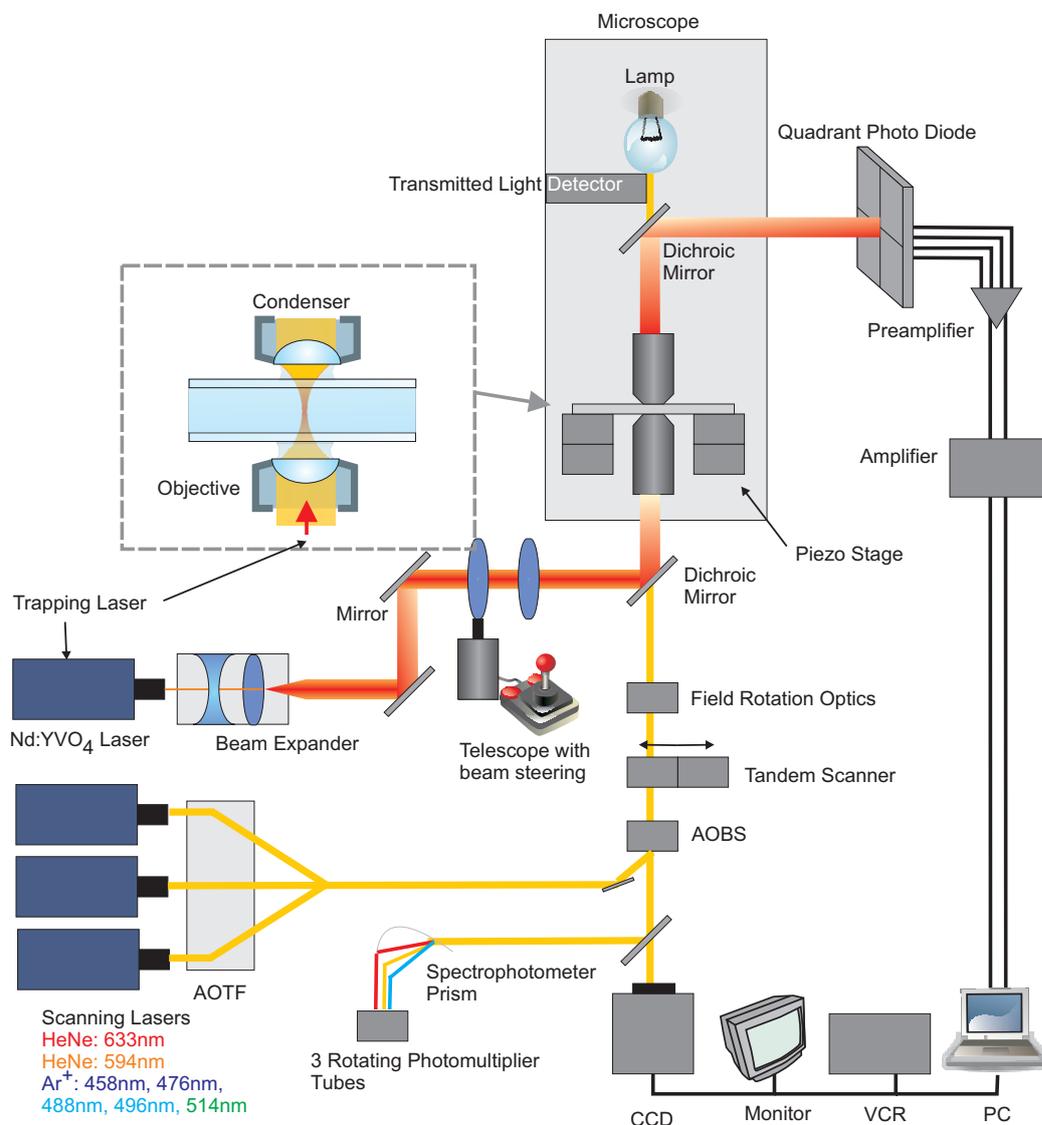
Figure 3.4: Schematic drawing of the experimental setup including the optics used for the optical trap as well as the confocal scanning system [112].

cle. We did not use this function in our experiments. The optical tweezers setup was combined with Leica's TCS SP5 confocal system, making it possible to do both trapping and 2D confocal imaging at the same time. For further technical details see Richardson et al.[112]. Seven different excitation wavelengths were possible thanks to two helium-neon lasers emitting 594 nm and 633 nm. An argon laser provided laser beams at 458 nm, 476 nm, 488 nm, 496 nm and 514 nm. Laser powers, scanning rates, types of scans (xy, xyz,

xyt etc) and detection ranges could be tuned. For a schematic drawing of our setup see Figure 3.4. A mercury lamp was also mounted to the microscope. The vesicles could be observed in fluorescence mode using a TX2 (Texas red/green) filter cube from Chroma. This made navigation in the sample easier.

Temperature control

In order to explore the phase dependence of the vesicle response to the laser trap we had to control the temperature of both the sample holder and the oil immersion objective. The latter, being in contact with the sample, acts as a heat sink giving rise to a temperature gradient inside the sample. By circulating water through the sample holder and a custom made objective heater we could make measurements at temperatures spanning from 15 to 40 °C. The thermostat with a 4 liter bath was a Lauda RE204 with a temperature range of -10 to 200 °C and an accuracy of 0.2 °C. Due to heat loss in the tubing and the metal parts, the temperature of the sample is different from the one of the circulating fluid. See Figure 3.5 for a calibration curve. There might be deviations from it due to fluctuations of the ambient temperature of the laboratory. The calibration curves were used both to choose the thermostat settings and to estimate the temperature inside the sample chamber in the case of experiment **B** described in the next section.
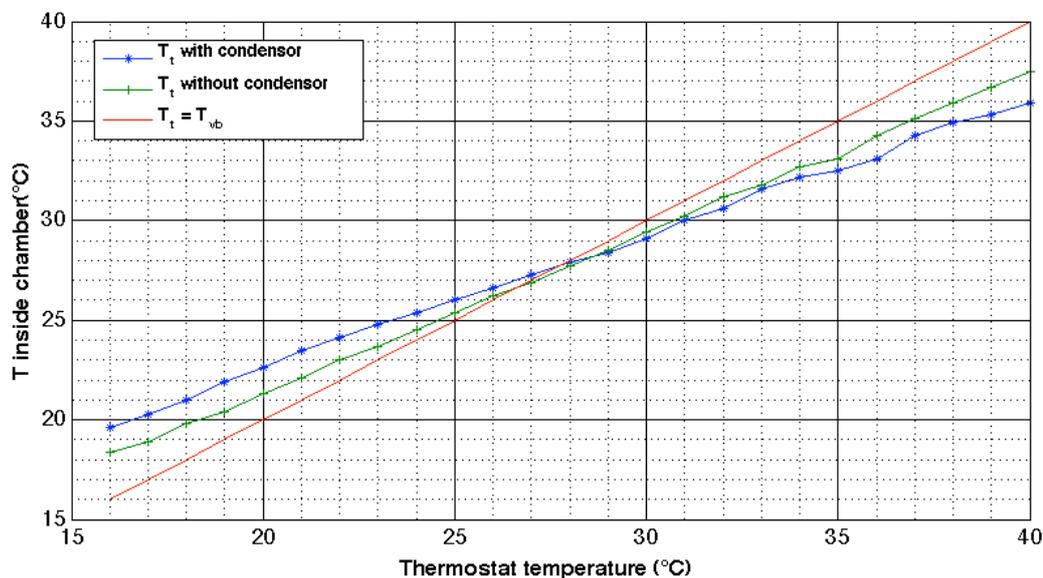
Figure 3.5: Calibration curves for the temperature control of the sample with and without contact with the condensor.

3.3.4 Experiment

We mainly carried out two types of experiments; **A**) a repeated exposure of the same vesicle to gradually increased laser power (laser off before each increase) or **B**) a constant exposure of a vesicle to a fixed laser power until its collapse. See Figure 3.6. The aim of both experiments was to determine and quantify the direct effect of optical tweezers on lipid membranes. All GUVs were made from a DMPC:DPPC 50:50 mixture.

There will often be references to low, intermediate and high laser powers. Low will be defined as laser powers from 0 mW to 30 mW, intermediate from 30 mW to 70 mW and high from 70 mW and above. These are not very high compared to the laser powers used in standard optical tweezers experiment. To stably trap a polystyrene bead of 1μm a laser power of a few hundred milliwatts at the sample is typically used. This rough classification is somewhat linked to the degree of deformation, although the later varies with temperature. All laser powers referred to in this report are laser powers at the sample.

Experiment A

When a big vesicle was found in the sample, with a diameter typically varying between 15 and 40μm and a nice round shape, the trap focus was placed at the centre of its equatorial cross-section (see Figure 3.7). After setting the temperature and letting it stabilise a series of confocal images was taken with stepwise increased laser power, which was indirectly controlled by increasing the laser diode current in 0.1 A steps. This corresponds approximately to steps of 7 to 12 mW at the sample, the power increase being a bit smaller at low laser powers. The trap was turned off between each increase. Ten images were taken at each laser power. At high laser powers the trap was turned on and off three times at each power to prevent the vesicles from breaking and to be able to continue the experiment longer. We chose an acquisition time of 1.318 s (400 Hz) in order to optimise for both image quality and speed. It was the same for all experiments.
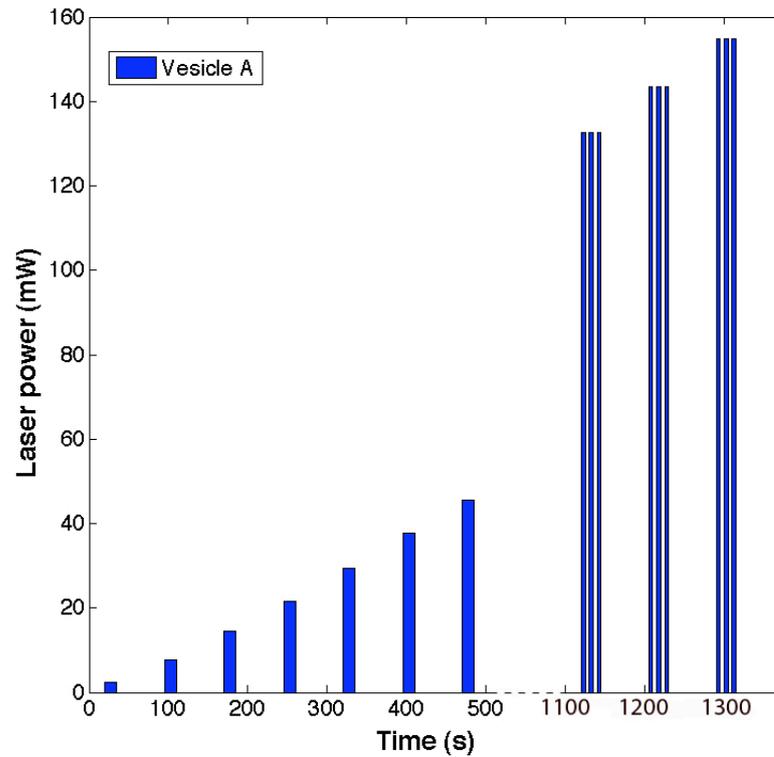
(a) ExperimentA : The same vesicle is exposed to stepwise increasing laser power. At low and intermediate laser powers the trap was switched on and off once. At high laser powers, if the vesicle fluctuations were large, the trap was switched on and off three times at 10s intervals. This was done to prevent premature rupture of the vesicle.
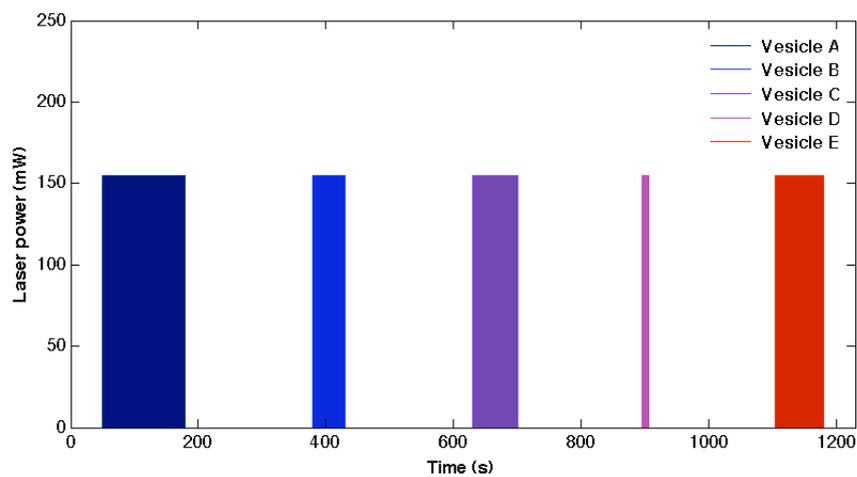
(b) ExperimentB : Each vesicle was exposed to the same laser power P=155 mW. The trap was on until the vesicle had either burst or become a vesicle aggregate.

Figure 3.6: Figures illustrating experiments **A** and **B** showing laser power (mW) versus time (s). Every new vesicle is represented by a new colour.
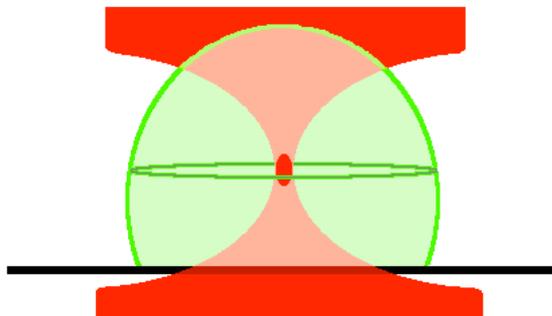
Figure 3.7: Sketch of the laser trap (in red) focused at the centre of the equatorial cross-section of a vesicle. This is the case in both experiment **A** and **B**.

Experiment B

The trap focus was as previously placed at the centre of the vesicle's equatorial cross-section. The laser power was chosen such that large vesicles would eventually collapse, but that small ones would still survive for a few seconds. $P = 155$ mW was found to be a good compromise. The point of collapse was defined as the point were the vesicle broke, no main vesicle was distinguishable (see Figure 3.8) or when the top of the vesicle was below the focal plane, hence not visible anymore. This experiment gave us access to information on both the role played by the phase of the lipid membrane and by the size of the vesicles on their ability to withstand stress.
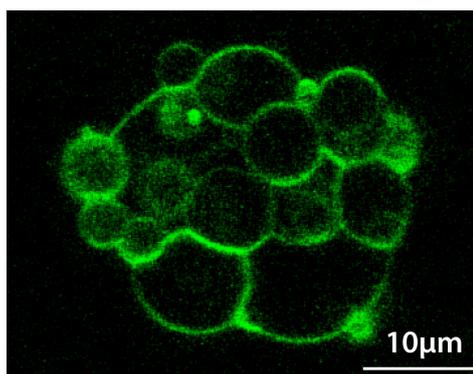
Figure 3.8: DMPC/DPPC 50:50 vesicle at $T = 22.9\,°C$ after 78 s exposure to a laser power $P = 176$ mW.

Other experiments

We also conducted less extensive experiments to address specific issues, mostly related to the investigation of the forces involved in the observed deformations. The aim was to get an idea of the overall deformations of the vesicles, not only of a cross-section. But the trapping laser and the scanning laser both go through the same objective, hence the trap and scanning foci are coupled. We tried to circumvent this problem by scanning small xz-sections of the trapped vesicle right after laser exposure, in an attempt to catch the overall shape of the vesicle before it had relaxed back completely to its original shape. We will come back to these experiments when discussing the forces responsible for the deformations.

3.3.5 Data analysis

The data analysis was carried out using a custom made Matlab program. All images concerning one vesicle, i.e. one experiment of type **A**, were imported. They were first converted into grayscale and filtered using a difference of Gaussian filter, a so-called DOG filter. Using the built in Matlab function *edge* with the *canny* option we defined the contour of the vesicle. If a break in the edge was found, the image was analysed by drawing the contour by hand. This was the case for about 10% of the images. Both the number of pixels in the circumference and in the area of the vesicle cross-section where counted and saved in vectors. These vectors were later divided up in smaller vectors for further analysis, one for each laser power.

3.4 General observations

Long term exposure to a constant and high laser power led either to the rupture of the illuminated vesicle or more often to the formation of aggregates of many smaller vesicles as shown in Figure 3.9 A and B; a $22\,\mu$m vesicle before and after continuous exposure to a high laser power P $=176\,$mW. The vesicle started budding, forming smaller vesicles until the main vesicle was no longer distinguishable from the minor vesicles.
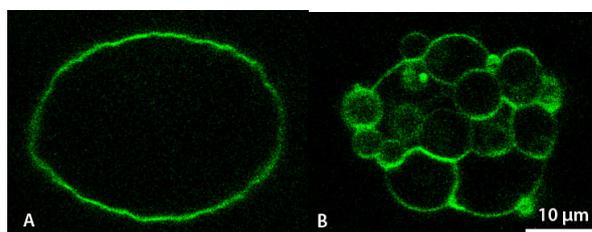
Figure 3.9: $22\,\mu$m DMPC/DPPC 50:50 vesicle at $T = 22.9\,°$C. **A**: P $= 0\,$mW. **B**: After $78\,$s exposure to P $= 176\,$mW.

In experiment A, the laser was switched off between each increase and the vesicle was allowed to relax back to what we call the resting shape, the equilibrium shape it reaches between exposures. It was clear that fluctuations increased with increasing laser power. The observed deformations were instantaneous. Also the return to the resting shape was immediate once the laser was switched off. Three different types of deformation could be seen. At low laser powers the vesicle shape changed slightly, usually as a small increase in roundness. At intermediate powers the membrane underwent major shape fluctuations that stopped only once the trap was switched off. If the laser power was further increased the fluctuations rapidly went over into a dramatic decrease of the cross-section diameter while the trap was on. Once the laser was switched off the cross-section partially regained its original size. One possible explanation would be that the vesicle tried to escape upwards forming a sort of mushroom-like or cylinder-like shape. An hypothesis for the mechanism of this deformation will be presented and discussed in section 3.8.2. Permanent damage started to show at this stage. A decrease in the area of the cross-section at rest (between exposures to the laser) could be observed and small buds were forming on the surface of the vesicles. Pieces of membrane are likely to have been torn off [10]. Eventually the vesicle became an aggregate of several smaller vesicles, like in the case of a constant
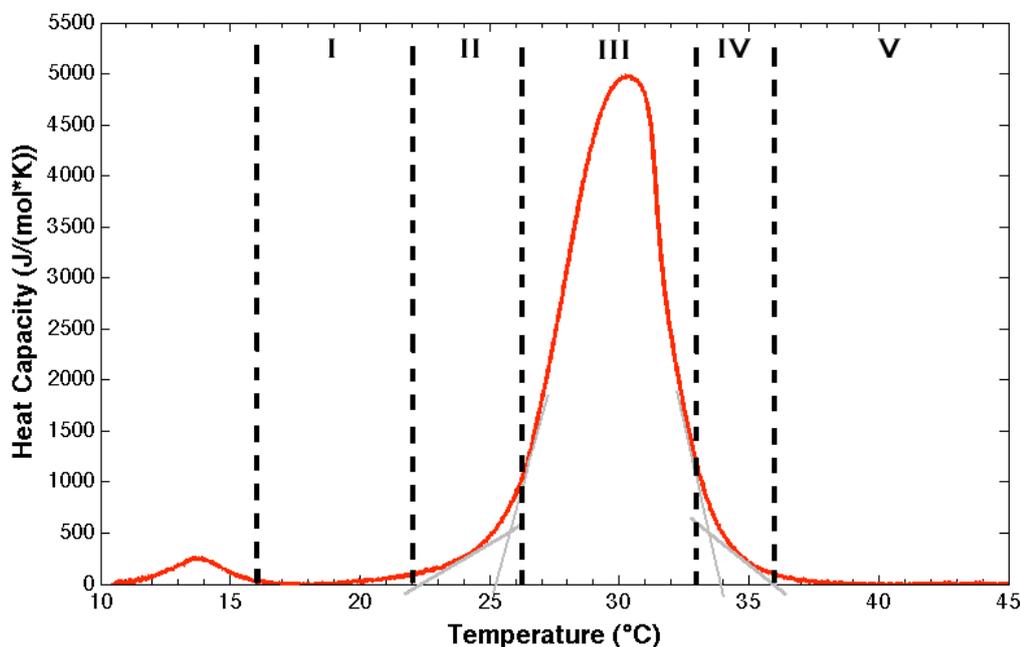
Figure 3.10: This graph shows the heat capacity profile for the studied lipid mixture DMPC:DPPC 50:50 as well as our phase classification into five categories: I Ripple Phase, II Beginning of Main Transition, III Main Transition, IV End of Main Transition, V Fluid Phase. The grey lines are possible tangents defining the beginning and the end of the phase transition. The data corresponds to a differential calorimetry scan at $5\,°C/h$.

exposure to the laser seen in figure 3.9.

By controlling the temperature of the sample we could control the state of the lipid bilayer. The graph in Figure 3.10 shows the heat capacity (C_p) profile of the studied lipid mixture with the phase classifications we made. What is shown is actually the excess heat capacity, which is a measure for the enthalpy necessary for increasing the temperature of the sample with one Kelvin. The larger peak at T $= 30\,°C$ corresponds to the main phase transition in which we have coexistence between solid-ordered (gel) and liquid-disordered (fluid) domains. There are different methods to determine the beginning and the end of the phase transition. One commonly used method is the tangent method, which is quite subjective since the tangents of the heat capacity peak can be drawn in many different ways, as shown by the grey lines in Figure 3.10. As mentioned in section 1.1 the transition is a continuous process, so it would in any case be difficult to define sharp boundaries. Phase categories II and IV are defined as these grey zones at the beginning and the end of the main phase transition. The first maximum in heat

capacity at T = 14 °C corresponds to the pretransition. It has been shown that the membrane can undergo a pretransition from the solid-ordered to the so-called ripple phase. This is not the case for all types of lipids, but phosphatidylcholines (used in this study) and phosphatidylglycerols show clear pretransitions. All is not known about the ripple phase, but it is believed to be due to the chain melting process. Among others, a model has been put forward by Heimburg where the membrane ripples consist of fluid lipid line defects [55]. This would not disrupt the hexagonal packing of the membrane seen in the gel phase. This model succeeded in predicting heat capacity profiles comparable to calorimetric data. Molecular dynamics simulations have also shown the spontaneous formation of ripples after lowering the temperature below the melting temperature (maximum of the main peak). They observed an asymmetric ripple structure made of two types of gel domains with different thickness, where the thinner domains show intercalation of the acyl chains of the lipid molecules. The two domains have a different tilt relative to the membrane normal and are linked by kinked areas where the lipids are highly disordered.[34] The view point that both the pretransition and main transition are part of the same melting process is also supported by Riske et al. [113]. Still the change in heat capacity is quite small in the pretransition (corresponding to approximately a 5% change in enthalpy compared to the main transition), so one would expect the elastic properties of the membrane to be similar to the ones in the gel phase. We will refer to the five phase categories as:

I Ripple Phase,
II Beginning of Main Transition,
III Main Transition,
IV End of Main Transition,
V Fluid Phase.

Although our main interest from a membrane state point of view lies in the melting transition, comparison with vesicle behaviour in a pure gel and fluid phase would have been enlightening. Due to technical constrains such as the working temperature of the objective and the difficulty of reaching temperatures far below room temperature, data could only be collected for temperatures ranging from T = 15 °C to T = 45 °C. This unfortunately prevented us from investigating the behaviour of a pure gel phase membrane, though by focusing on the phase transition we hope to resolve some of the underlying mechanisms of the melting process.

A few phase specific observations could be noted. In the *ripple phase* (I) the vesicles tended to break rather than form vesicle aggregates like in Figure 3.9 B. In the *main transition* (III) deformation of gel domains might have been seen. At temperatures corresponding to the *beginning of the main transition* (II) a relaxation effect could be observed. The deformed vesicles went back to their original shape while the laser was still on. We will come back to this in section 3.7.3. At temperatures corresponding to the *fluid phase* (V), thermal fluctuations could be observed in the membrane without the laser being on. Still GUVs in the fluid phase were less affected by the laser trap than GUVs in the gel phase or the main phase transition. Despite these differences, the different stages of deformation were mainly the same at all temperatures (for all phase categories) and are summed up in Figure 3.11 in the form of sketches.
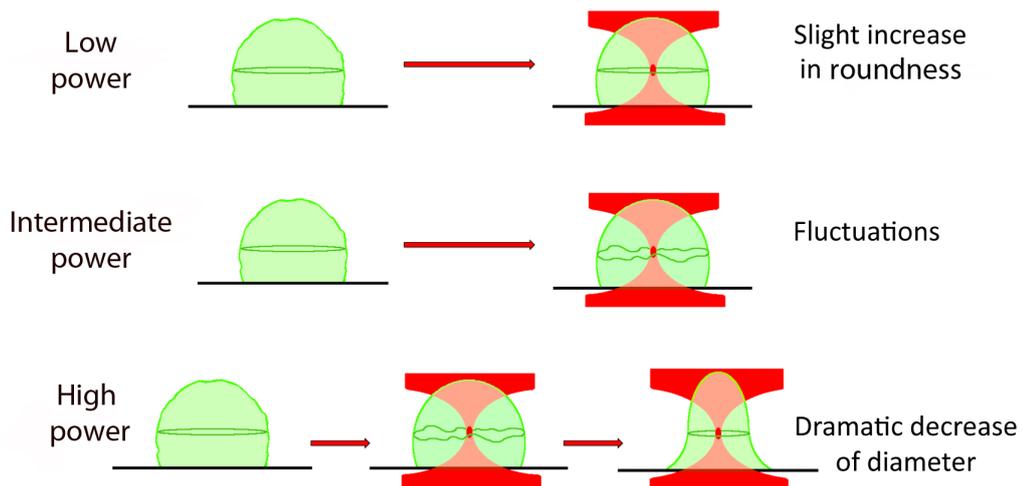
Figure 3.11: Sketches of the deformations observed at low (0-30mW), intermediate (30-70mW) and high laser powers (70mW and above).

3.5 Vesicle survival

3.5.1 A story about laser power, size and phase

The most straight forward way of illustrating the effect of laser power, temperature and size is to plot the number of vesicles surviving as a function of laser power. All data in this section was collected from experiments of type **A** with repeated "on/off" exposure to increasing laser power. For more details see section 3.3.4. In Figure 3.12a the data is colour coded according to the phase of the lipid bilayer. The five categories are the ones defined above in section 3.4. Figure 3.12b shows the same data but with focus on the initial vesicle size, i.e. the vesicle diameter before exposure to the laser trap. The size categories are the following: 16-18 μm, 19-21 μm, 22-24 μm, 25-27 μm, 28-32 μm and the last category contains all larger vesicles with diameters ranging from 34-50 μm.

The first conclusion we can draw is that the higher the laser power, the fewer vesicles survive. By survive we mean that they neither break nor form aggregates of smaller vesicles. This is of course not independent of the exposure time to the laser. The shorter time the laser is on at each laser power, the more likely it is that a vesicle survives higher laser powers. Nevertheless, this does not diminish in any way the power dependence of vesicle survival. If a vesicle is exposed to a laser power inducing fluctuations it cannot withstand, it will break regardless if it has been previously exposed.

Figure 3.12a would also suggest that the more fluid a membrane is, the higher are the laser powers it can withstand. The only phase category in which vesicles survive longer than expected is the *beginning of main transition*. To be sure that this tendency really reflected a phase dependency we decided to plot the same data again, but to colour code it according to initial vesicle size. This can be seen in Figure 3.12b. There is no doubt that the larger the vesicle, the higher laser powers it can survive. Only 8% of the vesicles survived laser powers greater than 200 mW. What does this implicate for the conclusions drawn previously about the role of membrane phase for the vesicle survival? To answer this question we made the same size plot, but for each phase category separately. This is shown in Figure 3.13. The size dependence seems to hold for each phase, with some discrepancies probably due to lack of statistics. Some size categories are also over-represented in one phase; especially 22-24μm in the *main transition*. It is also likely that the two vesicles from the category *beginning of main transition* that survived laser powers greater than 200 mW did it due to their very large size. They were 43 μm and 50 μm in diameter.
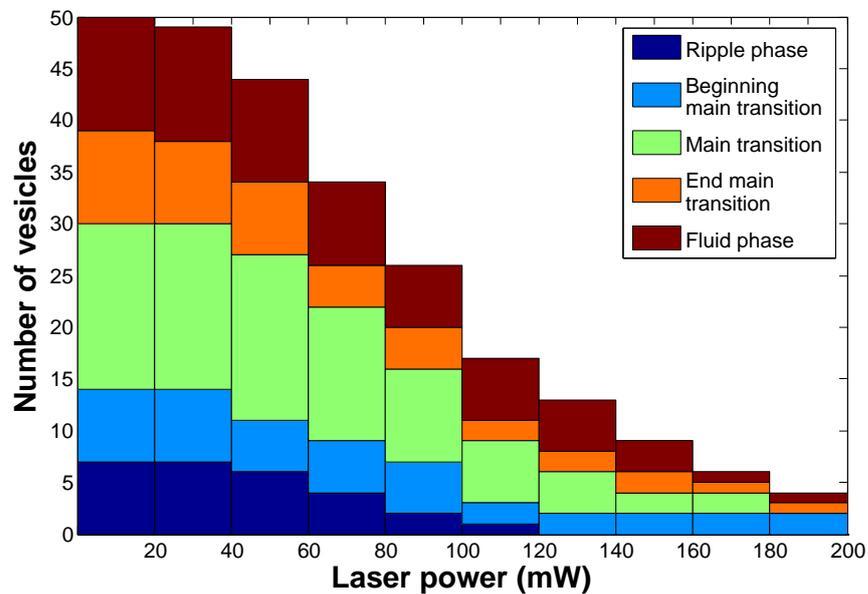
(a) Number of non-broken vesicles versus laser power. Each colour represents one of the five phase categories: I Ripple Phase (dark blue), II Beginning of Main Transition (light blue), III Main Transition (green), IV End of Main Transition (orange), V Fluid Phase (red).
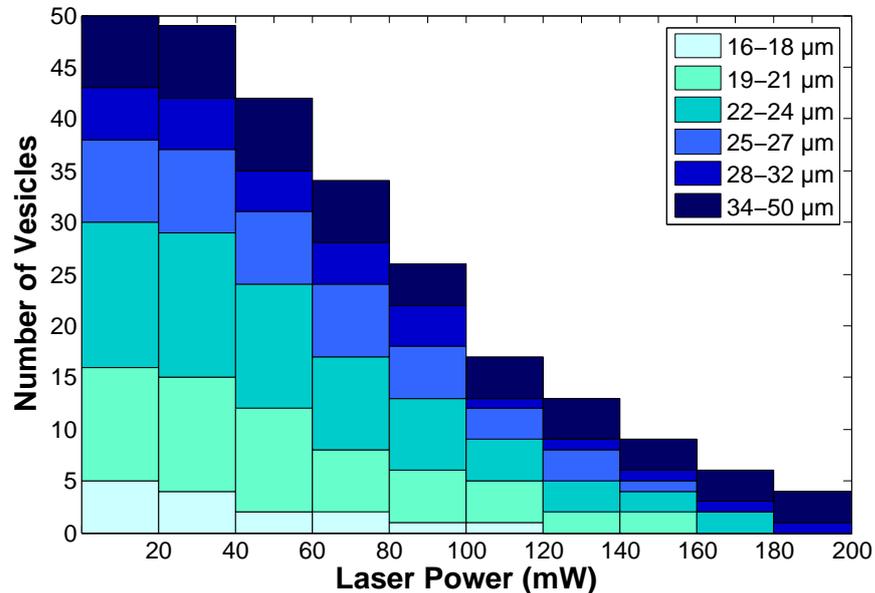
(b) Number of non-broken vesicles versus laser power. Each colour represents one of the six initial size categories: 16-18 μm, 19-21 μm, 22-24 μm, 25-27 μm, 28-32 μm and 34-50 μm.

Figure 3.12: Cumulative barplots over the number of vesicles surviving repeated exposure to increasing laser powers. The data shown in the two figures is the same, sorted either by phase or initial vesicle size.
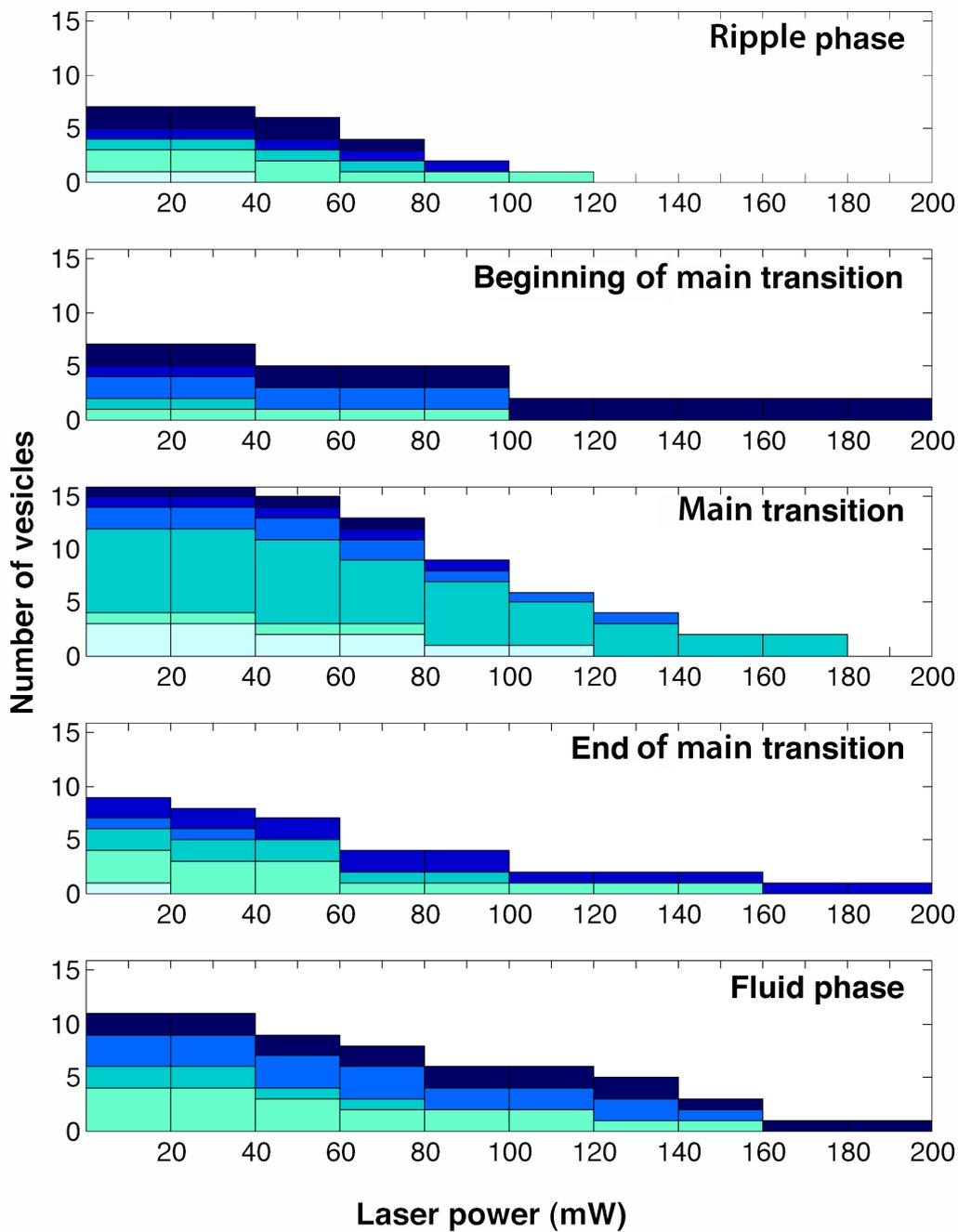
Figure 3.13: Cumulative barplots over the number of vesicles surviving repeated exposure to increasing laser powers. Each plot corresponds to one of the five phase categories. Each colour represents one of the six initial size categories: 16-18 μm, 19-21 μm, 22-24 μm, 25-27 μm, 28-32 μm and 34-50 μm. The legend is the same as in figure 3.12b. The darker the colour is, the larger the vesicles are.
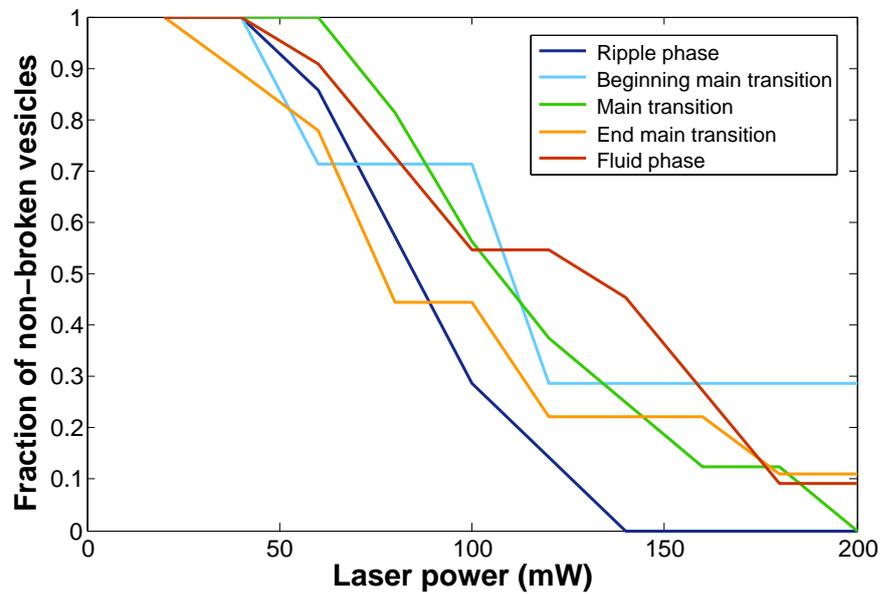
(a) Fraction of non-broken vesicles versus laser power. Each colour represents one of the five phase categories: I Ripple Phase (dark blue), II Beginning of Main Transition (light blue), III Main Transition (green), IV End of Main Transition (orange), V Fluid Phase (red).
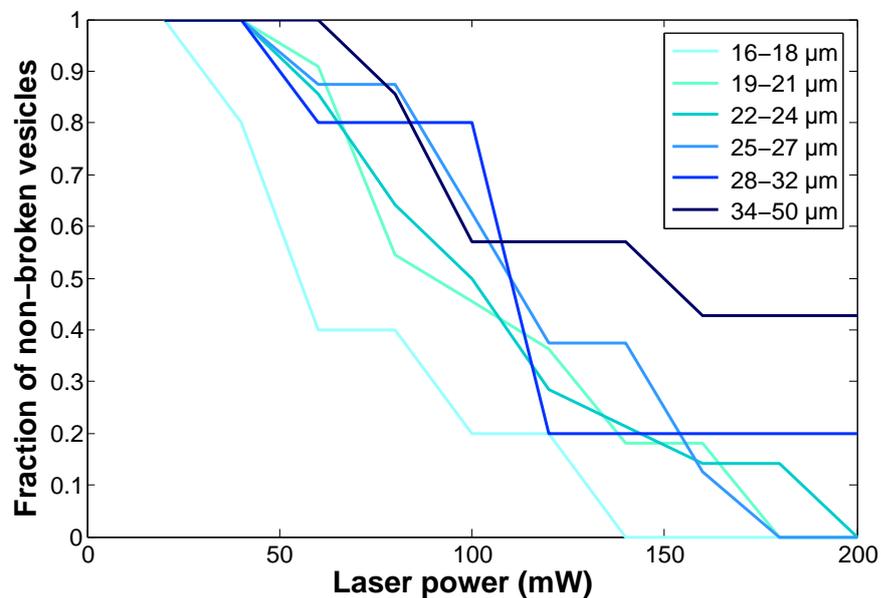
(b) Fraction of non-broken vesicles versus laser power. Each colour represents one of the six initial size categories: 16-18 μm, 19-21 μm, 22-24 μm, 25-27 μm, 28-32 μm and 34-50 μm.

Figure 3.14: Number of vesicles surviving repeated exposure to increasing laser powers sorted by phase and size, and normalised with respect to the number of vesicles in each category.

We also normalised the data with respect to the number of vesicles in each phase or size category. We then plotted the normalised fraction of non-broken vesicles as a function of laser power. This can be seen in Figure 3.14. Looking at the Figure over size dependence was helpful when deciding which vesicles to compare without having to take into account their size. Vesicles that are between 19 and 27 μm in diameter behave very similarly. They start to break at 50 mW, and all are collapsed at laser powers between 180mW and 200mW. 20% of the vesicles that are between 28 and 32 μm in diameter survived laser powers higher than 200 mW. Since they otherwise seem to behave like vesicles between 19 and 27 μm, we included them as well when looking at vesicle shape and size as a function of laser power, see section 3.6.

The curve showing the fraction of non-broken cells in the ripple phase has a higher slop than the curves of the other phase categories. All vesicles are broken at P = 140 mW, whereas at least 10% of the vesicles in each of the other phase categories survive 180 mW. This could be explained by the membrane having a higher bending rigidity in the gel and ripple phase than in the main transition and the fluid phase, see Figure 14.8 in [56]. More data is needed, but there seems to be a correlation between fluidity of the lipid membrane and vesicle survival at high laser powers.

3.5.2 Long-time exposure at constant laser power

A clearer way of visualising the size dependence of the deformations is to look at the survival time of vesicles of different sizes exposed to the same constant laser power (experiment of type **B**, see Section 3.3.4). Figure 3.15 shows the survival time of vesicles exposed to a constant laser power of P = 176 mW as a function of initial vesicle diameter. The studied vesicles were between 16 μm and 39 μm. T= 38.3 °C, which corresponds to the fluid phase.

It is clear that the bigger the vesicle, the longer it survives exposure to high laser powers. The data is best fitted by a polynomial, $f(R) = AR^4$. The dashed line is only a guide to the eye. The area available for distributing the stress induced by the scattering force is larger for a bigger vesicle. Also the distance between the trap focus and the lipid bilayer increases with radius, thus decreasing the photon density at the vesicle surface. This might be part of the reason for the clear size dependence of the vesicle survival time. One thing should be noted. In this plot we do not have any data for vesicles smaller than 15 μm. There are several reasons for this. The electroformation method yields a quite narrow size distribution, i.e. most vesicles are between 15 μm and 40 μm. Secondly, at the selected laser power vesicles smaller than 15 μm would break faster than the time resolution we had with the confocal
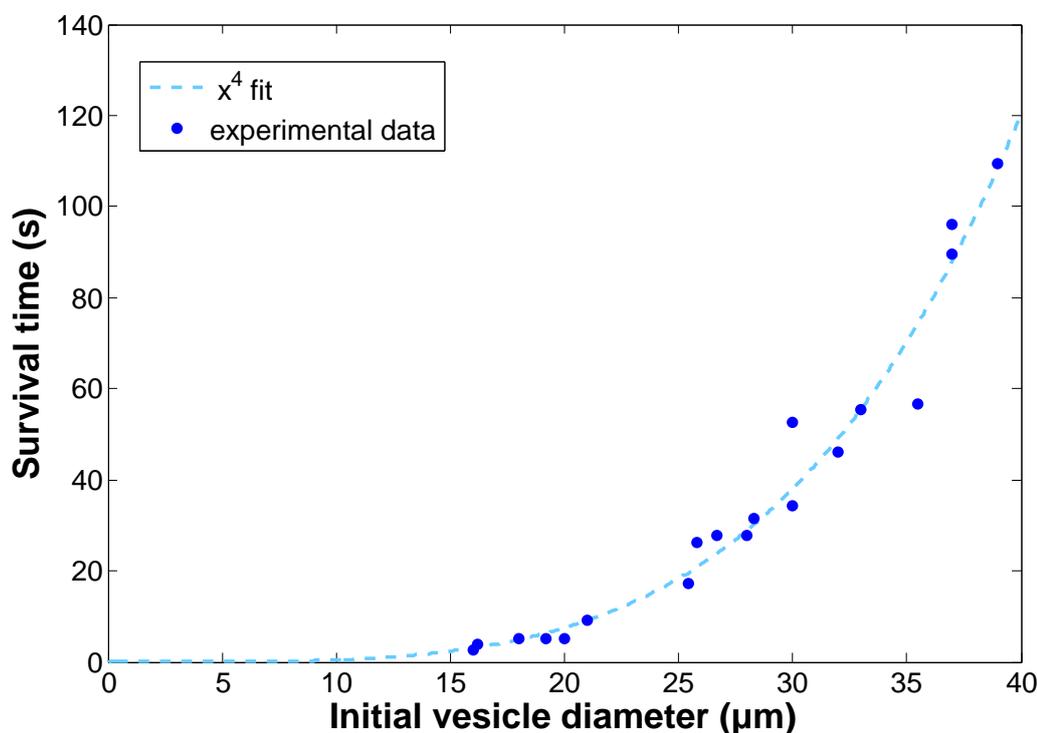
Figure 3.15: Survival time of vesicles exposed to a constant laser power of P = 176 mW versus initial vesicle diameter. Each point corresponds to one vesicle. T= 38.3 °C, which corresponds to the fluid phase (**V**).

microscope. The acquisition time was 1.152 s per image. It would have been possible to use a higher scanning rate, but the image quality would have been compromised, making data analysis more difficult. Third, when the diameter of the vesicles approaches 3-5 μm we enter another regime. The vesicles are no longer much larger than the focal volume of the trap, which has a diameter of about 1 μm in the xy-plan. There have been reports of vesicles of that size being trapped [27].

This experiment can also give us information about the phase behaviour of the lipid membrane, see Figure 3.16. Three of the five phase categories are represented in this figure, the *beginning of main transition*, the *main transition* and the *fluid phase*. Here as well the vesicles were exposed to a constant laser power P=176mW. Comparing vesicles in the beginning of the phase transition with vesicles in the fluid phase, it seems that the more fluid a membrane is, the longer it survives exposure to high laser powers. For vesicles in the main transition we could not see any significant difference in survival time
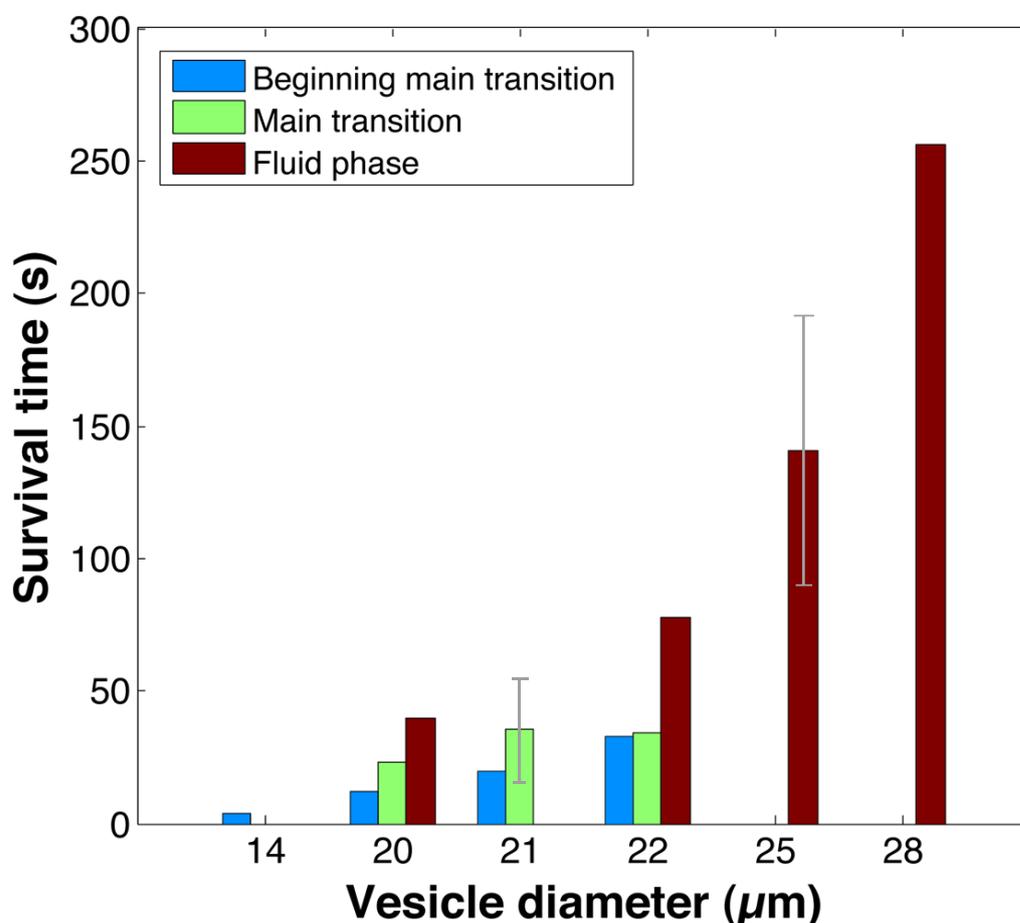
Figure 3.16: Mean maximum exposure time for vesicle of different sizes at three different temperatures; T = 22.7 °C (Beginning of the main transition), T = 30.4 °C (Main transition) and T = 38.4 °C (Fluid phase). P = 176 mW. Each bar represents one vesicle unless there is an errorbar, in which case there were three vesicles.

comparing with vesicles in the beginning of the main transition. It should be noted that the size range over which we have data for this phase category is very limited. Vesicles were between 20 μm and 22 μm. Again, looking only at vesicles in the fluid phase we see a clear size dependence of the survival time. Vesicles that are 28 μm in diameter survive more than five times longer than vesicles that have a diameter of 20 μm. More data is needed, but these results are promising.

At T= 26 °C (data not shown), the vesicles behaved differently from what we have seen earlier. All started by showing a decrease in diameter and subsequent budding as expected, but six out of twelve vesicles started growing again. A vesicle that had become 10 μm in diameter grew to be 40 μm while the laser was still on. Vesicles exposed to the laser usually loose lipid material. In this case, it is likely that lipids were instead recruited from the lipid film covering the ITO surface. The temperature at which this was observed corresponds to the boundary between the beginning of the main transition and the main transition itself. In the main transition the bending modulus is a factor ten smaller than in the gel and the fluid phase [56, p. 240]. This could explain why it was not observed at T = 22.7 °C and T = 38.4 °C, but not why we could not observe it at T = 30.4 °C.

3.6 Vesicle shape and size upon repeated laser exposure

3.6.1 Roundness

A commonly used measure for roundness is the isoperimetric quotient Q. It is defined as the area of a closed curve divided by the area of a circle with the same perimeter. If $Q = 1$ the analysed shape is circular. Any other shape would generate a Q value smaller than 1.

$$R = \frac{S_{pix}C}{2\pi},$$ (3.1)

where S_{pix} is the pixel size, i.e. the conversion factor between pixels and μm. C is the circumference in pixels of the cross-section and R the radius of a circle with the equivalent area A_{circle}.

$$A_{circle} = \pi R^2 = \frac{S_{pix}^2 C^2}{4\pi}$$ (3.2)

and

$$Q = \frac{S_{pix}^2 A_{measured}}{A_{circle}} = \frac{4\pi A_{measured}}{C^2},$$ (3.3)

where $A_{measured}$ is the area in pixels of the vesicle cross-section. In Figure 3.18 we see the isoperimetric quotient plotted against laser power both for vesicle during exposure and vesicles after exposure to a given laser power.
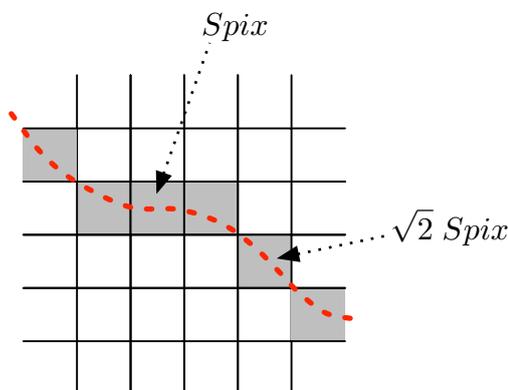
Figure 3.17: Sketch of a part of the vesicle contour. The grey pixels are the contour as seen in the raw data and the doted red line is a representation of the actual circumference.

We get Q values greater than 1. This can not be, since it would correspond to a shape more optimal than a circle in minimising the circumference to area ratio C/A. The reason is that we underestimated the perimeter C of the vesicle cross-section. This is due to the way the data analysis is conducted, counting the number of pixels contained by the perimeter and area of each cross-section. It does not take into account the difference in length between the side of a pixel and its diagonal. This is illustrated in Figure 3.17. When running the analysis program on a perfect circle of similar size as the studied vesicles (same apparent size in a 512x512 pixels image) one gets $Q = 0.81$. For a vesicle ten times smaller $Q = 0.79$. The discrepancy is due to a slightly different ratio between pixels following the contour diagonally or side by side. The circular area is proportional to the circumference squared. This gives a correction factor $cc = 1.11$ ($C_{cor} = ccC$) and an underestimation of the perimeter of about 10% for a perfect circle. For a given circumference there is a very large number of possible non-spherical configurations. All would have a different correction factor cc. $1 \leq cc \leq \sqrt{2}$, the two extreme cases being all pixels aligned in straight rows, as for a square, and all pixels diagonally positioned relative to one another, as for a lozenge. This makes the plots in Figure 3.18 very noisy and prevents us from drawing more than very general observations about the roundness of the vesicles. As a reference, we plotted Q for a perfect circle and some different degrees of deformation. They are shown with dotted lines in Figure 3.18.
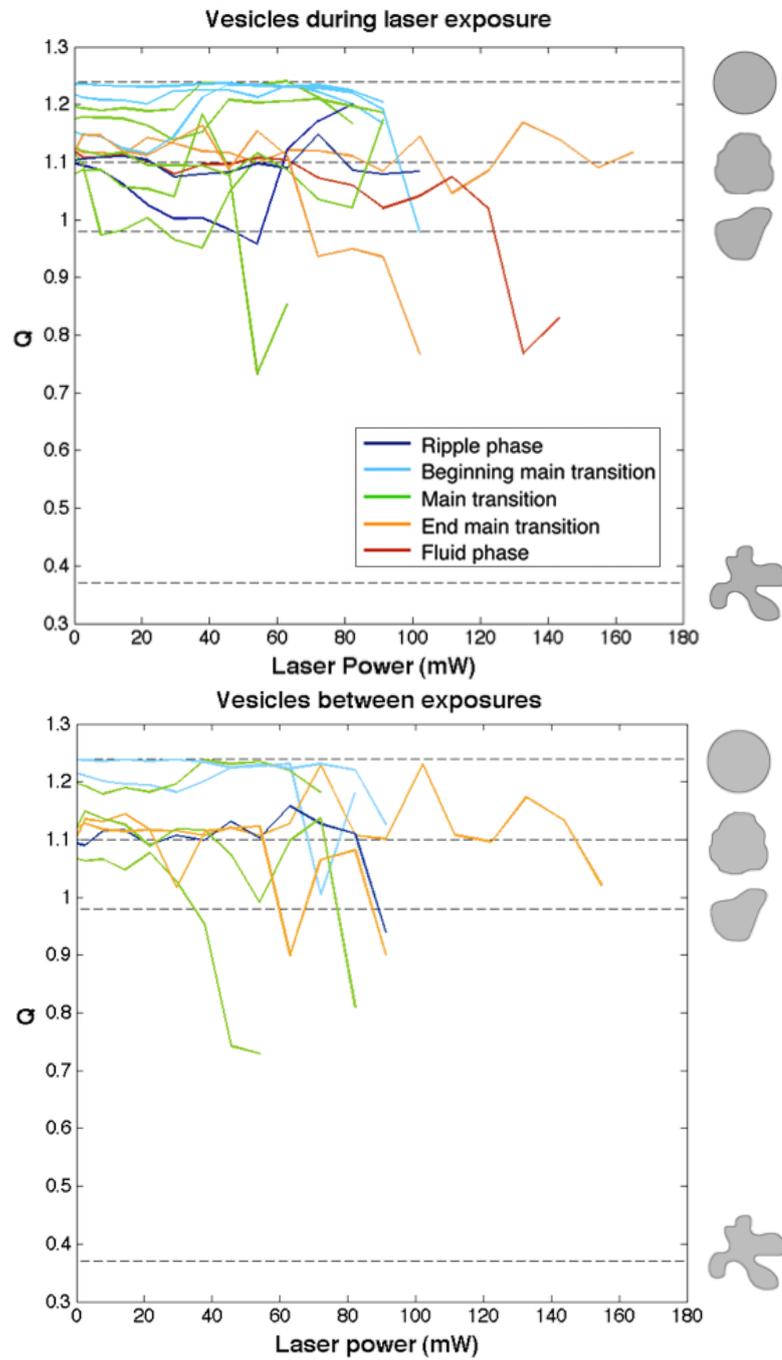
Figure 3.18: The isoperimetric quotient Q versus laser power (mW). **Above**: Vesicles during exposure to the laser trap, **Below**: Vesicles between laser exposures.

No significant difference can be seen between the two figures. We would have expected vesicles at rest to show more constant and smaller Q values. By direct observation, one can see that the fluctuations cease immediately after turning off the laser. There might be two reason for Q not to show any "laser on" specific behaviour. The shape of the cross-section never deviates much from a circle. The fluctuations are a highly dynamic phenomenon not very well captured by measuring the area and circumference of the vesicle cross-section. Still we can see an overall laser dependence, both during and between laser exposures. With only a couple of exceptions Q decreases with increasing laser power, meaning the vesicles get less and less spherical the higher the laser power. It should also be noted that vesicles in the beginning of the phase transition are rounder than vesicles in any other phase category. They also seem to show smaller fluctuations in Q. Vesicles in the phase transition behave differently depending on if they are close to category II (*beginning of main transition*) or really from the middle of the main transition. The more fluid the membrane, hence the higher the temperature, the more Q seems to fluctuate. It is possible that we capture the thermal fluctuations.

3.6.2 Size decrease

We now want to characterise the shape of the deformed vesicle. Since, as mentioned earlier, the focus of the laser trap and the scanning focus of the confocal are coupled, we chose to look at the equatorial cross-section of the studied vesicles. We measured the area A and the circumference C of these cross-sections. In Figure 3.19 we show the cross-sectional area and circumference plotted as a function of laser power. The data was normalised with respect to the cross-sectional area and circumference of the vesicle before laser exposure. An increase in the measured area gives rise to a value greater than 1 and a decrease in area gives a value smaller than 1. Should be noted that a circle is the shape with the largest area for a given perimeter. If the circumference stays constant but the area increases or decreases we learn something about the shape of the cross-section. If the circumference decreases as well as the area we now we have a decrease in size of the cross-section and potentially of the vesicle. This was observed for all vesicles at laser powers greater than 60 mW. This means that repeated exposure to increasing laser power lead to a loss of lipid material.

For reference we plotted the cross-sectional area showing vesicle sizes in Figure 3.20. There is no obvious size dependence for this data set. Most vesicles survived until around 100 mW. Larger vesicles might have a slight tendency to survive a little bit longer, but a 19 μm vesicle was the most
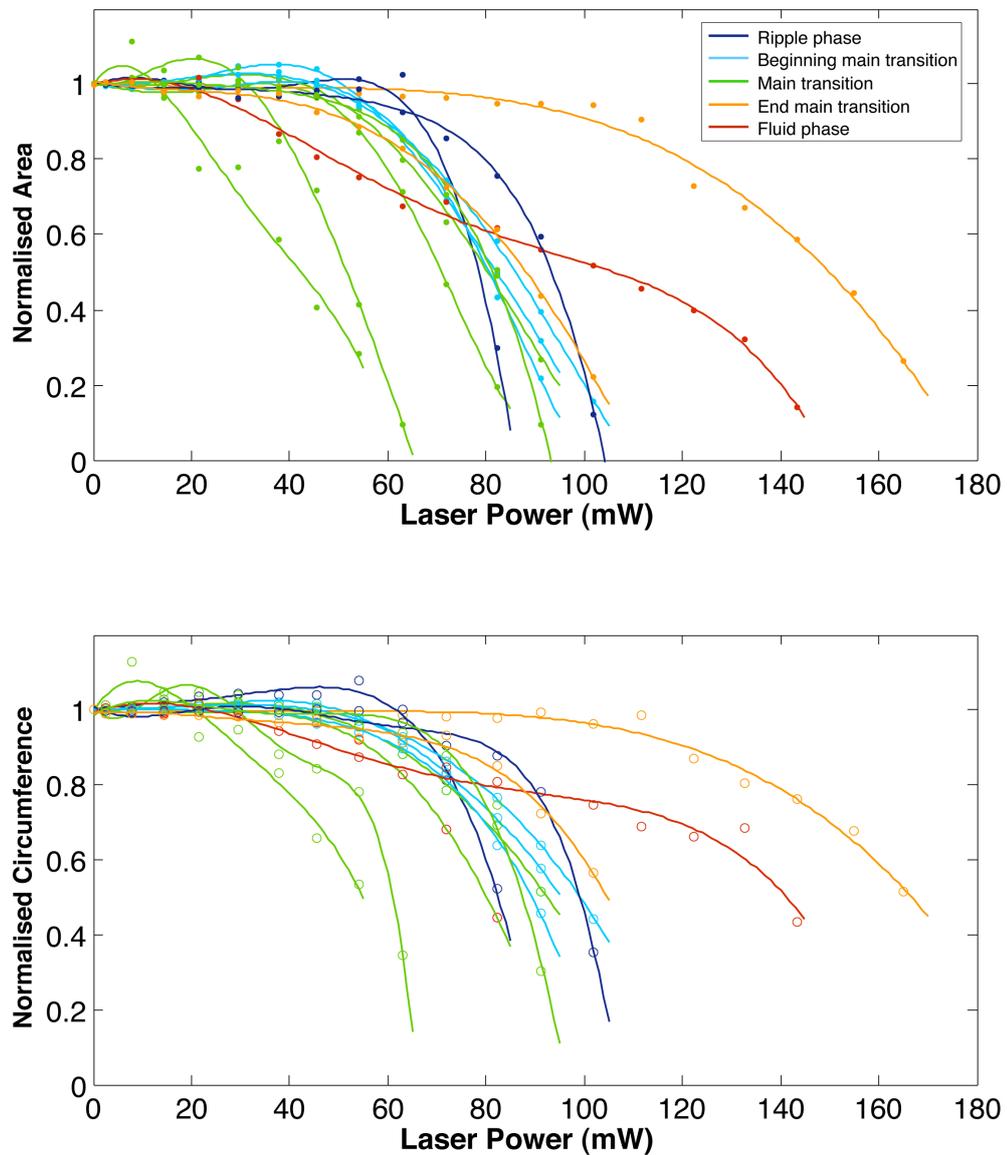
Figure 3.19: Normalised cross-sectional area (above) and perimeter (below) versus laser power (mW). The phase of the vesicles is also shown.

long lived at $T = 34.6\,°C$. We will therefore look at the phase dependence without worrying too much about the vesicle size. The data in Figure 3.19 was colour coded according to the phase categories defined earlier. The behaviour of vesicles at the end of the phase transition or in the fluid phase, orange and dark red in Figure 3.19 and Figure 3.21 C and D, are the easiest
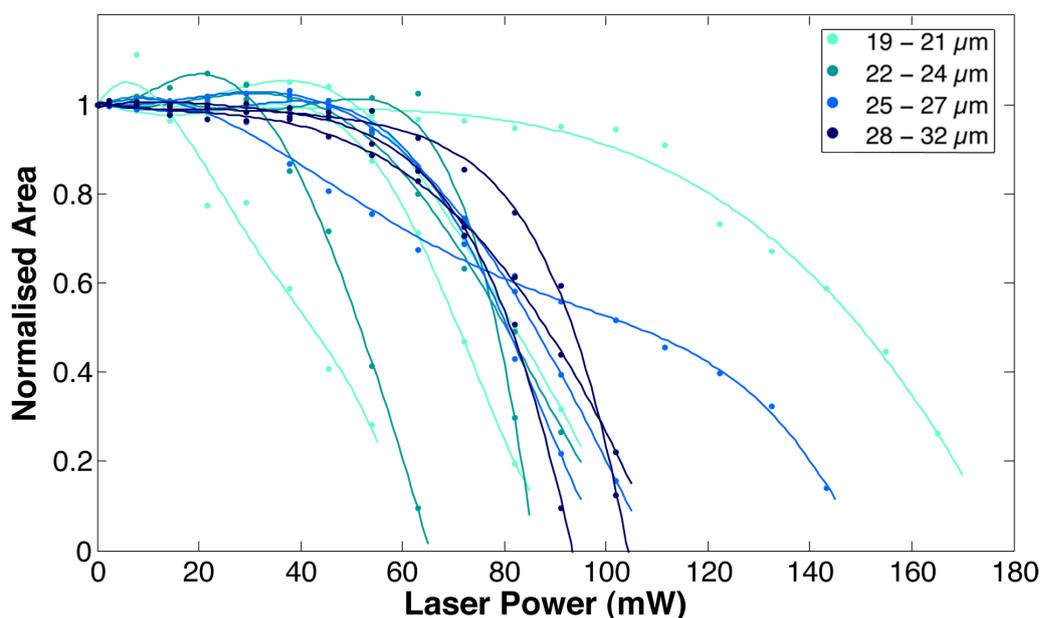
Figure 3.20: Normalised area versus laser power (mW) showing the size of each vesicle.

to differentiate from the other traces. The loss in size seems to be more gradual and the vesicles survived higher laser powers. This can be put in contrast to vesicles in the gel phase, shown in dark blue. They survived the same laser power as vesicles in the beginning of the phase transition, but seemed to have a much more abrupt loss in size. We will try to quantify the rates at which vesicles decreased in size in Section 3.7.1. Vesicles in the phase transition showed varying responses to the laser trap. They either behaved similarly to vesicles in the beginning of the phase transition (see Figure 3.21 A and B) or broke at very low laser power showing a response, meaning a decrease in cross-sectional size, very early. The behaviour of vesicles in the phase transition seems very sensitive to temperature. A small change in temperature can lead to a great change in the ratio between gel and fluid domains. This would alter the membranes elastic properties notably.

Vesicles are rarely perfectly spherical. Sometimes a slight increase in area could be observed when laser light started influencing the membrane around 30-40 mW. This can be seen in Figure 3.21 A that shows the behaviour of vesicles at temperatures around T=26 °C. At intermediate laser powers an increase in area could be seen while the perimeter stayed constant. This means the cross-section got more circular, suggesting that the vesicle itself got more spherical or at least more tense. Small kinks might have been
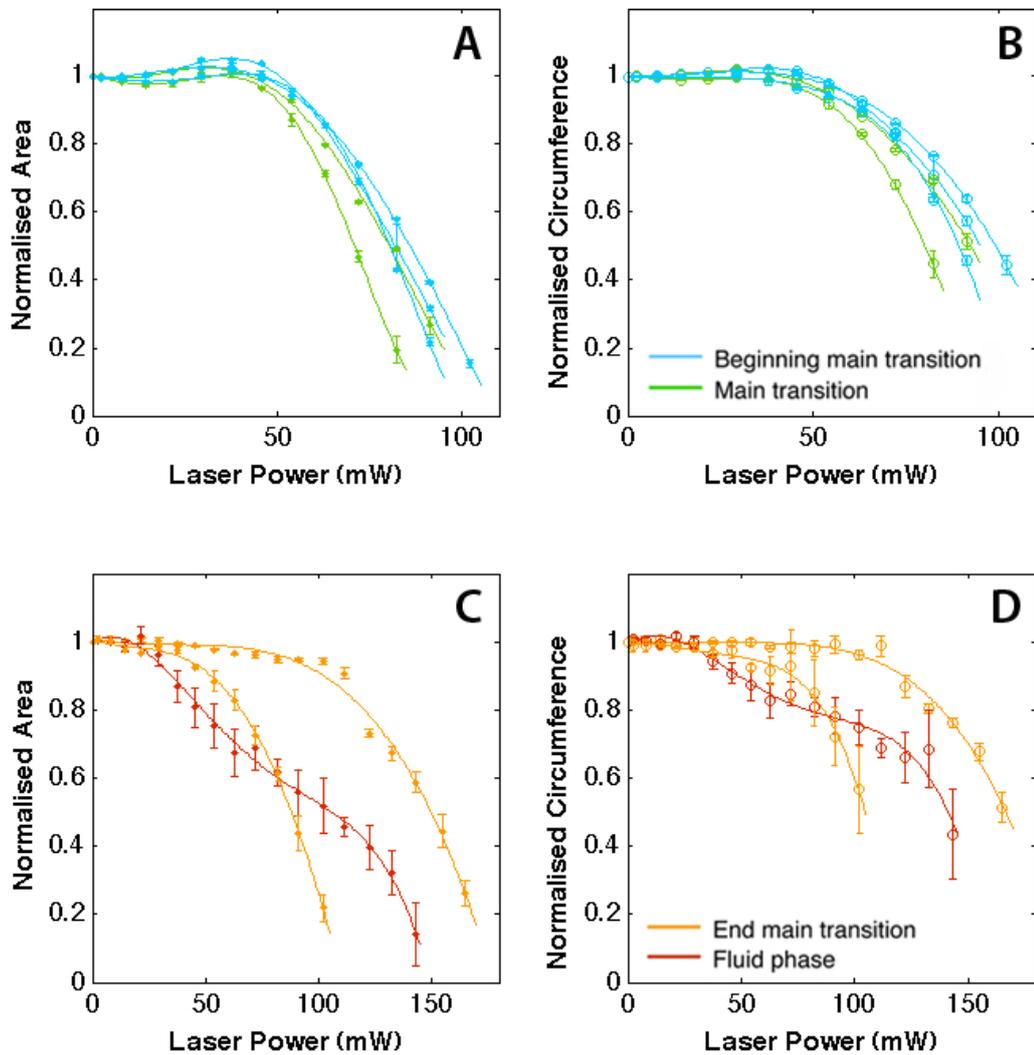
Figure 3.21: Normalised cross-sectional area and perimeter for vesicles in A/B: the beginning of the phase transition and phase transition, C/D: the end of the phase transtion and the fluid phase. The standard deviation is also plotted as error bars.

pushed out by an increase in tension induced by the scattering force. In the liquid-disordered (fluid) phase this was not observed. Already at rest thermal fluctuations were visible. In the gel phase the pushing out of the kinks was quite obvious when looking at the raw data, but both the area and perimeter plots show an increase. The kinks in the gel phase were much bigger than in the beginning of the phase transition, hence the overall shape of the entire

vesicle might have been more affected, also leading to a change in measured perimeter.

As a last observation looking at Figure 3.21, we can mention that the errorbars seem to get larger with increasing temperature and increasing laser power. Both observations can be argued for. With increasing temperature we also have increasing thermal fluctuations. The vesicles also survive longer and are hence exposed to higher laser powers giving rase to larger deformations. The same argument is also valid for the error bars of one vesicle exposed to increasing laser powers; low laser powers correspond to smaller error bars.

3.7 Phase dependence

3.7.1 Deformation rates

We also looked at the ratio between circumference and area (C/A), with the aim of saying something more about the rates at which the vesicles decrease in size. It should be noted that an increase in C/A in theory describes both deformations towards a less spherical shape and a decrease in vesicle size. We have shown that the change in size dominates. We will therefore neglect the change in roundness. C/A can be seen in Figure 3.22 as a function of laser power. Also the phase of the vesicles is indicated. This is the same data as shown in the area and perimeter plots in Figure 3.19.

To compare the rate of size decrease for the different phases, we made exponential fits and compared the inverse of their exponential coefficients λ. $1/\lambda$ corresponds to the laser power at which C/A has increased with a factor e. The fitting function was the following:

$$F(P) = Ae^{-\lambda(\mathrm{B}-\mathrm{P})} + 1 \qquad (3.4)$$

where P is the laser power and B is an approximation of the laser power at which C/A started increasing rapidly. λ is quite robust to changes in B. A is a constant estimated together with λ. $1/\lambda$ is plotted as a function of temperature together with the heat capacity profile of DMPC:DPPC 50:50, see Figure 3.23. There seems to be an increase of $1/\lambda$ with temperature. The more fluid the membrane is, the more gradual the change in size. In other words, at give laser power a vesicle in the fluid phase suffers less damage than a vesicle in the gel phase.
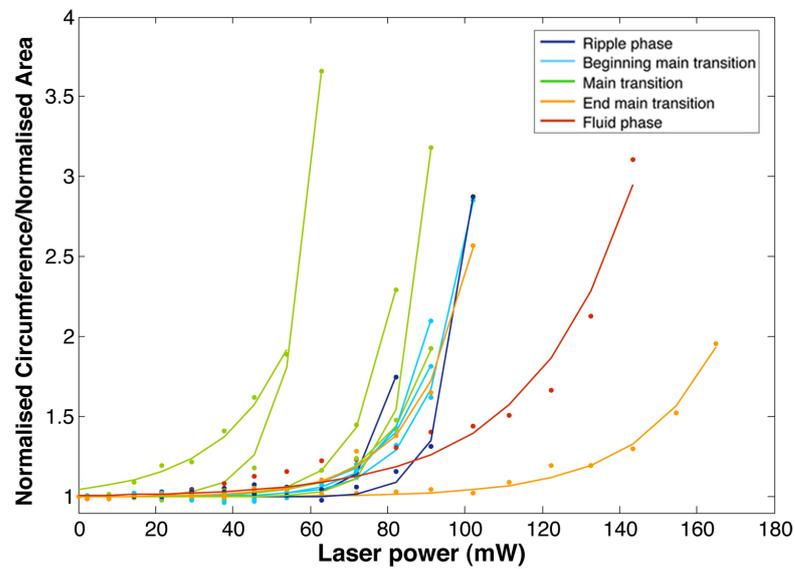
Figure 3.22: Normalised circumference divided by normalised area versus laser power. The phase of each vesicle is shown by color coding.
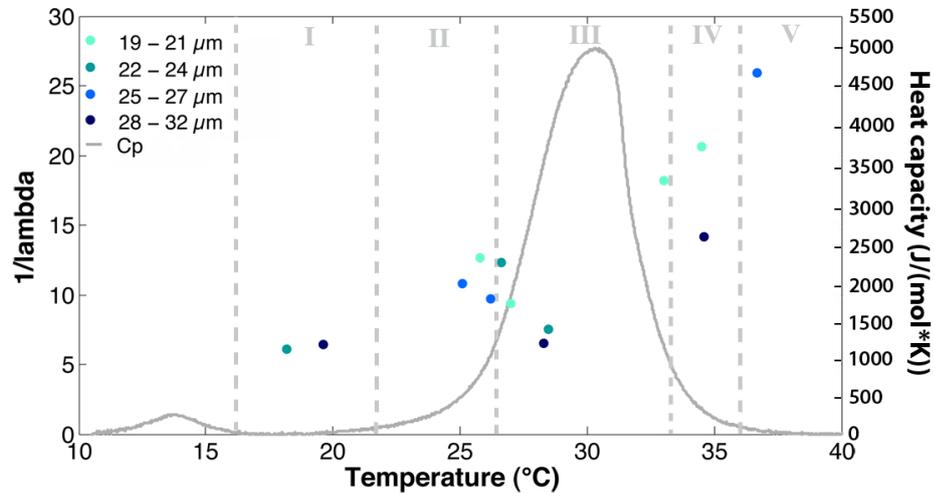
Figure 3.23: $1/\lambda$ (mW) versus temperature (°C). The data is divided in four size categories, 19-21 μm, 22-24 μm, 25-27 μm and 28-32 μm. Also the excess heat capacity C_p (J/molK) and the five phase categories are indicated in grey. I Ripple Phase, II Beginning of Main Transition, III Main Transition, IV End of Main Transition, V Fluid Phase.

3.7.2 A 3% change in the circumference to area ratio

We also looked at the laser power at which C/A changed with 3% from its initial value (3%Pc), either increasing or decreasing (see Figure 3.24). A 3% upward deflection of the curve is marked by a star and a 3% downward deflection is marked by a square. The dashed line is a guide to the eye. 3%Pc seems to decrease with increasing temperature. The 3%Pc value at $T = 20\,°C$ is three times larger than at $T = 40\,°C$. Allthough the data spread is large this is a significant change in response. The membrane is more flexible in the liquid-disordered phase than in the solid-ordered. The question is whether we catch a phenomenon due to the exposure to optical tweezers, i.e. laser induced deformations, or if it only reflects the increase in thermal fluctuations with increasing temperature. It is also unclear if there is any effect due to the phase transition. There are two points in the main phase transition, at T=28 °C and T=33 °C, that have a quite low 3%Pc value, but we do not have enough data to conclude anything with certainty.

As a last observation it seems like downward deflections, with a few exceptions, occur at lower laser power than upward deflections measured at similar temperatures. This would go hand in hand with the empirical observation made in section 3.4 that the vesicle cross-section seems to get rounder at lower laser powers.

3.7.3 Relaxation times

At intermediate laser powers ranging from 29.4 mW to 72 mW and for temperatures between 18.1 °C and 27 °C we often observed vesicles relaxing back to their resting shape while still exposed to the laser. The two image series shown in Figure 3.25 illustrate this. If the fluctuations were too big this could not be seen. Most of these observations were made at temperatures close to 20 °C or 26 °C . In terms of membrane state these two temperatures correspond to the end of the rippled phase and the beginning of the phase transition (see Figure 3.10). The laser power needed for this to occur was on average 48.3 ± 12.5 mW close to 20 °C and 41.7 ± 4.5 mW around 26 °C. The very large standard deviation for vesicles in the rippled phase is especially due to one very low laser power. This still concords with previous results showing that the more fluid a membrane is the lower are the laser powers needed to induce deformations.

The time scale of the relaxation also seems slightly different for the two temperature regimes. Around 20 °C the relaxation time is of the order of half a minute whereas at 26 °C it is closer to 10 s, i.e. higher temperature seem to shorten the relaxation time. Figure 3.26 shows sliding window plots of
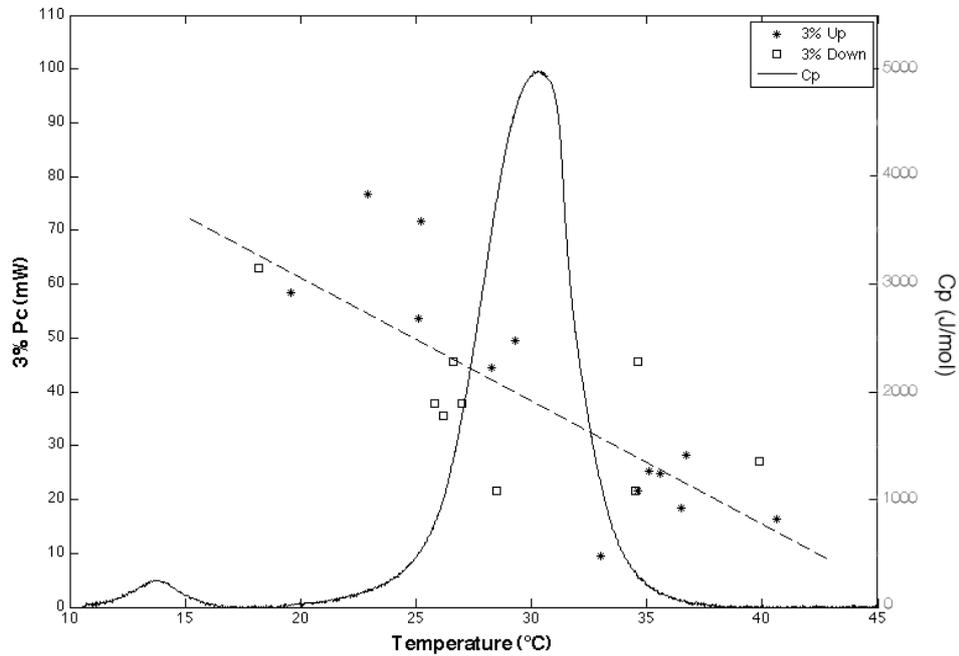
Figure 3.24: Laser power at which a 3% change in C/A can be observed as a function of temperature. The C_p-profile of DMPC/DPPC 50:50 is shown as well.

C/A versus time for $T_1 = 20\,°C$ at three different laser powers. As expected the circumference to area ratio decreased with time, i.e. the cross-section of the observed vesicle got rounder with time. This process seemed to be faster with increasing laser power, around $25\,s$ for $P = 72\,mW$ whereas it more of the order of $30\,s$ or 40 at the two lower laser powers.

This relaxation phenomenon might also occur at other temperatures. Two hypotheses could explain why we did no make this observation. The relaxation might have been so fast that it could not be captured with the frame rate we had. An other explanation could be that the thermal fluctuations observed at higher temperatures mask the relaxation process. Using a high speed camera could potentially tell us more about this.
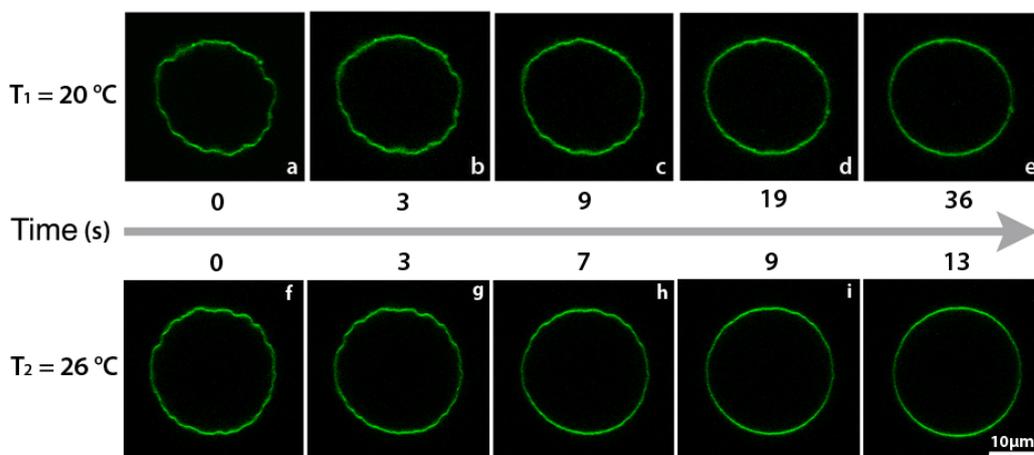
Figure 3.25: The first time series shows a $29\,\mu\text{m}$ vesicle exposed to a constant laser power of $63\,\text{mW}$ at a: $\text{t}=0\,\text{s}$, b: $\text{t}=3\,\text{s}$, c: $\text{t}=9\,\text{s}$, d: $\text{t}=19\,\text{s}$, e: $\text{t}=36\,\text{s}$. $T_1 = 19.6\,^\circ\text{C}$. These confocal images correspond to the $63\,\text{mW}$ curve in Figure 3.26. The second time series shows a $26\,\mu\text{m}$ vesicle exposed to a constant laser power of $37.8\,\text{mW}$ at f: $\text{t}=0\,\text{s}$, g: $\text{t}=2.6\,\text{s}$, h: $\text{t}=6.6\,\text{s}$, i: $\text{t}=9.2\,\text{s}$, j: $\text{t}=13.2\,\text{s}$. $T_2 = 26\,^\circ\text{C}$.

3.8 Hypothesis regarding the deformation mechanism

3.8.1 Our hypothesis

We will in this section try to get a physical understanding for the interaction between the lipid bilayer of the studied vesicles and the tightly focused laser light of the optical tweezers. In our experiments the trap focus was placed at the center of the equatorial plane of the vesicle. This made the distance from the trap focus to the lipid bilayer of the order of tenths of micrometers. This would suggest a very weak gradient force acting on the lipid bilayer and the domination of the scattering force at intermediate and high laser powers. We therefore formulated the hypothesis that the fluctuations and deformations we saw were due to the transfer of momentum from the impinging photons to the bilayer, the scattering force deforming the vesicles in the direction of propagation of light. To test our hypothesis, we will in the following section try to estimate the scattering force and calculate the force necessary to deform a GUV into a more cylindrical shape. We will also show experimental data that seems to support such a model. Still the short-comings of
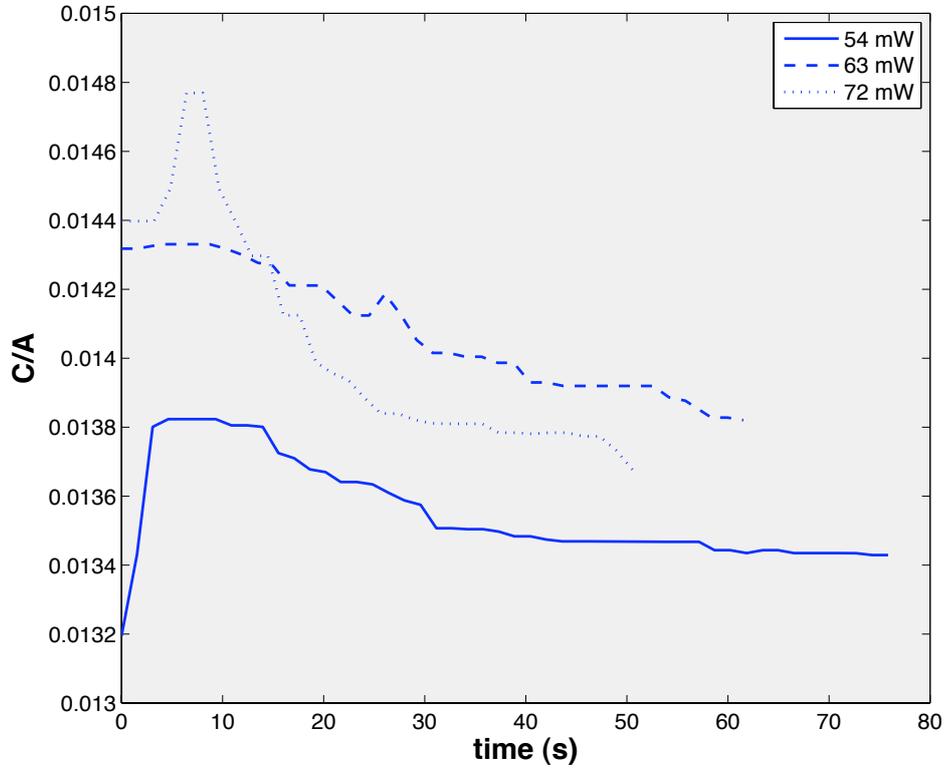
Figure 3.26: Sliding window plot (over 11 data points) showing C/A, i.e. the level of roundness, versus time for a $29\,\mu$m vesicle at three different laser powers; P $= 54\,$mW, $63\,$mW and $72\,$mW. $T_1 = 19.6\,°$C. The vesicle was the same as in the first image series in figure 3.25.

our experimental setup do not allow us to fully exclude an other mechanism. Laser induced heating might also be a cause of the observed fluctuations. According to Peterman *et al.* [106] a laser power of 100mW would lead to a temperature increase of $0.8\,°$C at the trap focus. This is not likely to be the cause of the heavy fluctuations observed at the that laser power.

3.8.2 Estimation of the forces involved

We estimated the force needed to deform a half-spherical vesicle into an elongated shape in the following way. The energy needed to stretch a lipid membrane is much higher than the energy needed to bend it, we will therefore assume that the area of the vesicle is constant. The bending energy of these shapes can be found in table 7.1 in reference [17]. In the following we use the parameters defined in figure 3.27 and set $h = R$. The bending energy of a half-sphere E_s is

$$E = 4\pi(\kappa_b + \kappa_G), \tag{3.5}$$

where κ_b is the bending modulus and κ_G is the Gaussian curvature. The bending energy of a cylinder with a half-spherical cap E_c is

$$E_c = 4\pi(\kappa_b + \kappa_G) + \pi\kappa_b\frac{h'}{r}. \tag{3.6}$$

This gives us an energy difference of

$$\Delta E = \pi\kappa_b\frac{h'}{r}. \tag{3.7}$$

The force needed to deform the vesicle can be expressed as

$$F = \frac{\Delta E}{h'} = \frac{\pi\kappa_b}{r}. \tag{3.8}$$

A typical value for the bending modulus is $\kappa_b = 10^{-19}$J and $r = 5\cdot 10^{-6}$m, which gives

$$F \approx 6 \times 10^{-14}\text{N}. \tag{3.9}$$
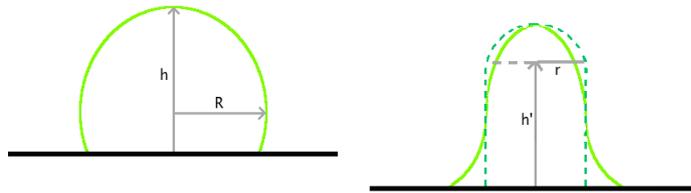
Figure 3.27: Sketches of a vesicle before and after elongation.

The scattering force acting on the membrane can be estimated in the following way:

$$F_{scat} = \frac{PC_{scat}}{c_{H_2O}}, \tag{3.10}$$

where P is the total incoming laser power, c_{H_2O} is the speed of light in water and C_{scat} is the likelihood of the incoming photons to be scattered by the membrane. This likelihood corresponds to the scattering efficiency that is defined as

$$C_{scat} = \frac{\sigma_A}{A}, \tag{3.11}$$

where σ_A is the scattering cross-section of a scattering unit of area A. The general expression for the differential scattering cross-section for a collection of scatterers is (see equation 10.18 in [61])

$$\frac{d\sigma}{d\Omega} = \frac{k^4}{(4\pi\epsilon_0 E_0)^2} \left| \sum_j \left[\overrightarrow{\epsilon^*} \cdot \overrightarrow{p_j} + (\overrightarrow{n} \times \overrightarrow{\epsilon^*}) \cdot \frac{\overrightarrow{m_j}}{c} \right] e^{i\overrightarrow{q}\cdot\overrightarrow{x_j}} \right|^2, \tag{3.12}$$

where k is the wave number, E_0 is the amplitude of incoming electric field, $\overrightarrow{\epsilon}_0$ is the incident polarization vector, $\overrightarrow{\epsilon}^*$ is the complex conjugation of the polarization vector, $\overrightarrow{p}_j$ and $\overrightarrow{m}_j$ are the induced dipole moments at the position $\overrightarrow{x}_j$ of the j-th scatter, $\overrightarrow{n}$ is a unit vector in the direction of observation, $\overrightarrow{q}$ is the scattering vector, and c is the speed of light.

We consider the lipid bilayer as being a collection of dielectric spheres with a radius $a = 2.5\,\text{nm}$, corresponding to half the thickness of the lipid membrane. Within a wavelength λ of the incoming light the scatterers can be seen as correlated. Within a small angle from the membrane normal, $\theta = \lambda/L$ with L being the dimension of the scattering array, there is constructive interference both forward and backward. We chose our unit scattering area to be a $\lambda \times \lambda$ piece of the lipid membrane, hence $\theta = 1\,\text{rad}$. For a $\lambda \times \lambda$ piece of the lipid membrane made of n identical scatterers the total electric field can be written as being

$$\sum_{i=1}^n E_i = n \cdot E_1. \tag{3.13}$$

The differential scattering cross-section for a $\lambda \times \lambda$ piece can then be expressed as

$$\frac{d\sigma}{d\Omega} = \frac{k^4}{(4\pi\epsilon_0 E_0)^2} \left| n \left[\overrightarrow{\epsilon^*} \cdot \overrightarrow{p_1} + (\overrightarrow{n} \times \overrightarrow{\epsilon^*}) \cdot \frac{\overrightarrow{m_1}}{c} \right] e^{i\overrightarrow{q}\cdot\overrightarrow{x_1}} \right|^2 = n^2 \left(\frac{d\sigma}{d\Omega} \right)_{single}. \tag{3.14}$$

The differential scattering cross-section for a single scatterer is (see equation 10.10 in [61])

$$\frac{d\sigma}{d\Omega} = n^2 k^4 a^6 \left| \frac{\epsilon_r - 1}{\epsilon_r + 2} \right|^2 \frac{1}{2}(1 + \cos^2 \theta). \tag{3.15}$$

For the back (or forward) scattered light the scattering cross-section can be calculated as follows

$$
\begin{aligned}
\sigma_{\lambda\lambda} &= \int_0^1 2\pi \sin\theta \frac{d\sigma}{d\Omega} d\theta \\
&= \pi n^2 k^4 a^6 \left| \frac{\epsilon_r - 1}{\epsilon_r + 2} \right|^2 \int_0^1 2\pi \sin\theta (1 + \cos^2\theta) d\theta \quad (3.16) \\
&= \frac{2}{3} \pi n^2 k^4 a^6 \left| \frac{\epsilon_r - 1}{\epsilon_r + 2} \right|^2 .
\end{aligned}
$$

We can get the number of scatterers n by dividing the volume of one scattering unit area by the volume of a single scatterer.

$$
n = \frac{2a\lambda^2}{\frac{4}{3}\pi a^3} = \frac{3\lambda^2}{2\pi a^2} \quad (3.17)
$$

By putting equation 3.17 into equation 3.16 we finally obtain

$$
\sigma_{\lambda\lambda} = 24\pi^3 a^2 \left| \frac{\epsilon_r - 1}{\epsilon_r + 2} \right|^2 . \quad (3.18)
$$

As we mentioned earlier the scattering efficiency is defined as

$$
C_{scat} = \frac{\sigma_{\lambda\lambda}}{A_{\lambda\lambda}} . \quad (3.19)
$$

This reflects the probability of a photon to get scattered, we therefore only need to consider one $\lambda \times \lambda$ unit. So finally the total force transferred to the membrane in the z direction is:

$$
F_z = F_{in} q_z \frac{\sigma_{\lambda\lambda}}{A_{\lambda\lambda}} \quad (3.20)
$$

$$
= \frac{48\pi^3 a^2 k n_{H2O} P}{c\lambda^2} \left| \frac{\epsilon_r - 1}{\epsilon_r + 2} \right|^2 . \quad (3.21)
$$

$$
\quad (3.22)
$$

where P is the total incoming laser power, n_{H2O} the refraction index of water, c the speed of light in vacuum and q_z the z-component of the scattering vector. Since we have both forward scattered and back scattered light $q_z = 2k$. By putting in the following value; P = 100 mW, $n_{H2O} = 1.33$, $c = 3 \cdot 10^8$ m·s^{-1}, $k = 2\pi\lambda$, $\lambda = 1064$ nm and $a = 2.5$ nm into equation 3.20 we get

$$
F_z = 7 \cdot 10^{-14} N \quad (3.23)
$$

This is of the same order of magnitude as the force necessary to deform a half-spherical vesicle into a cylindrical shape. Although we should keep in mind that this is a ruff estimation of the forces involved, the scattering force seems to push the membrane along the optical axis.

3.8.3 Experimental data

The main limitation of the setup preventing us from affirming with certainty that our hypothesis is correct is the fact that the scanning focus is coupled to the trapping focus. Hence we can not at the same time focus the trap in the centre of the equatorial plan and scan through the vesicle. Some experimental observations can still be made that speak in favour of the hypothesis that the gradient force is pushing the vesicle upward.

The first observation that led us to our hypothesis was the sudden decrease of the cross-section seen at higher laser powers. When the laser was switched off the cross-section increased again, suggesting an elongation of the vesicle in the direction of propagation of the light. In Figure 3.28 we can see a series of images of a vesicle before exposure to the laser, during exposure to $P = 45.6\,\text{mW}$, and after.

Before ——————————— **During** ——————————— **After**
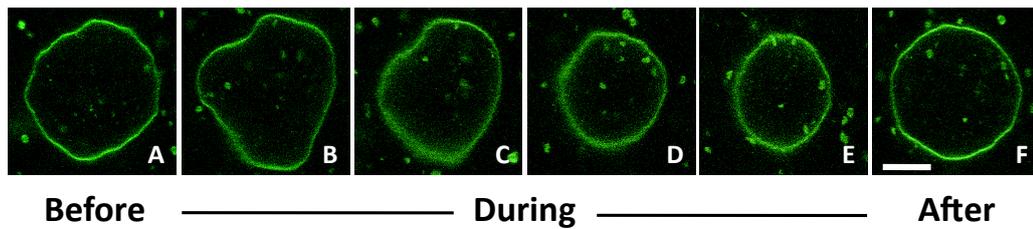
Figure 3.28: $23\,\mu\text{m}$ vesicle: A) before, B) to E) during, and F) after exposure to a laser power of $P = 45.6\,\text{mW}$. $T = 28.3\,^\circ\text{C}$.

In order to estimate the elongation of the vesicle in the axial direction the following experiment could be done. From sections in xy and xz it is easy to estimate the area of the vesicle before and after exposure to the tweezers. By measuring the radius of the cross-section during exposure it is then possible to calculate the height of the elongated vesicle. Confocal images as well as sketches defining the parameters used in the calculations that follow can be seen in Figure 3.29. We get the radius R of the vesicle from the equatorial cross-section and can cross check it with the xz-section which will also give us the height h of the vesicle at rest. The area of the adhered vesicle, seen as a truncated sphere is given by:

$$A = 2\pi R h. \tag{3.24}$$

As we have shown in the previous subsection, the force exerted by the optical tweezers is not large enough to induce a stretching of the lipid bilayer. We can therefore assume a constant area, provided no lipids are lost during
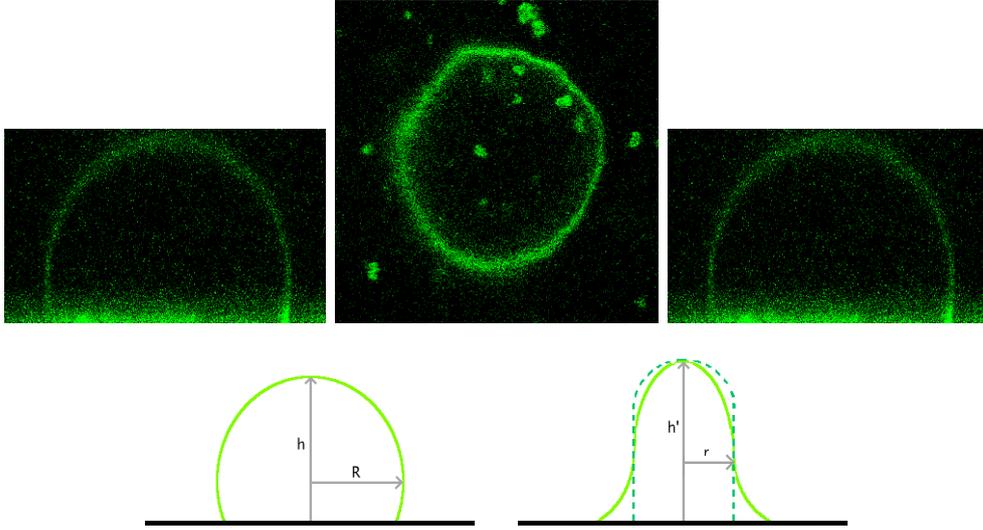
Figure 3.29: A: xz-scans of the vesicle before and after exposure to a laser power of P=45.6mW, as well as an xy-scan during exposure. B: Sketches defining the radius R and height h of the vesicle at rest and the new radius r and height h' during elongation by the optical tweezers.

the exposure to the laser. Assuming as we did before that the vesicle deforms into a cylinder with a spherical cap its surface area can also be expressed as

$$A_{def} = 2\pi r^2 + 2\pi r(h' - r) = 2\pi r h' \tag{3.25}$$

where h' is the height after deformation and r the new radius. $A = A_{def}$, hence

$$h' = \frac{Rh}{r}. \tag{3.26}$$

What we also did was to expose a vesicle to a given laser power, as usual centering the trap in the equatorial plan, and then rapidly scan the top part of the vesicle after switching off the laser. The xz-scans were made in about 3 s. In order to see any difference in height the relaxation time of the vesicle would have to be shorter than the acquisition time of the image. Results from a rheology relaxation experiment indicated that the relaxation time of a pure phospholipid membrane upon a small deformation was greater than 10 s [20]. Figure 3.30 shows a series of xz-scans of the top part of a vesicle before, just after exposure to $P = 45.6$ mW and after letting the vesicle equilibrate for a couple of minutes. The experiment was repeated 11 times. This was the only time an upward displacement of the top of the vesicle could clearly be

observed, the main problem being a decrease in size often coupled to heavy deformations of the vesicle.
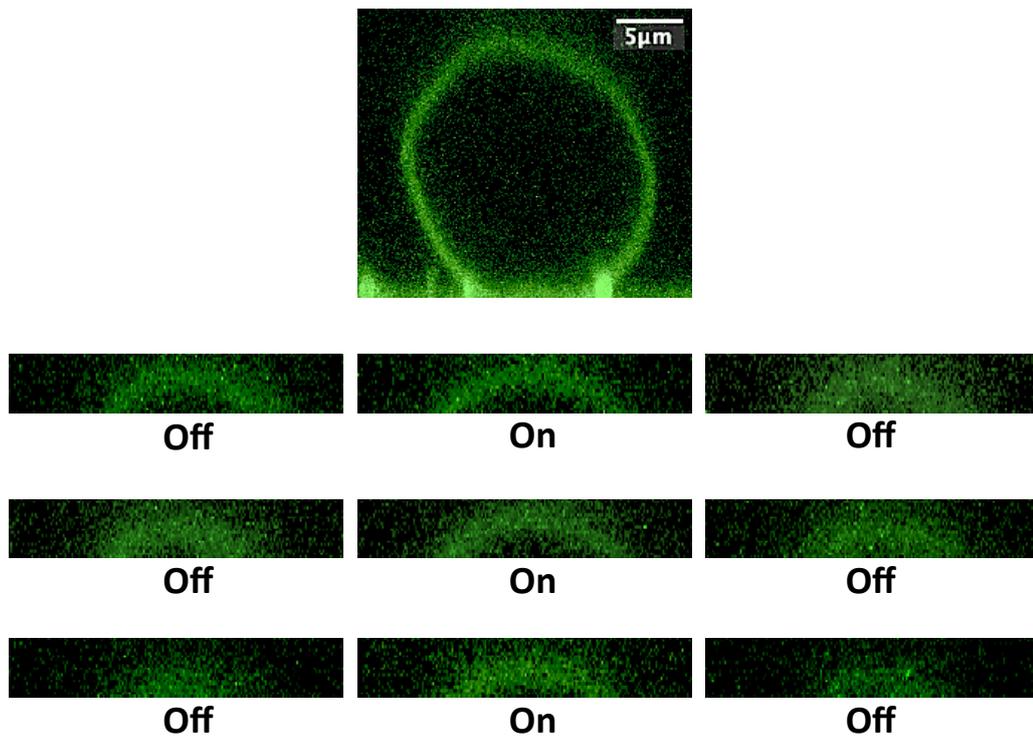
Figure 3.30: Three "Off-On-Off" series of confocal images showing the top part of the $18\,\mu$m vesicle seen above. All sections are in the xz-plan. The "On" images were scanned just after exposure of the vesicle to the laser. The trap was focused at the centre of the equatorial plane of the GUV. P $= 45.6$ mW. The scale bar corresponds to $5\,\mu$m.

Although we need more experimental evidence, the theoretical estimation of the gradient force would suggest that our hypothesis is for the least plausible.

3.9 Discussion

3.9.1 The effect of optical tweezers on a cell

There is now an awareness around the risks of photodamage and phototoxicity coupled to the exposure of cells to strongly focused light (see Section 3.2.2). We will now discuss the implications of a possible stress response of trapped cells due to the optical forces acting on them.

The extend to which our results on GUVs are applicable to the case of a cell trapped by optical tweezers can be discussed. All cells do have a plasma membrane as well as many internal lipid structures, for instance the bilayers surrounding their organelles. Although their cytoskeleton does not permit them to deform in the same way as a vesicle, they will experience forces. One difference should be noted though, in our case the index of refraction is the same on both sides of the membrane. This is not valid in the case of a cell for which the internal refractive index is both heterogeneous and higher than the one of water [30]. Still our results show that light and lipid membranes do interact, which in a cell could lead to a mechanical stress response.

Cells do respond to mechanical stress, both in a passive and in an active way. The deformation of cells by external forces can be seen as a passive response. The rigidity of a cell depends on the state of its cytoskeleton. In cancer cells for example, it is more irregular and compliant than in healthy cells. This makes cell elasticity an excellent mark for differentiating healthy and malignant cells, but also as a mean for cell sorting. One simple method that allows for high throughput is the optical stretcher, an optical trap composed of two counter propagating laser beams.[21][111] Cells also show an active response to their environment and the mechanical forces that act on them. They do this by remodelling their cytoskeleton. Fibroblasts adhered to a repeatedly stretched substrate, reoriented perpendicular to the direction of deformation. So did the actin stress fibres of the cells.[125] These deformations have been treated theoretically, also including noise from internal cellular processes [119]. Similar studies have also been conducted on cells adhering to curved surfaces [14]. The question now is to know whether the forces exerted by the optical tweezers are large enough to induce restructuring of the cytoskeleton, or if the deformations observed only reflect a passive responses. In the case of direct exposure to the optical tweezers, the latter would be more likely since our estimation of the scattering force acting on a vesicle at a laser power of 100mW is of the order of 10^{-2}pN. By using handles much larger forces can be exerted.

3.10 Outlook and conclusion

3.10.1 Further experiments

Constant laser exposure (Experiment **B**) is a quite promising experimental procedure. Not switching the laser on and off makes this experiment potentially more reproducible. If further experiments should be conducted on the phase dependence of the deformations, measuring only survival time would also permit higher throughput and better statistics .

To verify the hypothesis that the scattering force is responsible for the elongation of the vesicles in the axial direction, we would like to perform the same experiment on free-standing vesicles, to see if the scattering force pushes them in the direction of propagation of the light.

It could be interesting to conduct our deformation experiments on vesicles filled with an actin network and see to which extend the GUVs would be stabilised. For example, would they still form vesicle aggregates after long-time exposure? This would also make the comparison with cells more accurate.

3.10.2 Conclusion

We have shown that optical tweezers can induce deformations in adhered unilamellar vesicles without the use of any handle. This was done in pure water without having a difference in refractive index between the inside and outside solutions. The larger a vesicle is the longer it survives both repeated and constant exposure to the laser trap. Repeated exposure to an increasing laser power leads to a decrease in vesicle size. Eventually the vesicle starts budding and forms vesicle aggregates or ruptures. Also the phase of the lipid membrane seems to influence vesicle survival. The more fluid the membrane is the higher are the laser powers it can withstand. Deformations might start at lower laser powers than in the gel phase, but the rate of size loss is much lower.

At high laser powers ($> 50\,\mu$m) a decrease of the vesicle diameter could be observed during laser exposure, indicating an elongation of the vesicle in the direction of propagation of light. We have advanced the hypothesis that the scattering force dominates over the gradient force due to the large distance between the trap focus and the membrane. Comparing the estimation of the z-component of the exerted scattering force with the force needed to bend the lipid bilayer supports this hypothesis. At the moment more experimental data is needed to fully confirm it.

From having been an *in vitro* instrument, optical tweezers are increasingly applied to the study of live cells, also looking at intracellular processes. The risk of photodamage has been known for a long time, but maybe mechanical stress should also be taken into account, although weak in the case of direct exposure to optical tweezers. On a positive note optically induced cell deformation can be utilised for biotechnical or medical applications, since each cell type has a distinct viscoelastic response to deformation. Optical tweezers and optical stretchers can be used for cell characterisation and sorting [137], or even as a diagnostic tool in early detection of blood diseases [19] or different types cancers [21, 111].

Part II

Nuclear organisation and silencing

CHAPTER 4

DNA localisation in *Schizosaccharomyces pombe*

4.1 Introduction

An increasing number of studies show the importance of the non-random 3D organisation of the nucleus. Current models for the regulation of gene expression and recombination in eukaryotes suggest that trans-acting factors are non-uniformly distributed within the nucleus. This could cause chromosomal loci to respond differently depending on the subnuclear compartment they occupy [131]. Also, the level of compaction or accessibility of the DNA to the transcription machinery plays a very important role in gene regulation. Heterochromatin, seen as more compact, tends to be found in transcriptionally silent areas of the genome that often contain repetitive sequences. Euchromatin, on the other hand, contains most of the genes and is transcriptionally active.[120] The two types of chromatin are characterised by very distinct methylation and acetylation patterns that facilitate or inhibit the binding of proteins important for gene regulation. DNA is not just a code to be deciphered on a nucleotide level, the epigenetic regulation is just as important. Chemical modifications and the binding of specific proteins to the building blocks of our chromosomes leave an imprint that can be passed one from cell generation to cell generation through replication [4].

We are interested in the mechanisms of silencing both at a molecular level and at the scale of the whole nucleus at which gene localisation is important. By fluorescently labelling gene domains or proteins, microscopy techniques have become a good complement to more traditional methods within the fields of genetics, molecular biology and biochemistry. In addition

to global information on expression levels, fluorescence microscopy can give us information on the 3D organisation of cells and even the dynamics of cellular processes.

We work with *Schizosaccharomyces pombe* (*S. pombe*), a fission yeast commonly used as a model system for eukaryotes. Although much smaller, it shows many homologies to mammalian cells. We focused our study on its mating-type region, not so much for its function, but because it is one of the few heterochromatic regions in the genome of *S. pombe*. The silent part of the region is flanked by two identical inverted repeats, the Inverted Repeat-Left (IR-L) and the Inverted Repeat-Right (IR-R) [123]. Other heterochromatic regions are also delimited by this type of boundaries, like for example the centromeres. The exact mechanism by which these boundaries separate transcriptionally active and passive domains is still unknown. We started by screening the whole genome of *S. pombe* for other boundary or silencing elements. By replacing the *IR-R* with a ribosomal DNA repeat, referred to as *rDNA-R*, we obtained a similar silencing effect. Therefore, we studied both the nuclear localisation of the mating-type region by measuring its distance to the nucleolus and tried to identify proteins involved in the silencing of part of the region. We did this for the wild-type strain and the rDNA mutant, as well as for two types of control strains.

The first two sections present data on the silencing and the 3D localisation of the mating-type region in the four strains we worked with. The last two sections summarise the paths we are currently following in order to understand the underlying mechanisms of silencing both in the wild-type and in the rDNA strain. This includes making qualified guesses about which proteins might be involved and test our hypothesis by making knockout strains, as well as trying to identify the part or parts of the *rDNA-R* that are responsible for the silencing of the mating-type region in the rDNA mutant.

4.2 Biological background

4.2.1 *Schizosaccharomyces pombe*

As mentioned in the Introduction *S. pombe* is a eukaryote belonging to the kingdom of Fungi. It is a rod-shaped cell with a rigid cell wall mainly composed of polysaccharides [41, ch.17]. It has, as all eukaryotes, a nucleus surrounded by a double lipid bilayer membrane called the nuclear envelope. Also its organelles are the same as in higher eukaryotes, see the transmission electron micrograph (TEM) in Figure 4.2C [102]. Together with budding yeast, *Saccharomyces cerevisiae* (*S. cerevisiae*), *S. pombe* is the most common model system for unicellular eukaryotes. Comparison between the two yeast species gives valuable information, since they parted evolutionarily several hundred million years ago. If homologies are found, they are most likely conserved in higher eukaryotes as well.[46] Fission yeast also has the great advantage of showing little genomic redundancy. It is easy to modify and well characterised. This also makes it a good model system for studying cell division. The fact that it is a unicellular organism makes it easy to follow the cell cycle, where both size and shape of the cells help in the recognition of the different phases, see Figure 4.1. Yeast cells can also enter meiosis when they
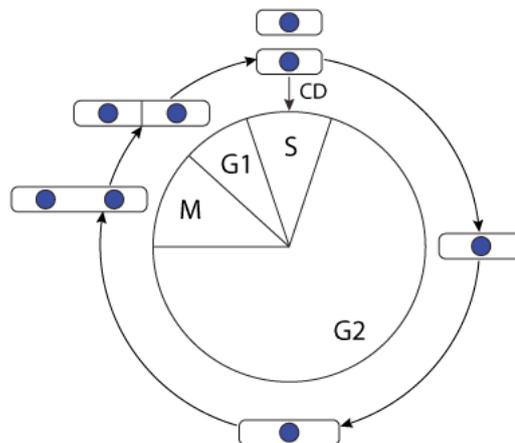
Figure 4.1: Schematic drawing of the cell cycle of *S. pombe* showing the relative duration of each phase. M stands for mitosis and S for DNA synthesis. During the S phase the DNA is replicated. In *S. pombe* this happens very soon after mitosis. It starts even before the two cells have fully divided. CD stands for cell division. G1 and G2 are the two gap phases separating the M and S phases. G1 is very short, whereas G2 is remarkably long. There are also check-points during the cell cycle, halting progress while ensuring that the cell is ready to enter the next phase.[95]

are under environmental stress, particularly nitrogen starvation. Two cells fuse, mix their DNA and form spores. We will not go into details about this, but it is related to the topic of mating-type switching that we will briefly discuss in section 4.2.2.
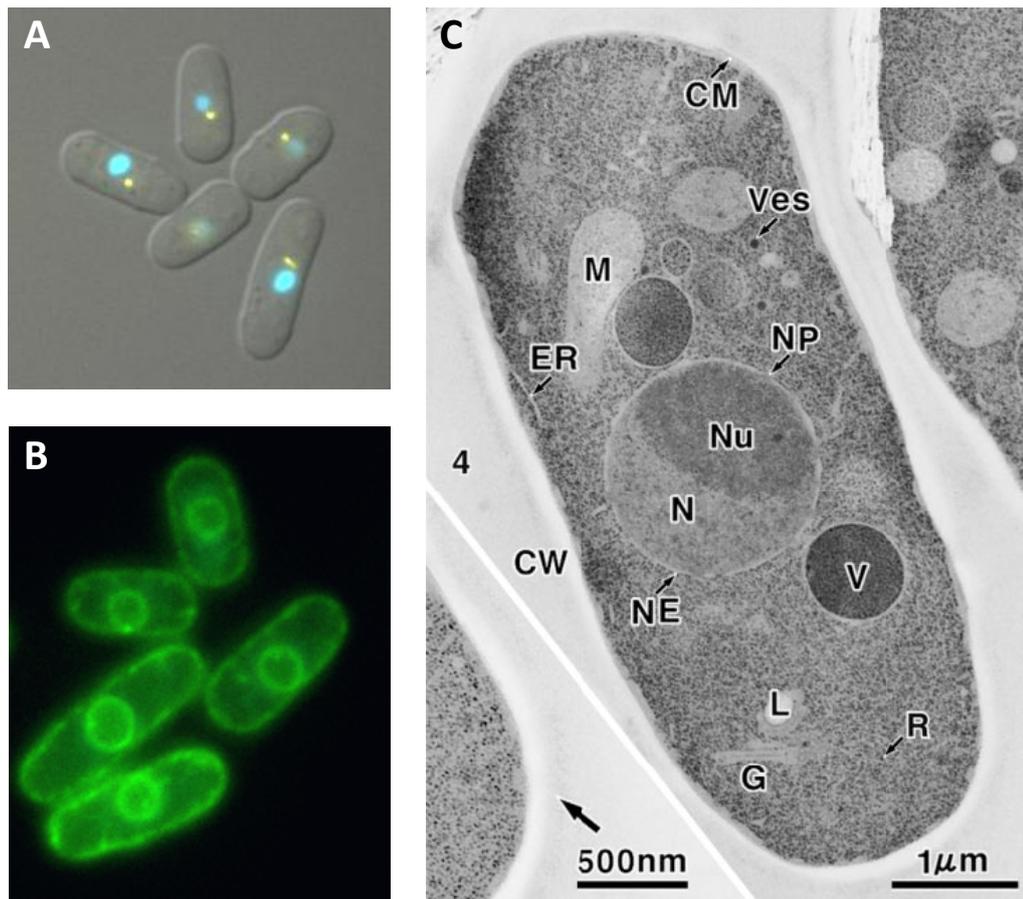
Figure 4.2: A: Overlay of a DIC (differential interference contrast) and two fluorescence images of *S. pombe*. The mating-type region (yellow dot) is marked with GFP and visualised in the YFP channel. The nucleolus (in blue) is marked with CFP. **B:** Confocal fluorescence image of *S. pombe* cells where the membrane was made visible by labelling a membrane protein with the green fluorescent protein (GFP). **C:** A TEM image of *S. pombe* showing the cellular structure, published by Osumi et al. [102]. N stands for nucleus, Nu for nucleolus, NE for nuclear envelope, NP for nuclear pore, R for ribosome, ER for endoplasmic reticulum, G for Golgi apparatus, M for mitochondrion, V for vacuole, Ves for vesicles, L for lipid granules, CM for cell membrane and CW for cell wall.

S. pombe only has a few heterochromatic regions. These are the centromeric and telomeric regions of the three chromosomes, as well as the mating-type region. Two ribosomal DNA (rDNA) domains, which are of interest for this study, also display heterochromatic features. A sketch of the localisation and size of these regions can be found in Figure 4.3.
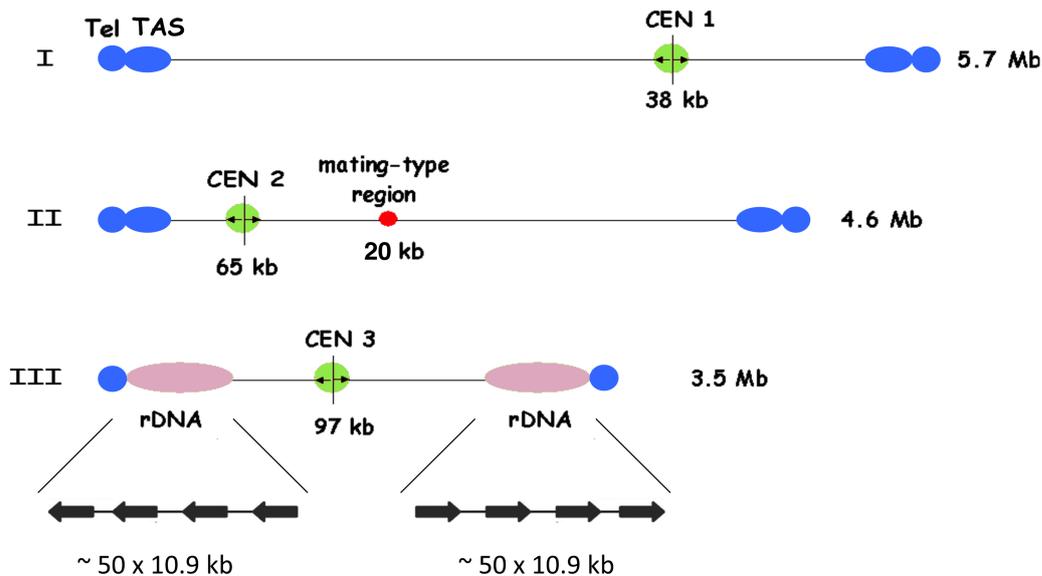
Figure 4.3: Schematic drawing of *S. pombe*'s three chromosomes highlighting the heterochromatic regions; the telomeres (Tel) and telomere associated domains (TAS) at the chromosome extremities (blue), the centromeres (CEN) (green) that are tethered to the spindle-pole body at the nuclear periphery, the mating-type region (red) on chromosome II and the rDNA domains (pink) on chromosome III.

4.2.2 The mating-type region

As just mentioned, the mating-type region is one of the few heterochromatic regions of the *S. pombe* genome. It comprises three loci *mat1*, *mat2-P* and *mat3-M*, see Figure 4.4. *mat1* determines the mating-type of the cell, either Plus (*mat1-P*) or Minus (*mat1-M*). One could say that the mating-type in yeast corresponds to its sex. In order to mate, two *S. pombe* cells must have opposite mating-types. *mat2-P* and *mat3-M* are part of a silenced region stretching over about 20 kb and code for the P respectively M phenotype. The silenced region is delimited by two identical inverted repeats, *IR-L* and *IR-R*. Cells having this wild-type mating-type region (h^{90}) can switch between mating-types. The information in the *mat1* cassette is replaced by either *P* or *M* depending on the current mating-type. This results in colonies where about 90% of the cells mate upon nitrogen starvation, i.e. we have an almost perfectly equal repartition between P and M cells.[41, Ch.9]
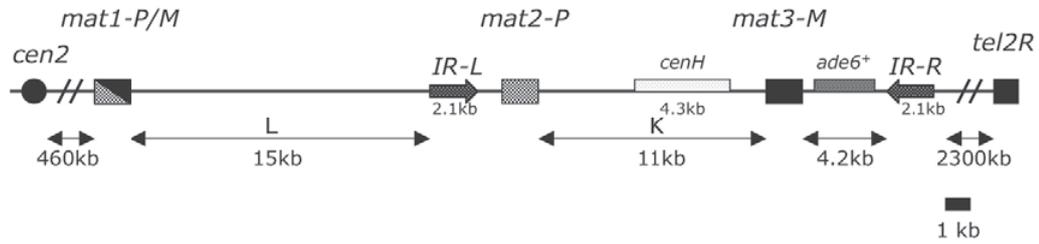
Figure 4.4: Schematic representation of the mating-type region taken from Alfredsson-Timmins et al. [2]. It consists of three linked loci; *mat1* (checkered /black box), *mat2-P* (checkered box) and *mat3-M* (black box). Two identical inverted repeats, *IR-L* and *IR-R* (block arrows), delimit the heterochromatic region. There is an inserted ade6$^+$ reporter gene (grey box) between *mat2-P* and *IR-R*, also used in our strains.

The switching follows a very specific pattern. Two rules apply, the "One-in-four" rule and the "Consecutive" rule. Only one out of four grand-daughter cells is of the opposite mating-type, if the grand-parent cell is unswitchable. This is highlighted in grey in Figure 4.5. By unswitchable we mean a cell that can only divide into two daughter cells with the same mating-type. They are referred to as Pu. The "Consecutive" rule refers to the fact that the sister of a cell that has switched will be able to switch at the next division. These cells are referred to as Ps cells in Figure 4.5 and give rise to a chain of recurrent switching.[41, Ch.9]
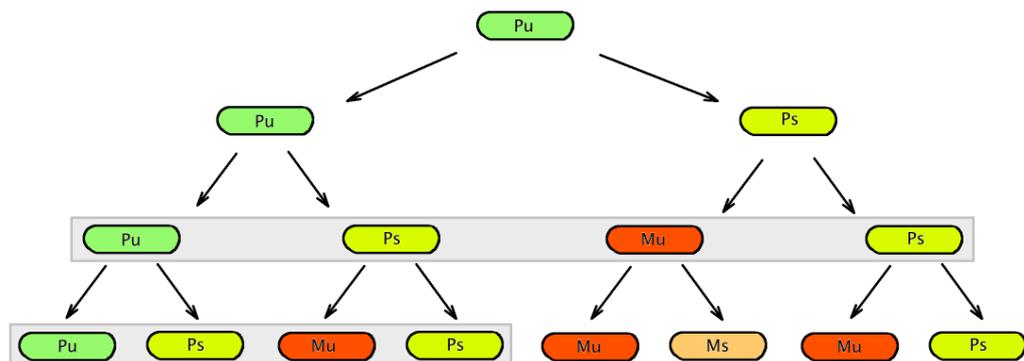
Figure 4.5: Switching scheme for the mating-type in *S. pombe*. Unswitchable P cells (Pu, green) will divide into two P cells. One is still unswitchable, while the other will be able to change mating-type during the next cell division. It is a so-called switchable P cell (Ps, yellow). The same is valid for unswitchable and switchable M cells, Mu (red) and Ms (orange). The grey rectangles illustrate the "One-in-four" rule. The Ps cells on the far right form a chain of recurrent switching.

We will not get into details about the switching mechanism, but just mention that the heterochromatic state of the *mat2-P* and *mat3-M* cassettes, combined with homologous recombination, plays a crucial role. There are also strong indications of a single-strand lesion (SSB) of the DNA near the *mat1* locus in cells able to switch mating-type.[59] Three proteins seem important for the formation of the SSB. Sap1 (switch activating protein) binds to the switch activating sequence SAS1 near *mat1*, and participates in the arrest of the replication fork, which is crucial for successful switching [82]. Swi1 and Swi3 form a complex that plays a role in the stabilisation of these arrested replication forks, preventing them from forming other structures. This is worth mentioning since Sap1, Swi1 and Swi3 also participate in fork arrest and stabilisation in the rDNA domains [69][70].

4.2.3 Silencing mechanisms

We will in this section try to give an overview of the heterochromatin formation process necessary for silencing. We will concentrate on *S. pombe*, but many of the proteins involved have homologues in higher eukaryotes. We will briefly describe the nucleation and spreading mechanisms of heterochromatin as well as the role of the so-called boundary elements, which are important in delimiting the silenced domains.

Heterochromatin formation

The nucleus is filled with chromatin, combining DNA molecules with RNA, histones and other proteins. Eukaryotic chromatin shows local variations in the degree of condensation, making the DNA more or less accessible for factors regulating for instance transcription, replication and recombination. In *S. pombe*, as we have mentioned earlier, euchromatin makes out the major part of the chromatin. It contains most of the genes and is transcriptionally active. Heterochromatin, on the other hand, is often found in transcriptionally silent areas of the genome.[120] The two types of chromatin are characterised by very distinct methylation and acetylation patterns that facilitate or inhibit the binding of proteins important for gene regulation. This is part of the epigenetic control of the genome. Heterochromatic structures are characterised by the methylation of lysine 9 of histone H3 (H3-mLys9) by the methyltransferase Clr4 (cryptic loci regulator 4).[94] There is also a corresponding enrichment of the protein Swi6 . This is illustrated in Figure 4.6 adapted from Figure 4 in reference [50]. It shows that Swi6 and H3-mLys9 enrichment coincides with the 20 kb silenced region of the mating-type region.
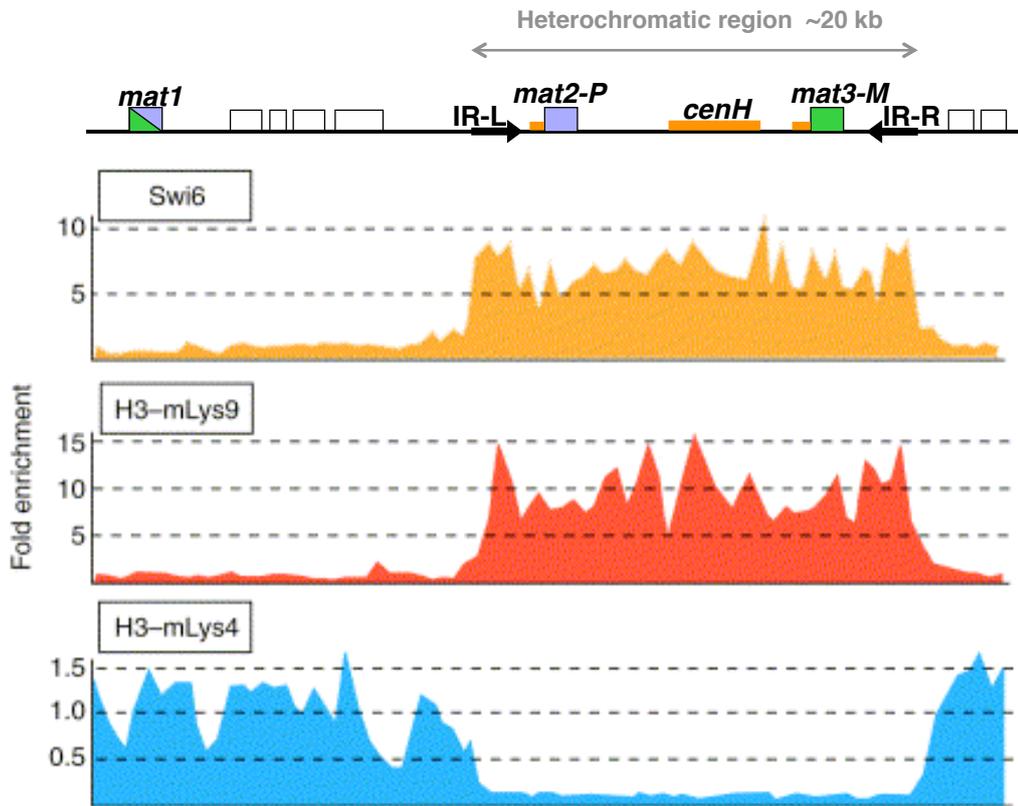
Figure 4.6: Distribution of Swi6 and distinct site-specific histone H3 methylation patterns. H3-mLys9 is associated with the heterochromatic domain in the mating-type region of *S. pombe*, whereas H3-mLys4 is more common in the euchromatic domains.[50]

We have mentioned the existence of heterochromatin-specific proteins and histone modifications, but what are the nucleation and spreading mechanisms of heterochromatin in the K-region of the mating-type region? *mat2-P* and *mat3-M* form a heterochromatin-like structure, but there is a window of lower degree of compaction during replication when the new histones have not yet been modified [67][25]. Replication seems to be an important part of the silencing mechanism. There are two heterochromatin nucleation sites in the silenced part of the mating-type region, each one of them corresponding to a different pathway. The main one involves a 4.3 kb centromere homologous (cenH) region located between *mat2* and *mat3* [49]. The interaction between small interfering RNAs (siRNA) and this region leads to methylation of lysine 9 of histone 3, through a quite complex pathway involving many proteins. For more details on this heterochromatin nucleation mechanism see

references [132] and [48]. The heterochromatic region is spread in *cis* to the neighbouring histones in the following way. H3-mLys9 recruits Swi6 that in turn recruits more Clr4 [53].

The second pathway involves two proteins, Atf1 and Pcr1, that both belong to a family of proteins (ATF/CREB) part of the cellular response to environmental stress [63]. Activation of this pathway by nucleotide depletion can lead to the spreading of the silenced region [124]. Clr3, a histone deacetylase, is recruited which stabilises the above mentioned H3-mLys9 methylation and in turn recruits more Clr4, hence leading to the spreading of the heterochromatic region [136].

Boundary elements

Evidence has been provided that heterochromatin can spread in *cis*. This is also the case for euchromatin [129]. In order to have a well defined and sharp transition from a silent to a transcriptionally active domain, a boundary is needed. Such elements seem to flank all heterochromatic regions, such as the centromeres and the mating-type region in yeast [121][123]. These boundary elements do not necessarily have a silencing function on their own, but would rather work as a stop sign for the propagation of both hetero- and euchromatin. This does not mean that they have a passive role. Currently little is known about the actual boundary mechanisms, but in the discussion we will present and discuss the current models. For now, we will present some evidence for their existence and importance in maintaining functional domains in the genome. The focus will continue to lie on the mating-type region in *S. pombe*, where two identical inverted repeats, *IR-L* and *IR-R*, are delimiting *mat2-P*, *mat3-M* and the heterochromatic domain K from the surrounding euchromatin. See Figure 4.4. *IR-L* and *IR-R* are 2.1 kb long and have opposite orientation [123]. These inverted repeats coincide with the changes in histone methylation characteristic for heterochromatin shown in the previous section [94]. Experiments have been conducted by several groups, such as Grewal et al. [94], Thon et al. [129] and Klar et al. [123], where the boundary elements were deleted. Deletion of either or both of the boundaries resulted in variegation. The expression and repression of reporter genes on both sides of the repeats changed, which would indicate a less well defined limit between heterochromatin and euchromatin.

4.2.4 Ribosomal DNA

Ribosomal DNA (rDNA) codes for the ribosomal RNAs (rRNAs) that make out parts of the ribosomes. The transcription is done by RNA polymerase I (Pol I), that is specific to rDNA. The initial 47S rRNA is post-transcriptionally modified and cleaved into three mature rRNA.[18] In *S. pombe* the rDNA is located in two domains near the telomeres of chromosome III (see Figure 4.3). They are formed by approximately hundred identical tandem repeats, meaning that they are all pointing in the same direction.[41, ch.21] Each repeat consists of one transcribed region (in pink in Figure 4.25), one autonomous origin of replication (ars, grey box) and three replication fork barriers, two binding Reb1 and one binding Sap1. The role of the replication fork barriers might be to prevent collision between the replication and the transcription machineries by only allowing replication in one direction [82]. The rDNA can be found in a subnuclear compartment called the nucleolus [58]. Although ribosome biogenesis is its main function, the nucleolus has lately been associated with other functions such as small RNA modifications, cell-cycle and ageing control and many forms of stress response.[18][74]
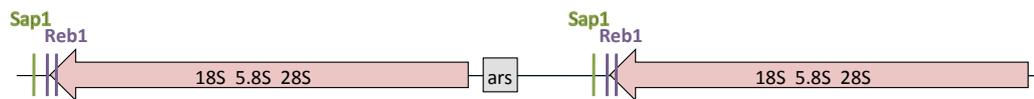
Figure 4.7: Schematic drawing of two rDNA repeats showing the transcribed region (in pink), the autonomous origin of replication (grey box), two replication fork barriers binding Reb1 (in purple) and one binding Sap1 (in green).

4.2.5 Nuclear organisation

This brings us to the non-random organisation of the nucleus. This section will be treated on a more general level, looking at common nuclear features among eukaryotes. The territorial organisation of chromosomes in interphase constitutes a basic feature of nuclear architecture [28]. Figure 4.8 [40] shows a 3D model of the genome of *S. cerevisiae*, each colour representing a gene. The centromeres are all clustered at one pole of the nucleus. The nucleolus is also visible and marked out by a white arrow.

The periphery of the nucleus has often been associated with gene silencing. This is the case for the telomeres and the centromeres, the latter being tethered to the spindle-pole body which is a protein complex bridging the nuclear envelope [13]. The view on this is changing and recent work would
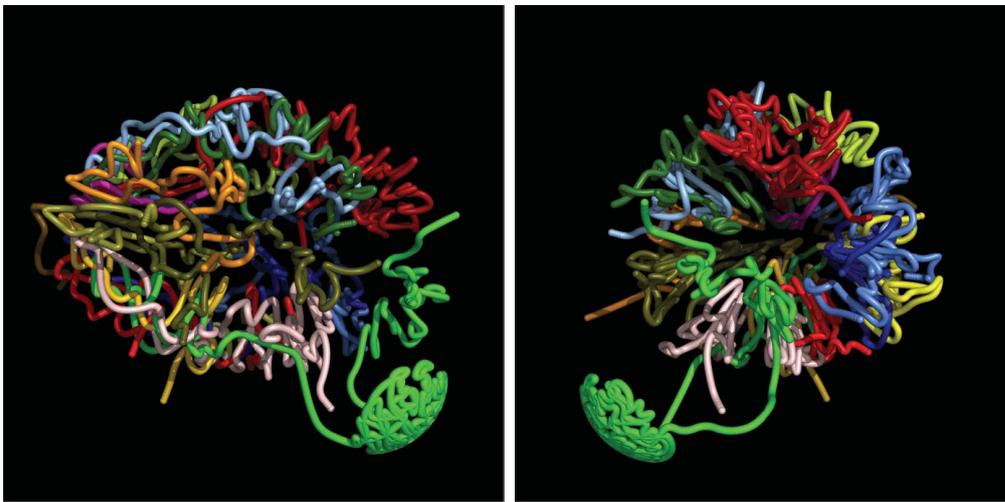
Figure 4.8: Figure published by Duan et al. [40] showing the chromosomal territories in *S. cerevisiae*. Each of the sixteen chromosomes are marked with a colour. The detached green domain corresponds to the nucleolus.

suggest that there are both active and silent regions at the nuclear periphery [131]. Certain genes have been shown to undergo dynamic recruitment to the periphery upon transcriptional activation [1]. They are believed to associate with the nuclear pore complex, which has been suggested to improve messenger RNA export out of the nucleus [23]. Nevertheless, resent studies on *S. pombe* has shown the relocalisation of genes away from the nuclear membrane as a response to nitrogen starvation [3]. The nucleus, although having some conserved structural features, seems quite dynamic in its organisation.

Gene localisation at the periphery has also been been coupled to DNA repair mechanisms [127] [128]. This brings us to the concept of specialised loci in the nucleus that would promote specific activities. Two such examples are the so-called transcription [101] and replication [66][81] factories in which proteins and nucleic acids necessary for these cellular process are concentrated. Genes would either be recruited there, as in the case of transcription factories, or the loci themselves would be mobile, as for the replication factories, their nuclear distribution changing according to S phase progression.

For recent reviews on genome organisation and function see references d[96] and [118].

4.3 Materials and Methods

4.3.1 Cloning protocols

All media recipes can be found in Appendix A. This includes YES, AA, EMM2 and MSA. YES and AA are rich media, whereas EMM2 and MSA are minimal media, meaning they contain less nutrients. These media are used as a base to which different amino-acids or other molecules can be added.

Crossing

A new strain can be obtained by crossing two existing strains, each having some part of the desired genotype. Sometimes a series of crosses is necessary in order to reach the goal. Crossing two strains with each other is quite straightforward, given that at least one of them has the wild type mating-type region (h^{90}) allowing for switches between P and M, or that they have different mating-types. Patches were made on YES plates from single colonies of each strain. The amount corresponding to a pinhead was taken from each strain and mixed directly on sporulation plates, i.e. agar plates with minimum media. Most mating mixes were made on MSA+leu+ura+ade. For exact medium composition see appendix A. The amount of cells taken from each strain can be adjusted according to their mating-type. If one of the strain is unable to switch, a bit more of it can be added to force switching with a switchable h^{90} strain. The plates were then incubated at 33 °C for two days. Due to the lack of nutrients cells of opposite mating-type would fuse, enter meiosis and form four haploid spores. It is important to mix well and not spread the cells too much in order to optimise for crosses between the two parent strains. In order to harvest the spores we incubated them over night (O/N) at 33 °C in 0.5 ml H2O + 2.5 μl snail enzyme (Beta-Glucuronidase/Acrylsulfatase, Roche Diagnostics). The spores were counted and spread on YES plates or directly on selective plates; about 300-600 spores per plate. If the expected frequency of recombinants was high, fewer spores were spread.

Strain selection

The next step is to select for the wanted strain. By having reporter genes or genes coding for drug resistance tightly linked to the wished for genes, it is possible to either positively or negatively select for certain genotypes. This is done by studying the phenotype of the candidate strains, when grown on an appropriate medium. For example, if the wanted strain should have a kanamycin resistance ($kanR$) the spores obtained by crossing are replicated on a YES+G418 plate. G418 is an antibiotic similar to kanamycin. If a colony forms, those cells are kanamycin resistant. The colonies showing the right phenotype are then streaked on YES plates. It is always wise to recheck the phenotypes before naming and freezing a new strain.

Saving strains

The freezing protocol was the following. We patched each strain to be saved on half a YES plate and let the cells grow for two days at 33 °C. With an innoculation loop or a wooden applicator stick we collected the cells and resuspended them in 1.8 ml sterile 20% glycerol solution in CryoTubes (Nunc). The cell suspensions were then shaken and vortexed briefly. Each strain was stored in two different -80 °C freezers to minimise the risk of loss.

Transformation

Crossing is not the only method available to modify a strain. If the goal is to insert a new resistance or add a reporter gene, transformation can be the preferred solution. Instead of allowing two strains to mate, a plasmid or DNA fragment containing the gene of interest is inserted into the cells. There are several ways of facilitating DNA entry into the cell. As we mentioned in Part I, electroporation is one option. In this study we used a method combining lithium acetate and heat chock that will be briefly described here. The detailed transformation protocol can be found in Appendix B.

Cells grown O/N in rich medium were spun down and washed in water. They were then resuspended in 0.1M lithium acetate with a pH of 4.9. 100 μl aliquots were incubated at 30 °C for 30 minutes. After that, 1-2 μg DNA (the plasmid to insert) was added to each aliquot. After another 30 minutes of incubation 290 μl of 40% PEG 4000 (polyethylene glycol) in lithium acetate was added, followed by 30 minutes of incubation. The cells were then exposed to a heat chock for 15 minutes at 42 °C and centrifuged 3 minutes at 3000 rpm (rounds per minute) to remove the supernatant. Resuspended in water, they were plated on selective plates. Prior to the transformation the plasmids that were to be integrated into the chromosome were cut open using restriction enzymes.

Genome screening

The screening of the genome for boundary or silencing elements was what initiated this project. It was done by a former student Camilla Bünner in the following way.
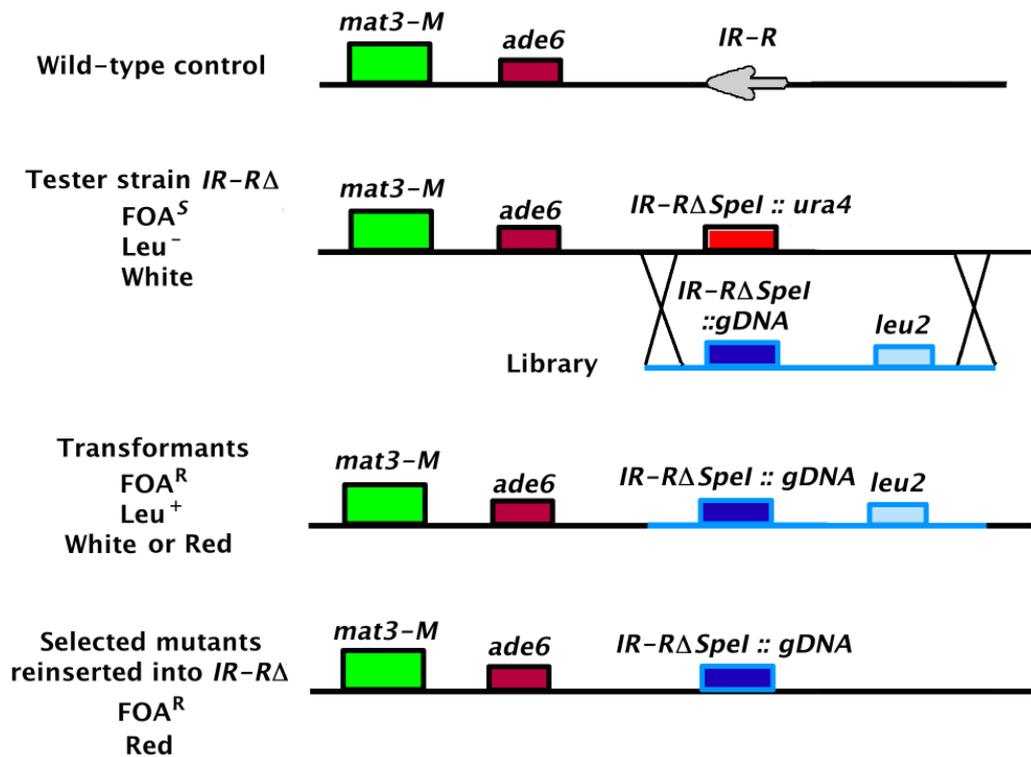
Figure 4.9: Some of the steps in the screening for mutants with other boundary elements than *IR-R*. The tester strain had *IR-R* deleted and replaced by a *ura4* reporter gene. The plasmid (Library in the figure) was inserted by transformation, replacing the deleted boundary and *ura4*. The transformants were then tested for FOA resistance (no Ura4 production), production of leucine (Leu$^+$) and their phenotype on adenine poor plates was checked. The gDNA of the mutants having the correct phenotype was reinserted in the tester strain without *LEU2*.

Three genomic libraries were built by Geneviève Thon and Janne Verhein-Hansen by cutting the entire yeast genome in smaller pieces using three restriction enzymes, *SpeI*, *XbaI* and *NheI*. Each piece of genomic DNA (gDNA) was inserted into a plasmid (pGT299) containing a clone of the *mat3-M* centromere distal DNA with a right-hand repeat deletion (*IR-RΔ*), as well as a *LEU2* reporter gene from *S. cerevisiae*, see Figure 4.9. This reporter gene served to select transformants. By combining the three librairies most of the

yeast genome was covered. The insertion of the gDNA into the *IR-RΔ* tester
strain was done by transformation. Having the gDNA replacing *IR-R*, we
could now screen the transformants for the sought for phenotype:

- Leu$^+$ to make sure the new strain had the piece of gDNA.

- FOA^R to insure insertion of the gDNA at the right location replacing
  the *IR-RΔSpeI::ura4*. FOA (5-fluoro-orotic acid) is only toxic when
  converted to other compounds by orotidine-5'-phosphate decarboxy-
  lase, coded for by *ura4* [51].

- Ade$^-$ since we wanted to identify elements with boundary properties,
  i.e. silencing of the mating-type region and the inserted *ade6* reporter
  gene.

For a sketch of the screening strategy see Figure 4.9. Strains with the right
phenotype were then rescued using long range PCR [26] or Gap repair [79]
and analysed. The candidates selected for further studies were then rein-
serted into the *IR-RΔ* tester strain without the *LEU2* reporter gene. Many
of them were part of the centromere region, which was not surprising since
boundary elements have already been identified there [121].

A few mutants caught the attention of the group. Those having a piece
of rDNA replacing *IR-R* were showing a strong silencing of the mating-type
region. One of these rDNA mutants was selected for further studies together
with the *IR-RΔ* tester strain, the wild-type strain and a wild-type control.

4.3.2 *S. pombe* strains

The genotypes of the strains used in this thesis can be found in the table in
appendix C. In this section we will briefly describe how they were constructed.

The four original strains

We worked with four strains that were later modified to include deletions;
a **wild-type strain** (MAM26), a **control strain** (MAM56) identical to
MAM26 except for an *ade6* reporter gene inserted between *mat3* and *IR-
R*, an **IR-RΔ mutant** (MAM46) lacking *IR-R*, and a **rDNA mutant**
(MAM36) obtained through genome screening, as described above. The two
latter strains also had the *ade6* reporter gene. For a sketch of their mating-
type regions see Figure 4.10. The four MAM strains, MAM26, MAM36,
MAM46 and MAM56, were constructed by Mazhoura Aït Mebarek, a former
student in Geneviève Thon's group. We also worked with four very simi-
lar strains; PM7 (**wild-type strain**), PM2 (**rDNA mutant**), PM3 (**IR-
RΔ mutant**) and PM8 (**control strain**). The only difference between

the two strain series is an antibiotic resistance. The MAM strains have a kanamycin resistance (*kanR*) at *his2* that was replaced by transformation (*pcr2.1-hph1/AscI+SacI*) with a gene coding for hygromycin B phosphotransferase (*hph*) that made the PM strains resistant to hygromycin. This was done to facilitate later strain constructions. These strains also have fluorescent markers. Their mating-type region was marked with green fluorescent protein (GFP) and their nucleolus with cyan fluorescent protein (CFP). We will describe this more in detail in section 4.3.5. Some strains were constructed using a non-fluorescent **control strain** (Hu52), ***IR-RΔ* mutant** (PG2897) or **rDNA mutant** (PC148 and PG3506). We also had one strain with a smaller piece of rDNA replacing *IR-R*. We called it the **small rDNA mutant** (PG3188 and PG3486). We will refer to these last six strains as the mother strains.
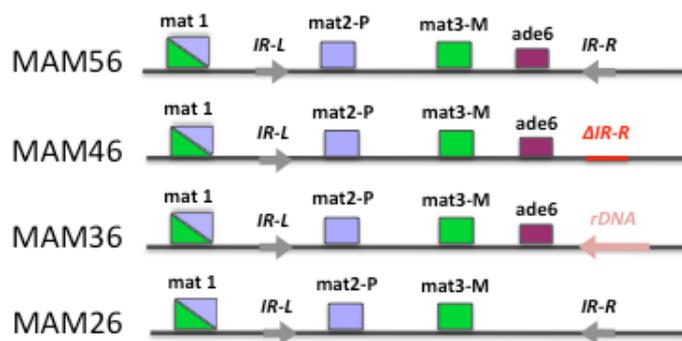
Figure 4.10: Sketches of the mating-type region of the four MAM strains, the **wild-type strain** (MAM26), the **rDNA mutant** (MAM36), the ***IR-RΔ* mutant** (MAM46) and the **control strain** (MAM56). *ade6* is the inserted reporter gene and the arrows symbolise the boundary elements of each strain.

The *clr3* and *clr4* deleted strains

In order to construct strains deleted for the *clr3* gene we had to make two consecutive crosses. We first crossed a *clr3Δ* strain (PG3439) that is h^- with the mother **control strain** Hu52 in order to get a strain that is both *clr3Δ* and has an *ade6-DN/N* modification of its natural *ade6* gene. This cross made it possible to use the *ade6* reporter gene. The intermediate strain, PM40, was then crossed with the non-fluorescent mother strains. This gave us PM45 to 50.

We made two sets of *clr4* deleted strains. One is fluorescently marked and was obtained by crossing PM7, PM2, PM3 and PM8 with a *clr4Δ* strain PG3639. These strains are called PM13 to 16. The second was constructed

in the same way but by crossing PG3639 with the six non-fluorescent mother strains. This resulted in the new strains PM26 to 31.

The *swi1* and *swi3* deleted strains

We wanted to construct the *swi1Δ* and *swi3Δ* strains as *ade6-DN/N*. Therefore we selected from a cross between PM8 and the *swi1Δ* strain Y211, a strain that was h^-, *ade6-DN/N* and *swi1Δ::kanR*. We proceeded in the same way for *swi3Δ* with PM3 and Y668. We called these intermediate strains PM11 and PM12 respectively. To obtain the four fluorescently marked *swi1Δ* (PM13 to PM16) and *swi3Δ* (PM17 to PM20) strains we finally crossed PM11 and PM12 with PM7 (**wild-type strain**), PM2 (**rDNA mutant**), PM3 (**IR-RΔ mutant**) and PM8 (**control strain**). Later we also constructed non-fluorescent *swi1Δ* and *swi3Δ* **small rDNA mutants**. This was done by crossing PG3486 (**small rDNA mutant**) with PM11 and PM12 respectively.

4.3.3 Spot tests

Spot tests are an extension of the strain selection method described earlier. They are useful not only for checking the phenotype of a given strain, but can in addition give information about the expression level of a given gene. This is not a quantitative method, but it is quite powerful when qualitatively comparing strains.

Cells are grown on selective plates that either lack a nutrient or contain a specific antibiotic to check for resistance. Each row in a spot test corresponds to one strain and each column to a different concentration of cells. We made six dilutions going from $2 \cdot 10^8$ cells/ml to $2 \cdot 10^2$ cells/ml. Each spot corresponds to $5\,\mu$l. In our spot tests we wanted to see if the mating-type region was expressed or repressed. As we have shown, the strains we used had an *ade6* reporter gene inserted in the region silenced in the wild-type strain. If the mating-type region is expressed, the cells can grow on plats lacking adenine. We therefore used the following plates:

- YES : to test the ability of cells to form colonies in the absence of stress and selection.

- YE : has a low concentration of adenine. If *ade6* is silenced the cells form pink colonies.

- AA - ade : contains no adenine. Only strains expressing *ade6* can grow. The successive dilutions help to distinguish between different levels of expression.

This can of course be used to test the expression of other genes or for example the ability to switch mating-type. The latter can be done by growing the cells on poor medium and then stain the colonies with iodine vapours that colour spores in brown and cells in yellow, thus assessing the level of sporulation.

4.3.4 Treatment of cells with Trichostatin A

Trichostatin A (TSA, US Biologicals) is a histone deacetylase inhibitor. Cells were treated with this drug in order to investigate the role of deacetylases in the silencing of the mating-type region in the MAM strains, more specifically in the **rDNA mutant**. The protocol was the following. Cells were grown O/N in 2 ml EMM2+leu+ura+ade+his+0.1μM thiamine at $30\,^{\circ}$C. Next morning the cells were divided into two 1 ml samples. $0.35\,\mu$l of a 1 mg/ml TSA solution were added to one of them, while the other was kept as a control. A 20-fold dilution of both samples was made. After 24 hours the TSA treated cells were washed and resuspended in EMM2+leu+ura+ade+his+ 0.1μM thiamine. Their recovery was monitored. Dilutions were made morning and evening in order to add fresh medium and prevent the cell density from becoming too high. Fluorescence images were taken before the TSA treatment as well as regularly during and after.

4.3.5 Fluorescence microscopy and labelling

Fluorescent labeling

The mating-type region was labelled by insertion of a lac-Op array at the tightly linked *his2* locus. A strain with this insertion was obtained from Ding et al. [39] and the lac-Op array was combined with the mating-type region through crosses. LacI-GFP was expressed in the same strain. *lacI-GFP* was inserted at the *his7* locus and under control of the *dis1* promoter [39]. The nucleolus was labelled as by Matsuyama et al. [80] using 08C03. 08C03 corresponds to the open reading frame (ORF) SPBC947.07. It encodes the ribosome biogenesis protein Rrp14-C predominantly localised in the nucleolus. 08C03 was tagged with YFP by Matsuyama et al. but for the purpose of this experiment YFP was replaced with CFP. The CFP fusion protein was expressed from the *leu1* locus, under control of the thiamine-repressible promoter *nmt1*.

Control of the fluorescent signal

The intensity of the fluorescence signal of both GFP and CFP was very dependent of cell concentration, indicating that the population growth state mattered. In the exponential phase, when cells grow and divide leading to an increase of the population, the GFP signal from the mating-type region was good whereas the CFP signal from the nucleolus was weak or non-existent. On the contrary, in the stationary phase the GFP signal was very weak and CFP often overexpressed. The growth state is reflected by the optical density (OD) of the cell suspension. An OD of approximately 1 turned out to be optimal for both a good GFP and CFP signal. This corresponds to the transition between the exponential and the stationary phase. If CFP was overexpressed or GFP weak, it was possible to improve the fluorescence signal by adding fresh medium and let the cells grow for another hour.

Cell preparation

Prior to microscopy the cells were grown O/N in 4 ml of liquid medium, either AA with $0.25\,\mu$M thiamine or a minimum medium EMM2 with $0.1\,\mu$M thiamine. When the cultures had an optical density of approximately 1 as discussed above, 0.5 ml of the culture to be looked at was pipetted into an eppendorf tube and gently centrifuged for 3 min at 3000 rpm. Most of the supernatant was removed, leaving a dense cell suspension. The chamber was made of a thick 76x26 mm microscope slide (Menzel Gläser) on which 2.5 μl of the cell solution was deposited. A thin 24x24 mm coverslip (Menzel Gläser) was put on top of the drop. Capillary forces kept it in place, also preventing the cells from moving.

Setup

For the fluorescence microscopy an Imager.Z1 microscope from Zeiss was equipped with a cooled Orca-ER CCD camera (Hamamatsu, Japan). The illumination source was a HXP 120C lamp from Leica, Germany. All images were captured at 100-fold magnification using a Plan-Apochromat 100x, 1.4 NA objective. The microscope has a motorised stage allowing for z-scans of the sample. For each field of cells, 11 fluorescent images at each of the relevant wavelengths were obtained at $0.4\,\mu$m intervals along the z-axis. Fluorophores were visualised using band-pass CFP (31044 v2) and YFP (41028) filter sets from Chroma (Brattleboro, VT). Image acquisition times were 500 ms to 1 s for the GFP signal visualised through the YFP band-pass filter and 200 ms to 600 ms for the CFP signal.

4.3.6 Data Analysis

In order to handle the large amount of data, we wrote a custom-made matlab program. Each image stack contained eleven slices, two channels and five to twenty cells to analyze. The goal was to handle all cells at the same time. The organigram of the program can be seen in Figure 4.11. The fluorescent signal from the mating-type region was quite weak. In order to visualise it we performed contrast enhancement directly in the acquisition program Volocity. This was also done for the CFP signal from the nucleolus. The program used to analyse the images works in the following way:

Step1: The n slices of each of the two channels are imported, filtered and converted to binary images. The YFP channel showing the mating-type region signal is directly converted to a binary image using the *im2bw* function of Matlab. The threshold has to be optimised in order to detect as many mating-type regions as possible. The CFP channel is filtered with a so-called DOG (Difference of Gaussians) filter which also converted it to a binary image. Here the sigma value and the cutoff have to be optimised. When possible the same parameters were used for each image stack. This produced two stacks of n slices, one for each channel. Steps 2 to 5 are identical for the two stacks.

Step2: Each detected mating-type region or nucleolus corresponds to a cluster in the binary images obtained after filtering. The clusters in each of the n slices are found and labelled, i.e. the x- and y-coordinates of the centroid of each cluster is determined and assigned an integer number. The Matlab function *regionprops*(L,'centroid') was used for this purpose.

Step3: Each cluster is coupled to the original intensity of the centroid pixel.

Step4: The next step is then to match identical clusters from different slices and assign them the same cluster number. The slices are compared two by two, each cluster from slice j with all clusters from slice $j + 1$. Clusters from two consecutive slices having similar coordinates are assigned the same cluster number. In the same step their intensities are compared and the coordinates of the brightest cluster are saved in a vector together with its intensity, the slice number and the cluster number.

Step5: We now have a 3D-matrix containing n-1 2D-matrices, each containing information about the comparison between two consecutive slices. Clusters with the same number are compared and the vector from the cluster with the highest intensity is saved in a new matrix. This matrix only contains the data for the brightest cluster centroid of each mating-type region or nucleolus and is likely to correspond to their actual centroid.
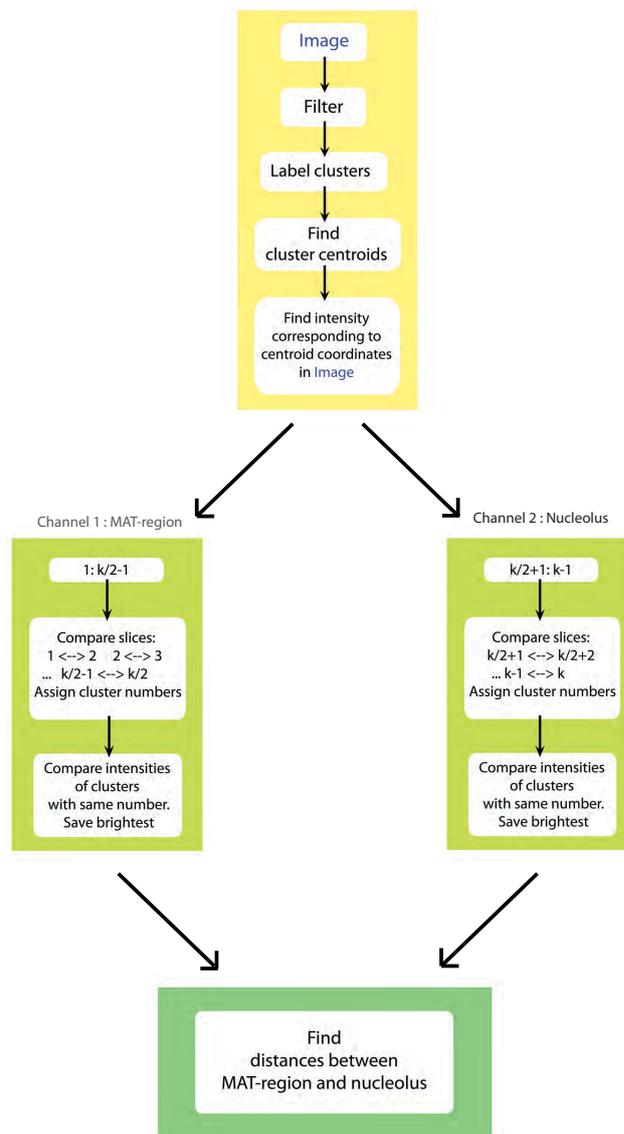
Figure 4.11: The organigram of the Matlab program. **Yellow box :** All images from both channels are first imported into Matlab, filtered, clusters are identified and labelled, the coordinates of their centroid is coupled to the intensity of the cluster. **Light green boxes :**. Each channel corresponds to a 3D-matrix. They are treated separately, but in the same way. **Dark green box :** The matrices of the YFP (mating-type region) channel and the CFP (nucleolus) channel are compared. The distance between the mating-type region of each cell and its corresponding nucleolus is calculated.
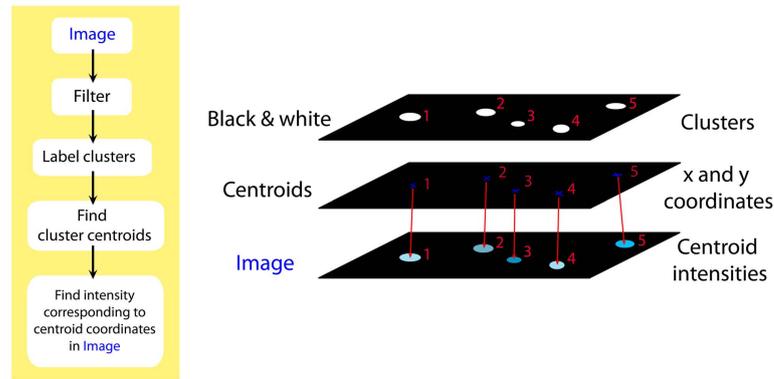
Figure 4.12: Step2 of the data analysis program. The centroids of the clusters are identified and assigned an intensity.

Step6: In the last step the matrix corresponding to the mating-type region is compared to the one for the nucleolus. If the x- and y-coordinates of two clusters are within a certain confidence interval from each other, they are coupled as belonging to the same cell. These confidence intervals have to be tuned carefully if cells are close to each other. The distance between the mating-type region centroid and the nucleolus centroid is calculated. The x- and y-coordinates are converted into micrometers. The slice number multiplied by the distance between slices is used as the distance in z-direction. Of course the resolution is better in xy than in z, where we are limited by the scanning step size of 400 nm, but foremost by the fact that axial resolution in standard microscopy is of the order of 500 nm [13].
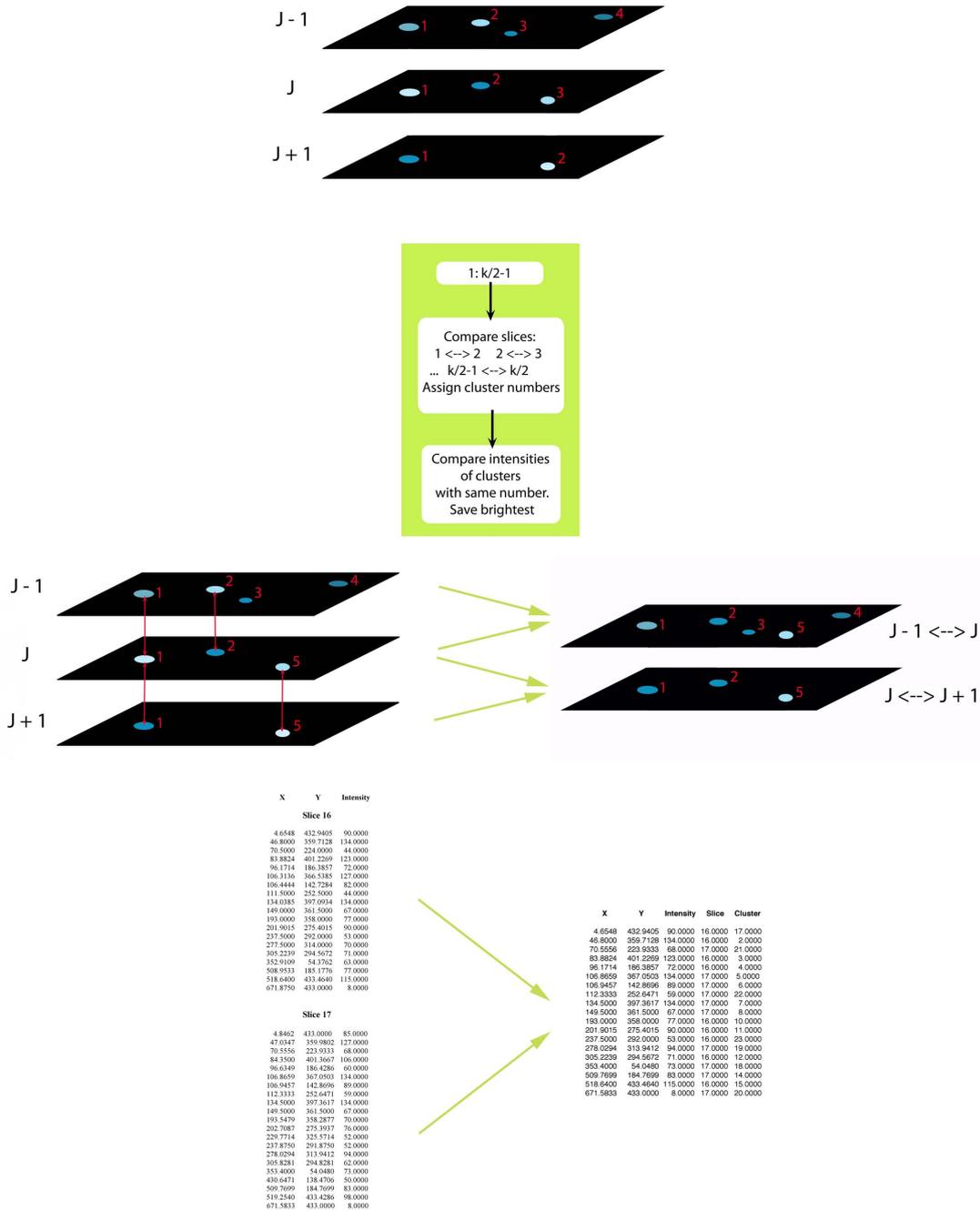
Figure 4.13: Illustration of **Step4** of the data analyse program. Three slices are compared two by two giving rise to a new 3D matrix composed of two instead of three 2D matrices. In this step the slice number and cluster numbers are additionally saved.

4.4 rDNA boundary and silencing

In this first Results section, we will present the initial motivation for this project, as well as show central data. The idea was to screen the genome of *S. pombe* for boundary elements and elements with a silencing effect. The screening method is described in section 4.3.1. In short, the right-hand repeat of the mating-type region was replaced by pieces of the yeast genome taken from three genomic libraries.

One type of mutants caught our attention. In these mutants the right-hand boundary element (*IR-R*) of the mating-type region was replaced by a piece of rDNA, causing a similar silencing effect as for the wild-type strain. This is illustrated in Figure 4.14. The four strains used in this study are described in details in section 4.3.2. The so-called **wild-type strain** (MAM26) has the wild-type mating-type region as shown in the sketches in Figure 4.14. The **control strain** (MAM56) is identical to the wild-type strain but for an *ade6* reporter gene inserted in the silenced region, close to *IR-R*. This gene is also present in the two other mutants. One has a deletion of *IR-R* and we call it the **IR-RΔ mutant** (MAM46). The fourth strain is our **rDNA mutant** (MAM36). The spot tests displayed in Figure 4.14 were made on YE and AA-ade plates (for more details see section 4.3.3). The most striking result is that the **rDNA mutant** showed the same pink phenotype as the **wild-type strain** and **control strain**, meaning that the reporter gene was repressed. This indicates, as we already mentioned, that by replacing the right-hand repeat by a piece of rDNA, we can restore silencing of part of the mating-type region. This of course does not tell us anything about the silencing mechanism itself. We do not know whether the rDNA boundary (*rDNA-R*) is truly a boundary element. The localisation of the mating-type region in the rDNA mutant might also play a role. We will investigate this in section 4.5.

Figure 4.15 shows spot tests of PM7, PM2, PM3 and PM8 on YES, YE, AA-ade and sporulation (EMM2+leu+ura+ade+arg+his) plates. These four strains are almost identical to the MAM26, MAM36, MAM46 and MAM56 strains described above. PM7 corresponds to the **wild-type strain**, PM2 to the **rDNA mutant**, PM3 to the **IR-RΔ mutant** and PM8 to the **control strain**. The only difference between these two sets of strains is a resistance to hygromycin replacing the original G418 resistance (see section 4.3.2). This should not influence their phenotype, except if they are grown on plates containing either of these antibiotics. The function of the YES plate is to verify that the strains are healthy and have the same phenotype when growing on rich media.
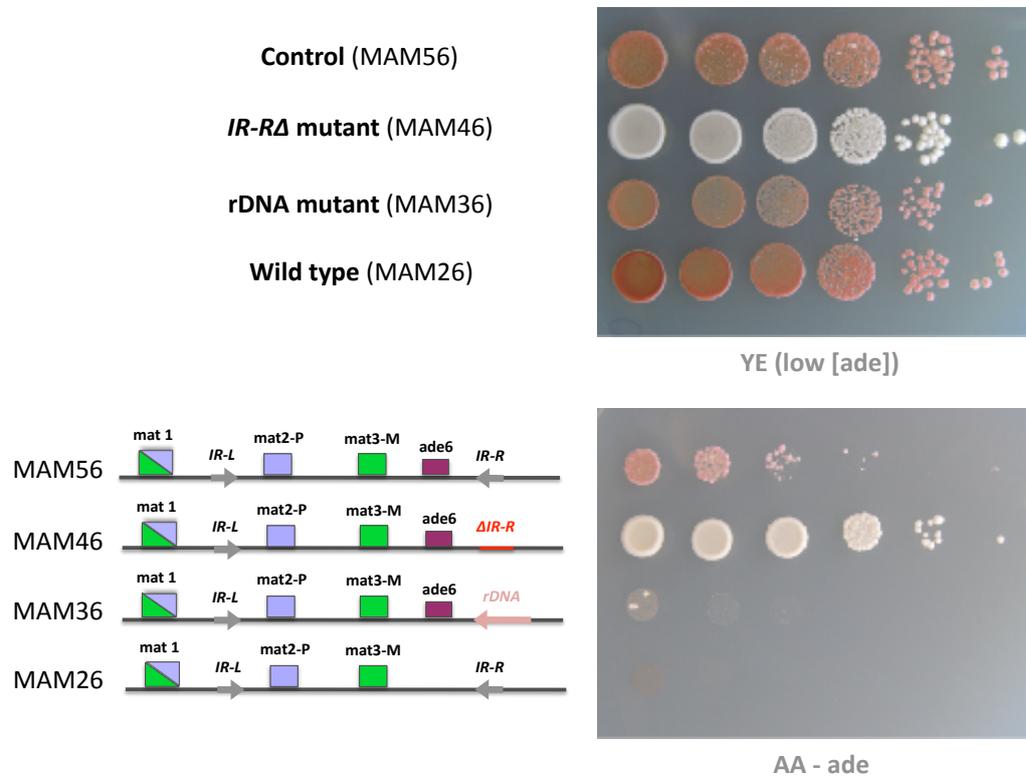
Figure 4.14: Spot tests on YE and AA-ade plates showing the four MAM strains; the **wild-type strain** (MAM26), **rDNA mutant** (MAM36), **IR-RΔ mutant** (MAM46) and **control strain** (MAM56). YE is poor in adenine, whereas AA-ade lacks it completely, thus inhibiting the growth of cells with a silenced *ade6* gene in their mating-type region.

On the YE plate, the same silencing effect by the *rDNA-R* could be observed for PM2 as for MAM36. Let us now look at the AA-ade plates in both Figure 4.14 and 4.15. These plates do not contain any adenine. Cells that do not produce Ade6 cannot grow on these plates. MAM36 did not grow at all and PM2 grew a little at the two highest cell concentrations. The control strains MAM56 and PM8 grew at the three highest concentrations. For both the MAM and the PM strains, it seems like the rDNA boundary had a stronger silencing effect than the wild-type *IR-R* boundary. This would suggest a different silencing mechanism.
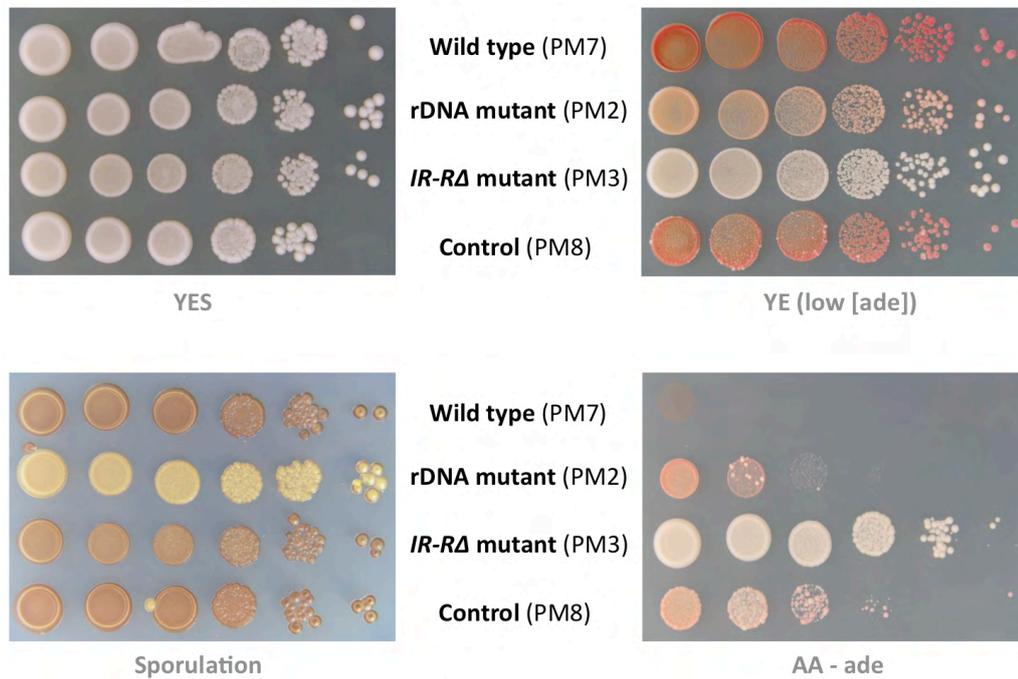
Figure 4.15: Spot tests on YES, YE, EMM2 and AA-ade plates showing strains equivalent to the four MAM strains; the **wild-type strain** (PM7), **rDNA mutant** (PM2), **_IR-RΔ_ mutant** (PM3) and **control strain** (PM8). These strains are different from the MAM strains only in their resistance to hygromycin which does not affect their phenotype in the absence of adenine.

On YE and AA-ade plates, white **control strain** and **rDNA mutant** colonies could occasionally be observed. This could be due to variegation or to _cis-_ or _trans_-acting mutations disabling the boundary elements, allowing the euchromatic region to spread into the mating-type region and derepress _ade6_. The mutations could also be located in genes coding for proteins taking part in the silencing of the mating-type region. This never happened for the **wild-type strains**, since they lack a functional _ade6_ gene.

The sporulation plate shown in Figure 4.15 provided us with an interesting result. All colonies grew white, but were later stained with iodine vapour that colours the starch in the spore envelopes in brown [71]. The **wild-type strain**, the **control strain** as well as the **_IR-RΔ_ mutant** were stained brown, but the **rDNA mutant** did not show a strong sporulation phenotype. The spots were streaked with brown, but gave a much more yellow impression. Hence, replacing the right-hand boundary by a piece of rDNA seems to inhibit the mating-type switching described in section 4.2.2.

We do not know the reason for this yet, but it could again suggest a different silencing mechanism, relocalisation or that the boundaries (*IR-L* and *IR-R*) somehow are involved in mating-type switching. It is known that the localisation of a gene domain within the nucleus can affect its expression. We will therefore in the next section examine the localisation of the mating-type region in the four types of strains. MAM26, MAM36, MAM46, MAM56 and PM7, PM2, PM3, PM8 will be regarded as equivalent, but it will always be specified which strains are used.

4.5 rDNA boundary and localisation

It has been reported that the mating-type region localises at the periphery of the nucleus [2]. It is also known that the rDNA can be found in a nuclear subcompartment called the nucleolus [58]. In this section we will investigate the localisation of the mating-type region in the **wild-type strain**, the **control strain**, the ***IR-RΔ* mutant** and the **rDNA mutant**. More specifically we measured the distance in 3D between the mating-type region and the centre of the nucleolus. We will provide the mean distance and standard deviation for each data set, as well as for pooled data sets combining all cells with a given mating-type region. We will also compare these results with the mating-type to nucleolus distances computed for randomly distributed points within the nucleus, including or excluding the nucleolus.

4.5.1 Cell, nucleus and nucleolus size

Before measuring distances in the nucleus, one should be aware of the fact that the size of the nucleus and nucleolus varies with cell size. Neumann *et al.* [90] showed that in *S. pombe*, the volume ratio between nucleus and cell (N/C) stays constant over a wide range of cell sizes. In mutants unable to form a septum, but where the nucleus kept dividing, they observed that the inner nuclei were smaller than the outer ones, suggesting that the local cytoplasmic environment plays a role. By artificially perturbing N/C, they showed that the nucleus adapts its volume to the cell size, rather than the other way around. They also showed that DNA content does not directly influence the nuclear size. N/C was measured to be around 0.082 for the wild-type strain. The volume ratio between the nucleolus and nucleus also proved to be constant. They measured it to be 0.24±0.06.[90] Similar results have been obtained for *S. cerevisiae* [64]. To know more about the coupling between cell size, growth rates and cell cycle see references [117] and [11].

Using transmission electron microscopy Osumi *et al.* measured the nucleus of an *S. pombe* cell ($7\,\mu$m long and $2.8\,\mu$m in diameter) to have a diameter of $1.8\,\mu$m, and the nucleolus to be an ellipsoid with long and short axis of $1.5\,\mu$m and $0.9\,\mu$m respectively [102]. We do not know if the section was through the equatorial plane of the nucleus. Assuming that it was, this would give us a volume ratio between the nucleolus and the nucleus of 0.35 and N/C $= 0.046$. This differs from the results given by Neumann *et al.*, but one should bare in mind that Neumann *et al.* averaged over several hundred cells.

By tagging membrane proteins with GFP, we were able to visualise the nuclear envelope and measure its mean diameter. The strain used was PG2747 (see strain table in Appendix C) and the cells were taken from an O/N culture in EMM2 $+ 0.1\mu$m thiamine with an optical density of approximately 1. An average over 18 cells gave a mean nucleus diameter of $2.30 \pm 0.23\,\mu$m. We also measured the mean length and diameter of the cells. We measured them to be $10.66 \pm 1.85\,\mu$m and $4.05 \pm 0.33\,\mu$m respectively. This gave us N/C $= 0.0463$. This is consistent with what we calculated for the cell from Usumi *et al.* This would suggest that the observed discrepancy between our nucleus to cell volume ratio and Neumann's is due to the way we approximate the nucleus volume. They do not specify in detail their calculations but they mention that the cell was approximated with a rod and the nucleus with a prolate ellipsoid [90]. We did the same approximation for the cell, but approximated the nucleus with a sphere. By measuring two axes of the nucleus we might have obtained a result closer to theirs. We also measured the mean length and diameter of 20 cells from each of the MAM strains in data set 2, see below Table 4.2. The measured cells showed no signs of division.They can be seen in Table 4.1 where they are reported together with the calculated cellular volume and the nucleus diameter calculated using N/C $= 0.046$. The values found for the latter are consistent with the measured nucleus diameter. We will therefore use $2.3\,\mu$m in section 4.5.3, when simulating an intranuclear random distribution of mating-type region positions.

Notably, the fluorescent signal from the nucleolus can vary in intensity. As we have shown earlier the optimisation of the signal is not trivial, see section 4.3.5. But an optimal signal often corresponded to a certain cell size. Although we fluorescently tagged nucleolar proteins and not the DNA itself, our data would be in accordance with a nucleolus taking up between a quarter and a third of the nucleus. In which phase of the cell cycle a cell is would also influence intra-nuclear distances, especially during mitosis. We therefore only analysed cells in the end of S phase (after completed cell division) and in the G2 phase. We still had some spread in cell size.

Strain	Measured cell length (μm)	Measured cell diameter (μm)	Calculated cell volume (μm^3)	Calculated nucleus diameter (μm)
MAM26_2	11.08 ± 1.44	3.84 ± 0.33	130 ± 32.21	2.24 ± 0.19
MAM36_2	10.93 ± 1.37	3.99 ± 0.33	137.71 ± 31.34	2.28 ± 0.17
MAM46_2	13.93 ± 1.80	3.48 ± 0.20	124.59 ± 24.92	2.21 ± 0.14
MAM56_2	10.57 ± 1.85	3.81 ± 0.30	121.96 ± 31.23	2.19 ± 0.20
PG2747	10.66 ± 1.85	4.05 ± 0.33	139.80 ± 39	2.29 ± 0.21

Table 4.1: Mean cell length and diameter measured on MAM cells from data set 2 (see Table 4.2) as well as PG2747 that has lipid membranes marked with GFP. N/C $= 0.046$ was used to calculate the nucleus diameter. All cells were grown O/N in EMM2 $+ 0.1 \, \mu$m thiamine.

4.5.2 Mating-type region and nucleolus

Visual inspection of the fluorescence images in Figure 4.16 of our four MAM strains, the **wild-type strain** (MAM26), the **rDNA mutant** (MAM36), the ***IR-RΔ* mutant** (MAM46) and the **control strain** (MAM56) give us an indication of what to expect when measuring the 3D distance between the mating-type region (yellow dot) and the nucleolus (in blue). The mating-type region seems to be localised closer to the nucleolus in the **rDNA mutant** than in the other three strains.

Using the custom made Matlab program described in section 4.3.6 we measured the 3D distance between the mating-type region and the nucleolus for all cells in the end of S phase or in the G2 phase of the cell cycle, i.e. all cells with only one nucleus and showing no signs of division, such as elongation of the nucleus or formation of a septum. In table 4.2 the results for each data set are shown, as well as the mean distance for each strain. MAM26_1, MAM36_1, MAM46_1 and MAM56_1 correspond to data collected the same day with the four strains grown under the same conditions. This is also the case for the data sets marked with 2 and 3 respectively. Cells from data set 1 were grown overnight in AA $+ 0.25 \, \mu$M thiamine, whereas cells from data sets 2 and 3 were grown in EMM2 $+ 0.1 \, \mu$M thiamine. We do not believe that the type of growth medium influenced the measured distances. It is true that AA is a rich medium, while EMM2 is a minimum medium, but the cells still had the nutrients they needed. The cells could have been expected to be smaller in EMM2 than in AA, hence leading to smaller mating-type region to nucleolus distances. This was not the case. MAM26_2, grown in EMM2, even showed larger mean distances than MAM26_1, grown in AA. The change of media was motivated by an improvement of the fluorescence signal, especially for the nucleolus, marked with CFP. With AA we often had problems with fluorescent aggregates in
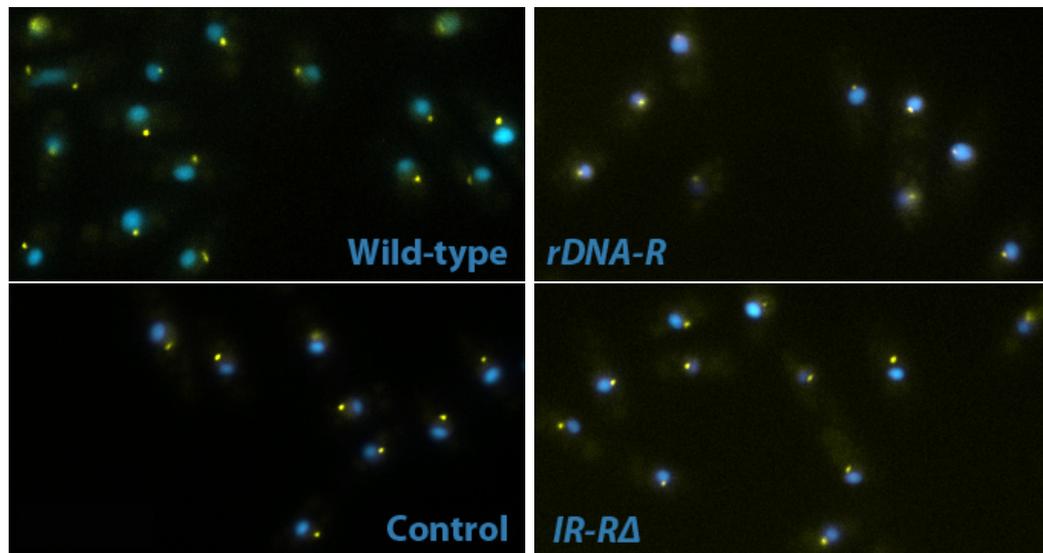
Figure 4.16: Fluorescence images of the MAM strains grown in AA + 0.25μM thiamine; the **wild-type strain** (MAM26), the **rDNA mutant** (MAM36), the **IR-RΔ mutant** (MAM46) and the **control strain** (MAM56). These images correspond to the z-stack slice containing the greatest number of GFP-marked mating-type regions (in yellow). The nucleolus was marked with CFP (in blue).The two channels were superimposed.

the cytoplasm. The amount of added thiamine was tuned for each medium in order to get the best fluorescence signal out. The reason why the **IR-RΔ mutant** showed larger mating-type region to nucleolus distances for data sets MAM46_2 and MAM46_3 does not seem to be related to the choice of growth medium either. Grown in the same EMM2 medium for the same amount of time, this strain gave rise to longer cells than the three other types of strains, see Table 4.1. Control experiments were made with AA medium in which the *IR-RΔ* cells also grew to be longer. One explanation could be that MAM46 is uracil prototroph, meaning that the **IR-RΔ mutant** can synthesise uracil by itself. This could lead to a faster growth than for the other strains that need to take uracil up from the medium. But after all, their length might not be the reason for their larger mean distance. They were not only longer, but also thinner, which resulted in a cellular volume very close to the one calculated for the other three strains, see Table 4.1.

The mean 3D distance between the mating-type region and nucleolus was measured to be $1.25 \pm 0.43\,\mu$m for the **wild-type strain**, $0.99 \pm 0.36\,\mu$m for the **rDNA mutant**, $1.32 \pm 0.40\,\mu$m for the ***IR-RΔ* mutant** and $1.25 \pm 0.36\,\mu$m for the **control strain**. We performed Student's t-tests comparing the **wild-type strain** with the three other strains assuming near Gaussian distributions and equal variance, the hypothesis being that their mean mating-type region to nucleolus distance are the same. This showed that:

- As expected, the mean mating-type region to nucleolus distances in the **wild-type strain** and the **control strain** are not significantly different from each other, p=1.

- The **wild-type strain** and the ***IR-RΔ* mutant** do not show significantly different mean distances either, although the p-value is smaller p=0.3260.

- The mean mating-type region to nucleolus distances in the **wild-type strain** and the **rDNA mutant** are significantly different from each other, $p < 1 \cdot 10^{-7}$.

Strain	Data set	Growth media	Mean MAT/nucleolus distance (μm)	Number of cells
Wild-type strain	MAM26_1	AA	1.26 ± 0.50	51
	MAM26_2	EMM2	1.31 ± 0.42	38
	PM7_3	EMM2	1.20 ± 0.38	48
Wild-type strain	All data sets		$\mathbf{1.25 \pm 0.43}$	137
rDNA mutant	MAM36_1	AA	1.01 ± 0.37	78
	MAM36_2	EMM2	1.01 ± 0.38	50
	PM2_3	EMM2	0.92 ± 0.32	33
rDNA mutant	All data sets		$\mathbf{0.99 \pm 0.36}$	161
***IR-RΔ* mutant**	MAM46_1	AA	1.28 ± 0.42	98
	MAM46_2	EMM2	1.37 ± 0.34	39
	MAM46_3	EMM2	1.37 ± 0.41	46
***IR-RΔ* mutant**	All data sets		$\mathbf{1.32 \pm 0.40}$	183
Control strain	MAM56_1	AA	1.30 ± 0.39	68
	PM8_3	EMM2	1.19 ± 0.32	51
Control strain	All data sets		$\mathbf{1.25 \pm 0.36}$	121

Table 4.2: Mean mating-type region to nucleolus distance measured in the **wild-type strain** (MAM26/PM7), the **rDNA mutant** (MAM36/PM2), the ***IR-RΔ* mutant** (MAM46) and the **control strain** (MAM56/PM8). The results for three data sets are shown. The growth media used were AA + $0.25\,\mu$M thiamine (AA) and EMM2 + 0.1μM thiamine (EMM2).
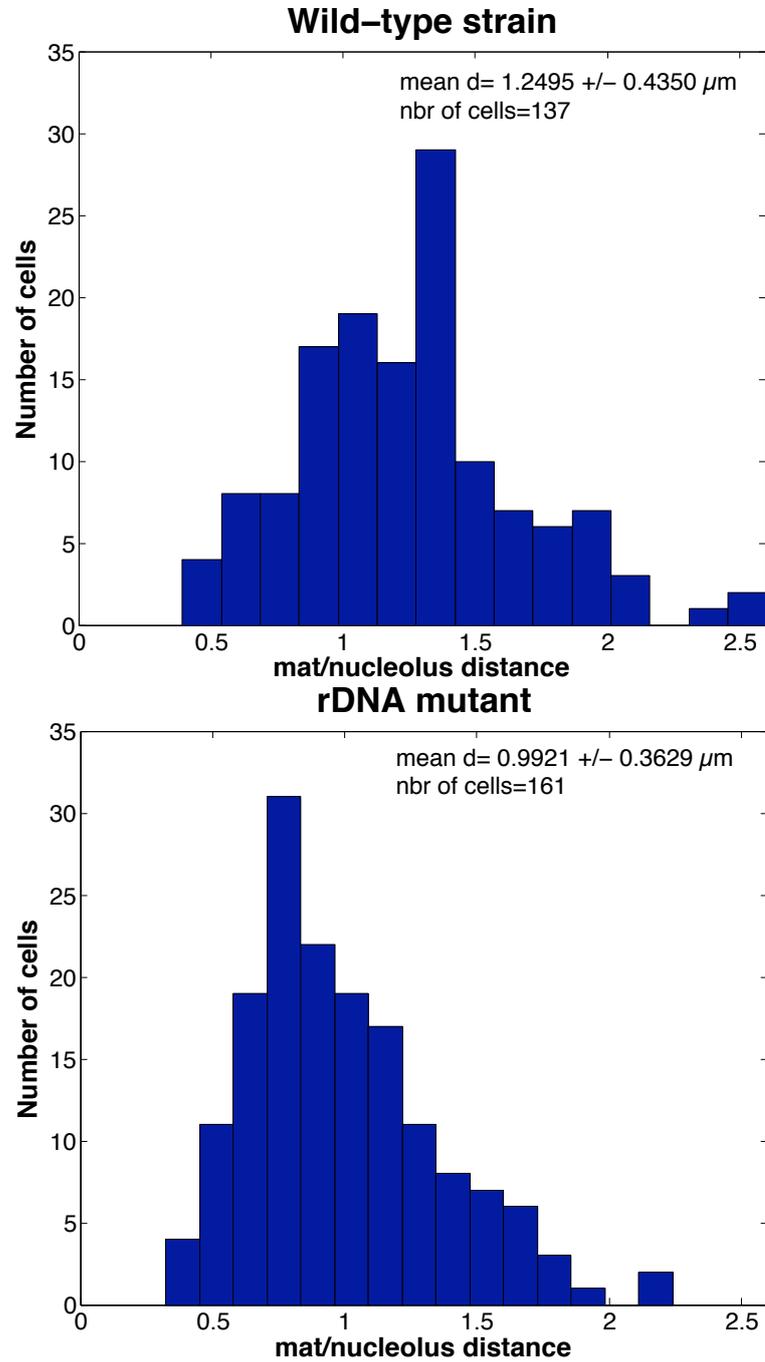
Figure 4.17: Histograms of the measured mating-type region to nucleolus distance in the **wild-type strain** (above) and the **rDNA mutant** (below).
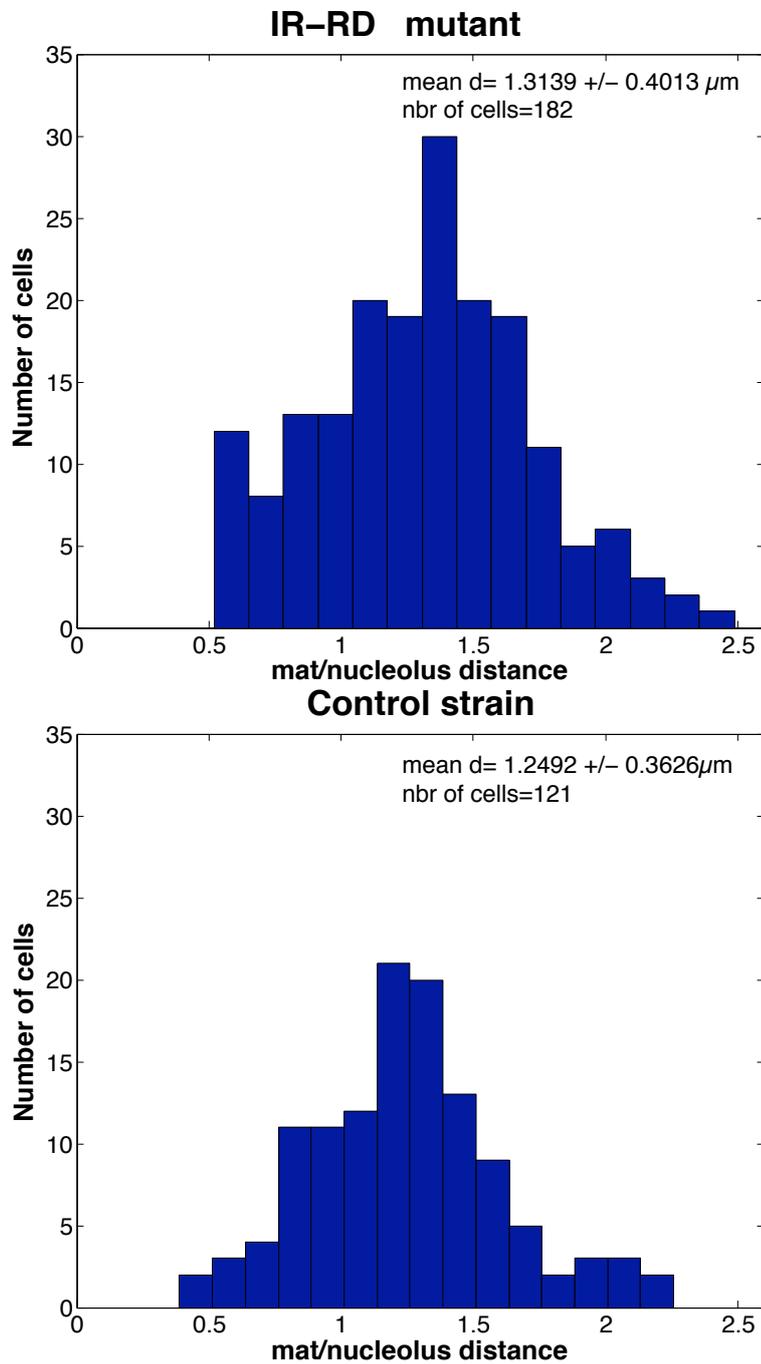
Figure 4.18: Histograms of the measured mating-type region to nucleolus distance in the **IR-RΔ mutant** (above) and the **control strain** (below).

The data were also plotted as histograms, showing the distance distribution for each strain. The distributions for the **wild-type strain** and the **rDNA mutant** are shown in Figure 4.17. The data for the **IR-RΔ mutant** and the **control strain** can be found in Figure 4.18. We will discuss these distributions in the next section.

In conclusion, replacing the right-hand boundary of the mating-type region by a piece of rDNA relocalises the mating-type region closer to the nucleolus, the distance between the two being significantly reduced.

4.5.3 Distance distributions

To improve our understanding of the distributions of mating-type to nucleolus distances obtained for the four MAM strains, we decided to model three scenarios; that the mating-type region was allowed anywhere in the nucleus (I), anywhere but in the nucleolus (II) and only in the nucleolus (III). All three distributions were random within the permitted volume. We assumed the nucleolus to be spherical with a radius $R = 1.15\,\mu$m. According to Neumann *et al.* [90] the volume of the nucleolus is about a quarter of the volume of the nucleus. From a TEM micrograph [102] we measured it to be a third. This would give us a nucleolus volume $1.53\,\mu$m$^3 \leq V_n \leq 2.23\,\mu$m^3. The nucleolus is always touching the nuclear envelope. If we now assume that the nucleolus is the sum of two spherical caps and that it reaches $1\,\mu$m into the nucleus, then we can calculate the radius of the caps. Figure 4.19 shows the nucleus in dark grey and the nucleolus in light grey for a nucleolus to nucleus volume ration of 0.25. The blue dots represent a random distribution within the nucleolus. The histograms corresponding to the three scenarios are also shown in Figure 4.19. The mean mating-type region to nucleolus distances was calculated for each of them. Scenario I gave a mean distance of $1.39 \pm 0.46\,\mu$m. Excluding the nucleolus as in scenario II gave, as expected, a greater mean distance that varied between $1.56 \pm 0.33\,\mu$m and $1.61 \pm 0.30\,\mu$m depending on the relative size of the nucleolus. And last, scenario III gave a mean distance comprised between $0.71 \pm 0.19\mu$m and $0.81 \pm 0.24\,\mu$m. Although the result for the **IR-RΔ mutant** is very similar to what we obtained for scenario I, we should be careful before drawing any hasty conclusions based on these values since we made several assumptions regarding the size and shape of the nucleolus. Looking at the shape of the distance distributions will hopefully give us some valuable means of comparison.
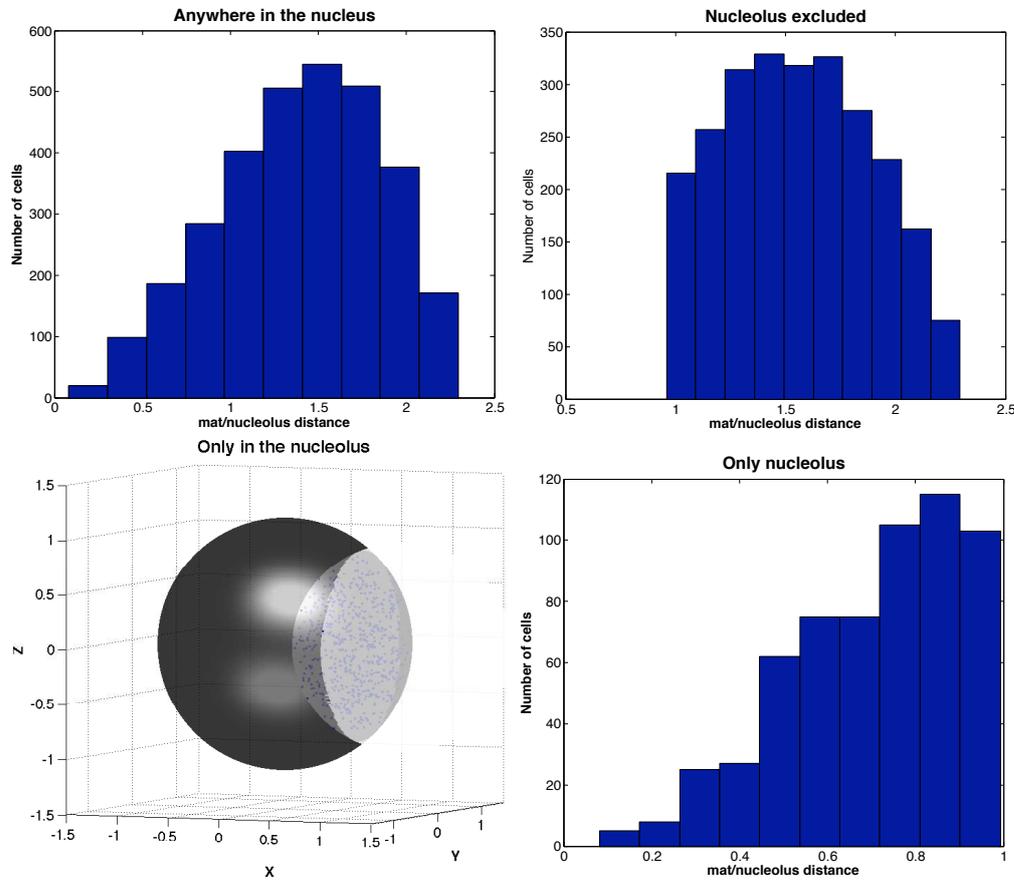
Figure 4.19: Histograms of the computed mating-type region to nucleolus distances for the three scenarios: (I) the mating-type region allowed anywhere in the nucleus (top left), (II) anywhere but in the nucleolus (top right) and (III) only in the nucleolus (bottom right). The random distribution for scenario III is shown in the bottom left panel. The nucleus is in dark grey, the nucleolus in light grey and the mating-type region positions in blue.

Let us first look at the distance distribution in the **IR-RΔ mutant**. It has features that resemble both the histogram of scenario I and II. All three have a maximum around $1.5\,\mu$m. The distance distribution in the **IR-RΔ mutant** (see Figure 4.18) has a sharp boundary at $0.5\,\mu$m, below which no cells were found. This is similar to the sharp cutoff seen for scenario II, in which the mating-type region is excluded from the nucleolus. The distribution of scenario I shows a much more gradual decrease of the number of cells with shorter mating-type region to nucleolus distances. This would suggest that the mating-type region is excluded from the nucleolus in the **IR-**

RΔ **mutant**. Still its histogram shows the same type of slight asymmetry as for scenario I, where the allowed volume includes the whole nucleus. Given that the mean distance for scenario I and the ***IR-RΔ*** **mutant** are very similar, maybe the truth lies somewhere in between. The **wild-type strain** (see Figure 4.17) and the **control strain** (see Figure 4.18), show much more symmetric distribution. That would make sense if the mating-type region has a preferred localisation inside the nucleus. Alfredsson-Timmins *et al.* [2] showed that the mating-type region localises near the spindle-pole body at the periphery of the nucleus. A deletion of both boundaries led to a delocalisation of the mating-type region away from the spindle-body, but still at the periphery of the nucleus [2]. This could support an interpretation of the data where the mating-type region in the **wild-type strain** is localised in a specific region of the nuclear periphery, whereas it is more randomly distributed in the ***IR-RΔ*** **mutant**. We are planning to make localisation experiments where, in addition to the mating-type region and the nucleolus, the spindle-pole body will be fluorescently marked. Hopefully this will help us clarify whether there is a difference in mating-type region localisation between the **wild-type strain** and the ***IR-RΔ*** **mutant**.

The distance distribution for the **rDNA mutant** (see Figure 4.17) does not at all resemble the distribution for scenario III, where the nucleolus is the only allowed volume. First of all it shows the inverse asymmetry. This could be due to some cells not being affected by the mutation in the same way, not leading to a relocalisation of the mating-type region. In the real distribution the maximum is found around $0.8\,\mu$m. This could correspond to a localisation of the mating-type region between the nucleolus and the spindle-pole body as well as in some parts of the nucleolar periphery since the nucleolus is not spherical. Both types of localisation have been seen, although the latter seems more common, see Figure 4.16. Also, the minimum mating-type to nucleolus distance we measured was very similar to the ones measured for the **wild-type strain** and **control strain**, around $0.4\,\mu$m and $0.5\,\mu$m respectively. Keeping in mind that this minimum distance is the same as our resolution in the z-direction, this still strengthens the conclusion that the substitution of *IR-R* by the *rDNA-R* leads to the relocalisation of the mating-type region nearer, but not into the nucleolus.

4.6 Derepression of the mating-type region

The results presented above established that the rDNA boundary causes silencing and relocalisation of the mating-type region closer to the nucleolus. Since this is still an ongoing project, we will in sections 2.7 and 2.8 describe the paths we are currently following in trying to elucidate the underlying mechanisms. We tried to make qualified guesses about the proteins that might be involved. We looked at proteins related to heterochromatin formation such as Clr3 and Clr4. We also looked at proteins such as Swi1 and Swi3, involved in replication of both the mating-type region and the rDNA .

4.6.1 *clr3* and *clr4* deletions

Function

We have already mentioned the two proteins Clr3 and Clr4 in the introduction chapter. Clr3 is a class II histone deacetylase present in the heterochromatic regions of *S. pombe*. Its role is not only to facilitate heterochromatin formation, but it is also crucial for heterochromatin maintenance. It does so by stabilizing the trimethylation of lysine 9 of histone H3.[136] Deleting Clr3 also leads to a specific increase in the acetylation of lysine 14 on histone H3. Clr3 colocalises with the centromeric regions, the mating-type region and the ribosomal DNA. In the nucleolus it contributes to the silencing of genes transcribed by the polymerase Pol II.[15] Its function in the mating-type region is related to the secondary heterochromatin formation mechanism. Clr3 is recruited there by proteins in the ATF/CREB family.[136]

The methyltransferase Clr4 plays a role in the silencing of the mating-type region by methylating lysine 9 of histone 3. This histone mark recruits the protein Swi6 that binds to the chromatin and recruits more Clr4, creating a positive feedback loop [53]. Clr4 seems to play a similar role in the silencing of Pol II transcribed genes in the nucleolus [130]. The localisation of the mating-type region has also been shown to be affected by the deletion of *clr4*. From being localised near the spindle-pole body at the nuclear periphery in the wild-type strain, the mating-type region showed a random distribution within the nucleus of *clr4 Δ* strains.[2]

In short, both Clr3 and Clr4 are essential for the formation and maintenance of heterochromatin and hence silencing of both the mating-type region and the rDNA in *S. pombe*.

Silencing

clr3 and *clr4* deletions produce very similar phenotypes, see Figure 4.20. Although we do not have a spot test showing the **wild-type strain** with a *clr3* deletion (*clr3Δ*), we would expect it to have the same pink phenotype as the *clr4* deleted (*clr4Δ*) **wild-type strain**. Even if the mating-type region was derepressed, we would not be able to see it since these strains lack the *ade6* reporter gene. The **control strain** was totally derepressed in both the *clr3Δ* and *clr4Δ* strains. It showed exactly the same phenotype as the **IR-RΔ** **mutant**. This indicates that Clr3 and Clr4 are crucial for the formation of heterochromatin at the mating-type region, which is consistent with published data.

The same was not observed for the *clr3* or *clr4* deleted **rDNA mutants**. The *rDNA-R* still strongly silenced the mating-type region. This is especially clear when looking at the AA-ade plate in both Figure 4.20a and 4.20b. Only a few white colonies grew, which would indicate that these were mutants. At the moment we do not know the mechanism of repression. Both Clr3 and Clr4 have been found to colocalise with rDNA, so it is likely that there is a secondary mechanism maintaining the silencing of the *ade6* reporter gene.

4.6.2 Swi1 and Swi3 deletions

Function

Both Swi1 and Swi3 play a role in the stabilisation of stalled replication forks. It can either be an accidental stalling or a programmed pausing like in the case of the mating-type region [69]. Swi1 was first identified as stabilising the single-strand break at the mat1 locus, necessary for successful mating-type switching [31]. Swi1 and Swi3 also prevent fork collapse in the rDNA repeats [69]. Swi1 is important as well for the activation of Cds1. Cds1 is a kinase crucial for the replication checkpoint, preventing the cell from dividing as a response to fork arrest.[92] Swi1 and Swi3 associate with DNA only in the S phase of the cell cycle, during DNA replication. They seem to form a complex moving with the replication fork. Their abundance is also correlated. Swi3 is only present in very small amounts in *swi1Δ* mutant. *swi3Δ* mutant show unchanged levels of Swi1, but the protein relocalises to the cytoplasm.[93]

(a)

(b)
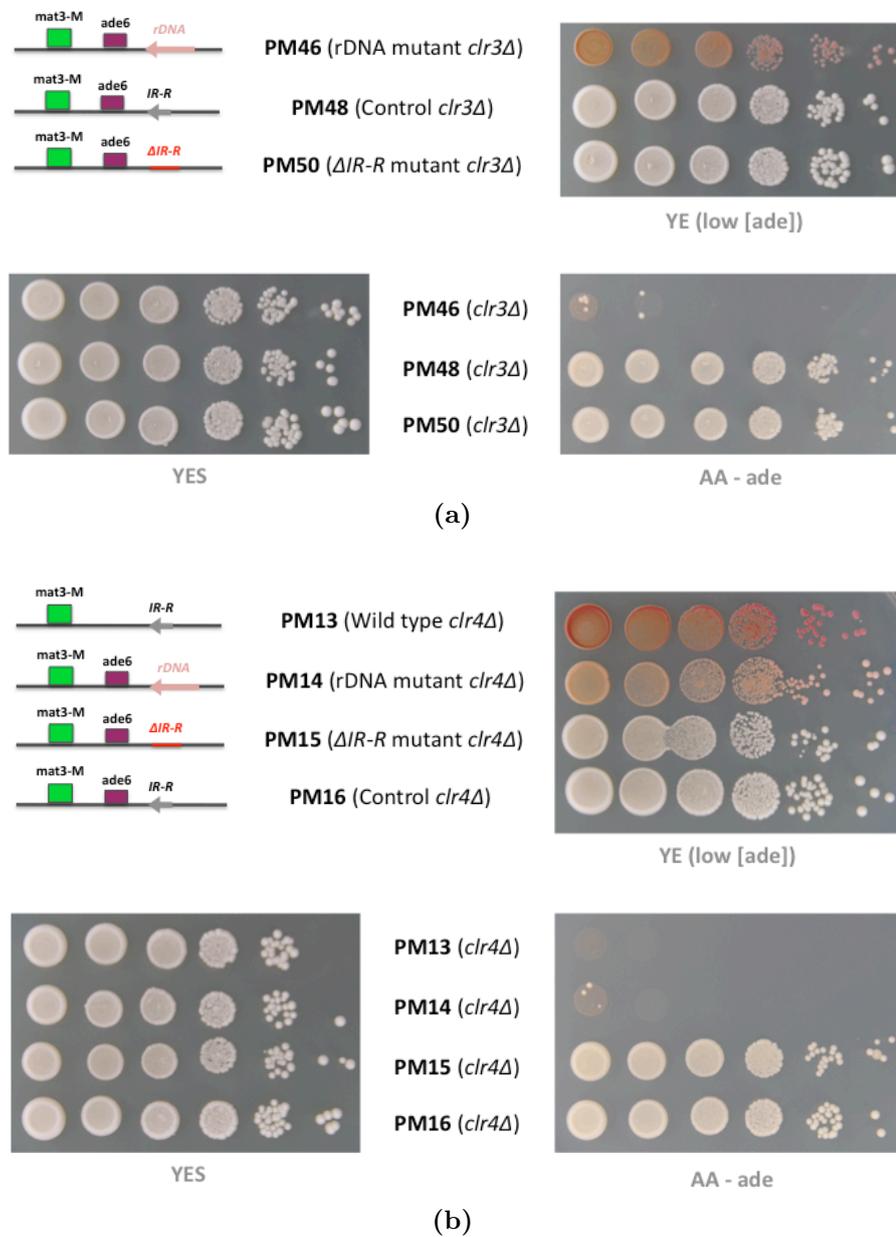
Figure 4.20: (a) Spot tests of the *clr3Δ* **rDNA mutant** (PM46), **control strain** (PM48) and **IR-RΔ mutant** (PM50) on YES, YE and AA-ade plates. (b) Spot tests of the *clr4Δ* **wild-type strain** (PM13), **rDNA mutant** (PM14), **IR-RΔ mutant** (PM15) and **control strain** (PM16) on YES, YE and AA-ade plates. Both (a) and (b) show that the silencing of the mating-type region by the *rDNA-R* is unaffected by these deletions.

Silencing

As for the *clr4* and *clr3* deleted strains, we made spot tests on YES, YE and AA-adenine, but the observed phenotypes were slightly different. See Figure 4.21. For both the *swi1* and *swi3* deleted strains (*swi1Δ* and *swi3Δ*), the phenotype of the **IR-R*Δ* mutant** was unchanged, the mating-type still being derepressed. The **control strain** on the other hand was not completely derepressed as it was for the *clr3Δ* and *clr4Δ* strains. Both the *swi1Δ* and *swi3Δ* strains had a slightly pink phenotype and showed no growth at the lowest cell concentration (right-most spot column). Still they grew quite well, indicating that the formation of heterochromatin was to a large extent affected. It appears that Swi1 and Swi3 do not only play a crucial role in the mating-type switching, but also in the silencing of the wild-type mating-type region. To our knowledge similar results have only been reported once by Nakayama *et al.* [86]. Upon deletion of *swi1*, *swi3* and *swi7*, an associated protein, they could show an increased level of expression of a *ura4* reporter gene inserted into the silenced K-region of the mating-type region.

For *swi1Δ*, the **rDNA mutant** showed the same phenotype as for *clr3Δ* and *clr4Δ* strains. The mating-type region still seemed efficiently silenced and only a few white colonies could be seen on the AA-ade plate, see Figure 4.21a. The *swi3* deleted strain did grow at the two highest cell concentrations (first two columns from the left). Although unlikely, this might indicate that Swi3 has a more crucial role in the silencing of the *rDNA-R*. Spot test were repeated with these strains and no significant difference between the two strains could be observed. Measuring the expression level of *ade6* in these strains would give us more quantitative data.

To summarise, the four proteins we have tested so far have no or little influence on the silencing of the mating-type region by the *rDNA-R*. Either the silencing mechanism is different from the silencing of the wild-type mating-type region or it is simply not the only mechanism involved. Relocalisation could also play a part. The role of the *rDNA-R* will be discussed further in section 4.7.

(a)

(b)
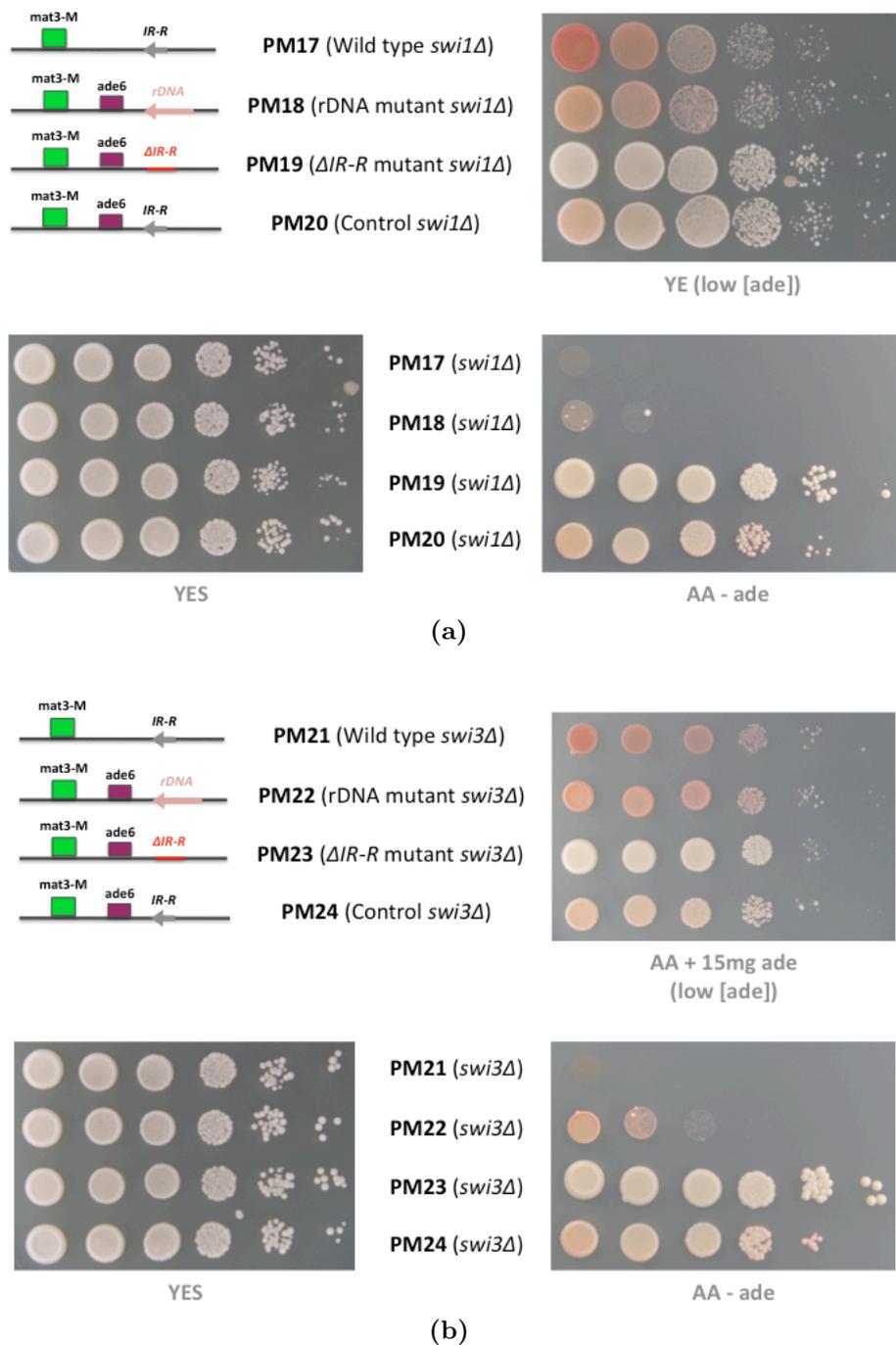
Figure 4.21: (a) Spot tests of the *swi1Δ* **wild-type strain** (PM17), **rDNA mutant** (PM19), ***IR-RΔ* mutant** (PM19) and **control strain** (PM20) on YES, YE and AA-ade plates. (b) Spot tests of the *swi3Δ* **wild-type strain** (PM21), **rDNA mutant** (PM22), ***IR-RΔ* mutant** (PM23) and **control strain** (PM24) on YES, YE and AA-ade plates. Both *swi1Δ* and *swi3Δ* **rDNA mutants** show a continued strong repression of the mating-type region, although slightly weaker for the *swi3Δ* strain.

4.6.3 Relocalisation

For the four knockout **rDNA mutant** strains, preliminary data suggest that there is no major relocalisation of the mating-type region from the viciny of the nucleolus towards the periphery of the nucleus. Figure 4.22 shows a histogram of the mating-type region to nucleolus distances for the *clr4* deleted **rDNA mutant** (PM14). For easier comparison the histogram for the undeleted *clr4*$^+$ **rDNA mutant** (MAM36) was added as an insert. The distance distribution for PM14 shows an asymmetry similar to the one for MAM36. Both have their maximum around $0.8\,\mu$m. For PM14, 75 of the 108 cells had a mating-type to nucleolus distance smaller than $1\,\mu$m. An average over the 108 cells gave a mean distance of $0.89 \pm 0.3\,\mu$m. The measured mean distance is $0.1\,\mu$m smaller than for the unmodified **rDNA mutant**. Performing a Student's t-test we tested the hypothesis that the mean distance for the *clr4*$^-$ and the *clr4*$^+$ **rDNA mutant** are the same. We found that $p = 0.06$. This low p-value makes it difficult to affirm with certainty that the two mean distances are the same. As we have mentioned before, the deletion of *clr4* in a wild-type strain leads to its delocalisation away from the nuclear perifery [2]. A similar effect is not excluded in the case of the **rDNA mutant**. We still need to clarify, by improving our statistics, whether the *clr4*, *clr3*, *swi1* and *swi3* deletions affect the mating-type region to nucleolus distance in the **rDNA mutant**, as well as investigate their effect in the other three strains.

4.6.4 TSA experiment

Deleting *clr3*, *clr4*, *swi1* and *swi3* individually has so far not shown any effect on the silencing of the mating-type region by the rDNA boundary. The preliminary data shown in the previous section would also support the hypothesis that these proteins, at least solely, do not affect the localisation of the mating-type region in our **rDNA mutant**. Making one deletion might not be sufficient to induce a change in phenotype if other complementary pathways exist. On the other hand, double knockouts are difficult to work with, since these strains often are sick. This is for example the case for mutants lacking several histone deacetylases. There is a way of temporarily inhibiting the activity of several relevant proteins at the same time. Trichostatin A is a histone deacetylase inhibitor that affects class I and class II histone deacetylases [132] such as Clr3 which, as we have mentioned, plays a crucial role in the formation of heterochromatin. Cells get sick, but once the treatment is interrupted they recover over a period of 24-48 hours.
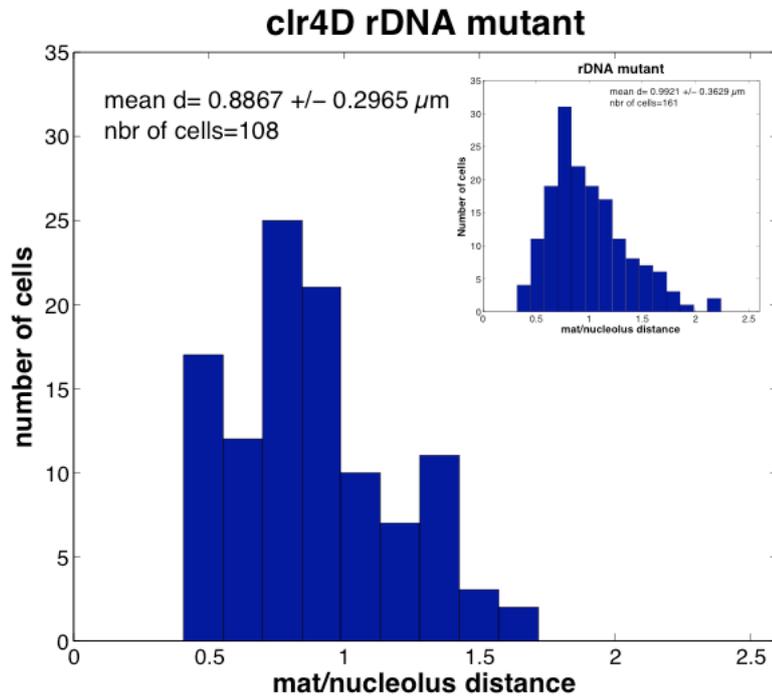
Figure 4.22: Histogram of distances between the mating-type region and the centroid of the nucleolus for the *clr4Δ* **rDNA mutant**. The insert shows the *clr4⁺* **rDNA mutant**. The cells had been grown O/N in EMM2 + 0.1μM thiamine. All cells were either in the S phase or the G2 phase of the cell cycle.

We treated both the **control strain** PM8 and the **rDNA mutant** PM2 with TSA, following the protocol described in section 4.3.4 in Material and Methods. Figure 4.23 shows fluorescence/DIC images of both strains before, during TSA treatment and after the recovery phase. Images of the control cultures are also shown. After 12 h of exposure to TSA both PM2 and PM8 cells started to loose their rod-like shape, looking more swollen. They were also more fragile, sometimes bursting during the preparation of the sample chamber. Their growth rate slowed down and after 24 h they seemed to no longer divide. The images have not yet been analysed using the Matlab program, hence we do not have the mean mating-type region to nucleolus distances. From the pictures we can still get a feeling for whether the distance remained the same or changed during the TSA treatment. In the case of the **control strain** PM8, we could not see any difference between the localisation of the mating-type region in the control culture and in the culture exposed to TSA. The mating-type region was quite far from the nucleolus, likely at the periphery of the nucleus as in Figure 4.16. The control culture of the **rDNA**

mutant PM2 did not show any relocalisation of the mating-type region. It remained near the nucleolus throughout the 72 hours of the experiment. The culture treated with TSA, on the other hand, did show an increase of the mating-type region to nucleolus distance. It started to be visible after 24 hours and was very clear after 36 hours. After 24 hours of treatment part of the TSA treated cultures was spun down, washed and resuspended in EMM2+leu+ura+ade+his+0.1μM thiamine. Figure 4.23 shows the cells after full recovery, 48 hours after the interruption of the TSA treatment (72 hours after the beginning of the experiment). For both strains, the cells ability to grow was first recovered 36 hours after the end of the TSA treatment (60 hours after the beginning of the experiment). In PM2 the localisation of the mating-type region near the nucleolus seemed to be recovered a little bit earlier than that, the first signs showing after 24 hours (48 hours after the beginning of the experiment).

As we have shown it is possible to perform localisation experiments in parallel with the TSA treatment. Saying something about the effect of TSA on the silencing of the mating-type region is more difficult. It would be very difficult to make spot tests during the localisation experiment, since cells would not start growing on the agar plates before they have nearly recovered. One way to circumvent this issue could be to harvest cells at specific time points during the experiment and measure the expression levels of *ade6*. Another solution could be to replace the *ade6* reporter gene by a gene coding for mCherry tagged with, for example, a nuclear target sequence. mCherry is a fluorescent protein, so if the mating-type region is derepressed during the TSA treatment, the nucleus of the cells would start to fluoresce.

At the moment we do not know if TSA affects the silencing of the mating-type region in the **rDNA mutant**. What we do know is that one or several proteins from the histone deacetylase family seem to affect its localisation. Learning more about a potential derepression of the mating-type region would clarify whether, in this case, silencing and localisation are two coupled mechanisms.
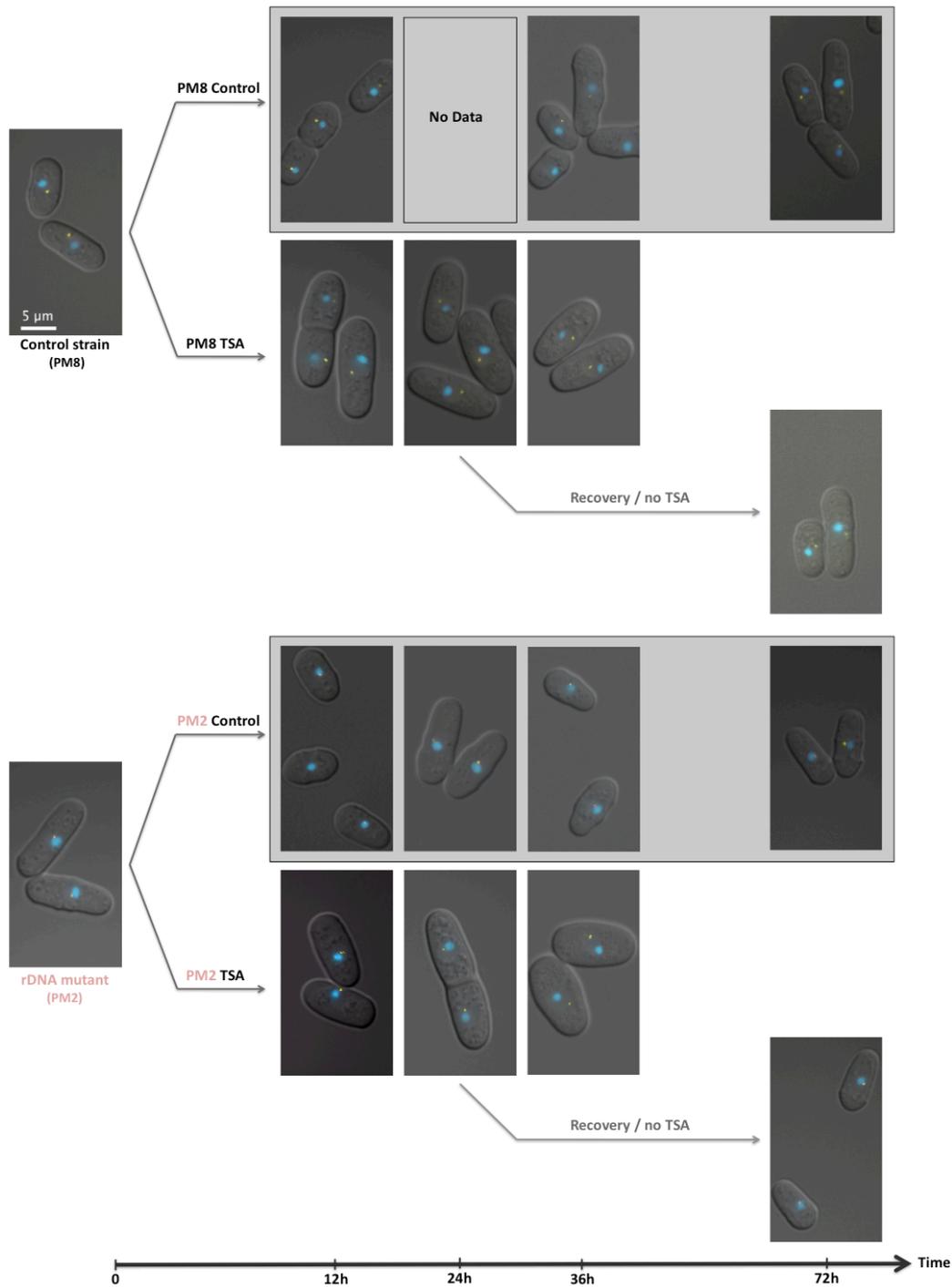
Figure 4.23: Two image series showing the **control strain** (PM8) and the **rDNA mutant** (PM2) before, during and after being treated with TSA. The non-treated controls are also shown. In PM2 a relocalisation of the mating-type region further away from the nucleolus can be seen as a result of the treatment ($t = 36$h). Time is indicated in hours, zero being the moment where TSA was added to the cell cultures. The white scale bar is the same for all images.

4.7 Small rDNA boundary

As mentioned in the Introduction, the rDNA domains are composed of repeated unit sequences of about 11 kb. Each repeat has a transcribed region (in pink in Figure 4.24), one autonomous origin of replication (ars, grey box) and three replication fork barriers of which two bind the protein Reb1 and the third binds Sap1 [70][82]. As described earlier these proteins are crucial for gene replication.

So far we have only discussed one type of rDNA mutant in which *IR-R* was replaced by a full unit sequence, but slightly shifted as can be seen in Figure 4.24. We will keep referring to it as the **rDNA mutant**. Another mutant with silencing properties was also found to have a piece of rDNA replacing *IR-R*. This rDNA insert is only about a third of the length of the larger one. It is 3.8 kb long and makes out the centre of the transcribed region. It does not contain the origin of replication or any of the binding sites for Sap1 or Reb1, see Figure 4.24. We will refer to it as the **small rDNA mutant**. We will in this section look at the differences in silencing between these two rDNA mutants. This might give us an indication on whether there are multiple silencing mechanisms involved.
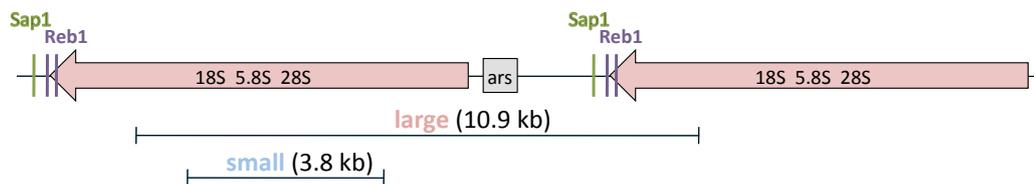
Figure 4.24: Schematic drawing of two rDNA repeats showing the transcribed region (in pink), the autonomous origin of replication (grey box), two replication fork barriers binding Reb1 (in purple) and one binding Sap1 (in green). Both the *rDNA-R* of the **rDNA mutant** (pink text) and the **small rDNA mutant** (blue text) are defined.

4.7.1 Silencing in *clr3*, *clr4*, *swi1* and *swi3* deleted mutants

We repeated the derepression experiments we had conducted with the **rDNA mutant**, using instead the **small rDNA mutant**. New strains with either a *clr3*, *clr4*, *swi1* or *swi3* deletion were constructed. Here again we assessed the result by performing spot tests on YE and AA-ade plates. In Figure 4.25 the strain names are colour coded according to which type of strain they belong to. The **wild-type strain** in grey, the **control strain** in black, the **IR-RΔ mutant** in red, the **rDNA mutant** in pink and the **small rDNA mutant** in blue. PG2897, Hu52, PC148, PG3506, PG3188 and PG3486 are
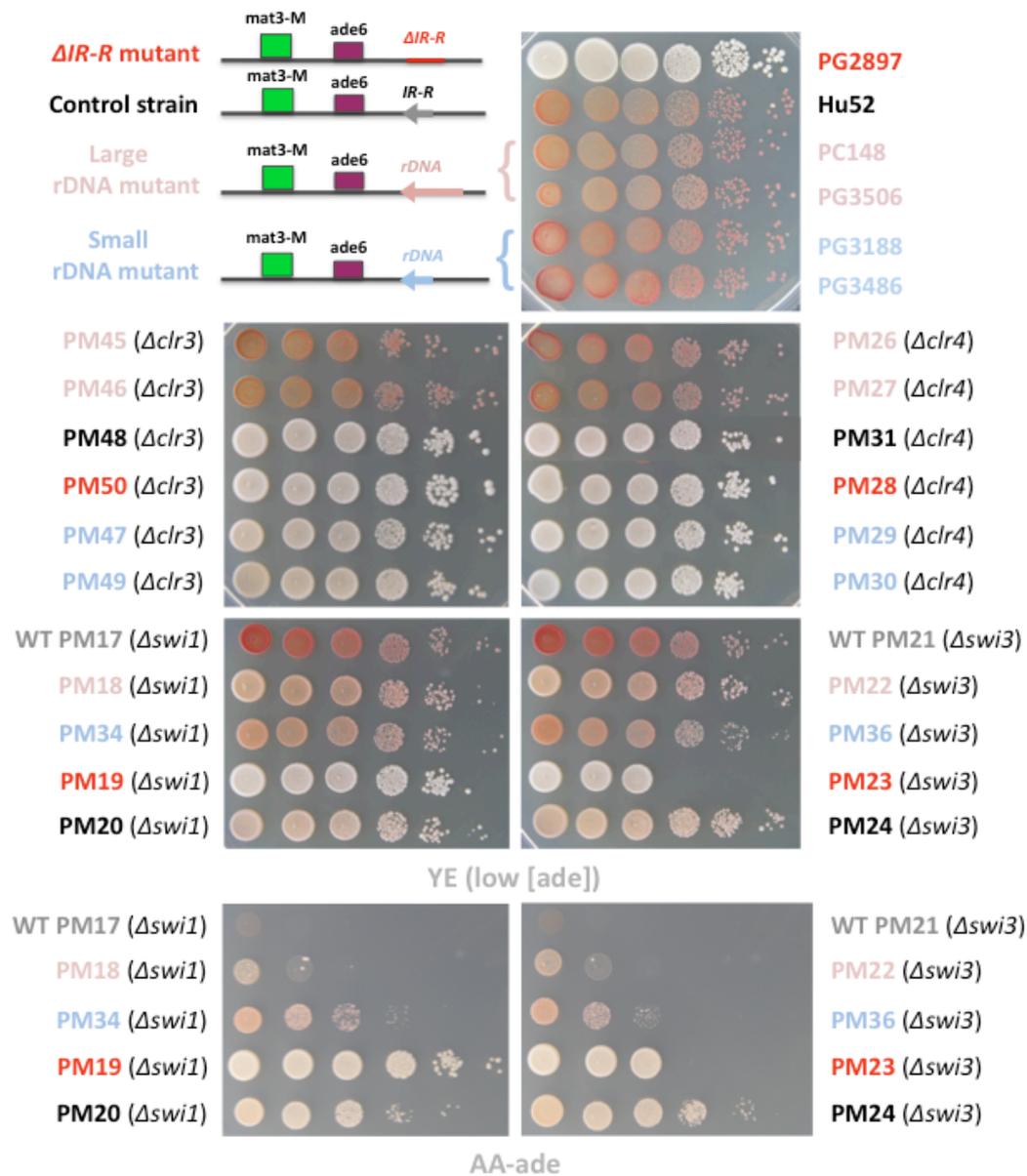
Figure 4.25: Spot tests on YE and AA-adenine of the six mother strains and the same *clr3*, *clr4*, *swi1* and *swi3* deleted strains. The two AA-adenine plates showing the *swi1Δ* and *swi3Δ* strains are there to complement the result from the YE plates just above. The strain names are colour coded in the following way : the **wild-type strain** in grey, the **control strain** in black, the ***IR-RΔ* mutant** in red, the **rDNA mutant** in pink and the **small rDNA mutant** in blue. A sketch of part of the mating-type region is also shown.

the mother strains of the *clr3*, *clr4*, *swi1* or *swi3* deleted strains and have none of these deletions. They are identical to the MAM strains but for the fluorescent markers. For further details see the strain table in appendix C. The **rDNA mutant** and the **small rDNA mutant** are represented by two strains each. One has a *LEU2* reporter gene next to the *rDNA-R* boundary (PC148, PG3188, PM26, PM29, PM45 and PM47) and the other not. This has to do with the way the strain were constructed, see section 4.3.1. We used both strains to see if *LEU2* had any influence on the silencing of the mating-type region. That does not seem to be the case.

Now to the results. All the control (mother) strains, except for the **IR-RΔ mutant**, showed a strong repression of the mating-type region made visible by their pink phenotype on YE plates. This includes both the **rDNA mutant** and the **small rDNA mutant**. Let us now look at the *clr3* and *clr4* deleted strains. The *clr3Δ* and *clr4Δ* **control strains** showed the same white phenotype as *IR-R* deleted strain, which would indicate that the mating-type region was strongly derepressed, *ade6* being expressed. This leads us to the conclusion already drawn in section 4.6.1 and found in literature, that Clr3 and Clr4 are essential for the silencing of the wild-type mating-type region. The results for the **rDNA mutant** are in accordance with data presented earlier in section 4.6.1. The absence of either Clr3 or Clr4 did not lead to any derepression of the mating-type region. The **small rDNA mutant**, on the other hand, behaved differently. The *clr4* deletion completely derepressed the mating-type region and the *clr3Δ* strain only showed a very faint pink colour indicating that the silencing was very weak.

We will now look closer at the *swi1* and *swi3* deletions. The **IR-RΔ mutant** was derepressed as expected. All the other strains had a pink phenotype on the YE plates, the **control strain** growing a bit lighter. Here the AA-adenine plates could give us some additional information. The **control strain**, despite its partial repression of the mating-type region, grew quite well on the AA-adenine plates seen in the lower part of Figure 4.25. For *swi1Δ* it grew at the three highest cell concentrations and for *swi3Δ* it grew at the four highest concentrations. Both the **rDNA mutant** and the **small rDNA mutant** showed a strongly repressed mating-type region. Still they grew at the highest, respectively second highest cell concentration. The difference in the expression level of *ade6* between the two rDNA mutants still has to be confirmed. Transcript levels could be estimated by RT-PCR. Another complementary experiment could be to grow the strains under the microscope on AA-adenine agar slabs for a period of 24 h. Intranuclear distances and growth measurements could be made simultaneously by taking fluorescence image-stacks and by counting the number of cells per colony.

To summarise, a *clr3* or *clr4* deletion affects the two mutants very differ-

ently. Any of these deletions strongly derepressed the mating-type region in the **small rDNA mutant**, whereas the **rDNA mutant** seemed unaffected, still showing the phenotype of a very strong silencing. Their response to a *swi1* and *swi3* deletion was more similar. Both still showed a very strong silencing of the mating-type region.

4.7.2 Mating-type switching

An interesting result is that the two rDNA mutants showed different phenotypes on sporulation plates, see Figure 4.26. As we reported in section 4.4 the **rDNA mutants** had a yellow phenotype, i.e. showed little spore formation. The two **small rDNA mutant**, on the other hand, behaved in the same way as the **control strain** and the **IR-RΔ mutant**, showing clear iodine staining, indicative of successful mating and spore formation. This would strongly suggest that what is inhibiting mating-type switching in the **rDNA mutant** is not present in the **small rDNA mutant**.
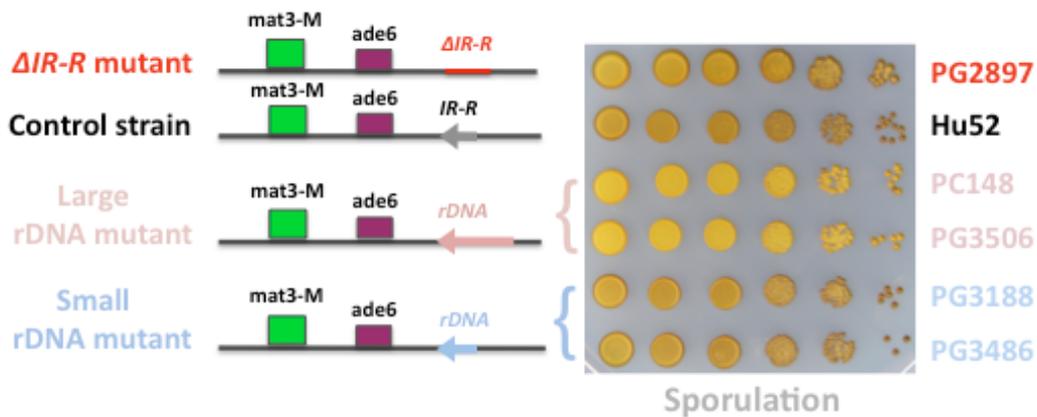
Figure 4.26: Spot test on a EMM2 +leu+ura+ade+arg+his sporulation plate after iodine staining. The **rDNA mutants** are stained yellow whereas the other strains, including the **small rDNA mutants**, show a brown colour reflecting successful mating and spore formation. This would indicate that the **rDNA mutant** has difficulties in switching mating-type.

Another piece of valuable information is that the **rDNA mutants**, PC148 and PG3506, do have the single strand break near *mat1*, necessary for mating-type switching [59], just as the **small rDNA mutants** PG3188 and PG3486, the **control strain** Hu52 and the **IR-RΔ mutant** PG2897. This can be seen on the Southern blot in Figure 4.27 made by Geneviève Thon using a standard method. Digestion was made using the restriction enzyme HindIII,

that cuts the DNA in very specific sites. The largest band corresponds to a piece of 10.4 kb including *mat1*. The third and the fourth band correspond to the same *mat1* piece cut in two due to the single strand break. It should be noted that the fourth band also includes *mat3* because of the insertion of the *ade6* reporter gene, thus making it as big as the smallest of the *mat1* pieces. The second band corresponds to a 6.3 kb piece containing *mat2*. The fact that both the **rDNA mutant** and the **small rDNA mutant** have the single strand break means that the difference between the two strains does not lie in their ability to successfully imprint *mat1*.
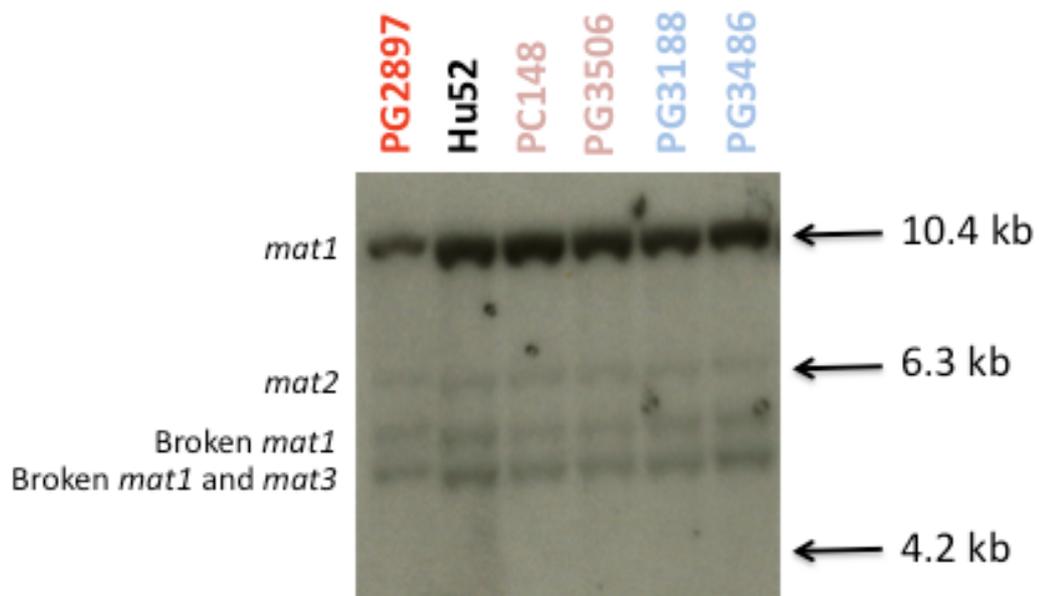
Figure 4.27: Southern blot showing the sizes of the mating-type region loci, making the centromere distal single strand break near *mat1* visible for the **control strain** Hu52, the ***IR-RΔ* mutant** PG2897, the rDNA mutants PC148 and PG3506, and the small rDNA mutants PG3188 and PG3486.

4.8 Outlook and Conclusion

4.8.1 Future directions

More localisation experiments will be conducted, both with the *clr3Δ*, *clr4Δ*, *swi1Δ* and *swi3Δ* strains discussed previously, as well as new candidates for the derepression of the mating-type region in strains with *rDNA-R* replacing *IR-R*. Such a candidate could be the class III histone deacetylase Sir2, crucial for silencing in the telomeric regions and rDNA domains [44]. Mutations affecting the rDNA, such as deletion of *reb1* or point mutations in *sap1* could also be examined. If deleting one protein proves to be insufficient to derepress the mating-type region in the **rDNA mutant**, we could consider constructing double-knockouts. Although we have leads, such as the effect of TSA on localisation indicating the importance of histone deacetylases, this still involves making many assumptions when trying to identify plausible protein candidates.

Learning more about the localisation of the mating-type region in the **small rDNA mutant** is one of our priorities at the moment. Knowing whether its mating-type region is localised at the periphery of the nucleus or near the nucleolus, as in the **rDNA mutant**, will hopefully provide us with a large piece of the puzzle. If the mating-type regions of the two strains are found in different parts of the nucleus, it is likely that localisation is at least one of the reasons for their diverging behaviour upon *clr3* and *clr4* deletion. This brings us to work currently undertaken, investigating the role of different parts of the rDNA repeat in the very strong silencing of the mating-type region observed in the **rDNA mutant**.

We could further test the coupling between relocalisation and silencing by making 24 hours localisation experiments, starting with a low concentration of cells on agar poor in adenine. The fluorescence images would tell us about the localisation of the mating-type region, whereas the number of cells per colony would give us information about its level of repression. It would be interesting as well to study the boundary properties of the *rDNA-R* more in detail. Is it a barrier that prevents heterochromatin from spreading outside of the silenced region or is gene expression also affected to the "right" of the *rDNA-R*? This could be investigated by inserting reporter genes in the euchromatic region centromere-distal to the mating-type region.

4.8.2 Conclusion

This is still an ongoing project. We have so far clearly established the effect of replacing the *IR-R* boundary of the mating-type region by a piece of rDNA. Both a strong silencing of the region as well as a relocalisation closer to nucleolus was observed for the so-called **rDNA mutant**, its *rDNA-R* boundary composed of a full rDNA repeat. At the moment we can only speculate about the underlying mechanisms. Silencing and relocalisation might be coupled. We do have some exciting leads to follow in future experiments, such as the potential role played by deacetylases in the localisation of the mating-type region in the **rDNA mutant**, as suggested by the TSA experiment. Also the comparison with the **small rDNA mutant** gave some interesting results. Both show a strong silencing of the mating-type region, but their interactions with *trans*-acting factors differ. More than just showing different phenotypes upon *clr3* and *clr4* deletion, the two mutants show different abilities to mate and form spores. Interestingly, this is not due to a failure to form the single strand break near *mat1*, which might suggest that two silencing mechanisms are involved.

CHAPTER 5

Conclusion and Outlook

In this thesis we have presented results from work conducted on two model systems commonly used in the fields of biology and biophysics; giant unilamellar vesicles and the unicellular eukaryote *Schizosaccharomyces pombe.* Both could be said to mimic a cell, but on different levels of abstraction. The study of GUVs focuses on the role played by the material properties of lipid bilayers in cellular processes such as ion transport or endo- and exocytosis. It reflects the view point that by understanding each individual component of a system one can learn something about the whole. The study of yeast or other unicellular organisms, on the other hand, reflects a more holistic approach. The system is simpler, but all components are present. We will now summarise our findings and briefly present future directions.

Electrodeformation of lipid membranes
GUVs can be deformed by short electric pulses in the presence of 80 nm gold particles. This gave rise to cylindrical deformations, either tube-like or disc-like. The directionality of the deformation, as in the presence of salt, depends on the ratio between the conductivities of the inner and outer vesicle solutions. It is likely that only the ions present in the gold solution contributed to the directionality of the deformation, but we have shown that the gold particles can and most probably do participate in the flattening of the equatorial region of the deformed vesicles.

In order to really identify the role of the gold particles in the observed deformations, it is necessary to separate them from the rest ions. This is not trivial, but the use of PEG might facilitate the washing procedure. Another future direction could be to further investigate the interaction between the nanoparticles and the lipid bilayer. A first step would be to perform a calorimetric scan of a gold particle and lipid mixture.

Optically induced deformations of lipid membranes

We have shown that optical tweezers can induce deformations in adhered GUVs without the use of any handle. Repeated exposure to the focused laser light led to a decrease in vesicle size followed by budding and eventually rupture of the membrane. The larger the vesicle and the more fluid its membrane was the longer it survived exposure to constant or stepwise increasing laser power. Moreover, we believe that the scattering force was responsible for the upward deflection of the GUVs observed at laser powers greater than 50 mW. This hypothesis is supported by the fact that our estimation of the scattering force corresponds to the energy needed to bend the lipid membrane.

To verify this hypothesis we would like to perform the same experiments on free-standing GUVs. Filling them with an actin network could be a further step in modelling the effect of optical forces on cells. Both electrical fields and optical traps can be utilised to probe the elastic properties of cells. This can be used for biotechnical applications, such as cell sorting, as well as for diagnostic purposes in medicine.

DNA localisation in *Schizosaccharomyces pombe*

The silenced part of the mating-type region in fission yeast is delimited by two so-called boundary elements, *IR-L* and *IR-R*. If the *IR-R* is replaced by a piece of *rDNA* a strong silencing of the mating-type region has been observed as well as its relocalisation closer to the nucleolus. The distance between the mating-type region and the nucleolus was measured in 3D using a custom made Matlab program. Failure so far to derepress the *ade6* reporter gene by deleting single proteins and comparison with a mutant having a smaller *rDNA-R* suggests that two silencing mechanisms are involved. One of them could be the relocalisation of the mating-type region from the nuclear periphery to another nuclear subcompartent.

Apart from repeating the localisation experiment to further test the effect of current and new protein candidates on the relative position of the mating-type region and the nucleolus, our main goal is to localise the mating-type region in the **small rDNA mutant**. This combined with time-lapse microscopy could help us understand the coupling between localisation and silencing. Looking at the expression of genes outside of the normally silenced region could give use information on the nature of the *rDNA-R* boundary.

APPENDIX A

Appendix A : Media recipes

AA drop-out:

For 1 l plates:

Soln 1:   6.7 g Yeast Nitrogen Base w/o amino acids
     (or 1.7g YNB w/o aa w/o (NH4)2SO4 and 5g (NH4)2SO4)
     2 g drop-out mix (see below)
     450 ml H_2O

Soln 2:   20 g agar
     500 ml H_2O

Autoclave both solutions in separate flasks. Add 50 ml 40% glucose to soln 1.
Add soln 2 to soln 1. Stir. Pour plates.

Drop-out mix:

2 g each: L-alanine
     L-arginine
     L-asparagine
     L-cysteine
     L-glutamine
     L-glutamic acid
     L-glycine
     L-histidine
     L-isoleucine
     L-lysine
     L-methionine
     L-phenylalanine
     L-proline
     L-serine
     L-threonine
     L-tryptophan
     L-tyrosine
     L-valine
     myo-inositol
     adenine
     uracil
0.4 g   para-amino benzoic acid
4 g   L-leucine

Combine powders, leaving out ingredients as needed. Shake or mix thoroughly.
Store in air-tight container. Of course, you can make up any amount of mix as
long as you keep the right proportions.

Reference for AA drop-out: ROSE, M., F. WINSTON and P. HIETER, 1990
Methods in Yeast Genetics: a laboratory course manual. (Cold Spring Harbor
Laboratory Press).
and Methods in Enzymology 194.

EMM2 :

Components shown as g/Liter

Base:
Potassium Hydrogen Phthalate 3.00
Sodium Phosphate Dibasic   2.20
Ammonium Chloride   5.00
Glucose   20.00

Salt Stock:
Magnesium Chloride*6H2O   1.05
Calcium Chloride*2H2O 0.0147
Potassium Chloride   1.00
Sodium Sulfate   0.04

Vitamin Stock:
Pantothenic Acid*Ca   0.001
Nicotinic Acid   0.01
Inositol   0.01
Biotin 0.00001

Mineral Stock:
Boric Acid   0.0005
Manganese Sulfate 0.0004
Zinc Sulfate*7H2O   0.0004
Ferrous Chloride   0.0002
Molybdic Acid   0.00004
Potassium Iodide   0.0001
Copper Sulfate *5H2O   0.00004
Citric Acid   0.001

MSA :

Arginine HCl	2 g
KH2PO4	1 g
NaCl	0.1 g
MgSO4-7H2O	0.2 g
CaSO4-2 H2O	0.1 g
TE	1 ml
BIO	1 ml
VIT	2 ml

Autoclave in 0.45 l H_2O

glucose   10 g
Autoclave in 50 ml H_2O

agar   25 g
Autoclave in 0.5 l H_2O

Mix everything after autoclaving and pour plates.

VIT, BIO and TE for MSA

VITamins
Calcium pantothenate	100 mg
Nicotinic acid	1 g
Meso-Inositol	1 g
nanoH_2O	100 ml

Heat in steam-pot <u>without</u> pressure, store in fridge

BIOtin
Biotin	1 mg
nanoH_2O	50 ml
EtOH 96%	50 ml

No further sterilization, do not flame. Store in fridge.

TE (Trace Elements)
H_3BO_3	100 mg
$CuSO_4$ - $5H_2O$	10 mg
KJ	20 mg
$FeCl_3$ - 6 H_2O	40 mg

$MnSO_4 - 4H_2O$	100 mg
MoO_3	30 mg
$ZnSO_4 - 7H_2O$	80 mg
$nanoH_2O$	200 ml

Heat in steam-pot <u>without</u> pressure, store in fridge.

FOA plates:

 1 g FOA (800 mg-1 g)
 50 mg uracil
 2 g AA-uracil
1.7 g Yeast Nitrogen Base (w/o amino acids w/o ammonium sulfate)
5 g ammonium sulfate
50 ml 40% glucose
450 ml H_2O

Stir until disolved. Filter sterilize.

Mix with 500 ml molten sterile 4% agar. Pour.

APPENDIX B

Appendix B : Protocols

B.1 Transformation of *S. pombe* using Lithium acetate

1. Grow 100 ml culture in YEL to a density of $0.5 - 1 \cdot 107$ cells/ml. This can be done by inoculating an O/N culture with few cells, or by diluting a saturated O/N and letting it grow ≈3-5 hours.

2. Harvest cells by centrifugation at 3000 rpm (rounds per minute) for 5 min and wash cells once in 40 ml of water and once in 5-10 ml 0.1 M Lithium acetate adjusted to pH 4.9 with acetic acid.

3. Resuspend the cells at $1 \cdot 109$ cells/ml in 0.1 M Lithium acetate pH 4.9 and dispense 100 μl aliquots into Eppendorf tubes. Incubate at 30 °C or room temperature (RT) for 30 min. $(0 - 120 \min$ incubation times can be used, but long incubations in Lithium acetate tend to stress the cells without improving the efficiency of tranformation.)

4. Add $1 - 2 \mu$g DNA. Incubate at 30 °C or RT for 30 min (This step is optional; it might improve the efficiency of transformation). Add 290 μl of 40% PEG 4000 in Lithium acetate pH 4.9. The PEG solution can be prewarmed at 30 °C if the transformation is done at that temperature, but RT works also very well. Incubate at 30 °C or RT for 30 min.

5. Heat shock at 42 °C for 15 min.

6. Pellet cells by centrifugation 3 min at 3000 rpm.

7. Remove supernatant. Resuspend in $50 - 100\,\mu$l water and plate on selective plates. (Use several plates and plate a dilution if many transformants are expected.) When selecting for an antibiotic resistance (G418, hygromycin, FOA...). plate on non-selective plates such as YES, incubate O/N at 33C, and replicate onto selective plates next day.

Remember to process a no-DNA control in parallel with the transformations. An alternative to growing a liquid culture is to pick a few freshly-growing yeast colonies from a plate.
PEG = polyethylene glycol

APPENDIX C

Appendix C : Yeast strains

strain	parents	mat1	mat2	mat3	clr ; swi	leu1	ura4	ade6	his	others
MAM26		h90		mat3-M (EcoRV)::ade6 ori1 D(XbaI-XmnI) (SpeI)::rDNA		leu1+CO3-CFP	ura4-D18	ade6-210	his7+::lacI-GFP	his2[::kanR-ura4+-lacOp]
MAM36		h90		mat3-M (EcoRV)::ade6 ori1 D(XbaI-XmnI) (SpeI)::rDNA		leu1+CO3-CFP	ura4-D18	ade6-210 or 216	his7+::lacI-GFP	his2[::kanR-ura4+-lacOp]
MAM46		h90		mat3-M (EcoRV)::ade6 ori1 D(XbaI-XmnI) (SpeI)::ura4 ori2		leu1+CO3-CFP	ura4-D18	ade6-DN/N or 210 or 216	his7+::lacI-GFP	his2[::kanR-ura4+-lacOp]
MAM56		h90		mat3-M(EcoRV)::ade6		leu1+CO3-CFP	ura4-D18	ade6-DN/N or 210 or 216	his7+::lacI-GFP	his2[::kanR-ura4+-lacOp]
PM2	MAM36 + pcr2.1-hph1/AscI+SacI	h90		mat3-M (EcoRV)::ade6 ori1 D(XbaI-XmnI) (SpeI)::rDNA		leu1+CO3-CFP	ura4-D18	ade6-DN/N or 210 or 216	his7+::lacI-GFP	his2[::hph1-ura4+-lacOp]
PM3	MAM46 + pcr2.1-hph1/AscI+SacI	h90		mat3-M (EcoRV)::ade6 ori1 D(XbaI-XmnI) (SpeI)::ura4 ori2		leu1+CO3-CFP	ura4-D18	ade6-DN/N or 210 or 216	his7+::lacI-GFP	his2[::hph1-ura4+-lacOp]
PM7	MAM26 + pcr2.1-hph1/AscI+SacI	h90				leu1+CO3-CFP	ura4-D18	ade6-210	his7+::lacI-GFP	his2[::hph1-ura4+-lacOp]
PM8	MAM56 + pcr2.1-hph1/AscI+SacI	h90		mat3-M(EcoRV)::ade6		leu1+CO3-CFP	ura4-D18	ade6-DN/N or 210 or 216	his7+::lacI-GFP	his2[::hph1-ura4+-lacOp]
PM11	Y211 PM8	h-		mat3-M(EcoRV)::ade6	swi1Δ::kanR	leu1-32	ura4-D18	ade6-DN/N		
PM12	Y668 PM3	h-		mat3-M(EcoRV)::ade6	swi3Δ::kanR	leu1-32	ura4-D18	ade6-DN/N		
PM13	PM7 PG3639	h90		mat3-M (EcoRV)::ade6 ori1 D(XbaI-XmnI) (SpeI)::rDNA	clr4Δ::kanR	leu1+CO3-CFP	ura4-D18 or DS/E	ade6-210	his7+::lacI-GFP	his2[::hph1-ura4+-lacOp]
PM14	PM2 PG3639	h90		mat3-M (EcoRV)::ade6 ori1 D(XbaI-XmnI) (SpeI)::ura4 ori2	clr4Δ::kanR	leu1+CO3-CFP	ura4-D18 or DS/E	ade6-210 or 216	his7+::lacI-GFP	his2[::hph1-ura4+-lacOp]
PM15	PM3 PG3639	h90		mat3-M (EcoRV)::ade6 ori1 D(XbaI-XmnI) (SpeI)::ura4 ori2	clr4Δ::kanR	leu1+CO3-CFP	ura4-D18 or DS/E	ade6-DN/N or 210 or 216	his7+::lacI-GFP	his2[::hph1-ura4+-lacOp]
PM16	PM8 PG3639	h90		mat3-M(EcoRV)::ade6	clr4Δ::kanR	leu1+CO3-CFP	ura4-D18 or DS/E	ade6-DN/N or 210 or 216	his7+::lacI-GFP	his2[::hph1-ura4+-lacOp]
PM17	PM7 PM11	h90		mat3-M (EcoRV)::ade6 ori1 D(XbaI-XmnI) (SpeI)::rDNA	swi1Δ::kanR	leu1+CO3-CFP	ura4-D18	ade6-DN/N	his7+::lacI-GFP	his2[::hph1-ura4+-lacOp]
PM18	PM2 PM11	h90		mat3-M (EcoRV)::ade6 ori1 D(XbaI-XmnI) (SpeI)::rDNA	swi1Δ::kanR	leu1+CO3-CFP	ura4-D18	ade6-DN/N	his7+::lacI-GFP	his2[::hph1-ura4+-lacOp]
PM19	PM3 PM11	h90		mat3-M (EcoRV)::ade6 ori1 D(XbaI-XmnI) (SpeI)::ura4 ori2	swi1Δ::kanR	leu1+CO3-CFP	ura4-D18	ade6-DN/N	his7+::lacI-GFP	his2[::hph1-ura4+-lacOp]
PM20	PM8 PM11	h90		mat3-M(EcoRV)::ade6	swi1Δ::kanR	leu1+CO3-CFP	ura4-D18	ade6-DN/N	his7+::lacI-GFP	his2[::hph1-ura4+-lacOp]
PM21	PM7 PM12	h90		mat3-M (EcoRV)::ade6 ori1 D(XbaI-XmnI) (SpeI)::rDNA	swi3Δ::kanR	leu1+CO3-CFP	ura4-D18	ade6-DN/N	his7+::lacI-GFP	his2[::hph1-ura4+-lacOp]
PM22	PM2 PM12	h90		mat3-M (EcoRV)::ade6 ori1 D(XbaI-XmnI) (SpeI)::rDNA	swi3Δ::kanR	leu1+CO3-CFP	ura4-D18	ade6-210 or 216	his7+::lacI-GFP	his2[::hph1-ura4+-lacOp]
PM23	PM3 PM12	h90		mat3-M (EcoRV)::ade6 ori1 D(XbaI-XmnI) (SpeI)::ura4 ori2	swi3Δ::kanR	leu1+CO3-CFP	ura4-D18	ade6-DN/N	his7+::lacI-GFP	his2[::hph1-ura4+-lacOp]
PM24	PM8 PM12	h90		mat3-M(EcoRV)::ade6	swi3Δ::kanR	leu1+CO3-CFP	ura4-D18	ade6-DN/N	his7+::lacI-GFP	his2[::hph1-ura4+-lacOp]
PM26	PG3639 PC148	h90		mat3-M (EcoRV)::ade6 ori1 D(XbaI-XmnI) (SpeI)::rDNA (BlpI)::LEU2	clr4Δ::kanR	leu1+CO3-CFP	ura4-D18	ade6-DN/N		
PM27	PG3639 PG3506	h90		mat3-M (EcoRV)::ade6 ori1 D(XbaI-XmnI) (SpeI)::rDNA	clr4Δ::kanR	leu1+CO3-CFP	ura4-D18	ade6-DN/N		
PM28	PG3639 PG2897	h90								
PM29	PG3639 PG3188	h90		mat3-M (EcoRV)::ade6 ori1 D(XbaI-XmnI) (SpeI)::rDNA (small) (BlpI)::LEU2	clr4Δ::kanR	leu1-32	ura4-D18	ade6-DN/N		
PM30	PG3639 PG3486	h90		mat3-M (EcoRV)::ade6 ori1 D(XbaI-XmnI) (SpeI)::rDNA (small)	clr4Δ::kanR	leu1-32	ura4-D18	ade6-DN/N		
PM31	PG3639 Hu52	h90		mat3-M(EcoRV)::ade6 ori1	clr4Δ::kanR	leu1-32	ura4-D18	ade6-DN/N		
PM34	PG3486 PM11	h90		mat3-M (EcoRV)::ade6 ori1 D(XbaI-XmnI) (SpeI)::rDNA (small)	swi1Δ::kanR	leu1-32	ura4-D18	ade6-DN/N		
PM36	PG3486 PM12	h90		mat3-M (EcoRV)::ade6 ori1 D(XbaI-XmnI) (SpeI)::rDNA (small)	swi3Δ::kanR	leu1-32	ura4-D18	ade6-DN/N		
PM40	PG3439 Hu52	h-		mat3-M(EcoRV)::ade6 ori1	clr3Δ::kanR	leu1-32	ura4-D18	ade6-DN/N		
PM45	PC148 PM40	h90		mat3-M (EcoRV)::ade6 ori1 D(XbaI-XmnI) (SpeI)::rDNA (BlpI)::LEU2	clr3Δ::kanR	leu1-32	ura4-D18	ade6-DN/N		
PM46	PG3506 PM40	h90		mat3-M (EcoRV)::ade6 ori1 D(XbaI-XmnI) (SpeI)::rDNA	clr3Δ::kanR	leu1-32	ura4-D18	ade6-DN/N		
PM47	PG3188 PM40	h90		mat3-M (EcoRV)::ade6 ori1 D(XbaI-XmnI) (SpeI)::rDNA (small) (BlpI)::LEU2	clr3Δ::kanR	leu1-32	ura4-D18	ade6-DN/N		
PM48	Hu52 PM40	h90		mat3-M(EcoRV)::ade6 ori1	clr3Δ::kanR	leu1-32	ura4-D18	ade6-DN/N		
PM49	PG3486 PM40	h90			clr3Δ::kanR	leu1-32	ura4-D18	ade6-DN/N		
PM50	PG2897 PM40	h90		mat3-M(EcoRV)::ade6 ori1	clr3Δ::kanR	leu1-32	ura4-D18	ade6-DN/N		
Hu52		h90		mat3-M(EcoRV)::ade6 ori1		leu1-32	ura4-D18	ade6-DN/N		
PC148		h90		mat3-M (EcoRV)::ade6 ori1 D(XbaI-XmnI) (SpeI)::rDNA (BlpI)::LEU2		leu1-32	ura4-D18	ade6-DN/N		
PG2897		h90		mat3-M (EcoRV)::ade6 ori1 D(XbaI-XmnI) (SpeI)::ura4 ori2		leu1-32	ura4-D18	ade6-DN/N		
PG3188	PG2897/XbaI library, X16	h90		mat3-M (EcoRV)::ade6 ori1 D(XbaI-XmnI) (SpeI)::gDNA (BlpI)::LEU2		leu1-32	ura4-D18	ade6-DN/N		
PG3439	SPK19 PG1636	h-	mat1-P17::LEU2		clr3Δ::kanR	leu1-32	ura4-D18	ade6-DN/N		
PG3486	PG2897/pGT393 insert, #15 (rDNA)	h90		mat3-M (EcoRV)::ade6 ori1 D(XbaI-XmnI) (SpeI)::gDNA		leu1-32	ura4-D18	ade6-DN/N		
PG3506		h90		mat3-M (EcoRV)::ade6 ori1 D(XbaI-XmnI) (SpeI)::rDNA	clr4Δ::kanR	leu1-32	ura4-D18	ade6-DN/N		
PG3639										
Y211	Nogushi Genetics 175:553-566, 2006	h-			swi1Δ::kanR	leu1-32	ura4-D18	ade6-210 or 216	his7+::lacI-GFP	
Y668	Nogushi Genetics 175:553-566, 2006	h-			swi3Δ::kanR	leu1-32	ura4-D18			
PG2747	SP837/D817 (Hiraoka)						ura4-D18	ade6-216	his7+::LEU2	

APPENDIX D

Appendix D : Article

Vesicles in electric fields: Some novel aspects of membrane behavior†

Rumiana Dimova,*[a] Natalya Bezlyepkina,[a] Marie Domange Jordö,[b] Roland L. Knorr,[a] Karin A. Riske,[c] Margarita Staykova,[a] Petia M. Vlahovska,[d] Tetsuya Yamamoto,[a] Peng Yang‡[a] and Reinhard Lipowsky[a]

This review focuses on the effects of electric fields on giant unilamellar vesicles, a cell-size membrane system. We describe various types of behavior of vesicles subjected to either alternating fields or strong direct current pulses, such as electrodeformation, -poration and -fusion. The vesicle response to alternating fields in various medium conditions is introduced and the underlying physical mechanisms are highlighted, supported by theoretical modeling. New aspects of the response of vesicles with charged or neutral membranes, in fluid or gel-phase, and embedded in different solutions, to strong direct current pulses are described including novel applications of vesicle electrofusion for nanoparticle synthesis.

1. Introduction

The response of biological membranes and cells to electric fields has received a lot of attention, both because of fundamental interest and because of potential practical applications. External electric fields, whether weak alternating (AC) fields or strong direct current (DC) pulses, have emerged as a powerful method for cell manipulation in biomedical and biotechnological applications. For example, electric fields are employed in novel *in-vivo* and *in-situ* applications for tissue ablation, wound healing and cancer treatment.[1–6] Strong electric fields can cause a significant increase in the electric conductivity and permeability of the cell plasma membrane. This phenomenon, also referred to as electroporation or electropermeabilization, is used for introducing various molecules into the cell, to which the membrane is otherwise impermeable.[7,8] Because of its efficiency, this method is rapidly becoming an established approach for treatment of carcinoma, melanoma and connective tissue cancer,[9–12] and it also holds great promise for gene therapy.[13,14] Membrane electroporation and electrofusion are of particular interest because these methods are widely used in cell biology and biotechnology as means for cell hybridization.[15]

Synthetic lipid vesicles provide biomembrane models suitable for systematic investigations of the impact of electric fields on lipid bilayers. Studies on small vesicles with a size about 100 nm[16–18] and on giant unilamellar vesicles with a diameter of several tens of microns,[19–31] have been performed to elucidate the

[a] Max Planck Institute of Colloids and Interfaces, Science Park Golm, 14424 Potsdam, Germany. E-mail: Rumiana.Dimova@mpikg.mpg.de; Fax: +49 331 567 9615; Tel: +49 331 567 9612
[b] Niels Bohr Institute, University of Copenhagen, Blegdamsvej 17, 2100 Copenhagen, Denmark
[c] Depto. de Biofísica, Universidade Federal de São Paulo, R. Botucatu, 862, CEP 04023-062 São Paulo, Brazil
[d] Thayer School of Engineering, Dartmouth College, Hanover, NH, 03755, USA

response of the membrane to electric fields; for a partial overview see Dimova *et al.*[32] Membrane behavior in electric fields is a topic of active research. Here, we will focus mainly on new developments by our group. Even though we will attempt to cite all important contributions in the field, the selection is subjective and far from being exhaustive.

The paper is organized as follows; first we introduce some basic timescales that govern the interaction of electric fields with membranes. Then we consider the response of vesicles to AC fields and DC pulses, discussing some new observations (both reported and not yet published). We conclude with a short outlook.

2. Membranes in electric fields: some relations

The response of membranes to electric fields involves dynamic physical processes occurring on different time scales. Free charges accumulate on boundaries separating media with different electric properties. A spherical vesicle polarizes on the Maxwell–Wagner time scale[33]

$$t_{\mathrm{MW}} = \frac{\varepsilon_{\mathrm{in}} + 2\varepsilon_{\mathrm{ex}}}{\lambda_{\mathrm{in}} + 2\lambda_{\mathrm{ex}}} \quad (1)$$

where $\varepsilon_{\mathrm{in}}$ and $\varepsilon_{\mathrm{ex}}$ are the dielectric constants, and λ_{in} and λ_{ex} are the conductivities of the solutions inside and outside the vesicle, respectively.

The lipid bilayer is impermeable to ions and free charges pile up on both membrane surfaces. Hence, the vesicle acts as a capacitor, which charges on a time scale[34,35]

$$t_{\mathrm{c}} = RC_{\mathrm{m}} \left(\frac{1}{\lambda_{\mathrm{in}}} + \frac{1}{2\lambda_{\mathrm{ex}}} \right) \quad (2)$$

where R is the vesicle radius and C_{m} is the membrane capacitance.

The capacitor charging time t_{c} is typically much longer than the Maxwell–Wagner time t_{MW}. For example, we can estimate $t_{\mathrm{c}} \sim 10$ μs and $t_{\mathrm{MW}} \sim 0.01$ μs for conditions corresponding to experiments on vesicles in 1 mM NaCl, namely $\varepsilon_{\mathrm{in}} \sim \varepsilon_{\mathrm{ex}} = 80\varepsilon_0$,

where ε_0 is the vacuum permittivity, $\lambda_{in} \sim \lambda_{ex} \sim 10$ mS/m, $C_m \sim 0.01$ F/m^2, and $R \sim 10$ μm.

These time scales are a key to understanding the dynamic response of vesicles subjected to short electric pulses discussed in section 4, as well as frequency dependence of vesicle deformation discussed in section 3. Note that characteristic angular frequencies are defined as the inverse of the time scales in eqn (1) and (2), *e.g.* $\omega_{MW} = 1/t_{MW}$. The experimental frequency, ν, is related to the angular one *via* $\nu = \omega/2\pi$.

3. Vesicle response to AC fields

When subject to AC fields, cells and vesicles can deform. Studies of cell deformation in AC fields have been carried out by many groups and effects on the cell shape, motility and orientation have been reported.[26,36–38] Vesicle deformations have been treated both experimentally and theoretically, but a comprehensive description reconciling observations and calculations is still to emerge.

A detailed understanding of the membrane behavior in AC fields is important for various electromanipulation techniques, as well as for vesicle electroformation protocols[39,40] (including some of the recent developments[41–45]). Even though vesicle electroformation is widely used, the underlying mechanism is not well understood.[46,47] This motivates further studies on effects of AC fields on membranes. Most of the current research in this direction as well as the following sections 3.1 and 3.2 has focused on lipid bilayers with only a few components, whereas biological membranes contain a large number of different components. Bridging the gap would require the exploration of more complex systems.

3.1 Vesicle deformation in AC fields

The deformation of vesicles subjected to AC fields depends on the field frequency ω (or ν) and the conductivity conditions. The latter can be described by the ratio between the internal and the external conductivities λ_{in} and λ_{ex}:

$$x = \lambda_{in}/\lambda_{ex} \qquad (3)$$

Systematically varying the field frequency and solution conductivities allowed us to construct a morphological diagram of the shape transitions observed in phosphatidylcholine vesicles;[48] see Fig. 1a. At high frequencies, the vesicles are spherical independently of x. As the frequency decreases, vesicles with $x > 1$, *i.e.*, with the internal salinity higher than the external one become prolate ellipsoids corresponding to transition 1 in Fig. 1a, while vesicles with $x < 1$ adopt oblate shapes after undergoing transition 2. Further decrease in frequency changes the vesicle shape at transition 4 from oblate to prolate for $x < 1$. For intermediate frequencies an oblate vesicle can become prolate at transition 3.

Theoretical studies of vesicle deformation in AC fields have been limited to rather simple systems. For example, these studies omit the asymmetry in the media conductivities,[24,25,27] and their theoretical predictions are at odds with experiments; see *e.g.* the supplementary material of Aranda *et al.*[48] Our recent progress
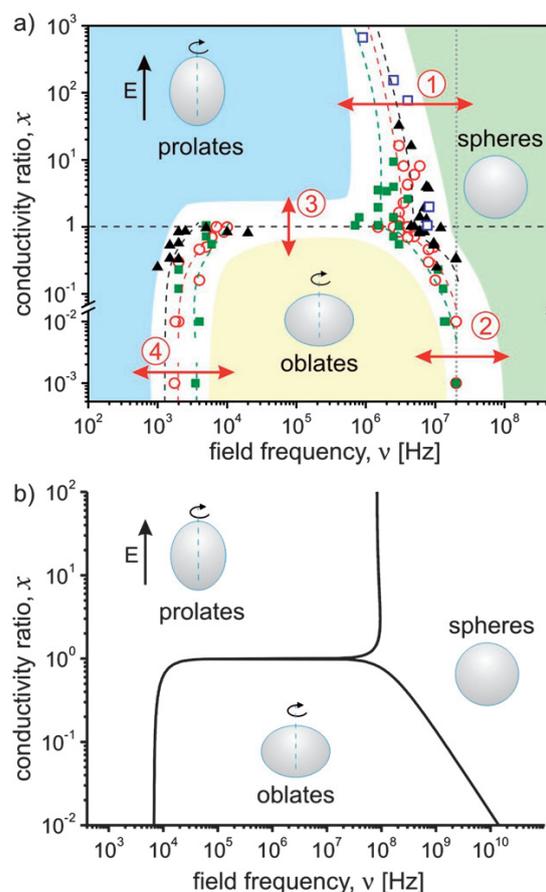
Fig. 1 Morphological diagram of the shapes of vesicles at different conductivity conditions and various field frequencies (a) as determined experimentally, and (b) theoretically predicted for $\lambda_{in} = 6.5$ mS/m. The symbols in (a) correspond to different internal conductivity, λ_{in}, in units mS/m: 1.5 (solid squares), 6.5 (open circles), 13 (solid triangles), 1000 (open squares). The dashed lines are guides to the eye and the shaded areas indicate zones of specific morphology. The four types of morphological transitions are discussed in the text. The dotted vertical line in (a) shows the experimentally accessible frequency limit ($\nu = 2 \times 10^7$ Hz). Schematic views of the vesicle shapes are included as insets and the electric field is indicated by an arrow.

towards realistic theoretical modeling is discussed in the next two sections.

3.1.1 Morphological diagram: energy minimization approach.
Vesicle shapes in AC fields can be investigated within the framework of the energy minimization approach introduced by Winterhalter and Helfrich.[24] The original work, however, is limited to symmetric conductivity conditions with $x = 1$ and thus the model predicts only prolate shapes independent of x. We extended the Winterhalter–Helfrich model to asymmetric conductivity conditions with $x \neq 1$.

The electric field deforms a vesicle from a sphere with radius R into an ellipsoid. The vesicle deformation s_2 is assumed to be small with $s_2 \ll R$; see also Fig. 2a for definition of s_2. Prolate and
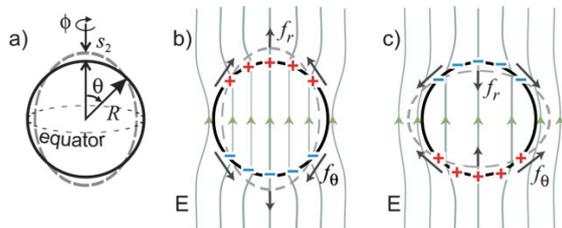
Fig. 2 (a) The vesicle geometry and (b, c) the net charge distribution Q at the vesicle interfaces at intermediate frequencies. Due to the difference in the conductivity conditions, the net charges across the membrane, illustrated with pluses and minuses, differ depending on the value of the conductivity ratio x. The forces (f_r and f_θ) applied to the charges by the normal and the tangential electric fields deform the vesicles into prolates for $x > 1$ (b) and oblates for $x < 1$ (c).

oblate shapes correspond to $s_2 > 0$ and $s_2 < 0$, respectively. The free energy of a vesicle in AC electric fields can be presented as $F = F_{bend} - W$, where F_{bend} is the bending energy of the vesicle in the elliptic deformation, and W is the work done by the Maxwell stresses arising from the electric fields. The deformation s_2 can be determined by minimizing the free energy F or by balancing stresses exerted on the membrane as in section 3.1.2. Fig. 1b shows the morphological diagram predicted by the model just described. The shapes of the boundaries and the transition frequencies agree well with the experimentally determined morphological diagram as shown in Fig. 1a.

The physical mechanism responsible for the vesicle electrodeformation is the interplay between the electric field partitioning in normal and tangential components, and the charging of the membrane interfaces. The lipid bilayer is an insulator, and acts as a capacitor. At low frequencies, $\omega \ll 1/t_c$, the large membrane impedance blocks current from flowing into the vesicle interior and the electric field lines are tangent to the membrane. The vesicle is squeezed at the equator and pulled at the poles by the radial Maxwell stress or pressure arising from the tangential electric field. As a result, the vesicle adopts a prolate shape.

At intermediate frequencies, $1/t_c < \omega < \omega_{MW}$, the membrane is capacitively short-circuited and displacement currents flow through it. The electric field lines penetrate the vesicle interior and the electric field acquires a component normal to the membrane. Because of $x \neq 1$, i.e., of the asymmetry of the internal and external conductivities, the charge densities on the inner and outer membrane interfaces become imbalanced. Within the continuum theory, these charges arise from the discontinuity of the permittivities across the interfaces and represent local accumulation of cations and anions at these interfaces. The resulting net free charge density Q is given by

$$Q(t) = 3E_0\cos\theta \frac{\lambda_{ex}\lambda_{in}}{2\lambda_{ex} + \lambda_{in}} \left(\frac{\varepsilon_{ex}}{\lambda_{ex}} - \frac{\varepsilon_{in}}{\lambda_{in}} \right) \frac{\cos(\omega t + \phi)}{\sqrt{1 + \omega^2/\omega_{MW}^2}} \quad (4)$$

where E_0 is the magnitude of the external electric field, and θ and ϕ are the polar and azimuthal angles, respectively; see Fig. 2a. A schematic snapshot of Q is sketched in Fig. 2b and 2c. If $\varepsilon_{ex} \sim \varepsilon_{in}$, the sign of Q is determined solely by the conductivity ratio. The interaction of the tangential and normal electric fields with the free charges produces lateral and normal forces, f_θ and f_r,

respectively. Depending on the polarity of Q, f_θ is directed either towards the poles or the equator, and f_r is directed towards or away from the electrodes, leading to prolate or oblate vesicle shapes as sketched in Fig. 2b, c.[49]

In the high frequency regime, $\omega > \omega_{MW}$, the electric charges cannot follow the oscillations of the electric fields. As a result, the net charge density, Q, as defined in eqn (4), decreases with the field frequency. This relaxes the shape of the vesicle from prolate ($x > 1$) or oblate ($x < 1$) to spherical (transitions 1 and 2 in Fig. 1).

In summary, the charging dynamics of the membrane surfaces and the radial and shear Maxwell stresses play a key role in determining the vesicle morphology in AC fields. The frequency of transition 4 in Fig. 1a corresponds to the inverse charging time of the membrane capacitor, $1/t_c$, and frequency transitions 1 and 2—to the Maxwell–Wagner frequency ω_{MW}.

Quantitatively, the present theory provides reasonable values of the relative vesicle deformation s_2/R (~ 0.1) for small vesicles with size of the linear order of 1 μm. For giant vesicles ($R \sim 10$–100 μm), the theory gives unreasonably large values for s_2/R ($\sim 10^3$–10^6!). However, the shapes of the boundaries in the morphological diagram and the order of the transition frequencies agree with the experiment very well; see Fig. 1. The work W done by the Maxwell stresses is small at the vicinity of the transition frequencies and for small vesicles. Therefore, the present theory shows quantitative agreements with the experiments when W is small. It is necessary to take into account tension and hydrodynamic forces in order to achieve quantitative agreement with the experiments as discussed in the following section.

3.1.2 Vesicle deformation: force balance approach. Another method to determine the vesicle deformation in electric fields is based on the balance of all forces exerted on the membrane[49]

$$\mathbf{n} \bullet (\mathbf{T}^{ex} - \mathbf{T}^{in}) = \left[2\sigma H - \frac{\delta F_{bend}}{\delta r} \right] \mathbf{n} + \nabla_s \sigma \quad (5)$$

Here $\mathbf{n}$ a is normal vector to the vesicle membrane, $\mathbf{T}^{ex}$ and $\mathbf{T}^{in}$ denote the exterior and interior Maxwell stress, H is the mean curvature, r is the radial coordinate, and σ is the membrane tension.

An essential feature of this approach is the consideration of a variable membrane tension. First, flattening of the shape fluctuations due to vesicle elongation increases the homogeneous part of the tension. Second, because the membrane is nearly incompressible, the tension can become nonuniform along the surface. The resulting gradients in the tension, $\nabla_s \sigma$, are particularly important in the intermediate frequency regime, $1/t_c < \omega < \omega_{MW}$, in which the shear Maxwell stresses are significant and oblate shapes are observed.

For small deviations from sphericity, eqn (5) yields

$$s_2 = R \frac{3p^{el} - 2\tau^{el}}{12(6 + \sigma_h)} \quad (6)$$

where σ_h is the homogeneous tension (which is independent of position along the vesicle surface) and p^{el} and τ^{el} are the maximal values of the difference of the radial and shear Maxwell stresses across the membrane (the expressions for p^{el} and τ^{el} can be found

in Vlahovska *et al.*[49]). For a quasi-spherical vesicle, the homogeneous tension σ_h increases with the apparent area as[50,51]

$$\sigma_h = \sigma_0 \exp\left(\frac{16\pi}{5} \frac{\kappa}{k_B T} s_2^2\right) \quad (7)$$

where σ_0 is the initial membrane tension, κ is the membrane bending stiffness and $k_B T$ is thermal energy. Eqn (6) is a generalization of the Kummrow–Helfrich result[28] (see eqn (10) in section 3.1.3), which is strictly valid only for low frequencies ($\omega < 1/t_c$), where the shear Maxwell stress is zero. If $x < 1$, the numerator in eqn (6) changes sign at $\omega = 1/t_c$, which marks the prolate–oblate transition (transition 4 in Fig. 1a).

Vesicle shapes computed from eqn (6) are consistent with the experiment, see Fig. 3 (note that the vesicle semiaxis is simply $a = R + s_2$). The discrepancy in the high-frequency oblate–sphere transition frequency for $x < 1$ is presumably due to electric double layer effects.[49] The mechanical approach also explains why the energy approach (section 3.1.1) overestimates the vesicle deformation in strong fields. The reason is that the free energy balance does not take into account the tension. In strong electric fields, the membrane tension controls the extent of vesicle deformation.

3.1.3 Electrodeformation of vesicles as a method to determine the membrane bending stiffness. Vesicle deformation induced by AC fields can be used to measure the bending stiffness of membranes following the approach developed by Helfrich and coworkers.[28,30] The protocol of such measurements consists of subjecting a vesicle to an AC electric field of increasing strength and recording the induced deformation. One example of vesicle elongation due to stepwise increase in the field strength is shown in Fig. 4a. The degree of deformation is expressed as the aspect ratio a/b, where a and b are the vesicle semiaxes along and perpendicular to the field direction, respectively; see inset in Fig. 4a. Observations of the response time of different vesicles suggest that typically 2 s are sufficient to reach the equilibrium deformation after changing the field strength. Images recorded in
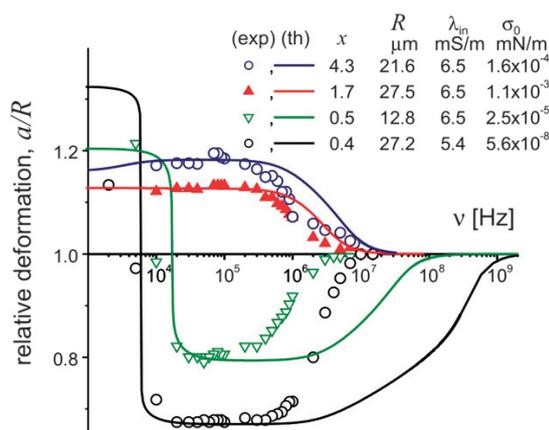
Fig. 3 Comparison between experimental data, symbols (exp), from Aranda *et al.*[48] and theory, solid curves (th), as introduced by eqn (6), for vesicle shapes in AC fields at conditions given in the legend. The initial tension σ_0 is an adjustable parameter for the theoretical curves.
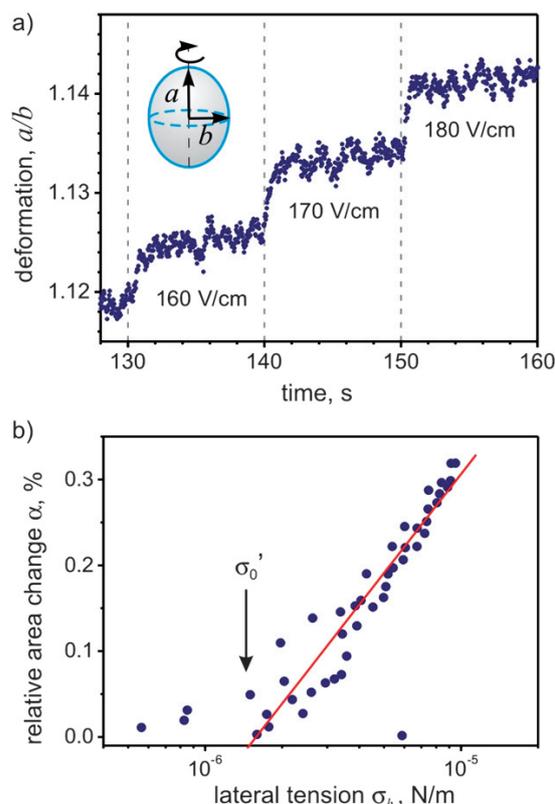
Fig. 4 Vesicle electrodeformation as a method for measuring the membrane bending stiffness. (a) Degree of deformation, a/b (as indicated in the inset) induced on a vesicle made of dipalmitoylphosphatidylcholine : cholesterol 9 : 1 (molar ratio) subjected to AC field with frequency 200 kHz. The applied electrical potential is increased every 10 s with a step of 0.5 V (10 V/cm), as indicated. The first two seconds after changing the field are excluded from averaging over the shape in time. (b) Relative area change of a vesicle subjected to AC field (300 kHz) as a function of the membrane tension. Each data point is a result of averaging the relative area change over 90 images. The solid line is a linear least squares fit, which slope yields $\kappa = (9.5 \pm 0.6) \times 10^{-20}$ J for the bending stiffness and the intercept gives $\sigma_0' = (1.7 \pm 1.4) \times 10^{-6}$ N/m.

the following 3–8 s can be time-averaged to achieve better precision in a/b. For the conductivity conditions and frequency range (between 1 kHz and 300 kHz) in such experiments, the vesicles adopt prolate deformation as discussed in the previous sections.

The vesicle deformation is associated with a change in the apparent area due to flattening the membrane fluctuations. Area stored in small membrane undulations is pulled out and made optically visible. The changes in apparent area is modulated by the membrane tension[50,51] (note that this equation is equivalent to eqn (7)):

$$\alpha \equiv \frac{A - A_0}{A_0} = \frac{k_B T}{8\pi\kappa} \log\left(\frac{\sigma_h}{\sigma_0'}\right) \quad (8)$$

where A is the area of the ellipsoid, A_0 is the area of the sphere with the same volume, and σ_0' is the positive parameter obtained by extrapolation to $\alpha = 0$. Note that σ_0' can be larger than the

actual tension at zero field strength. The tension of the deformed vesicle, σ_h, can be obtained from the electric stresses. The normal electric stress at the equator of the vesicle as given in the work of Helfrich and coworkers[28,30] is:

$$(T_{rr})_{eq} = -\frac{9}{8}\varepsilon_w E_0^2 \qquad (9)$$

where ε_w is the dielectric constant of water, and E_0 is the field strength far away from the vesicle. Since the pressure inside the vesicle must be constant, combining the Laplace equation at the poles and in the equator gives

$$(c_1 + c_2)_{eq}\sigma_h - (T_{rr})_{eq} = (c_1 + c_2)_{pole}\sigma_h \qquad (10)$$

where c_1, c_2 are the principal curvatures taken either at the equator (eq) or the pole (pole), and therefore measurable from the geometry of the vesicle.

Logarithmic plot of the membrane lateral tension obtained from eqn (10) against the change in apparent area gives a straight line with slope related to the bending rigidity as described in eqn (8). One example of this protocol applied to a vesicle composed of dipalmitoylphosphatidylcholine and cholesterol is given in Fig. 4b. A linear least squares fit of the dependence of the relative area change as a function of the applied tension following eqn (8) yields for the slope $\kappa = 9.5 \times 10^{-20}$ J. Repeating the measurement on the same vesicle shows reproducibility within about 22% deviation from the value of κ. Scatter within about 25% is observed when the measurements are performed on different vesicles with the same composition. The obtained value for the bending stiffness is consistent with published data.[52]

Note that this method does not apply to vesicles containing charged lipids and for vesicles embedded in salt solutions. In these cases, the Maxwell stress tensor used to evaluate the membrane tension has to account for the media conductivity (as discussed in the previous two sections) and the charges at the membrane surface.

3.2 Electrohydrodynamic flows in vesicles induced by non-homogeneous AC fields

As discussed above, electric fields induce forces at the vesicle interface, due to the difference in the media polarizabilities. At intermediate frequencies, $1/t_c < \omega < \omega_{MW}$, as shown in section 3.1, the lateral force is responsible for the vesicle deformation. In addition, this force may also lead to fluid flows, analogous to the flows induced in liquid droplets.[53] However, there is a fundamental difference between droplets and vesicles, which arises from the properties of the lipid bilayer.[54] The membrane behaves as a two dimensional nearly incompressible fluid. Under stress, it develops tension to keep its surface area constant. In uniform AC fields, membrane flow in the vesicle is not expected because the lateral electric stress is counterbalanced by the resulting axially symmetric gradient in the membrane tension. In inhomogeneous fields however, this force balance is broken and a flow of lipids occurs in order to restore it. Note that in most experimental conditions used for electromanipulation, vesicles, cells or other particles are exposed to inhomogeneous fields, arising from screening by neighboring particles, sedimentation or chamber geometry.

To study the lipid flow dynamics in AC fields, we used giant vesicles with mixed lipid bilayers, which, at room temperature, phase separate in liquid ordered (l_o) and liquid disordered (l_d) phases,[55] leading to the formation of l_o and l_d domains on the vesicles. A small fraction of fluorescent dye was added, which preferentially partitions in the l_d phase. The lipid ratio was such that the l_o phase appeared as dark circular patches in the surrounding fluorescently labeled l_d phase.

The membrane flow pattern was resolved by following the motion of the l_o patches with confocal microscopy.[56] The top or the bottom part of the vesicle were recorded as shown on the micrographs in Fig. 5a–c. The inner and outer vesicle solutions were 0.1 M sucrose and glucose, respectively. This ensures osmotic balance, i.e. constant vesicle volume, and causes the vesicles to sediment at the bottom of the chamber. The electric field was applied between two parallel cylindrical electrodes with a diameter of 200 μm and an inter-electrode gap of 500 μm. In AC fields, smaller vesicles experience lifting due to negative dielectrophoretic forces, but the larger ones ($R \geq 50$ μm), also being heavier, remain at the chamber bottom. The proximity of the bottom glass to the vesicle, as shown in Fig. 5d, leads to an asymmetric field distribution at the membrane surface. The field strength is much higher at the lower vesicle part, facing the glass, than at the top part.[56]

Such asymmetric field distribution leads to special membrane flow patterns, consisting of concentric closed trajectories organized in four symmetric quadrants, each extending from the bottom to the top of the vesicle; see Fig. 5d, e. The flow is fastest
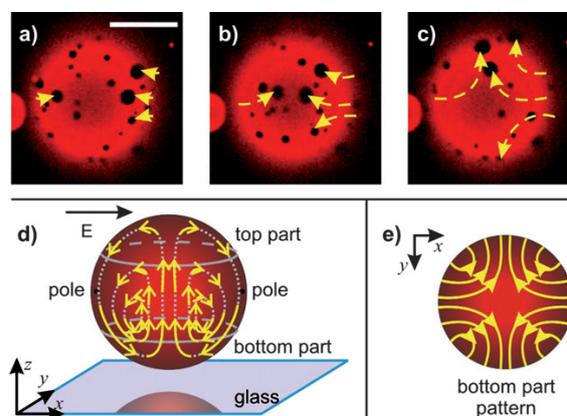
Fig. 5 Micrographs obtained on a confocal microscope (fully opened pinhole) illustrating the membrane flow on the bottom part (a–c) of a giant vesicle with a diameter of about 150 μm induced by an AC field (360 V/cm, 80 KHz), at external and internal conductivities of 25 mS/m and 0.3 mS/m, respectively. The vesicle was prepared from a mixture of dioleoylphosphatidylcholine : dipalmitoylphosphatidylcholine : cholesterol, 4.8 : 3.2 : 2 in mole fractions. The time between the consecutive snapshots is approximately 1.3 s. The yellow dashed arrows indicate the trajectories of selected domains in the consecutive snapshots. The scale bar corresponds to 50 μm. The vesicle is located close to the bottom of the observation chamber as illustrated in (d), where the vesicle top and bottom parts, the poles and the field direction are indicated. The side and the bottom views of the flow lines are sketched in (d) and (e), respectively. The length of the arrows in (d) roughly corresponds to the amplitude of the flow velocity.
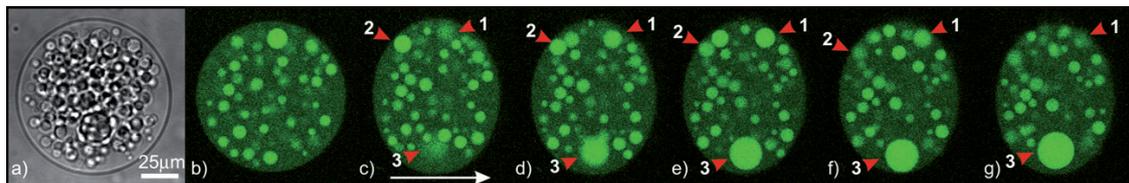
Fig. 6 (a) A phase-contrast image and (b–g) confocal cross sections of a giant lipid vesicle enclosing dextran-rich droplets (green fluorescence) in a PEG-rich phase. The cross section in (b), corresponding to the image in (a), is taken close to the equatorial plane of the vesicle and shows only the droplets in focus. Application of an inhomogeneous AC field (460 V/cm, 80 KHz) at an external conductivity of 40 mS/m leads to a vesicle shape deformation and an internal flow in the direction perpendicular to the plane of the image (c–g). The flow is visualized by following the motion of droplets 1, 2 and 3, which come in focus and go out of focus. The time period is 2.5 s between images (c–d) and (d–e) and 5 s between (e–f) and (f–g). The field direction is indicated by the arrow in (c).

at the periphery of the quadrant and at the bottom of the vesicle. The top and the bottom of the vesicle are stagnation points. The velocity of the domains reaches about 30 μm/s corresponding to laminar flows. The velocity can be further increased by the field strength and the conductivity of the external solution. Interesting effects are observed when the field frequency is varied. At frequencies less than about 3 MHz, the motion in the circular trajectories is directed downwards past the poles and upwards along the equator as sketched in Fig. 5d but reverses its direction at higher frequencies.[56]

Calculations of the lateral electric stress or surface force density on the membrane suggest that the vesicle experiences significant shear stress in the vicinity of the solid substrate.[56] As a result, a non-uniform and non-symmetric membrane tension builds up. It triggers lipid flow towards the regions of highest tension, in analogy to Marangoni flows in monolayers.

The flow in the membrane is coupled to fluid flows in the internal and external media. To visualize the effect of the membrane flow on the internal medium we used vesicles containing aqueous solution of the water-soluble polymers poly-(ethylene glycol) (PEG) and dextran. At specific polymer concentration, this solution undergoes phase separation[57,58] producing droplets of dextran-rich phase, which can be visualized *e.g.* by fluorescently labeled dextran. The droplets gradually coarsen. Before the coarsening is completed we subject such vesicles to non-uniform AC fields. As expected, the droplets move since they are coupled to the membrane flow. Therefore, when a cross section of the vesicle is observed with confocal microscopy as in Fig. 6, the droplets are observed to come into focus and to go out of focus again.

Membrane labelling *via* domains allows visualization of lipid motion and this approach should be helpful in order to elucidate other membrane phenomena such as membrane dynamics during electroformation of vesicles, or in the membrane behavior in vesicles subjected to shear flows[59] or mechanical stresses. Furthermore, the AC field-induced flows in the membrane and the interior of the vesicles may find application in microfluidic technologies. We have already demonstrated the effectiveness of the membrane flow for lipid mixing.[56]

4. Vesicle response to DC pulses

As discussed in section 3, vesicles exposed to AC fields can adopt stationary shapes. The application of DC pulses induces short-

lived shape deformations. We have previously explored the characteristic times associated with vesicle relaxation and poration,[60,61] as well as electrofusion of vesicles induced by DC pulses.[62,63] This section will be dedicated to some novel observations in this direction. In particular, we will discuss the influence of several other factors on the vesicle response to DC pulses: (i) presence of charged lipids in the membrane, see section 4.1; (ii) particles in the vesicle solution, see section 4.2; and (iii) phase state of the membrane, see section 4.3. Finally, we will introduce an interesting new application of electrofusion, namely for the synthesis of nanoparticles in vesicles; see section 4.4.

4.1 Unusual behavior of charged membranes exposed to DC pulses: vesicle bursting

Strong electric pulses applied to single component giant vesicles made of phosphatidylcholine induce the formation of pores, which reseal within milliseconds.[60] The mechanism of this pore formation, *i.e.*, electroporation, can be understood in terms of the stress in the bilayer created by the electric field.[32] In the presence of this field, the accumulated charges across the membrane create a transmembrane potential, which induces an effective electrical tension[19,60,64] as defined by the Maxwell stress tensor. Fluid membranes rupture if the tensions exceed about 10 mN/m[19,65] also known as lysis tension.

Studying phosphatidylcholine membranes is motivated by the fact that phosphatidylcholines are the most abundant lipids found in mammalian cells. In order to better mimic biological membranes, we investigated the behavior of multi-component vesicles containing a fraction of negatively charged lipids in different medium conditions.[66]

Two different types of charged vesicles were used: vesicles composed of mixtures of synthetic or natural lipids. In the first case, palmitoyloleoylphosphatidylcholine (POPC) and palmitoyloleoylphosphatidylglycerol (POPG), which is negatively charged, were used. In the second case, the vesicles were made of lipid extract (LE) from the plasma membrane of red blood cells, which contains approximately 10 mol% anionic lipids, mainly phosphatidylserines. When working with charged membranes, the medium pH and ionic strength are very important, as they can tune the bilayer electrostatic properties. Thus, three types of solutions for the vesicle preparation were considered: water, 1 mM Hepes buffer (pH 7.4) with 0.1 mM EDTA, and 0.5 mM NaCl, which provides the same ionic strength as the buffered

solution. Below, we refer to these solutions as non-buffered, buffered and salt solutions, respectively. To ensure good optical contrast, the vesicles in all preparations also contained 0.2 M sucrose inside and isotonic glucose solution outside.

Under certain conditions, POPC : POPG mixtures behave in the same way as pure PC vesicles,[60] *i.e.*, the pulses induce opening of macropores with a diameter up to about 10 μm, which reseal within 50 ms. This behavior was observed for mixed vesicles in buffered solutions at all molar ratios used: 9 : 1, 4 : 1 and 1 : 1, and for non-buffered or salt solutions at low POPG content (9 : 1 and 4 : 1). A very surprising response was observed for 1 : 1, POPC : POPG vesicles in non-buffered and salt solutions: they disintegrated after electroporation;[66] see Fig. 7a. Typically, one macropore formed and expanded in the first 50–100 ms at a very high speed of approximately 1 mm/s. The entire vesicle content is released and is seen as darker liquid in Fig. 7a. In order to better resolve the membrane reorganization after rupture, we used fluorescent labeling and confocal microscopy, as shown in Fig. 7b. The bursting was followed by restructuring of the membrane into what seemed to be interconnected bilayer fragments in the first seconds, and a tether-like structure in the first minute. Then the membrane stabilized into interconnected micron-sized tubules and small vesicles. These observations suggest that the vesicle bursting and membrane instability is related to the large amount of POPG in the bilayer and to the medium. No vesicle disintegration was observed in buffered solution and for lower content of POPG. Thus, we considered the hypothesis that vesicle bursting and membrane instability is related to the charged state of the bilayer.[67–69]

Interestingly, LE vesicles behave in the same way as synthetic 1 : 1, POPC : POPG vesicles. Conventional poration–resealing was observed in buffered solution, whereas the unusual bursting occurred in non-buffered and salt solutions. These results suggest that the bursting is not specific to PG but to the charged state of the membrane. The LE membranes contained approximately 10 mol% anionic lipids, which was enough to induce membrane destabilization. In the synthetic membranes 50 mol% of PG was needed to lead to the same effect.

The amount of PG in the bilayer is not the only factor triggering bursting of the synthetic membranes. In particular, vesicles with the same high content of PG (50 mol%) do not burst in buffered solution. Even though the main difference between buffered solution and the non-buffered and salt solutions seems to be the pH, significant protonation of PG should occur only for pH lower than 5.5, which is below the working pH values in this study. Thus, with respect to pH, the solutions are not very different.

As already mentioned, the ionic strengths of the buffered and the salt solutions were identical. Then, strictly speaking, the only composition difference between the two solutions is the presence of Hepes (1 mM) and EDTA (0.1 mM) in the buffer. To test which of the two components was responsible for preventing the bursting, we prepared giant vesicles (GUVs) composed of 1 : 1, POPC : POPG in 1 mM Hepes only as well as in 0.1 mM EDTA only. The experiments show that vesicles burst in the presence of 1 mM Hepes (without EDTA). On the other hand, in solutions containing 0.1 mM EDTA the conventional poration–resealing behavior was observed. Thus, EDTA is the essential component preventing vesicle bursting induced by the electric pulse. EDTA is a chelating agent, which is generally added in solutions to bind possible multivalent ions present as impurities in the solution, like calcium.[70] However, supplementing the 0.1 mM EDTA vesicle solution with excess of $CaCl_2$ (0.5 mM) to block the EDTA did not recover the bursting phenomenon.

Plasma membranes should exhibit similar bursting behavior as that of the LE vesicles, because their lipid composition is similar. However, cell membranes are subjected to internal mechanical constraints imposed by the cytoskeleton, which prevents their disintegration even if their membranes are prone to disruption when subjected to pulses. Instead, the pores in the cell membrane are stable for a long time[71] and can either lead to cell death by lysis or reseal depending on the media.[8,72] The latter is the key to efficient electroporation-based protocols for drug or gene transfer in cells. The results reported here suggest that membrane charge as well as minute amounts of molecules such as EDTA might be important but not yet well understood regulating agents in these protocols.

4.2 Vesicle behavior in the presence of nanoparticles

Gold and silver nanoparticles, as well as quantum dots are attractive tools for visualizing processes in cells. One possible application involves their employment in optical trapping as handles for force measurements inside living cells.[73,74] Another appealing feature is that magnetic and charged particles can be manipulated by electromagnetic fields. Thus, we were interested in the response of lipid membranes to electric fields in the presence of nanoparticles. For this purpose, we used GUVs made from the conventional lipid egg lecithin (L-α-phosphatidylcholine), and gold nanoparticles, 80 nm in diameter. The vesicles were electroformed in a sucrose solution and subsequently diluted in an isotonic glucose solution containing the particles at a concentration up to 2.2×10^{10} particles/ml. We applied DC pulses with a duration of 200 μs and a field strength of 3.4 kV/cm.
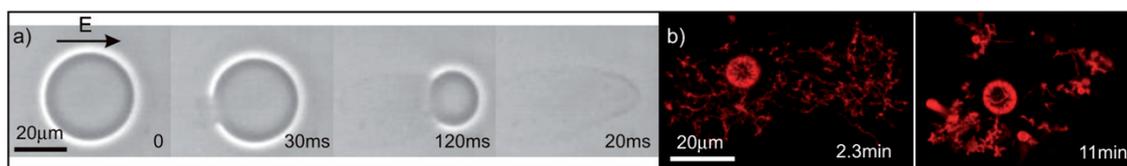
Fig. 7 Bursting of charged (POPC : POPG, 1 : 1) vesicles subjected to electric pulses. The time after the beginning of the pulse is marked on each image. (a) Phase contrast microscopy snapshots from fast camera observation of a vesicle in salt solution subjected to a pulse with field strength 1.2 kV/cm and duration 200 μs. The field direction is indicated in the first snapshot. The vesicle bursts and disintegrates. (b) Confocal cross-sections of a vesicle, which has been subjected to an electric pulse and has burst and rearranged into a network of tubes and smaller vesicles.
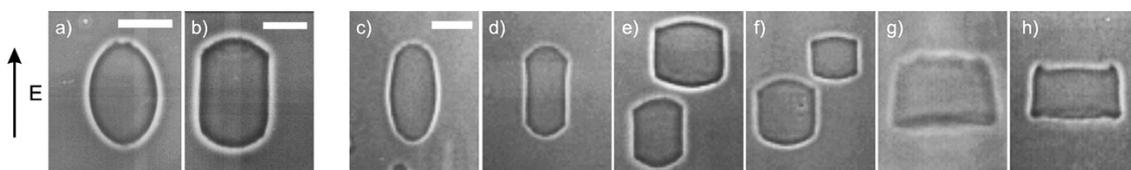
Fig. 8 Vesicle response to DC pulses in the presence and absence of salt and gold particles. The direction of the field is indicated by the arrow on the left. The first snapshot (a) shows a vesicle deformation in the absence of salt and particles. In this case, the DC pulse duration is 200 μs and the field strength is 1.4 kV/cm. The applied pulse is sufficient to porate the vesicle as visualized by dark eruptions of sucrose solution leaking out of the vesicle. In the presence of 0.03 mM salt in the vesicle exterior and no particles present, the vesicles adopt cylindrical shapes as shown in (b). In the latter, the DC pulse duration is 200 μs and the field strength is of 2 kV/cm. Snapshots (c) to (h) show vesicles deforming in the presence of 80 nm gold particles for a DC pulse with a duration of 200 μs and a field strength of 3.4 kV/cm. The gold concentration was successively increased from 1.1×10^8 particles/ml in (c), to 5.5×10^8 in (d), 1.1×10^9 in (e), 2.2×10^9 in (f), 1.1×10^{10} in (g), and 2.2×10^{10} particles/ml in (h). There is a clear concentration dependence of the shape adopted by the deformed vesicles. Snapshots (a), (c), (e) and (f) were taken 150 μs after the beginning of the pulse and (b), (d), (g) and (h) after 200 μs. All scale bars correspond to 15 micrometres.

Previous work, where GUVs were exposed to DC pulses, has shown cylindrical deformations when salt was present in the vesicle exterior;[61] note that in the absence of salt in the external solution, the vesicles deform only into prolates, see Fig. 8a. By applying a DC pulse and systematically varying the concentration of gold nanoparticles outside the vesicles, we observed very similar morphologies. Since the lifetime of these cylindrical deformations is very short, between a few hundred microseconds and a few milliseconds, we used a fast digital camera recording at 20 000 frames per second, *i.e.*, an acquisition speed that corresponds to one image every 50 μs.

By varying the concentration of gold nanoparticles in the surrounding media, we could influence the shape adopted by a vesicle exposed to a DC pulse, as shown in Fig. 8c–h. We observed an overall elongation or contraction of the GUV in the direction of the electric field. The images in Fig. 8c–h show how the vesicles respond to an increase in the concentration of gold nanoparticles. It should be noted that the particles are only present in the external medium. For the lowest explored concentration $c_{min} = 1.1 \times 10^8$ particles/ml, shown in Fig. 8c, the vesicles exhibit a similar behavior as in the absence of ions or particles, compare with the image in Fig. 8a. The vesicles elongate only in the direction of the field into a prolate shape. By increasing the gold concentration we could observe a flattening of the vesicle equatorial region; the vesicles adopt the shape of a cylinder with rounded caps. This is similar to the vesicle response in the presence of ions; compare with the image in Fig. 8b. The particle concentration influences the type of the cylindrical deformations observed. At concentrations slightly above c_{min}, the vesicles adopt tube-like shapes parallel to the direction of the electric field. When the gold concentration was increased tenfold, $10 \times c_{min}$, coexistence of "discs" and "tubes" occurred during the DC pulse, some of them almost looking "square" (Fig. 8e, f). At even higher particle concentrations, the vesicles adopted only a disc-like shape (Fig. 8g, h).

Parallels can be drawn between the above observations and the prolate and oblate shapes of vesicles subjected to AC fields described in section 3.1, but even more so to the shapes adopted by vesicles subjected to DC pulses in the presence of NaCl.[61] The overall behavior is the same, disc-like, square-like or tube-like deformation depending on the outer (and inner) salt or particle

concentration conditions. This suggests that the deformation mechanism in the presence of gold nanoparticles and salt is the same. Indeed, both ions and particles are charged. By measuring the electrophoretic mobility of the gold colloids, we could estimate their zeta potential to be slightly below −50 mV. This would indicate that the nanoparticles migrate towards the anode during the DC pulse. In the case of salt, Na^+ and Cl^- move in opposite directions, while the gold colloids move only in one direction. This might explain the observed asymmetry in the deformed vesicles, especially at the higher particle concentrations where the vesicles adopt a disc-like shape with a trapezoidal cross section; see Fig. 8g and h. The area of the side of the disc facing the anode seems to be larger than the one facing the cathode.

As discussed in a previous report,[61] one possible explanation could be that ions or particles flatten the equatorial zone of the deformed vesicle. At least during the first part of the pulse there is an inhomogeneity in the membrane tension due to the fact that the electric field is the strongest at the poles of the vesicle, and almost zero close to the equator. The kinetic energy of the accelerated ions hitting the equatorial region of the vesicle is higher than the energy needed to bend the membrane, thus leading to the observed deformation. In addition, particle-driven flows may be inducing membrane instability giving rise to higher order modes of the vesicle shape.[75] Yet another possible explanation may be related to a change in the spontaneous curvature of the bilayer due to the particle (or ion) asymmetry across the membrane.[76] During the pulse, local and transient accumulation of particles in the membrane vicinity can occur. The mechanism driving the cylindrical deformations might be a combination of nanoparticle electrophoresis and changes in the membrane spontaneous curvature.

The idea that the balance between the particle concentration in the inner and outer media influences the type of deformation is supported by the observation that repeated exposure of the same vesicles to many consecutive DC pulses leads to coexistence between "tubes" and "discs". Poration of the lipid membrane is frequent at these pulse strengths and durations[60] and depends, among other factors, on the vesicle radius and proximity to the electrode, *e.g.* larger vesicles porate at weaker pulses than smaller ones. The pulses might induce permeation of gold particles into the interior of some of the vesicles, which would explain the variation in the cylindrical deformations.

In summary, when subjected to DC pulses, vesicles in the presence of nanoparticles respond similarly to vesicles in salt solutions.[61] The mechanisms behind these responses are still to be clarified, and it remains to be seen whether the processes governing them are the same.

4.3 Electrodeformation and poration of vesicles in the gel-phase

In the previous two sections, the response of membranes in the fluid state has been discussed. The mechanical and rheological properties of such membranes differ significantly from those of membranes in the gel-phase; for a concise comparison see Dimova et al.[77] For example, the bending stiffness and the shear surface viscosity of gel-phase membranes are orders of magnitude higher than those of membranes in the fluid phase,[78–81] and membranes in the gel-phase are thicker.[82] These differences introduce new features in the response of gel-phase membranes to electric fields, which we discuss next.

We studied POPC and dipalmitoylphosphatidylcholine (DPPC) membranes, which undergo their main transition at -2 °C and 41.6 °C, respectively. We compared the response to square wave DC pulses of a POPC vesicle, which at room temperature is in the fluid phase, with the response of a vesicle made of DPPC, which is in the gel-phase. The applied DC pulses were weak enough not to induce formation of microscopic pores in the membranes and no leakage of the internal sucrose solution outside the vesicle was observed. Fig. 9 shows the deformation of one POPC and one DPPC vesicle in response to DC pulses 300 μs long. The deformation is characterized by the ratio of the two semiaxes, a/b, of the vesicles. To achieve similar maximal degree of deformation, stronger pulses had to be applied to the gel-phase vesicle as compared to the fluid one. Pulses with field strength about 1 kV/cm produce deformations in gel-phase vesicles, which are not detectable optically, while strong pulses about 5 kV/cm applied to the fluid-phase vesicles cause poration. The latter influences the relaxation dynamics.[60] Note that the
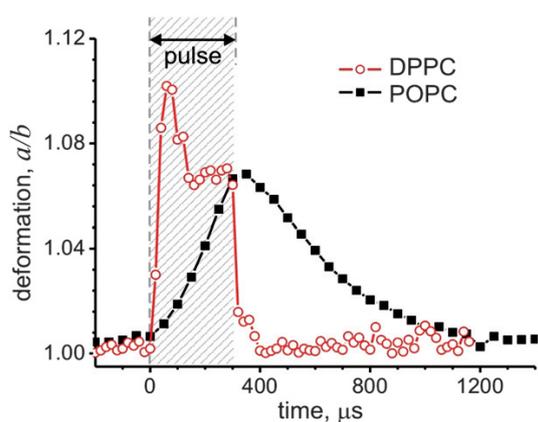
degree of deformation depends on the initial vesicle tension and excess area,[60] which are both unknown a priori.

The responses of the two vesicles differ significantly. The fluid vesicle gradually deforms and reaches maximum deformation at the end of the pulse. The gel-phase vesicle responds significantly faster, and exhibits a relaxation with a decay time of about 30 μs during the pulse. To our knowledge, such intra-pulse relaxation has not been previously reported. The vesicles had similar size and were both in salt-free solutions with conductivity of about 1 mS/m. For a fluid vesicle with radius $R = 20$ μm, the charging time is $t_c \cong 550$ μs, see eqn (2), i.e., longer than the pulse duration. Gel-phase membranes are thicker, and thus, have lower membrane capacitance,[83] leading to charging times shorter or comparable to the duration of the pulse. The faster response of the gel-phase vesicle as shown in Fig. 9 correlates with the shorter charging time as compared to the fluid vesicle.

After the end of the pulse, the relaxation of the gel DPPC vesicle is also much faster than that of the fluid membrane. The relaxation behavior depends on whether the membrane was porated or not.[60] In the example given in Fig. 9, no microscopic pores were detected, but it is plausible that in the gel-phase vesicle pores with sizes in the sub-optical range were formed during the pulse. The formation of such pores may explain the intra-pulse relaxation in the vesicle deformation.
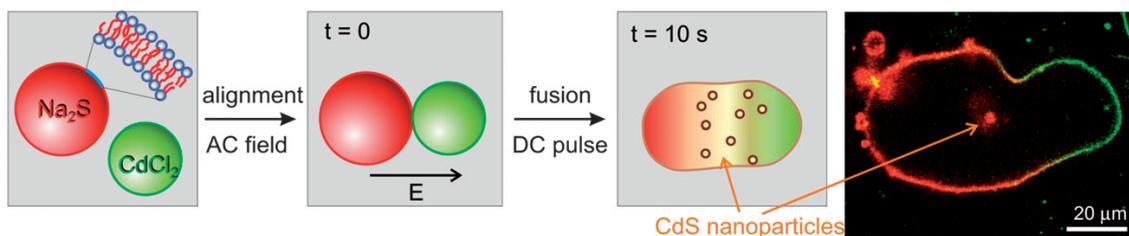
If DC pulses of field strength larger than the discussed above are applied, the gel-phase vesicles rupture: the pores resemble micrometre-sized cracks on a solid shell.[32] Contrary to pores in fluid membranes, which reseal within tens of milliseconds,[60] the cracks in gel-phase vesicles are stable and seem not to reseal.

Understanding the response of the gel-phase membranes will require thorough consideration of the membrane mechanical and rheological properties as well as the interaction of electric fields with such membranes. Both the intra- and after-pulse relaxations of the vesicles in gel-phase are poorly understood and will be the object of further investigation.

4.4 Vesicle electrofusion as a method for nanoparticle synthesis in vesicles

Strong electric pulses induce electrical breakdown of fluid lipid bilayers leading to formation of transient pores. The vesicles become permeable for a certain time. When two such porated vesicles are in close contact, fusion can occur. The concept to fuse two GUVs in order to initiate content mixing reactions has been proposed earlier.[84,85] In this section, we introduce the application of fusion of giant vesicles for the synthesis of nanoparticles in closed compartments.

The principle of fusion-mediated synthesis is simple: the starting reagents are separately loaded into different vesicles, and then the reaction is triggered by the fusion of these vesicles, which allows the mixing of their contents. The success of this approach is guaranteed by two important factors. First, the lipid membrane is impermeable to the reactants such as ions or macromolecules. Second, fusion can be initiated by a variety of fusogens such as membrane stress,[86,87] ions or synthetic fusogenic molecules,[62,88–90] fusion proteins,[91] laser beam radiation,[85] or electric fields.[63,92] Among the fusion methods listed above, electrofusion becomes increasingly important because of its reliable, fast and easy handling.[63] An immediate benefit of this strategy is

Fig. 9 Deformation response of a gel-phase DPPC vesicle with a radius of 22 μm, and a fluid phase POPC vesicle with a radius of 20 μm to DC pulses with a duration of 300 μs. The pulse duration is indicated by the shaded zone. The field strength of the pulses was 5 kV/cm and 0.8 kV/cm for the DPPC and the POPC vesicle, respectively.

Fig. 10 Electrofusion of vesicles as a method for nanoparticle synthesis: vesicles containing Na$_2$S and fluorescently labelled in red, and vesicles containing CdCl$_2$, labelled in green, are mixed in Na$_2$S- and CdCl$_2$-free environment and subjected to an AC field to align them in the direction of the field and bring them close together. A DC pulse initiates the electrofusion of the two vesicles and the reaction between Na$_2$S and CdCl$_2$ proceeds to the formation of CdS nanoparticles encapsulated in the fused vesicle. The last snapshot is a confocal scan of a vesicle obtained by fusion of a vesicle loaded with 0.3 mM Na$_2$S (red part of the fused vesicle) and a vesicle loaded with 0.3 mM CdCl$_2$ (labelled in green). The fluorescence signal from the synthesized CdS nanoparticles in the vesicle interior is visible as indicated by the arrow.[94]

that the precise temporal and spatial control on the synthesis process can be easily achieved.

According to our electrofusion protocol, two vesicle populations are mixed, one loaded with Na$_2$S and labeled with one fluorescent dye (red), the other loaded with CdCl$_2$ and labeled differently (green). The vesicle external media is Na$_2$S- or CdCl$_2$-free, which can be achieved either by significant dilution of the starting vesicle solutions or by exposure to ion-exchange resins. Application of AC field aligns the vesicles in the direction of the field due to dielectric screening, similarly to pearl-chain formation in suspensions of cells.[15] In order to monitor the nanoparticle formation process, we locate a red-and-green vesicle couple (approximately half of the couples fall in this category) and apply a DC pulse strong and long enough to porate each of the vesicles. For egg lecithin vesicles, pulses of 0.5–2 kV/cm field strength and 150–300 μs duration are sufficient. The steps of this protocol are schematically illustrated in Fig. 10.

Fluorescence in the interior of the fused vesicle was observed, see Fig. 10, which indicates formation of CdS nanoparticles. Fluorescence in the wavelength range between 400 and 800 nm has been previously reported for CdS particles with diameters in the range 1–25 nm.[93] Because the confocal sections show only fluorescence from a thin slice of the vesicle, out of focus fluorescence, which might be emitted from the upper and lower part of the vesicle, is not detected. The obtained product was also investigated using transmission electron microscopy and selected area electron diffraction, which showed the presence of dispersed nanoparticles of diameters ranging between 4 and 8 nm.[94] A noticeable advance of the above approach is that the whole reaction could be viewed and monitored in real time under the optical microscope.

Cells and microorganisms are able to synthesize inorganic nanoparticles.[95–97] The tentative interpretation of this observation is related to the involvement of specific molecules such as inorganic-binding peptides.[98–100] Our experiments suggest that nanoparticles could be synthesized in biological compartments even without the mediation of biomacromolecules. For example, the fusion of small vesicles with the cell membranes could be a possible mechanism for the cell-based synthesis of nanoparticles. The necessary condition according to such a scenario is that the vesicles are loaded with one reagent, while the local concentration of the other chemical at the cell is suitably matched. Low concentrations in the submillimolar range are sufficient to produce CdS nanoparticles.[94]

In general, vesicle fusion provides many unexplored opportunities for protein biosynthesis, enzyme-catalyzed reactions, and biomineralization processes.[101]

5. Conclusions

The results reported in this review demonstrate that cell-sized giant vesicles provide a very useful model for resolving the effect of electric fields on lipid membranes because vesicle dynamics can be directly observed with optical microscopy. We have examined the behavior of giant vesicles exposed to AC fields of various frequencies and elucidated the underlying physical mechanism for the vesicle deformations as well as stress-induced lipid flows in inhomogeneous AC fields. We have shown that the vesicle response to electric fields can be exploited to evaluate the mechanical properties of the membrane.

Until recently, the dynamics of vesicle relaxation and poration, which occur on microsecond time-scales, has eluded direct observation because the temporal resolution of optical microscopy observations with analog video technology is in the range of milliseconds. We used fast digital imaging to discover new features in the membrane response arising from the presence of charged lipids in the membrane, nanoparticles in the surrounding media, and compared the response of gel-phase membranes to fluid ones. Finally, we introduced a novel application of membrane electrofusion, which allowed us to perform nanoparticle synthesis in vesicles.

In conclusion, the reported observations demonstrate that giant vesicles can help advance fundamental knowledge about the complex behavior of cells and membranes in electric fields and can inspire novel practical applications.

References

1 *Electromanipulation of cells*, ed. U. Zimmermann and G. A. Neil, CRC Press, Boca Raton, 1996.
2 *Electroporation and electrofusion in cell biology*, ed. E. Neumann, A. E. Sowers and C. A. Jordan, Plenum Press, New York, 1989.
3 *Guide to electroporation and electrofusion*, ed. D. C. Chang, B. M. Chassey, J. A. Saunders and A. E. Sowers, Academic Press, New York 1992.
4 R. H. W. Funk and T. K. Monsees, *Cells Tissues Organs*, 2006, **182**, 59–78.
5 J. Voldman, *Annu. Rev. Biomed. Eng.*, 2006, **8**, 425–454.
6 M. Zhao, B. Song, J. Pu, T. Wada, B. Reid, G. P. Tai, F. Wang, A. H. Guo, P. Walczysko, Y. Gu, T. Sasaki, A. Suzuki, J. V. Forrester, H. R. Bourne, P. N. Devreotes, C. D. McCaig and J. M. Penninger, *Nature*, 2006, **442**, 457–460.
7 J. Teissie, M. Golzio and M. P. Rols, *Biochim. Biophys. Acta*, 2005, **1724**, 270–280.
8 E. Tekle, R. D. Astumian and P. B. Chock, *Proc. Natl. Acad. Sci. U. S. A.*, 1994, **91**, 11512–11516.
9 R. Heller, R. Gilbert and M. J. Jaroszeski, *Adv. Drug Deliv. Rev.*, 1999, **35**, 119–129.
10 A. Gothelf, L. M. Mir and J. Gehl, *Cancer Treat. Rev.*, 2003, **29**, 371–387.
11 R. Nuccitelli, U. Pliquett, X. Chen, W. Ford, R. J. Swanson, S. J. Beebe, J. F. Kolb and K. H. Schoenbach, *Biochem. Biophys. Res. Commun.*, 2006, **343**, 351–360.
12 L. M. Mir, P. Devauchelle, F. Quintin-Colonna, F. Delisle, S. Doliger, D. Fradelizi, J. Belehradek Jr and S. Orlowski, *Brit. J. Cancer*, 1997, **76**, 1617–1622.
13 M. Golzio, J. Teissié and M. P. Rols, *Proc. Natl. Acad. Sci. U. S. A.*, 2002, **99**, 1292–1297.
14 M. Golzio, M. P. Rols and J. Teissié, *Methods*, 2004, **33**, 126–135.
15 U. Zimmermann, *Rev. Physiol. Biochem. Pharmacol.*, 1986, **105**, 176–256.
16 J. Teissie and T. Y. Tsong, *Biochemistry*, 1981, **20**, 1548–1554.
17 R. W. Glaser, S. L. Leikin, L. V. Chernomordik, V. F. Pastushenko and A. I. Sokirko, *Biochim. Biophys. Acta*, 1988, **940**, 275–287.
18 S. Kakorin, T. Liese and E. Neumann, *J. Phys. Chem. B.*, 2003, **107**, 10243–10251.
19 D. Needham and R. M. Hochmuth, *Biophys. J.*, 1989, **55**, 1001–1009.
20 D. V. Zhelev and D. Needham, *Biochim. Biophys. Acta*, 1993, **1147**, 89–104.
21 O. Sandre, L. Moreaux and F. Brochard-Wyart, *Proc. Natl. Acad. Sci. U. S. A.*, 1999, **96**, 10591–10596.
22 E. Tekle, R. D. Astumian, W. A. Friauf and P. B. Chock, *Biophys. J.*, 2001, **81**, 960–968.
23 C.-H. Lee, Y.-F. Chang, C.-H. Tsai and P.-H. Wang, *Langmuir*, 2005, **21**, 7186–7190.
24 M. Winterhalter and W. Helfrich, *J. Colloid Interface Sci.*, 1988, **122**, 583–586.
25 P. Peterlin, S. Svetina and B. Žekś, *J. Phys.: Condens. Matter.*, 2007, **19**, 136220.
26 H. Engelhardt, H. Gaub and E. Sackman, *Nature*, 1984, **307**, 378–380.
27 M. Mitov, P. Méléard, M. Winterhalter, M. I. Angelova and P. Bothorel, *Phys. Rev. E.*, 1993, **48**, 628–631.
28 A. Kummrow and W. Helfrich, *Phys. Rev. A*, 1991, **44**, 8356–8360.
29 W. Harbich and W. Helfrich, *Z. Naturforsch. A*, 1979, **34**, 1063–1065.
30 G. Niggemann, M. Kummrow and W. Helfrich, *J. Phys. II*, 1995, **5**, 413–425.
31 S. Lecuyer, W. Ristenpart, O. Vincent and H. Stone, *Appl. Phys. Lett.*, 2008, **92**, 104105.
32 R. Dimova, K. A. Riske, S. Aranda, N. Bezlyepkina, R. L. Knorr and R. Lipowsky, *Soft Matter*, 2007, **3**, 817–827.
33 T. B. Jones, *Electromechanics of particles*, Cambridge University Press, New York, 1995.
34 H. P. Schwan, in *Interaction between EM fields and cells*, ed. A. Chiabrera, C. Nivolin and H. P. Schwan, Plenum Press, 1985, pp. 75–97.
35 C. Grosse and H. P. Schwan, *Biophys. J.*, 1992, **63**, 1632–1642.
36 H. Engelhardt and E. Sackman, *Biophys. J.*, 1988, **54**, 495–508.
37 A. W. Friend Jr., E. D. Finch and H. P. Schwan, *Science*, 1975, **187**, 357–359.
38 F. J. Iglesias, M. C. Lopes, C. Santamaria and A. Dominguez, *Biophys. J.*, 1985, **48**, 712–726.
39 M. I. Angelova and D. S. Dimitrov, *Faraday Discuss. Chem. Soc.*, 1986, **81**, 303–311.
40 M. I. Angelova, S. Soleau, P. Meleard, J.-F. Faucon and P. Bothorel, *Prog. Colloid Polym. Sci.*, 1992, **89**, 127–131.
41 D. J. Estes and M. Mayer, *Biochim. Biophys. Acta*, 2005, **1712**, 152–160.
42 T. Pott, H. Bouvrais and P. Meleard, *Chem. Phys. Lipids*, 2008, **154**, 115–119.
43 L. R. Montes, A. Alonso, F. M. Goni and L. A. Bagatolli, *Biophys. J.*, 2007, **93**, 3548–3554.
44 P. Taylor, C. Xu, P. D. I. Fletcher and V. N. Paunov, *Phys. Chem. Chem. Phys.*, 2003, 1732–1733.
45 P. Taylor, C. Xu, P. D. I. Fletcher and V. N. Paunov, *Chem. Commun.*, 2003, **5**, 4918–4922.
46 M. I. Angelova, in *Giant Vesicles*, ed. P. L. Luisi and P. Walde, John Wiley & Sons Ltd., Chichester, 2000, ch. 3, pp. 27–43.
47 P. Sens and H. Isambert, *Phys. Rev. Lett.*, 2002, **88**, 128102.
48 S. Aranda, K. A. Riske, R. Lipowsky and R. Dimova, *Biophys. J.*, 2008, **95**, L19–L21.
49 P. M. Vlahovska, R. S. Gracià, S. Aranda and R. Dimova, *Biophys. J.*, 2009, **96**, 4789–4803.
50 W. Helfrich and R. M. Servuss, *Nuovo Cimento D*, 1984, **3**, 137–151.
51 E. Evans and W. Rawicz, *Phys. Rev. Lett.*, 1990, **64**, 2094–2097.
52 J. J. Pan, T. T. Mills, S. Tristram-Nagle and J. F. Nagle, *Phys. Rev. Lett.*, 2008, **100**, 198103.
53 G. I. Taylor, *Proc. R. Soc. London, Ser. A*, 1966, **291**, 159–166.
54 D. Lacoste, G. I. Menon, M. Z. Bazant and J. F. Joanny, *Eur. Phys. J. E*, 2009, **28**, 243–264.
55 S. Veatch and S. Keller, *Phys. Rev. Lett.*, 2002, **89**, 268101.
56 M. Staykova, R. Lipowsky and R. Dimova, *Soft Matter*, 2008, **4**, 2168–2171.
57 M. Helfrich, L. K. Mangeney-Slavin, M. S. Long, K. Djoko and C. D. Keating, *J. Am. Chem. Soc.*, 2002, **124**, 13374–13375.
58 Y. Li, R. Lipowsky and R. Dimova, *J. Am. Chem. Soc.*, 2008, **130**, 12252–12253.
59 M. Abkarian and A. Viallat, *Soft Matter*, 2008, **4**, 653–657.
60 K. A. Riske and R. Dimova, *Biophys. J.*, 2005, **88**, 1143–1155.
61 K. A. Riske and R. Dimova, *Biophys. J.*, 2006, **91**, 1778–1786.
62 C. K. Haluska, K. A. Riske, V. M. Artzner, J. M. Lehn, R. Lipowsky and R. Dimova, *Proc. Natl. Acad. Sci. U. S. A.*, 2006, **103**, 15841–15846.
63 K. A. Riske, N. Bezlyepkina, R. Lipowsky and R. Dimova, *Biophys. Rev. Lett.*, 2006, **4**, 387–400.
64 I. G. Abidor, V. B. Arakelyan, L. V. Chernomordik, Y. A. Chizmadzhev, V. F. Pastushenko and M. R. Tarasevich, *J. Electroanal. Chem.*, 1979, **104**, 37–52.
65 K. Olbrich, W. Rawicz, D. Needham and E. Evans, *Biophys. J.*, 2000, **79**, 321–327.
66 K. A. Riske, R. L. Knorr and R. Dimova, *Soft Matter*, 2009, **5**, 1983–1986.
67 M. D. Betterton and M. P. Brenner, *Phys. Rev. Lett.*, 1999, **82**, 1598–1601.
68 V. Kumaran, *Phys. Rev. Lett.*, 2000, **85**, 4996–4999.
69 H. Isambert, *Phys. Rev. Lett*, 1998, **80**, 3404–3407.
70 K. A. Riske, H. G. Dobereiner and M. T. Lamy-Freund, *J. Phys. Chem. B*, 2003, **107**, 5391–5392.
71 K. Schwister and B. Deuticke, *Biochim. Biophys. Acta*, 1985, **816**, 332–348.
72 K. Kinosita and T. Y. Tsong, *Nature*, 1977, **268**, 438–441.
73 P. M. Hansen, V. K. Bhatia, N. Harrit and L. Oddershede, *Nano Lett.*, 2005, **5**, 1937–1942.
74 L. Jauffred, A. C. Richardson and L. B. Oddershede, *Nano Lett.*, 2008, **8**, 3376–3380.
75 V. Kantsler, E. Segre and V. Steinberg, *Phys. Rev. Lett.*, 2007, **99**, 178102.
76 R. Lipowsky and H.-G. Dobereiner, *Europhys. Lett.*, 1998, **43**, 219–225.
77 R. Dimova, S. Aranda, N. Bezlyepkina, V. Nikolov, K. A. Riske and R. Lipowsky, *J. Phys.: Condens. Matter*, 2006, **18**, S1151–S1176.
78 T. Heimburg, *Biochim. Biophys. Acta*, 1998, **1415**, 147–162.

79 R. Dimova, B. Pouligny and C. Dietrich, *Biophys. J.*, 2000, **79**, 340–356.
80 C.-H. Lee, W.-C. Lin and J. Wang, *Phys. Rev. E*, 2001, **64**, 020901.
81 K. R. Mecke, T. Charitat and F. Graner, *Langmuir*, 2003, **19**, 2080–2087.
82 J. F. Nagle and S. Tristram-Nagle, *Biophys. Biochem. Acta*, 2000, **1469**, 159–195.
83 M. A. Stuchly, S. S. Stuchly, R. P. Liburdy and D. A. Rousseau, *Phys. Med. Biol.*, 1988, **33**, 1309–1324.
84 D. T. Chiu, C. F. Wilson, F. Ryttsen, A. Stromberg, C. Farre, A. Karlsson, S. Nordholm, A. Gaggar, B. P. Modi, A. Moscho, R. A. Garza-Lopez, O. Orwar and R. N. Zare, *Science*, 1999, **283**, 1892–1895.
85 S. Kulin, R. Kishore, K. Helmerson and L. Locascio, *Langmuir*, 2003, **19**, 8206–8210.
86 F. S. Cohen, M. H. Akabas and A. Finkelstein, *Science*, 1982, **217**, 458–460.
87 J. C. Shillcock and R. Lipowsky, *Nat. Mater.*, 2005, **4**, 225–228.
88 D. J. Estes, S. R. Lopez, A. O. Fuller and M. Mayer, *Biophys. J.*, 2006, **91**, 233–243.
89 B. R. Lentz, *Eur. Biophys. J.*, 2007, **36**, 315–326.
90 M. Kunishima, M. Tokaji, K. Matsuoka, J. Nishida, M. Kanamori, K. Hioki and S. Tani, *J. Am. Chem. Soc.*, 2006, **128**, 14452–14453.
91 R. Jahn, T. Lang and T. C. Südhof, *Cell*, 2003, **112**, 519–533.
92 A. Strömberg, F. Ryttsén, D. T. Chiu, M. Davidson, P. S. Eriksson, C. F. Wilson, O. Orwar and R. N. Zare, *Proc. Natl. Acad. Sci. U. S. A.*, 2000, **97**, 7–11.
93 H. Weller, *Angew. Chem.*, 1993, **105**, 43–55.
94 P. Yang, R. Lipowsky and R. Dimova, *Small*, DOI: 10.1002/smll.200900560.
95 D. Bhattacharya and R. K. Gupta, *Crit. Rev. Biotechnol.*, 2005, **25**, 199–204.
96 C. Sanchez, H. Arribart, M. Madeleine and G. Guille, *Nat. Mater.*, 2005, **4**, 277–288.
97 D. Mandal, M. E. Bolander, D. Mukhopadhyay, G. Sarkar and P. Mukherjee, *Appl. Microbiol. Biotechnol.*, 2006, **69**, 485–492.
98 N. Kröger, M. B. Dickerson, G. Ahmad, Y. Cai, M. S. Haluska, K. H. Sandhage, N. Poulsen and V. C. Sheppard, *Angew. Chem.*, 2006, **118**, 7397–7401.
99 N. Kröger, M. B. Dickerson, G. Ahmad, Y. Cai, M. S. Haluska, K. H. Sandhage, N. Poulsen and V. C. Sheppard, *Angew. Chem., Int. Ed.*, 2006, **45**, 7239–7243.
100 R. R. Naik, S. J. Stringer, G. Agarwal, S. E. Jones and M. O. Stone, *Nat. Mater.*, 2002, **1**, 169–172.
101 P. Walde and S. Ichikawa, *Biomol. Eng.*, 2001, **18**, 143–177.

Bibliography

[1] S. Ahmed and J. H. Brickner. Regulation and epigenetic control of transcription at the nuclear periphery. *Trends in genetics : TIG*, 23(8):396–402, Aug. 2007.

[2] J. Alfredsson-Timmins, F. Henningson, and P. Bjerling. The Clr4 methyltransferase determines the subnuclear localization of the mating-type region in fission yeast. *Journal of cell science*, 120(Pt 11):1935–43, June 2007.

[3] J. Alfredsson-Timmins, C. Kristell, F. Henningson, S. Lyckman, and P. Bjerling. Reorganization of chromatin is an early response to nitrogen starvation in Schizosaccharomyces pombe. *Chromosoma*, 118(1):99–112, Feb. 2009.

[4] R. Allshire and W. Bickmore. Pausing for thought on the boundaries of imprinting. *Cell*, 102(6):705–8, Sept. 2000.

[5] R. Alvarez-Roman, A. Naik, Y. Kalia, and H. Fessi. Visualization of skin penetration using confocal laser scanning microscopy. *European journal of . . .*, 2004.

[6] M. Angelova, S. Soléau, P. Méléard, J. Faucon, and P. Bothorel. Preparation of giant vesicles by external AC electric fields. Kinetics and applications. *Progress in Colloid and Polymer Science*, 89:127–131, 1992.

[7] S. Aranda, K. a. Riske, R. Lipowsky, and R. Dimova. Morphological transitions of vesicles induced by alternating electric fields. *Biophysical journal*, 95(2):L19–21, July 2008.

[8] L. a. Bagatolli and E. Gratton. Two-photon fluorescence microscopy observation of shape changes at the phase transition in phospholipid giant unilamellar vesicles. *Biophysical journal*, 77(4):2090–101, Oct. 1999.

167

[9] L. a. Bagatolli, T. Parasassi, and E. Gratton. Giant phospholipid vesicles: comparison among the whole lipid sample characteristics using different preparation methods: a two photon fluorescence microscopy study. *Chemistry and physics of lipids*, 105(2):135–47, Apr. 2000.

[10] R. Bar-Ziv, E. Moses, and P. Nelson. Dynamic excitations in membranes induced by optical tweezers. *Biophysical journal*, 75(1):294–320, July 1998.

[11] S. Baumgärtner and I. M. Tolić-Nø rrelykke. Growth pattern of single fission yeast cells is bilinear and depends on temperature and DNA synthesis. *Biophysical journal*, 96(10):4336–47, May 2009.

[12] P. M. Bendix, S. N. S. Reihani, and L. B. Oddershede. Direct measurements of heating by electromagnetically trapped gold nanoparticles on supported lipid bilayers. *ACS nano*, 4(4):2256–62, Apr. 2010.

[13] A. B. Berger, G. G. Cabal, E. Fabre, T. Duong, H. Buc, U. Nehrbass, J.-C. Olivo-Marin, O. Gadal, and C. Zimmer. High-resolution statistical mapping reveals gene territories in live yeast. *Nature methods*, 5(12):1031–7, Dec. 2008.

[14] Y. Y. Biton and S. a. Safran. The cellular response to curvature-induced stress. Oct. 2009.

[15] P. Bjerling, R. Silverstein, G. Thon, and A. Functional divergence between histone deacetylases in fission yeast by distinct cellular localization and in vivo specificity. *Molecular and cellular biology*, 22(7):2170–2181, 2002.

[16] A. Blicher, K. Wodzinska, M. Fidorra, M. Winterhalter, and T. Heimburg. The temperature dependence of lipid membrane permeability, its quantized nature, and the influence of anesthetics. *Biophysical journal*, 96(11):4581–91, June 2009.

[17] D. Boal. *Mechanics of the Cell*. Cambridge Universy Press, Cambridge, 2002.

[18] F.-M. Boisvert, S. van Koningsbruggen, J. Navascués, and A. I. Lamond. The multifunctional nucleolus. *Nature reviews. Molecular cell biology*, 8(7):574–85, July 2007.

[19] M. M. Brandão, a. Fontes, M. L. Barjas-Castro, L. C. Barbosa, F. F. Costa, C. L. Cesar, and S. T. O. Saad. Optical tweezers for measuring

red blood cell elasticity: application to the study of drug response in sickle cell disease. *European journal of haematology*, 70(4):207–11, Apr. 2003.

[20] R. J. Bruckner, S. S. Mansy, a. Ricardo, L. Mahadevan, and J. W. Szostak. Flip-flop-induced relaxation of bending energy: implications for membrane remodeling. *Biophysical journal*, 97(12):3113–22, Dec. 2009.

[21] C. Brunner, A. Niendorf, and J. a. Käs. Passive and active single-cell biomechanics: a new perspective in cancer diagnosis. *Soft Matter*, 5(11):2171, 2009.

[22] M. F. Callaghan, T. Lund, P. Hashemzadeh, I. M. Roitt, and R. H. Bayford. An investigation of the impedance properties of gold nanoparticles. *Journal of Physics: Conference Series*, 224:012058, Apr. 2010.

[23] J. M. Casolari, C. R. Brown, S. Komili, J. West, H. Hieronymus, and P. A. Silver. Genome-wide localization of the nuclear transport machinery couples transcriptional status and nuclear organization. *Cell*, 117(4):427–39, May 2004.

[24] E. O. F. Cell and U. A. Pulsed-laser. BRIEF COMMUNICATION ELECTROPORATION OF CELL MEMBRANE VISUALIZED UNDER A PULSED-LASER FLUORESCENCE MICROSCOPE. *Biophysical Journal*, 53(June):1015–1019, 1988.

[25] E. S. Chen, K. Zhang, E. Nicolas, H. P. Cam, M. Zofall, and S. I. S. Grewal. Cell cycle control of centromeric repeat transcription and heterochromatin assembly. *Nature*, 451(7179):734–7, Feb. 2008.

[26] S. Cheng, C. Fockler, W. M. Barnes, and R. Higuchi. Effective amplification of long targets from cloned inserts and human genomic DNA. *Proceedings of the National Academy of Sciences of the United States of America*, 91(12):5695–9, June 1994.

[27] D. P. Cherney, T. E. Bridges, and J. M. Harris. Optical trapping of unilamellar phospholipid vesicles: investigation of the effect of optical forces on the lipid membrane shape by confocal-Raman microscopy. *Analytical chemistry*, 76(17):4920–8, Sept. 2004.

[28] T. Cremer and M. Cremer. Chromosome territories. *Cold Spring Harbor perspectives in biology*, 2(3):a003889, Mar. 2010.

[29] D. R. Crow. *Principles and Applications of Electrochemistry*. Chapman and Hall, London, 1974.

[30] C. L. Curl, C. J. Bellair, T. Harris, B. E. Allman, P. J. Harris, A. G. Stewart, A. Roberts, K. a. Nugent, and L. M. D. Delbridge. Refractive index measurement in viable cells using quantitative phase-amplitude microscopy and confocal microscopy. *Cytometry. Part A : the journal of the International Society for Analytical Cytology*, 65(1):88–92, May 2005.

[31] J. Z. Dalgaard and A. J. Klar. swi1 and swi3 perform imprinting, pausing, and termination of DNA replication in S. pombe. *Cell*, 102(6):745–51, Sept. 2000.

[32] M.-C. Daniel and D. Astruc. Gold nanoparticles: assembly, supramolecular chemistry, quantum-size-related properties, and applications toward biology, catalysis, and nanotechnology. *Chemical reviews*, 104(1):293–346, Jan. 2004.

[33] M. Dao, C. Lim, and S. Suresh. Mechanics of the human red blood cell deformed by optical tweezers,òÜ. *Journal of the Mechanics and Physics of Solids*, 51(11-12):2259–2280, Nov. 2003.

[34] A. H. de Vries, S. Yefimov, A. E. Mark, and S. J. Marrink. Molecular structure of the lecithin ripple phase. *Proceedings of the National Academy of Sciences of the United States of America*, 102(15):5392–6, Apr. 2005.

[35] R. Dimova, S. Aranda, N. Bezlyepkina, V. Nikolov, K. a. Riske, and R. Lipowsky. A practical guide to giant vesicles. Probing the membrane nanoregime via optical microscopy. *Journal of Physics: Condensed Matter*, 18(28):S1151–S1176, July 2006.

[36] R. Dimova, N. Bezlyepkina, M. D. Jordö, R. L. Knorr, K. a. Riske, M. Staykova, P. M. Vlahovska, T. Yamamoto, P. Yang, and R. Lipowsky. Vesicles in electric fields: Some novel aspects of membrane behavior. *Soft Matter*, 5(17):3201, 2009.

[37] R. Dimova, K. a. Riske, S. Aranda, N. Bezlyepkina, R. L. Knorr, and R. Lipowsky. Giant vesicles in electric fields. *Soft Matter*, 3(7):817, 2007.

[38] R. Dimova, U. Seifert, B. Pouligny, S. Förster, and H. Döbereiner. Hyperviscous diblock copolymer vesicles. *The European Physical Journal E: Soft Matter and Biological Physics*, 7(3):241–250, 2002.

[39] D.-Q. Ding, A. Yamamoto, T. Haraguchi, and Y. Hiraoka. Dynamics of homologous chromosome pairing during meiotic prophase in fission yeast. *Developmental cell*, 6(3):329–41, Mar. 2004.

[40] Z. Duan, M. Andronescu, K. Schutz, S. McIlwain, Y. J. Kim, C. Lee, J. Shendure, S. Fields, C. A. Blau, and W. S. Noble. A three-dimensional model of the yeast genome. *Nature*, 465(7296):363–367, May 2010.

[41] R. Egel, editor. *The molecular biology of Schizosaccharomyces pombe. Genetics, genomics and beyond.* Springer-Verlag Berlin, Heidelberg, 2004.

[42] A. Egner and S. Hell. Fluorescence microscopy with super-resolved optical sections. *Trends in cell biology*, 2005.

[43] M. Fischer and K. Berg-Sø rensen. Calibration of trapping force and response function of optical tweezers in viscoelastic media. *Journal of Optics A: Pure and Applied Optics*, 9(8):S239–S250, Aug. 2007.

[44] C. E. Fritze, K. Verschueren, R. Strich, and R. Easton Esposito. Direct evidence for SIR2 modulation of chromatin structure in yeast rDNA. *The EMBO journal*, 16(21):6495–509, Nov. 1997.

[45] a. Gothelf. Electrochemotherapy: results of cancer treatment using enhanced delivery of bleomycin by electroporation. *Cancer Treatment Reviews*, 29(5):371–387, Oct. 2003.

[46] K. L. Gould. Protocols for experimentation with Schizosaccharomyces pombe. *Methods (San Diego, Calif.)*, 33(3):187–8, July 2004.

[47] R. S. Gracià, N. Bezlyepkina, R. L. Knorr, R. Lipowsky, and R. Dimova. Effect of cholesterol on the rigidity of saturated and unsaturated membranes: fluctuation and electrodeformation analysis of giant vesicles. *Soft Matter*, 6(7):1472, 2010.

[48] S. I. Grewal. RNAi-dependent formation of heterochromatin and its diverse functions. *Current opinion in genetics & development*, 20(2):134–41, Apr. 2010.

[49] S. I. Grewal and A. J. Klar. A recombinationally repressed region between mat2 and mat3 loci shares homology to centromeric repeats and regulates directionality of mating-type switching in fission yeast. *Genetics*, 146(4):1221–38, Aug. 1997.

[50] S. I. S. Grewal and S. C. R. Elgin. Heterochromatin: new possibilities for the inheritance of structure. *Current opinion in genetics & development*, 12(2):178–87, Apr. 2002.

[51] C. Grimm, J. Kohli, J. Murray, and K. Maundrell. Genetic engineering of Schizosaccharomyces pombe: a system for gene disruption and replacement using the ura4 gene as a selectable marker. *Molecular & general genetics : MGG*, 215(1):81–6, Dec. 1988.

[52] J. Guck, R. Ananthakrishnan, H. Mahmood, T. J. Moon, C. C. Cunningham, and J. Käs. The optical stretcher: a novel laser tool to micromanipulate cells. *Biophysical journal*, 81(2):767–84, Aug. 2001.

[53] I. M. Hall, G. D. Shankaranarayana, K.-I. Noma, N. Ayoub, A. Cohen, and S. I. S. Grewal. Establishment and maintenance of a heterochromatin domain. *Science (New York, N.Y.)*, 297(5590):2232–7, Sept. 2002.

[54] P. M. Hansen, V. K. l. Bhatia, N. Harrit, and L. Oddershede. Expanding the optical trapping range of gold nanoparticles. *Nano letters*, 5(10):1937–42, Oct. 2005.

[55] T. Heimburg. A model for the lipid pretransition: coupling of ripple formation with the chain-melting transition. *Biophysical journal*, 78(3):1154–65, Mar. 2000.

[56] T. Heimburg. *Thermal biophysics of membranes*. Wiley-VCH-Verlag GmbH, Weinheim, 2007.

[57] T. Heimburg and A. D. Jackson. The thermodynamics of general anesthesia. *Biophysical journal*, 92(9):3159–65, May 2007.

[58] D. Hernandez-Verdun. The nucleolus: a model for the organization of nuclear functions. *Histochemistry and cell biology*, 126(2):135–48, Aug. 2006.

[59] A. Holmes, A. Kaykov, and B. Arcangioli. Molecular and cellular dissection of mating-type switching steps in Schizosaccharomyces pombe. *Molecular and cellular*, 25(1):303–311, 2005.

[60] F. J. Iglesias, M. C. López, C. Santamaría, and a. Domínguez. Orientation of Schizosaccharomyces POMBE Nonliving Cells under Alternating Uniform and Nonuniform Electric Fields. *Biophysical journal*, 48(5):721–6, Nov. 1985.

[61] J. D. Jackson. *Classical electrodynamics*, volume 67. John Wiley & Sons, New York, third edit edition, 1999.

[62] P. Jain, I. El-Sayed, and M. El-Sayed. Au nanoparticles target cancer. *Nano Today*, 2(1):18–29, 2007.

[63] S. Jia, K.-I. Noma, and S. I. S. Grewal. RNAi-independent heterochromatin nucleation by the stress-activated ATF/CREB family proteins. *Science (New York, N.Y.)*, 304(5679):1971–6, June 2004.

[64] P. Jorgensen, N. P. Edgington, B. L. Schneider, I. Rupes, M. Tyers, and B. Futcher. The Size of the Nucleus Increases as Yeast Cells Grow. *Molecular Biology of the Cell*, 18(September):3523–3532, 2007.

[65] D. Kim, S. Park, J. H. Lee, Y. Y. Jeong, and S. Jon. Antibiofouling polymer-coated gold nanoparticles as a contrast agent for in vivo X-ray computed tomography imaging. *Journal of the American Chemical Society*, 129(24):7661–5, June 2007.

[66] E. Kitamura, J. J. Blow, and T. U. Tanaka. Live-cell imaging reveals replication of individual replicons in eukaryotic replication factories. *Cell*, 125(7):1297–308, June 2006.

[67] A. Kloc, M. Zaratiegui, E. Nora, and R. Martienssen. RNA interference guides histone modification during the S phase of chromosomal replication. *Current biology : CB*, 18(7):490–5, Apr. 2008.

[68] C. Kojima, Y. Hirano, and K. Kono. Preparation of Complexes of Liposomes with Gold Nanoparticles. *Methods in enzymology*, 464(09):131–145, 2009.

[69] G. Krings and D. Bastia. swi1- and swi3-dependent and independent replication fork arrest at the ribosomal DNA of Schizosaccharomyces pombe. *Proceedings of the National Academy of Sciences of the United States of America*, 101(39):14085–90, Sept. 2004.

[70] G. Krings and D. Bastia. Sap1p binds to Ter1 at the ribosomal DNA of Schizosaccharomyces pombe and causes polar replication fork arrest. *The Journal of biological chemistry*, 280(47):39135–42, Nov. 2005.

[71] U. Leupold. Methodisches zur Genetik von Schizosaccharomyces pombe. 18:1141–1146, 1955.

[72] R. Lipowsky and H.-G. Döbereiner. Vesicles in contact with nanoparticles and colloids. *Europhysics Letters (EPL)*, 43(2):219–225, July 1998.

[73] Y. Liu, G. Sonek, M. Berns, and B. Tromberg. Physiological monitoring of optically trapped cells: assessing the effects of confinement by 1064-nm laser tweezers using microfluorometry. *Biophysical journal*, 1996.

[74] S. J. Lo, C.-C. Lee, and H.-J. Lai. The nucleolus: reviewing oldies to have new understandings. *Cell research*, 16(6):530–8, June 2006.

[75] L. a. MacQueen, M. D. Buschmann, and M. R. Wertheimer. Mechanical properties of mammalian cells in suspension measured by electro-deformation. *Journal of Micromechanics and Microengineering*, 20(6):065007, June 2010.

[76] D. Marsh. Elastic curvature constants of lipid monolayers and bilayers. *Chemistry and physics of lipids*, 144(2):146–59, 2006.

[77] L. Mathivet, S. Cribier, and P. F. Devaux. Shape Change and Physical Properties of Giant Phospholipid Vesicles Prepared in the Presence of an AC Electric Field Characterization of giant vesicles. *Biophysical Journal*, 70(March):1112–1121, 1996.

[78] B. Matsumoto, editor. *Cell Biological Applications of Confocal Microscopy.* Academic Press, 2 edition, 1992.

[79] Y. Matsuo, H. Kishimoto, T. Horiuchi, K. Tanae, and M. Kawamukai. Simple and Effective Gap-Repair Cloning Using Short Tracts of Flanking Homology in Fission Yeast. *Bioscience, Biotechnology, and Biochemistry*, 74(3):685–689, 2010.

[80] A. Matsuyama, R. Arai, Y. Yashiroda, A. Shirai, A. Kamata, S. Sekido, Y. Kobayashi, A. Hashimoto, M. Hamamoto, Y. Hiraoka, S. Horinouchi, and M. Yoshida. ORFeome cloning and global analysis of protein localization in the fission yeast Schizosaccharomyces pombe. *Nature biotechnology*, 24(7):841–7, July 2006.

[81] P. Meister, A. Taddei, A. Ponti, G. Baldacci, and S. M. Gasser. Replication foci dynamics: replication patterns are modulated by S-phase checkpoint kinases in fission yeast. *The EMBO journal*, 26(5):1315–26, Mar. 2007.

[82] E. Mejia-Ramirez, A. Sanchez-Gorostiaga, D. Krimer, J. Schvartzman, and P. Hernandez. The mating type switch-activating protein Sap1 is required for replication fork arrest at the rRNA genes of fission yeast. *Molecular and cellular biology*, 25(19):8755, 2005.

[83] P. Méléard, L. Bagatolli, and T. Pott. Giant Unilamellar Vesicle Electroformation : From Lipid Mixtures to Native Membranes Under Physiological Conditions. *Methods in enzymology*, 465(09):161–176, 2009.

[84] L.-R. Montes, A. Alonso, F. M. Goñi, and L. a. Bagatolli. Giant unilamellar vesicles electroformed from native membranes and organic lipid mixtures under physiological conditions. *Biophysical journal*, 93(10):3548–54, Nov. 2007.

[85] O. Mouritsen. *Life-as a matter of fat: the emerging science of lipidomics.* Springer-Verlag, Berlin Heidelberg, 2005.

[86] Nakayama Jun-ichi, R. C. Allshire, A. J. Klar, and S. I. Grewal. A role for DNA polymerase α in epigenetic control of transcriptional silencing in fission yeast. *The EMBO journal*, 20(11):2857–66, June 2001.

[87] D. Needham. Electro-mechanical permeabilization of lipid vesicles Role of membrane tension and compressibility Micropipet manipulation. 55(May):1001–1009, 1989.

[88] K. Neuman and S. Block. Optical trapping. *Review of Scientific Instruments*, 2004.

[89] E. Neumann, S. Kakorin, and K. Toensing. Fundamentals of electroporative delivery of drugs and genes. *Bioelectrochemistry and bioenergetics (Lausanne, Switzerland)*, 48(1):3–16, Feb. 1999.

[90] F. R. Neumann and P. Nurse. Nuclear size control in fission yeast. *The Journal of cell biology*, 179(4):593–600, Nov. 2007.

[91] J. A. Nicoloff. *Animal cell electroporation and electrofusion protocols.* Human Press Inc., New Jersey, 1995.

[92] E. Noguchi, C. Noguchi, L.-l. Du, and P. Russell. Swi1 Prevents Replication Fork Collapse and Controls Checkpoint Kinase Cds1. *Society*, 23(21):7861–7874, 2003.

[93] E. Noguchi, C. Noguchi, W. H. Mcdonald, J. R. Y. Iii, and P. Russell. Swi1 and Swi3 Are Components of a Replication Fork Protection Complex in Fission Yeast. *Society*, 24(19):8342–8355, 2004.

[94] Noma K, C. D. Allis, and S. I. Grewal. Transitions in distinct histone H3 methylation patterns at the heterochromatin domain boundaries. *Science (New York, N.Y.)*, 293(5532):1150–5, Aug. 2001.

[95] B. Novak, A. Csikasz-Nagy, B. Gyorffy, K. Chen, and J. J. Tyson. Mathematical model of the fission yeast cell cycle with checkpoint controls at the G1/S, G2/M and metaphase/anaphase transitions. *Biophysical chemistry*, 72(1-2):185–200, May 1998.

[96] E. Nunez, X.-D. Fu, and M. G. Rosenfeld. Nuclear organization in the 3D space of the nucleus - cause or consequence? *Current opinion in genetics & development*, 19(5):424–36, Oct. 2009.

[97] L. Oddershede, J. Dreyer, S. Grego, and S. Brown. The Motion of a Single Molecule, the λ-Receptor, in the Bacterial Outer Membrane. *Biophysical journal*, 2002.

[98] L. Oddershede and H. Flyvbjerg. Single-molecule experiment with optical tweezers: improved analysis of the diffusion of the λ-receptor in E. coli's outer membrane. *Journal of Physics: Condensed Matter*, 2003.

[99] L. Oddershede, S. Grego, and S. Nø rrelykke. Optical tweezers: probing biological surfaces. *Probe Microscropy*, 2:129–137, 2001.

[100] R. Of, O. Hydrocortisone, T. Lipid, B. Prolongation, A. Incorporated, I. Liposomes, C. Arthritis, and E. Method. Experimental method. *Sciences-New York*, 97(6):656–658, 1984.

[101] C. S. Osborne, L. Chakalova, K. E. Brown, D. Carter, A. Horton, E. Debrand, B. Goyenechea, J. A. Mitchell, S. Lopes, W. Reik, and P. Fraser. Active genes dynamically colocalize to shared sites of ongoing transcription. *Nature genetics*, 36(10):1065–71, Oct. 2004.

[102] M. Osumi, M. Konomi, T. Sugawara, T. Takagi, and M. Baba. High-pressure freezing is a powerful tool for visualization of Schizosaccharomyces pombe cells: ultra-low temperature and low-voltage scanning electron microscopy and immunoelectron microscopy. *Yeast*, 55(April):75–88, 2006.

[103] G. Pabst, H. Amenitsch, D. Kharakoz, P. Laggner, and M. Rappolt. Structure and fluctuations of phosphatidylcholines in the vicinity of the main transition. *Physical Review E*, 70:021908, 2004.

[104] J. B. Pawley, editor. *Handbook of Biological Confocal Microscopy.* Springer Science&Business Media, 2006.

[105] P. Peterlin. Frequency-dependent electrodeformation of giant phospholipid vesicles in AC electric field. *Journal of Biological Physics*, Mar. 2010.

[106] E. J. G. Peterman, F. Gittes, and C. F. Schmidt. Laser-induced heating in optical traps. *Biophysical journal*, 84(2 Pt 1):1308–16, Feb. 2003.

[107] E. Phez, C. Faurie, M. Golzio, J. Teissié, and M.-P. Rols. New insights in the visualization of membrane permeabilization and DNA/membrane interaction of cells submitted to electric pulses. *Biochimica et biophysica acta*, 1724(3):248–54, Aug. 2005.

[108] D. Pissuwan, S. M. Valenzuela, and M. B. Cortie. Therapeutic possibilities of plasmonically heated gold nanoparticles. *Trends in biotechnology*, 24(2):62–7, Feb. 2006.

[109] B.-K. Pong, H. Elim, J.-X. Chong, W. Ji, B. Trout, and J.-Y. Lee. New Insights on the Nanoparticle Growth Mechanism in the Citrate Reduction of Gold(III) Salt: Formation of the Au Nanowire Intermediate and Its Nonlinear Optical Properties. *Journal of Physical Chemistry C*, 111(17):6281–6287, May 2007.

[110] T. Pott, H. Bouvrais, and P. Méléard. Giant unilamellar vesicle formation under physiologically relevant conditions. *Chemistry and physics of lipids*, 154(2):115–9, Aug. 2008.

[111] T. W. Remmerbach, F. Wottawah, J. Dietrich, B. Lincoln, C. Wittekind, and J. Guck. Oral cancer diagnosis by mechanical phenotyping. *Cancer research*, 69(5):1728–32, Mar. 2009.

[112] A. C. Richardson, N. Reihani, and L. B. Oddershede. Combining confocal microscopy with precise force-scope optical tweezers. *Proceedings of SPIE*, 6326:632628–632628–10, 2006.

[113] K. a. Riske, R. P. Barroso, C. C. Vequi-Suplicy, R. Germano, V. B. Henriques, and M. T. Lamy. Lipid bilayer pre-transition as the beginning of the melting process. *Biochimica et biophysica acta*, 1788(5):954–63, May 2009.

[114] K. a. Riske and R. Dimova. Electric pulses induce cylindrical deformations on giant vesicles in salt solutions. *Biophysical journal*, 91(5):1778–86, Sept. 2006.

[115] N. Rodriguez, F. Pincet, and S. Cribier. Giant vesicles formed by gentle hydration and electroformation: a comparison by fluorescence microscopy. *Colloids and surfaces. B, Biointerfaces*, 42(2):125–30, May 2005.

[116] A. Rohrbach. Stiffness of Optical Traps: Quantitative Agreement between Experiment and Electromagnetic Theory. *Physical Review Letters*, 95(16):1–4, Oct. 2005.

[117] I. Rupes. Checking cell size in yeast. *Trends in genetics*, 18(9):479–85, Sept. 2002.

[118] J. Sáez-Vásquez and O. Gadal. Genome Organization and Function: A View from Yeast and Arabidopsis. *Molecular plant*, 3(4), July 2010.

[119] S. A. Safran and A. Zemel. IUTAM Symposium on Cellular, Molecular and Tissue Mechanics. *Nature Physics*, 16:91–101, 2010.

[120] H. Santos-Rosa, A. J. Bannister, P. M. Dehe, V. Géli, and T. Kouzarides. Methylation of H3 lysine 4 at euchromatin promotes Sir3p association with heterochromatin. *The Journal of biological chemistry*, 279(46):47506–12, Nov. 2004.

[121] K. C. Scott, S. L. Merrett, and H. F. Willard. A heterochromatin barrier partitions the fission yeast centromere into discrete chromatin domains. *Current biology*, 16(2):119–29, Jan. 2006.

[122] C. Selhuber-Unkel, P. Yde, K. Berg-Sø rensen, and L. B. Oddershede. Variety in intracellular diffusion during the cell cycle. *Physical biology*, 6(2):025015, Jan. 2009.

[123] G. Singh and A. Klar. DNA sequences flank the mat2, 3 silent region in two species of Schizosaccharomyces and are involved in epigenetic silencing in Schizosaccharomyces pombe. *Genetics*, 602(October):591–602, 2002.

[124] G. Singh and A. Klar. Mutations in deoxyribonucleotide biosynthesis pathway cause spreading of silencing across heterochromatic barriers at the mating-type region of the fission yeast. *Yeast*, 25(2):117–128, 2008.

[125] J. P. Spatz and R. Kemkemer. IUTAM Symposium on Cellular, Molecular and Tissue Mechanics. *Biophysical Journal*, 16, 2010.

[126] K. Svoboda and S. Block. Biological applications of optical forces. *Annual Review of Biophysics and Biomolecular Structure*, 23(1):247–-285, 1994.

[127] A. Taddei and S. M. Gasser. Repairing subtelomeric DSBs at the nuclear periphery. *Trends in cell biology*, 16(5):225–8, May 2006.

[128] P. Therizols, C. Fairhead, G. G. Cabal, A. Genovesio, J.-C. Olivo-Marin, B. Dujon, and E. Fabre. Telomere tethering at the nuclear periphery is essential for efficient DNA double strand break repair in subtelomeric region. *The Journal of cell biology*, 172(2):189–99, Jan. 2006.

[129] G. Thon, P. Bjerling, C. M. Bünner, and J. Verhein-Hansen. Expression-state boundaries in the mating-type region of fission yeast. *Genetics*, 161(2):611–22, June 2002.

[130] G. Thon and J. Verhein-Hansen. Four chromo-domain proteins of Schizosaccharomyces pombe differentially repress transcription at various chromosomal locations. *Genetics*, 155(2):551–68, June 2000.

[131] B. D. Towbin, P. Meister, and S. M. Gasser. The nuclear envelope– a scaffold for silencing? *Current opinion in genetics & development*, 19(2):180–6, Apr. 2009.

[132] A. Verdel, A. Vavasseur, M. Le Gorrec, and L. Touat-Todeschini. Common themes in siRNA-mediated epigenetic silencing pathways. *The International journal of developmental biology*, 53(2-3):245–57, Jan. 2009.

[133] P. M. Vlahovska, R. S. Gracià, S. Aranda-Espinoza, and R. Dimova. Electrohydrodynamic model of vesicle deformation in alternating electric fields. *Biophysical journal*, 96(12):4789–803, June 2009.

[134] M. Winterhalter. Deformation of spherical vesicles by electric fields. *Journal of Colloid and Interface Science*, 122(2):583–586, Apr. 1988.

[135] X. Xu, Z. Yu, Y. Zhu, and B. Wang. Effect of sodium oleate adsorption on the colloidal stability and zeta potential of detonation synthesized diamond particles in aqueous solutions. *Diamond and Related Materials*, 14(2):206–212, Feb. 2005.

[136] T. Yamada, W. Fischle, T. Sugiyama, C. D. Allis, and S. I. S. Grewal. The nucleation and maintenance of heterochromatin by a histone deacetylase in fission yeast. *Molecular cell*, 20(2):173–85, Oct. 2005.

[137] H. Zhang and K.-K. Liu. Optical tweezers for single cells. *Journal of the Royal Society, Interface / the Royal Society*, 5(24):671–90, July 2008.

[138] U. Zimmermann. Electric field-mediated fusion and related electrical phenomena. *Biochimica et biophysica acta*, 694:227–277, 1982.